Tether and Reinforcement Effects on Streptavidin-Biotin, and Induced Binding in Nanoapertures

Leonard C. Schendel

München 2020

Tether and Reinforcement Effects on Streptavidin-Biotin, and Induced Binding in Nanoapertures

Leonard C. Schendel

Dissertation
an der Fakultät für Physik
der Ludwig-Maximilians-Universität
München

vorgelegt von
Leonard Christian Schendel
aus München

München, den 08.05.2020

Erstgutachter: Prof. Dr. Hermann E. Gaub
Zweitgutachter: Prof. Dr. Joachim O. Rädler
Tag der mündlichen Prüfung: 26.06.2020

Zusammenfassung

Die Natur hat eine Vielzahl von winzigen Funktionseinheiten hervorgebracht, die es Zellen erlauben, mechanischen Kräften standzuhalten, diese wahrzunehmen und in biochemische Signale umzuwandeln. Das ermöglicht es ihnen, auf Umwelteinflüsse zu reagieren und mit ihrer Außenwelt zu interagieren. Dabei basiert die Funktionsweise der Mechanosensorik und Mechanotransduktion auf einer Konformationsänderung dieser durch Kraft regulierten Proteine. Hierbei verursacht ein mechanischer Stimulus beispielsweise die Freilegung einer im Protein befindlichen Bindungs-, Phosphorylierungs- oder enzymatisch aktiven Region, deren assoziierten Folgereaktionen die biochemische Signalkaskade in Gang setzen. Diese verschiedenen Pfade zum Auslösen eines Signals werden mit Hilfe von Einzelmolekülkraftspektroskopie untersucht, um mechanosensorische Proteine als solche zu identifizieren und einen tieferen Einblick in den zugrundeliegenden Mechanismus zu gewinnen. Viele der Techniken, die in der Mechanobiologie genutzt werden, verwenden dabei den Rezeptor-Ligand-Komplex Streptavidin-Biotin. Das Protein Streptavidin von *Streptomyces avidinii* besitzt eine femtomolare Affinität zu dem Molekül Biotin. Dabei gehört deren Bindung mit zu den stärksten bekannten, nicht kovalenten Bindungen und bleibt auch unter unwirtlichen Bedingungen und bei hohen Temperaturen stabil. Die Biotin-Streptavidin-Interaktion ist deswegen eine der am meist genutzten Rezeptor-Ligand-Verbindungen in der Biotechnologie als auch in der Medizin als System zur Fixierung, Detektion oder Verknüpfung von Molekülen oder Nanopartikeln. Genau aus diesen Gründen erfährt das Streptavidin-Biotin-System in vielen Studien ein vermehrtes Interesse als Forschungsobjekt.

Ein wesentliches Ziel dieser Arbeit bestand darin, ein tieferes Verständnis der mechanischen Stabilität des Streptavidin-Biotin-Komplexes zu erlangen. Im Zuge dessen wurde die Abhängigkeit der Stabilität von der Verankerungsposition innerhalb des Streptavidin-Moleküls untersucht. In Kapitel 3.1 wurde dafür die einzelne funktionale Untereinheit eines monovalenten Streptavidin-Tetramers jeweils mit dem N- oder C-Terminus ortsspezifisch an der Probenoberfläche verankert. Einzelmolekülkraftspektroskopie basierend auf Rasterkraftmikroskopie zeigte, dass der Streptavidin-Biotin-Komplex durch C-terminale Verankerung doppelt so starken Kräften, verglichen mit dem Fall der Verankerung am N-Terminus, standhalten konnte. Bei diesem Experiment ermöglichte die Einführung eines zweiten Rezeptor-Ligand-Systems, das als Kraftüberträger von der Spitze des Rasterkraftmikroskops auf das Untersuchungsobjekt fungierte, das Erfassen großer Datensätze. Zusätzlich wurden Molekulardynamiksimulationen des Streptavidin-Biotin-Komplexes durchgeführt. Bei diesen Simulationen wurde, unter Berücksichtigung aller Atome, der Ligand Biotin vom Rezeptor Streptavidin durch das Anlegen einer Kraft separiert, wobei die molekulare Verankerungsposition wie im *in vitro* Experiment variiert wurde. Die Ergebnisse dieser *in silico* erzwungenen Trennung des Rezeptor-Ligand-Komplexes lieferten Einblicke in den zugrundeliegenden Mechanismus und enthüllten darüber hinaus einen Dissoziationspfad für die N-terminale Verankerung, bei dem sich das erste β-Faltblatt teilweise entfaltete.

Die Resultate dieser partiellen Entfaltung in N-terminaler Zuggeometrie dienten als Inspiration für eine gentechnisch konstruierte Disulfidbrücke, die die betroffenen ersten beiden β-Stränge kovalent miteinander verknüpfen sollte. Um solch eine intramolekulare Disulfidbindung zu schaffen wurden zwei Aminosäuren, die sich jeweils im ersten und zweiten β-Strang befinden, durch die schwefelhaltige Aminosäure Cystein ersetzt. Die Ergebnisse, dargestellt in Kapitel 3.2, zeigen, dass für ein Streptavidin mit einer verstärkten N-terminalen Region eine eineinhalb mal größere Kraft zur Dissoziation von Biotin notwendig ist. In diesem Zusammenhang war es möglich, durch Zugabe eines Reduktionsmittels die Disulfidbindungen aufzulösen und damit die notwendige Kraft zur Dissoziation auf den Ursprungswert zu senken. Das Wiederherstellen einer oxidativen Umgebung ermöglichte die Rückkehr zu dem Ausgangszustand eines verstärkten Streptavidins. Diese Arbeit stellt damit einen experimentellen Beleg eines molekularen Mechanismus dar, der zuvor durch Molekulardynamiksimulationen entdeckt wurde und zeigt zudem auf, in welchem Maß die Entfaltung eines Proteins zur mechanisch erzwungenen Dissoziation eines Protein-Ligand-Komplexes beitragen kann.

Der zweite wesentliche Bestandteil dieser Arbeit war die Entwicklung eines vollautomatisierten, kombinierten, Fluoreszenz-Rasterkraftmikroskopie-Experiments, das in der Lage ist, mechanisch aktive Proteine zu untersuchen und zu identifizieren. Hierbei stellen geringe Affinitäten und hohe Michaeliskonstanten mechanosensorischer Proteine eine Herausforderung dar. Das hat zur Folge, dass nach einer mechanisch herbeigeführten Konformationsänderung hohe Substratkonzentrationen notwendig sind, um Folgereaktionen, die durch die Freilegung der reaktiven Region in Gang gesetzt werden, beobachten zu können. Kapitel 4.1 zeigt eine Möglichkeit auf, wie mit Hilfe von Nanostrukturen, die das beleuchtete Volumen reduzieren, Fluoreszenzsignale einzelner Moleküle trotz hoher Fluorophorkonzentration beobachtet werden können. Kombiniert wurden diese Nanostrukturen mit Einzelmolekülkraftspektroskopie basierend auf Rasterkraftmikroskopie. Mit Hilfe von Routinen zur Driftkorrektur und einer minimalinvasiven Methode zur Lokalisierung der Rasterkraftmikroskopiespitze konnte so eine automatisierte Technik geschaffen werden, die es erlaubt, in dichten fluoreszenten Bedingungen zu arbeiten. Um die Leistungsfähigkeit dieses Versuchsaufbaus zu testen, wurde der Streptavidin-Biotin-Komplex verwendet. Dabei wurde die mechanische Freilegung einer Biotin-Bindungstasche als Modell zur Kraftaktivierung genutzt und das zweite Rezeptor-Ligand-System, eingeführt in Kapitel 3.1, diente dazu, Biotin aus einer Streptavidin-Untereinheit zu ziehen. Die durch das Rasterkraftmikroskop verursachte mechanische Spannung legt die Bindungstasche frei, sodass das Binden eines fluoreszierenden Biotin-Moleküls an die nun zugängliche Streptavidin-Untereinheit beobachtet werden konnte. Auf diese Weise ist es möglich, in den erwähnten Nanostrukturen die Assoziation von Protein und Substrat nach mechanisch induzierter Freilegung einer zuvor unzugänglichen Proteinregion sichtbar zu machen.

Abstract

Nature has evolved a variety of nanometer sized devices which enable cells to withstand as well as to sense mechanical stimuli and transduce them into biochemical signals. With these tools, the cell can respond to external stimuli and interact with its environment. The process of mechanosensing and mechanotransduction relies on conformational changes of a mechanosensory protein induced by a force stimulus. Upon exertion of force, a cryptic binding, a phosphorylation or an enzymatically active site, for instance, can be exposed and its associated consecutive reactions initiate biochemical signaling. These activation pathways are investigated by means of single-molecule force spectroscopy to identify mechanosensory proteins and to decipher the underlying molecular mechanisms. Many of the single-molecule techniques used for mechanobiology assays, for example magnetic and optical tweezers or atomic force microscopy, rely on streptavidin-biotin complex. The protein streptavidin from *Streptomyces avidinii* has a femtomolar affinity for the small molecule biotin. Their bond is amongst the strongest non-covalent bonds known, and remains stable under harsh conditions and at high temperatures. The streptavidin-biotin interaction is therefore one of the most widely used receptor-ligand interactions in biotechnology as well as in medicine as a system for the fixation, detection or linkage of molecules or nanoparticles. It is precisely for these reasons that this system has repeatedly been a research object in many studies.

One main objective of this thesis was to gain deeper insights into the mechanical stability of the streptavidin-biotin complex, in particular its dependence on the intramolecular site at which the streptavidin molecule is tethered to the sample surface. In Section 3.1, the single functional subunit of a monovalent streptavidin tetramer was tethered either by its N- or C-terminus by using site-specific immobilization. Single-molecule force spectroscopy based on atomic force microscopy showed that by C-terminal tethering, the streptavidin-biotin complex can withstand forces twice as high as by N-terminal tethering. Here, the introduction of a second receptor-ligand system, utilized as a force transmitter between atomic force microscopy cantilever and the protein of interest, allowed the acquisition of large datasets. Furthermore, all-atom steered molecular dynamics simulations were performed on the streptavidin-biotin complex, taking account of the molecular anchoring points utilized in the *in vitro* experiment. The *in silico* forced separation of the complex gave insight into the underlying molecular mechanism. In addition, it revealed an unbinding pathway for N-terminal anchoring, which featured partial unfolding of the first β-sheet.

The finding of this partial unfolding in N-terminal tethering geometry inspired a genetically engineered disulfide bond which cross-links the first two β-strands. To create an intramolecular disulfide bond, two amino acids within the first and second β-strand were substituted by cysteines. Section 3.2 reports 1.5 times higher rupture forces for streptavidin with a reinforced N-terminus investigated by single-molecule

force spectroscopy based on atomic force microscopy. Additionally, it was possible to show that the disulfide bond breaks in the presence of a reducing reagent and that switching back to oxidizing conditions can promote the disulfide bond's recovery. This work provides experimental confirmation of a molecular mechanism previously discovered by steered molecular dynamics simulation and demonstrates to what extent protein unfolding may contribute to mechanically driven dissociation of a protein-ligand complex.

The second main objective was to develop a fully automated, combined fluorescence atomic force microscopy setup able to investigate and identify mechanoactive proteins. Here, low affinities and high Michaelis constants of mechanosensory proteins pose a challenge for experimental approaches whose goal is to directly observe mechanotransduction – after a force-induced conformational change, high substrate concentrations are required to be able to observe consecutive reactions promoted by the exposed reaction site. In Section 4.1, nanoapertures, which reduce the illuminated volume, were combined with single-molecule force spectroscopy based on an atomic force microscope. Together with drift-correction routines and noninvasive cantilever localization, a fully automatic technique able to perform in dense fluorescent substrate conditions was created. To test the performance range, the streptavidin-biotin system was used to mimic a force-activatable system. A construct featuring biotin and the ligand of the second receptor-ligand system introduced in Section 3.1 was used to block the biotin binding pocket of monovalent streptavidin. Then, mechanical tension induced by an atomic force microscope cantilever released the blocked binding pocket. Thus, binding of a fluorescent biotin was observed. Thereby, the conducted measurements showed binding after mechanical exposure of a cryptic binding site in nanoapertures.

Contents

Part I

Introduction

Introduction

Single-molecule techniques have emerged to become powerful tools in biotechnology, enabling the investigation of dynamics and structures within and in between single molecules. Divided in single-molecule imaging and single-molecule manipulation, they allow to measure dynamics and mechanistic properties of single molecules or receptor-ligand systems [1]. Detached from ensemble-averaging, they provide detailed information on individual dynamics of single molecules and enable the investigation of low-probability events. Two well-known single-molecule techniques that are based on fluorescence are total internal reflection fluorescence (TIRF) microscopy and the nanophotonic devices zero-mode waveguides (ZMWs). By reduction of the illumination volume both techniques allow the observation of single molecules despite the presence of fluorophores in bulk solution [2, 3]. Here, ZMWs in contrast to TIRF are able to provide clear single-molecule signals in up to micromolar fluorophore concentrations [3]. In this way, the use of ZMWs allowed the observation of single nucleotide incorporation events of a DNA polymerase that operates efficiently in nucleotide concentrations of 0.1 to 10 μM [4].

Single-molecule manipulation techniques, in turn, are used to perform force spectroscopy in order to decipher mechanics of receptor-ligand complexes, protein stability and mechanoenzymatics [5, 6]. Techniques to manipulate single molecules include magnetic tweezers [7], optical tweezers [8] and atomic force microscopy (AFM) [9, 10]. All these methods tether the system of interest in between artificial structures such as nanoparticles, glass slides or AFM tips and induce tension by moving the tether points apart.

In a myriad of studies, those manipulation techniques have demonstrated their potential to unravel mechanisms of receptor-ligand and protein complexes. Regarding these complexes, those methods are applied to investigate the unbinding behavior under mechanical tension. Considering the bound state trapped in a potential well, it needs to overcome its surrounding barriers in order to cause dissociation (*cf.* Figure 1). In the case of zero force, the escape can be achieved by following different pathways as thermal excitation can sample the energy landscape. So, for thermal unbinding, the system is prone to take the easiest 'ascent' along the energy landscape. This multitude of pathways can be probed by bulk, zero-force assays like surface plasmon resonance. Mechanically forced unbinding, in turn, assigns a direction through the energy landscape by exerting tension on the system [6]. The selection of direction can be influenced experimentally by defining the attachment geometry of the receptor molecule. Thus, for a forced unbinding, the system does not necessarily face the same energy landscape and barriers along the reaction coordinate compared to thermal unbinding and therefore it may encounter higher energy barriers. Similarly, different force-loading geometries will have different effects on the selected pathway through this complex, multidimensional free energy landscape. In single-molecule force

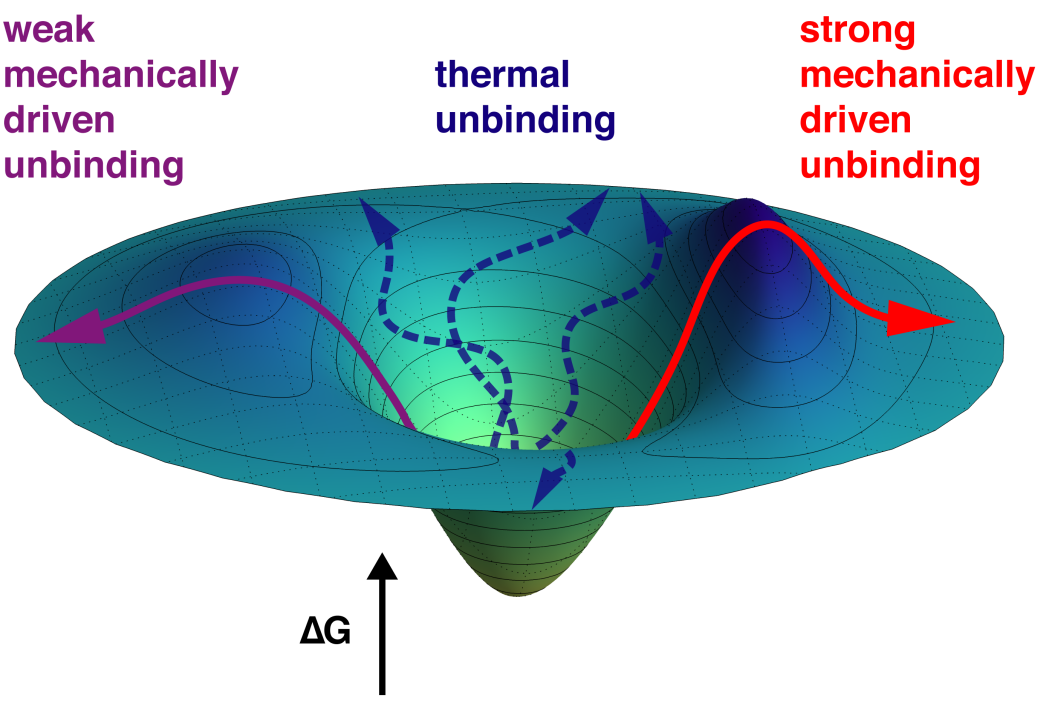

Figure 1: Schematic free energy landscape of a receptor-ligand complex in configuration space. The state of bound receptor-ligand complex is located on the bottom of the potential well. Blue dashed lines show the variety of unbinding pathways for thermal unbinding, whereas colored solid lines show unbinding pathways induced by mechanical force. Different mechanically driven unbinding pathways can be caused by differences in force-loading geometry. Compare Milles and Gaub [6].

spectroscopy (SMFS), a receptor protein can be tethered almost arbitrarily, however the most appealing sites are the N- and C-terminus (*cf.* Publication 4, Section 5.1). Regarding multimeric protein complexes, the attachment can be realized in even more ways (*cf.* Publication 6, Section 5.3). In the context of alternating force-loading geometries (*cf.* Figure 1), two different unbinding pathways which feature a weak and strong unbinding force were able to be identified for the interaction between streptavidin (SA) and biotin by changing the attachment point of the receptor protein from N- to C-terminus (*cf.* Publication 1, Section 3.1). This study further revealed a pathway in which partial unfolding of the protein occurred, representing a low-force unbinding pathway along the energy landscape. Increasing the stability of the concerned molecular region by protein engineering as a direct response to this finding allowed the switching of unbinding pathways (*cf.* Publication 2, Section 3.2). This directly addresses the question of how close unbinding and unfolding can be intertwined [11].

Taking advantage of both, single-molecule imaging and manipulation techniques, in a combined setup allows for the simultaneous acquisition of biochemical and biomechanical information on the molecule of interest. In addition, combining both techniques can provide a more detailed picture of dynamics and facilitates the inves-

tigation of force-regulated proteins. Thus, the combination of the aforementioned single-molecule techniques ZMW and AFM-based SMFS allows to gain mechanical properties synchronously with the observation of substrate or ligand association in dense fluorescent environments [12]. Persistent challenges in this area of research were tackled with the implementation of site-specificity in molecule attachment, stable fluorescent conditions and a fully automated, non-invasive measurement routine. Moreover, performance on a well-known protein model system was shown (*cf.* Publication 3, Section 4.1).

In the context of combining single-molecule techniques, hybrid approaches have to be mentioned as well. They pair single-molecule fluorescence with molecular tension sensors, thereby forming the emerging field of molecular tension fluorescence microscopy (MTFM) [13]. One application for MTFM, for example, is the investigation of transient mechanical events in the field of cell mechanobiology [14]. On a similar basis, molecular tension switches, such as the switch-like fluorescent protein dronpa, represent a potential tool for mechanobiology investigation using optogenetics (*cf.* Publication 5, Section 5.2).

Part II

Scientific Context

Chapter 1

Force Spectroscopy on Single Biomolecules

Force spectroscopy on single biomolecules provides detailed insights into the mechanics of protein complexes. One can not only investigate the mechanics of protein stability but also different types of interactions – between proteins themselves or between proteins and small molecules [6, 15]. In addition, it is used to study mechanoactive proteins [5] – proteins that bear cryptic reactive sites which are exposed by mechanical tension [16]. Several techniques exist to elicit mechanical properties of single molecules, like magnetic tweezers [7], optical tweezers [8], acoustic force spectroscopy [17] and AFM [10, 18]. In order to clamp and investigate single molecules, the system of interest is tethered in between artificial structures such as nanoparticles, glass slides and AFM cantilever tips and tension is induced by moving the tether points apart. For this purpose, the choice of the tethering site and the attachment chemistry applied is of great importance, since they define the pulling geometry. In the scope of this thesis, SMFS on the SA-biotin complex was performed using AFM, whose basic principles are outlined in the following chapter.

1.1 Single-Molecule Force Spectroscopy using Atomic Force Microscopy

AFM was developed by Binnig *et al.* as a type of scanning probe microscopy, able to measure forces on single atoms and to record topographic surface images with nanometer resolution [19]. Adopted for the purposes of single-molecule or single-cell manipulation in the field of life-science, it constitutes a powerful tool for mechanobiology ever since [20]. From a simple perspective SMFS based on AFM can be imagined as follows. The molecule of interest, *e.g.* a protein, is fixed with one end onto a surface while the other end is attached to the lower end of a force gauge like a spring scale. Then, the upper end of the spring scale is being lifted, which will induce increasing tension on the protein. This tension can be read off the spring

scale as force. At a certain force, the protein will unfold, causing the spring scale to relax as force drops. By recording the lifting distance, a force distance graph can be plotted similar to the graph shown in Figure 1.1 B.

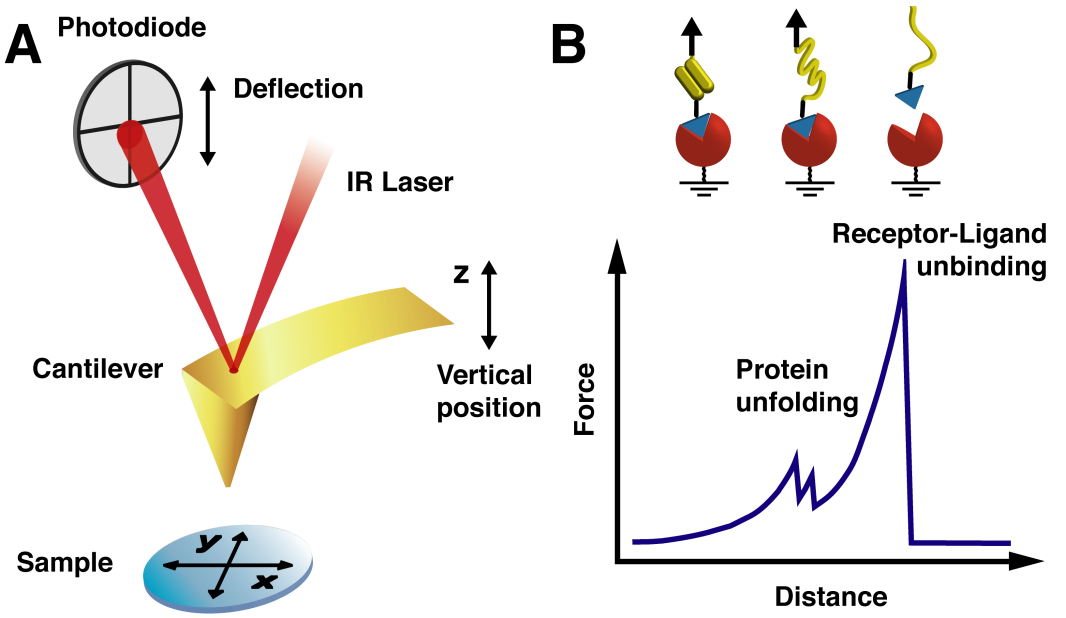

Figure 1.1: Schematic overview of SMFS based on AFM. **A**, deflection of the cantilever changes the position of the reflected spot on the photodiode. The corresponding differential signal is converted into force which acts on the cantilever. The vertical position of the cantilever is controlled by a piezo actuator. This position information serves to calculate the distance signal. **B** shows a schematic force vs. distance curve of a single-molecule experiment using a receptor-ligand system (red sphere, blue triangle) and a protein consisting of two domains (yellow). Retraction of the cantilever with constant velocity induces increasing tension on the protein complex. As long as the protein fold withstands the force exerted on it, the cantilever is further deflected during continuous retraction. Then, the first protein domain unfolds (first peak in graph) and releases additional contour length. Force drops. After unfolding of the second domain (second peak) force increases. The last peak shows receptor-ligand dissociation which breaks the tether between cantilever and sample surface. Consequently, measured force drops to zero baseline.

Figure 1.1 A shows the basic scheme of AFM employed for SMFS in the context of this thesis. An AFM cantilever with a reflective gold coating on its back bears a sharp silicon probe at its end. This cantilever is attached to the AFM setup. Here, BioLever Mini are used as cantilevers, with a typical tip radius of 10 nm (Olympus, Tokyo, Japan). An infrared laser is focused onto the reflective back of the cantilever and the position of the reflected beam is measured by a position sensitive device (PSD). A measurement is carried out by approaching the cantilever to the sample surface. After a short contact with the surface, the cantilever is again retracted. After contact, interactions of the nanometer sized tip with sample molecules deflect the cantilever upon retraction, which in turn changes the differential signal recorded by the PSD proportionally. Here, vertical movement is carried out by a piezo actuator to perform approach and retraction of the cantilever tip to the sample surface. For the analysis, the deflection signal of the PSD and the piezo position are converted into force and distance, respectively, see Figure 1.1 B. This conversion takes the spring

constant of the cantilever, an optical and a piezo sensitivity into account and assumes the cantilever to behave as a one-dimensional Hookean spring [21]. In order to determine the cantilever's spring constant, a calibration routine is carried out, using the thermal noise method described by te Riet *et al.* [22]. Therefore, a power spectral density analysis of thermally driven cantilever oscillations is employed to determine the spring constant of the cantilever, using the equipartition theorem. The baseline, which is defined as the flat line after the last force peak in the graph of Figure 1.1 B, is used to determine the zero-force line and the distance is corrected for cantilever bending. The distance measure can be converted into contour length, a molecular parameter for the maximum length of a stretched and unfolded polypeptide chain [23]. To obtain the contour length, a polymer elasticity model is employed which was proposed by Bustamante *et al.* [24] (see Section 1.7). The contour length can be used to sort and assign protein and especially fingerprint unfoldings [25] (protein fingerprints for SMFS are explained in Section 1.5).

In this way, force-distance traces can be recorded for single-molecule systems. An exemplary trace with associated molecular events is illustrated in Figure 1.1 B. There, experimental results are sketched for a system containing a protein consisting of two domains (yellow) attached to a ligand (blue). The protein-ligand-construct is tethered to the tip of an AFM cantilever. The receptor protein (red) is immobilized on the sample surface. After cantilever approach the ligand has bound to the receptor molecule and the start of cantilever retraction increases tension on the complex (first sequence). During further retraction, the protein cannot withstand mechanical tension any longer and its two domains unfold sequentially with a saw-tooth like pattern. Immediately after the unfolding events, force drops (second sequence). At last, the receptor-ligand interaction dissociates under mechanical force and the tether between AFM and surface is disconnected (third sequence).

Approach-Retraction Cycles

The sample, a microscope slide with immobilized molecules, is mounted on a piezo actuator allowing lateral movement. A probing cycle consists of the approach of the cantilever to the surface and the cantilever retraction. Here, velocities are kept constant, *i.e.* the AFM is used in constant speed mode, and typical values used are 3000 nm s^{-1} for tip to surface approach and 200 nm s^{-1} to 6400 nm s^{-1} for tip retraction. Upon approach, the cantilever is moved towards the surface. When the cantilever tip reaches the surface, the tip is pressed against the surface. The close proximity of tip and surface enables interactions between surface molecules and tip molecules. As soon as a preset trigger force is reached, the retraction process is started. The cantilever is being steadily lifted until a preset distance from the surface is reached, and the cycle is completed. After each approach-retraction cycle, the sample surface is moved 100 nm to a new, pristine spot.

In order to probe molecules one after the other, the interaction between cantilever and molecule of interest has to be reversible and must not hamper the integrity of surface, nor of cantilever molecules. In addition, to be able to probe single molecules, it is important to investigate the optimal concentration of molecules of interest on

the surface. This means one has to strike the balance between a too tense and too sparsely occupied sample surface. A surface which is too tense would result in more than one receptor on the cantilever being occupied. As a result, unfolding and rupture patterns of multiple molecules would occur at the same time. Those events would be indistinguishable, and therefore unsuitable for the analysis. On the other side, a sparsely occupied sample surface leads to clear signals but also to many approach events with no interaction between molecule of interest and AFM cantilever. Thus, the single-molecule approach used in this thesis relies on performing thousands of approach-retraction cycles with typical single-molecule interaction rates in the upper single-digit percentage range. With an additional vertical micromotor, it is possible to probe multiple spots millimeters apart, which allows measurements on different protein constructs with the same cantilever [26, 27]. This allows direct comparison of forces measured between different mutants and constructs immobilized on the same glass slide.

1.2 The Streptavidin-Biotin Complex

Streptavidin (SA) is a protein from the bacterium *Streptomyces avidinii*. Its quaternary structure consists of four equal subunits, thereby forming a homotetramer (see Figure 1.2). Each subunit is able to bind a single biotin, also called vitamin H, thereby SA has a biotin scavenging effect similar to the protein avidin from egg white [28]. The SA-biotin complex is known for its high affinity, resulting in a dissociation constant in the femtomolar range [29]. In addition, its great stability under harsh conditions makes it an abundantly used tool for molecule capture, detection and immobilization [30].

The bound biotin is located inside a β-barrel, which is formed by eight antiparallel β-strands. Starting from the N-terminus, four short β-strands (β-strands 1-4) followed by longer β-strands (β-strands 5-8) can be distinguished. Binding is mediated by several contributions. Hydrophobic interactions inside the β-barrel, the formation of a hydrogen bond network and the interaction of a binding loop facilitate the strong binding of biotin [32–36]. Here, the flexible binding loop (L3/4; residues 45-52) closes like a lid upon biotin binding [37].

It is advantageous to have a single functional subunit to guarantee a 1:1 binding stoichiometry between an SA tetramer and biotin. Howarth *et al.* developed an SA mutant based on three amino acids substitutions (N23A, S27D, S45A) within a single subunit that drastically lowered the affinity for biotin, thereby designing a non-functional SA subunit with negligible biotin binding [38]. By combining three non-functional with one functional subunit, a monovalent SA (mSA) can be created with a single functional biotin binding pocket. For site-specific attachment, mSA and other monovalent SA variants can be tethered with a single tether, thereby providing a single ligand binding site in its tetravalent assembly [39] (Publication 4, Section 5.1). These measures drastically narrow unbinding force dispersion and lead to higher and more long-lived force resistance [40] (Publication 6, Section 5.3).

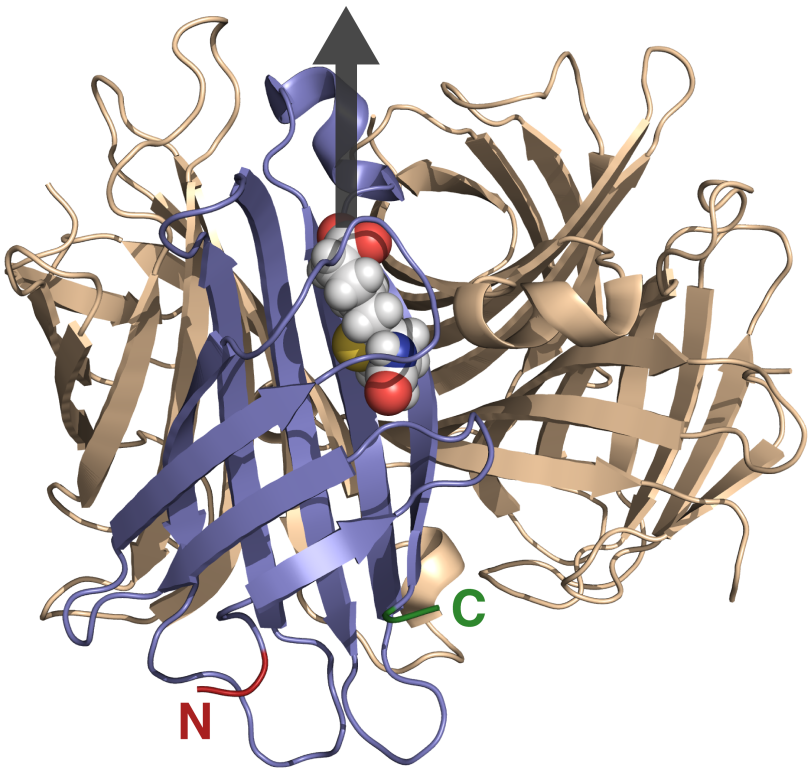

Figure 1.2: Crystal structure of wild-type SA with bound biotin adapted from PDB: 6M9B [31]. Bound biotin is shown only for one subunit for a more simple and better overview. SA is a homotetrameric protein and is shown with its four subunits, three in brown and the one with a bound biotin (spheres with hydrogen and carbon in gray, oxygen in red, nitrogen in blue, sulfur in yellow) is shown in blue. For this subunit, the N-terminus and C-terminus are colored in red and green, respectively. From the crystal structure, the β-barrel in which the biotin molecule is bound is clearly visible. It consists of eight antiparallel β-strands. A gray arrow illustrates at which end the biotin is connected in order to be pulled out of SA's binding pocket in an experimental setup.

1.3 Bioconjugation and Pulling Geometry

As pointed out earlier, in order to induce tension on a molecule, the molecule has to be tethered to artificial surfaces. For SMFS based on AFM, these surfaces are the AFM tip and a glass slide. At this point, it is favorable to know and be able to define the site at which the molecule of interest is anchored. Such a site-specific tethering minimizes dispersion of measured forces mediated by different unfolding and unbinding pathways due to unknown and diverse tethering sites (*cf.* Figure 1). In this way, it is also possible to differentiate between physiological relevant and artificial binding geometries to gain better insights into the underlying mechanism as shown by Milles *et al.* [41]. Here, unbinding forces for non-native, N-terminal pulling of a peptide out of a bacterial receptor protein differed by a factor of 40, compared to the native configuration. Besides, tethering must be covalent to prevent tether rupture during SMFS experiments. For the purpose of molecule attachment, the glass slides are treated to display a polyethylen glycol (PEG) layer which serves as both, linker and passivation layer [42]. Further attachment of molecules can

be realized by direct cysteine maleimide coupling, the latter displayed by the PEG layer, or performed using enzyme mediated covalent attachment using sortase- or sfp phosphopantetheinyl transferase-catalyzed tethering [43–45], with enzyme recognition and fusion sites engineered into the molecule of interest.

By employing the toolbox described above, it is possible to tether SA either by the N- or C-terminus of a single SA subunit, which was performed in Publications 1-4 for mSA and in Publication 6 for SA tetramers with different valences. From Figure 1.2 it can be deduced, that a change of the tethering site can affect the pulling geometry and thereby the unbinding pathway. This effect is described for mSA in Publication 1, Section 3.1.

1.4 Cysteine-Mediated Disulfide Bonds

Of all amino acids, cysteine plays a special role. As it contains an inherent sulfur-based functional group (thiol group, -SH), it fulfills catalytic, metal-binding, regulatory and structural tasks in proteins [46]. With its thiol group, it is able to form a covalent disulfide bond with other cysteines in oxidizing conditions. Exposing this cross-link to reducing conditions will break the bond again. In nature, this bond plays a vital role in protein folding, multimerization and stability [47–49]. In mechanobiology, cysteines are often used as single genetic mutation to tether the protein of interest by inserting a cysteine internally or either in the N- or C-terminus [39]. The protein of interest can then be tethered to a PEG spacer by a coupling reaction between reduced cysteines with a free thiol group and a maleimide modification on the PEG spacer [42].

Cysteines' ability to reinforce protein folds can be exploited to engineer proteins with increased stability [50, 51]. This is employed in Publication 2, Section 3.2. Steered molecular dynamics simulations performed in the context of Publication 1 showed an mSA-biotin unbinding pathway for N-terminal tethering in which partial unfolding of the first β-sheet was observed. This lead to the choice of two point mutations (T18C, A33C) in SA's first two β-strands, substituting threonine at position 18 and alanine at position 33 with cysteines to promote the formation of a disulfide bond between the inserted cysteines. This disulfide bond has proven to increase mechanical stability of the interaction between the mutated SA and biotin (Publication 2, Section 3.2).

1.5 Unique Protein Patterns – Fingerprints for SMFS

To identify single-molecule traces that do represent probing of the system of interest, known protein unfolding patterns can be used. In this thesis, the unfolding of the fourth filamin domain of *Dictyostelium discoideum* (ddFLN4) serves as such a known regular pattern [52]. Therefore, it is employed as an identification marker, like a fingerprint. Attached to the system of interest, it unfolds when the complex is manipulated. For analysis, those force distance traces bearing the ddFLN4 fingerprint unfolding pattern can be considered to represent probing of the system of interest.

In this way, force distance traces showing cantilever interaction of unknown cause, like unspecific interactions, are not considered in analysis. The graph in Figure 1.1 B schematically shows a two-step unfolding pattern of ddFLN4 before rupture of the receptor-ligand system. The choice of fingerprint has to be considered for each system separately, since unbinding forces of receptor-ligand systems employed for tether in an experiment have to be significantly higher than fingerprint unfolding forces. Otherwise, the receptor-ligand system is prone to unbind before the fingerprint unfolds, thereby biasing experimental results [53]. For the SA-biotin complex, the unbinding forces are higher and therefore ddFLN4 suits well as a fingerpint domain. This can be inferred from unbinding and ddFLN4 unfolding force histograms and from a plot showing all unsorted unbinding forces revealing no population with forces similar to ddFLN4 unfolding [54]. The fingerprint domains are inserted into the tethering of the protein of interest. The insertion can, therefore, be achieved either genetically by engineering the protein of interest tethered to the fingerprint, or by using attachment chemistry, *cf.* Section 1.3, to connect protein and fingerprint.

1.6 A Proxy Receptor-Ligand System for Receptor-Ligand SMFS

Preserving the integrity of the proteins immobilized on the cantilever tip is the most crucial part in order to allow for acquiring large datasets. It is hampered by the loss of functionality or irreversible blocking of receptor binding pockets tethered to the cantilever tip. This is particularly the case when probing SA-biotin in an AFM based SMFS assay with biotin on the cantilever tip and SA immobilized on the surface. This is due to SA's extremely high affinity for biotin. Here, introducing a second receptor-ligand system with a short construct containing the ligands of both systems offers a solution. Thereby, this ligand construct serves as a molecular force transmitter. This approach has to meet the following criteria: There has to be a force hierarchy between the receptor-ligand system to be probed and the proxy. The apparent reason is that the second receptor-ligand system must withstand the force needed to separate the system of interest. Additionally, the probability distributions of unfolding forces for both systems should not overlap to prevent biasing effects [53]. Furthermore, the zero-force off-rate of the molecular force transmitter system has to be much higher than for the system of interest. It has to be guaranteed that the cantilever is frequently unblocked from the force transmitter system to allow probing of the next molecule. In order to probe the receptor tethered to the surface in an SMFS experiment, a construct containing both ligands is needed, as it provides an interconnection between cantilever tip and target receptor protein on the surface.

The binding between the adhesin SD-repeat protein G (SdrG) and the short peptide from human fibrinogen β (Fgβ) turned out to be a suitable system for this approach [41, 55]. SdrG from *Staphylococcus epidermidis* with a bound Fgβ shows a nearly 10-fold higher unbinding force compared to the SA-biotin interaction [41]. Furthermore, the lower affinity of the SdrG-Fgβ system provides frequent Fgβ unbinding and thereby allows for the recovery of the cantilever tip [56]. Supplied with

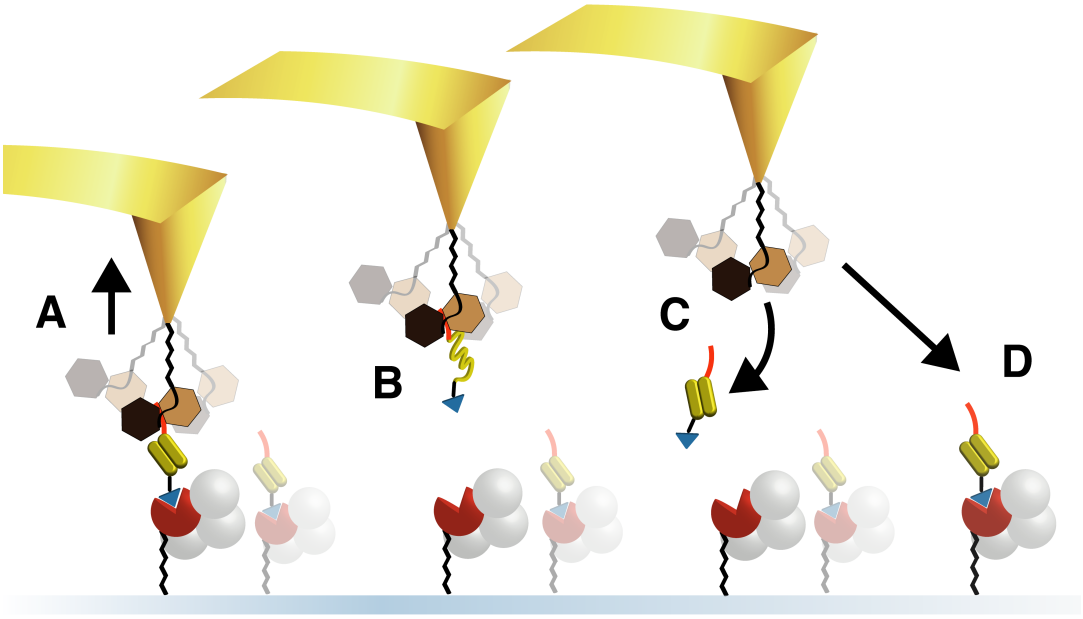

Figure 1.3: Single-molecule approach-retraction cycle showing the second receptor-ligand system used as proxy for force transmission. A schematic approach-retraction cycle is illustrated using the example of probing mSA-biotin by employing SdrG-Fgβ as second receptor-ligand system. Three different protein structures can be distinguished. The receptor (SdrG, brown) displayed by the cantilever tip, a ligand-fingerprint complex featuring the two ligands (Fgβ in orange, biotin in blue) which are covalently connected by a protein fingerprint (ddFLN4 in yellow), and the receptor to be investigated (mSA, red and white spheres) which is attached to a glass slide (light blue). **A**, the ligand-fingerprint complex is bound to mSA via its biotin. Upon cantilever approach, the receptor SdrG binds to its ligand peptide Fgβ. During retraction, fingerprint domains unfold and mSA-biotin interaction ruptures (**B**). **C**, fingerprint refolds and ligand-fingerprint complex dissociates from the cantilever tip. This enables successive probing (**D**).

a protein fingerprint, this second receptor-ligand system was successfully applied for investigation of SA-biotin unbinding mechanics (*cf.* Publication 1-3 and Publication 6, Section 3.1, 3.2, 4.1 and Section 5.3). Figure 1.3 shows the experimental setup for the use of the second receptor-ligand system. Here, the complex serving as a force transmitter between the two different receptor molecules (SdrG, mSA) consist of an Fgβ (orange), ddFLN4 fingerprint (yellow) and a biotin (blue).

1.7 The Worm-Like Chain Elasticity Model

Polymer elasticity models can be used to describe the behavior of polymers, like proteins, under force. The worm-like chain (WLC) model describes a linear, uniform chain which is characterized by the contour length l_c and the persistence length l_p. It was first introduced by Kratky and Porod [57]. Here, l_c is the total length of the fully-extended polymer, *i.e.* its maximum end-to-end distance. l_p is a measure for the polymer's bending stiffness. When selecting two positions along a WLC polymer, the

correlation of their tangent vectors decays exponentially with increasing distance between them. ${l_\mathrm{p}}^{-1}$ represents the decay constant of this exponential decay.

In SMFS experiments, the end-to-end extension of a polymer x is increased and the restoring force F, which builds up, can be measured (*cf.* Figure 1.1). An approximation of the force-extension behavior of WLC polymers was provided by Marko and Siggia [58] and is commonly used in SMFS assays:

$$F_{WLC}(x) = \frac{k_\mathrm{B}T}{l_\mathrm{p}}\left(\frac{1}{4\left(1-\frac{x}{l_\mathrm{c}}\right)^2}+\frac{x}{l_\mathrm{c}}-\frac{1}{4}\right) \tag{1.1}$$

with temperature T and Boltzmann constant k_B. By using fixed l_p and fixed T the contour length $l_\mathrm{c}(F,x)$ can be calculated for each point in a force-extension graph [23]. Alternatively, Equation 1.1 can be directly fitted to SMFS force-extension data to derive l_p and l_c. The contour length which is obtained in these ways can be used to assign contour length release to specific protein domain unfoldings.

1.8 The Bell-Evans Model

SMFS experiments provide data of inter- and intramolecular interactions by mechanically probing protein folds and receptor-ligand complexes. The data can be analyzed using approaches which model protein unfolding and receptor-ligand unbinding. A model introduced by Bell [59] describes the increase of bond dissociation frequency when the bond is exposed to mechanical tension. Evans and Ritchie [60], and Izrailev *et al.* [61] extended this model taking account of a time-dependent force and derived a model which is nowadays known as the Bell-Evans model. It describes a one-dimensional free energy landscape with the bound state located in a potential well. The bound and unbound states are separated by a potential barrier with height ΔG. The transition state is located at the maximum of the potential barrier. The distance from bound to transition state is termed Δx. In this model, a force F tilts the energy landscape and thereby increases the rate of unbinding k_off.

$$k_\mathrm{off}(F) = \omega_0 \exp\left(-\frac{\Delta G - F\Delta x}{k_\mathrm{B}T}\right) = k_\mathrm{off}^0 \exp\left(\frac{F\Delta x}{k_\mathrm{B}T}\right) \tag{1.2}$$

Here, ω_0 represents a natural vibration frequency of the bond originating from the model of Bell [59]. k_off^0 constitutes an off-rate at zero force and depends on the potential barrier.

For a constant increase in force, *i.e.* a constant force-loading rate $\dot{F}$, an equation for the probability of bond rupture at a given force was derived within the Bell-Evans model [60, 61].

$$p(F) = \frac{k_\mathrm{off}^0}{\dot{F}}\exp\left(\frac{F\Delta x}{k_\mathrm{B}T} - k_\mathrm{off}^0\frac{k_\mathrm{B}T}{\dot{F}\Delta x}\left(\exp\left(\frac{F\Delta x}{k_\mathrm{B}T}\right)-1\right)\right) \tag{1.3}$$

The experimentally gained data on forces of receptor-ligand rupture or protein unfoldings along with associated force-loading rates can be used to determine the zero-force off-rate k_off^0 and the distance to transition state Δx.

Another approach used within this thesis yields k_{off}^{0} and Δx by employing dynamic force spectra, *i.e.* rupture or unfolding data at differing force-loading rates. This analysis uses most probable rupture forces and force-loading rates. In order to derive an equation for the most probable rupture force F^{*}, the maximum of $p\,(F)$ can be determined by solving $\frac{\partial p(F)}{\partial F} = 0$. This yields an equation for the most probable rupture force dependent on the force-loading rate.

$$F^{*} = \frac{k_{\mathrm{B}}T}{\Delta x}\ln\left(\frac{\dot{F}\Delta x}{k_{\mathrm{off}}^{0}k_{\mathrm{B}}T}\right) \tag{1.4}$$

Chapter 2

Zero-Mode Waveguides – Dimming the Fluorescent Background

Single-molecule imaging techniques allow to study dynamic processes with the ability to identify small conformational changes. Such small conformational changes can be found in mechanoactive proteins that mediate mechanosensing and mechanotransduction. These proteins are essential for a cell to interact with its environment by converting mechanical force stimuli into a biochemical signal which affects a variety of cell functions, like proliferation, differentiation, cell shape and motility [62–67]. A force stimulus triggers conformational changes which can for example release a cryptic binding, a phosphorylation or an enzymatically active site of the mechanoactive protein [16]. Reactions associated to the exposed site then initiate biochemical signaling. In order to investigate such mechanoactive proteins, single-molecule manipulation and imaging techniques can be combined. Previous studies have already shown the successful combination of SMFS by AFM or magnetic tweezers and TIRF for mechanobiology investigations [68, 69]. The fluorescence technique, TIRF microscopy, reduces the illumination volume to allow single-molecule observation within a fluorophor populated sample. The reduction of the illuminated volume is realized by means of total internal reflection of the incident light. Thus, for angles of incidence exceeding the critical angle, set by Snell's law, only an evanescent field emerges, whose intensity decays within hundreds of nanometers [70].

Whereas TIRF can resolve single molecules against fluorescently populated backgrounds, it reaches the limit of applicability when fluorophore concentrations approach tens of nanomolar concentration [71]. However, concentrations exceeding this limit are needed to observe dynamics of many biological processes whose enzyme associated Michaelis constants are high [72]. A solution to this concentration limit pose ZMW nanostructures, which further reduce the illuminated volume such that higher concentrations up to micromolar can be realized [3]. A single ZMW consists of a subwavelength hole in a metal layer, which limits the optical observation volume. ZMWs' broad applicability allows a straightforward combination with SMFS by AFM [12, 73]. However, considerable challenges remain which impede long measurements

and high yields. These challenges have to be overcome in order to make substantial contribution to mechanobiology by investigating mechanoactive protein systems (*cf.* Figure 2.1). The following section outlines the measures developed in the context of this work to tackle these challenges. These measures comprise the realization of a fully automated setup along with covalent, site-specific protein immobilization and the prevention of fast photobleaching and photodamage.

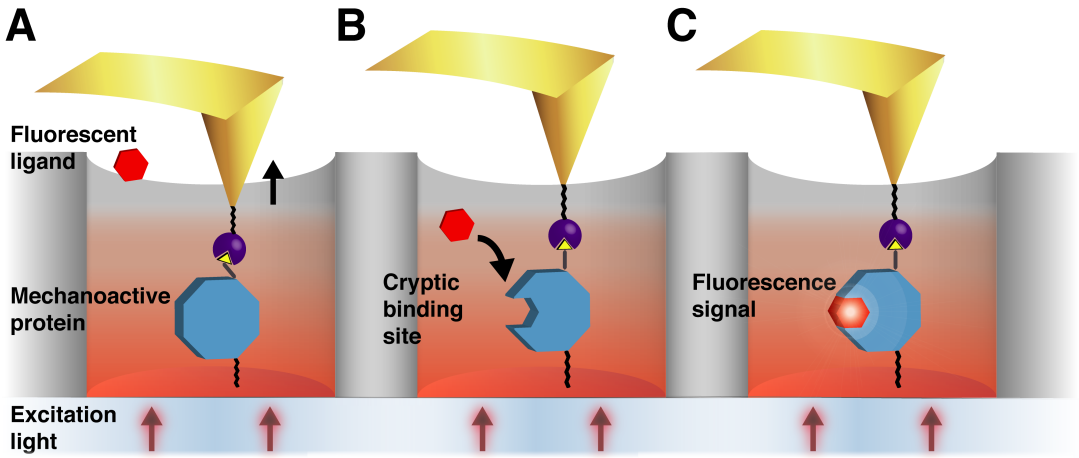

Figure 2.1: Schematic representation of force-activation of a mechanoactive protein inside a ZMW nanostructure. The mechanoactive protein (cyan) is covalently tethered to the glass floor (blue) of a ZMW nanostructure (gray). **A**, using a force handle comprised of a receptor-ligand system (receptor attached to cantilever in purple, ligand tethered to protein in yellow) tension is applied by retracting the AFM cantilever (gold-colored). **B**, upon retraction, the conformation of the protein changes releasing a cryptic binding or reaction site in the process of mechanoactivation. In this state, a fluorescently labeled ligand (red hexagon) is able to bind to the formerly inaccessible binding site. **C**, illumination from below excites this ligand and a fluorescence signal can be recorded for the duration of the binding interaction.

2.1 Confining the Illumination Volume

ZMWs are nanostructures in metal films with subwavelength dimensions that limit illumination and thereby optical observation to very small volumes. By attenuating the intensity of incident light, illumination volumes as small as zeptoliter (10^{-21} l) are considered feasible [3]. Used for single-molecule fluorescence imaging techniques, the smaller volumes reduce excitation of fluorophores outside this volume and in this way effectively dim the fluorescent background. This allows applications for biological investigations with fluorophore concentrations from hundreds of nanomolar to micromolar [3, 4, 72, 74, 75].

Referred to as zero-mode waveguides, these cylindrical nanostructures, considering a clad formed by a perfect conductor, typically allow no light propagating mode inside them [3]. For such a cylindrical aperture with diameter d confined by a clad which consists of a perfect conductor, light with wavelengths greater than a certain cut-off wavelength ($\lambda_c = 1.7d$) is evanescent inside the nanoaperture [3]. Within the

ZMW, the intensity of light with a longer wavelength ($\lambda > \lambda_c$) decays exponentially along the cylindrical axis of the aperture [3, 76]. Here, λ is the wavelength in the medium which fills the aperture.

Because cladding materials, like aluminum, are no perfect metals, a strict cut-off wavelength does not exist for ZMWs; instead, light intensity is attenuated with increased attenuation for longer wavelengths [76]. This attenuation accounts for the small illumination volumes and the aforementioned applicability in biological investigations with nanomolar to micromolar fluorophore concentrations. Due to the complex geometry and considering real material parameters, descriptions of optical properties of nanoapertures rely on numerical solutions and empirical measurements [76]. Light intensity attenuation along the cylindrical axis of the aperture is strongly dependent on the ZMW's diameter. With diameters greater than 100 nm, radial dependence of field strength can be observed. Moreover, the attenuation of light intensity along the cylindrical axis of the aperture increases for longer wavelengths as shown for a 150 nm diameter nanoaperture made of aluminum by Zhu *et al.* [76]. As aluminum is often used as cladding metal, it has been chosen as cladding material within this thesis. It has desirable optical properties in the visible wavelength region and naturally forms an oxide layer which prevents further oxidation [76]. Within the context of this thesis, a wavelength in the higher bound of the spectrum of visible light (640 nm) is used. In combination with a fluorophore, here Cy5, with excitation maximum near laser emission, combined ZMW and AFM measurements are carried out.

2.2 Fabrication of Nanostructures and ZMWs

In order to manufacture structures with nanometer dimensions, electron beam lithography based on a negative tone process is employed [77]. In general, nanolithographic methods dictate high cleanliness of workspace and substrate surfaces. Any residual particles cause defects in lithographic structures or impede proper and homogeneous coverage of the functional layers, causing functional layers with imprinted structures to prematurely exfoliate. To guarantee conditions which meet the high standards set for cleanliness, all steps for ZMW fabrication are carried out in a cleanroom. Figure 2.2 illustrates the steps needed to fabricate structures with nanometer dimensions by using electron beam lithography based on a negative tone process presented by Foquet *et al.* [77]. This method is based on coating the substrate with a photoresist which is sensitive to electron beam radiation. After deposition of photoresist, the resist is patterned using a scanning electron microscope. Upon exposure to the electron beam, the resist cross-links and becomes insoluble in the resist specific developer solution. Consequently, unexposed resist is dissolved in a developer solution. Following this, evaporation of the metal of choice is carried out and a subsequent lift-off releases the desired pattern.

Here, glass slides are used as object carrier for the nanostructures. They measure 22 mm in diameter and 170 µm in thickness. The final aluminum cladding has a height of 100 nm. To increase adhesion of the photoresist to the glass surface an aqueous based adhesion promoter was used which was spin-coated prior to the

photoresist. It was ensured that no residuals of the adhesion promoter remained after lift-off to avoid impairing the integrity of the glass surface, which is essential for the subsequent attachment of sample molecules. By this means, ZMWs and other structures with diameters and dimensions in a range from hundred nanometers to several micrometers were fabricated.

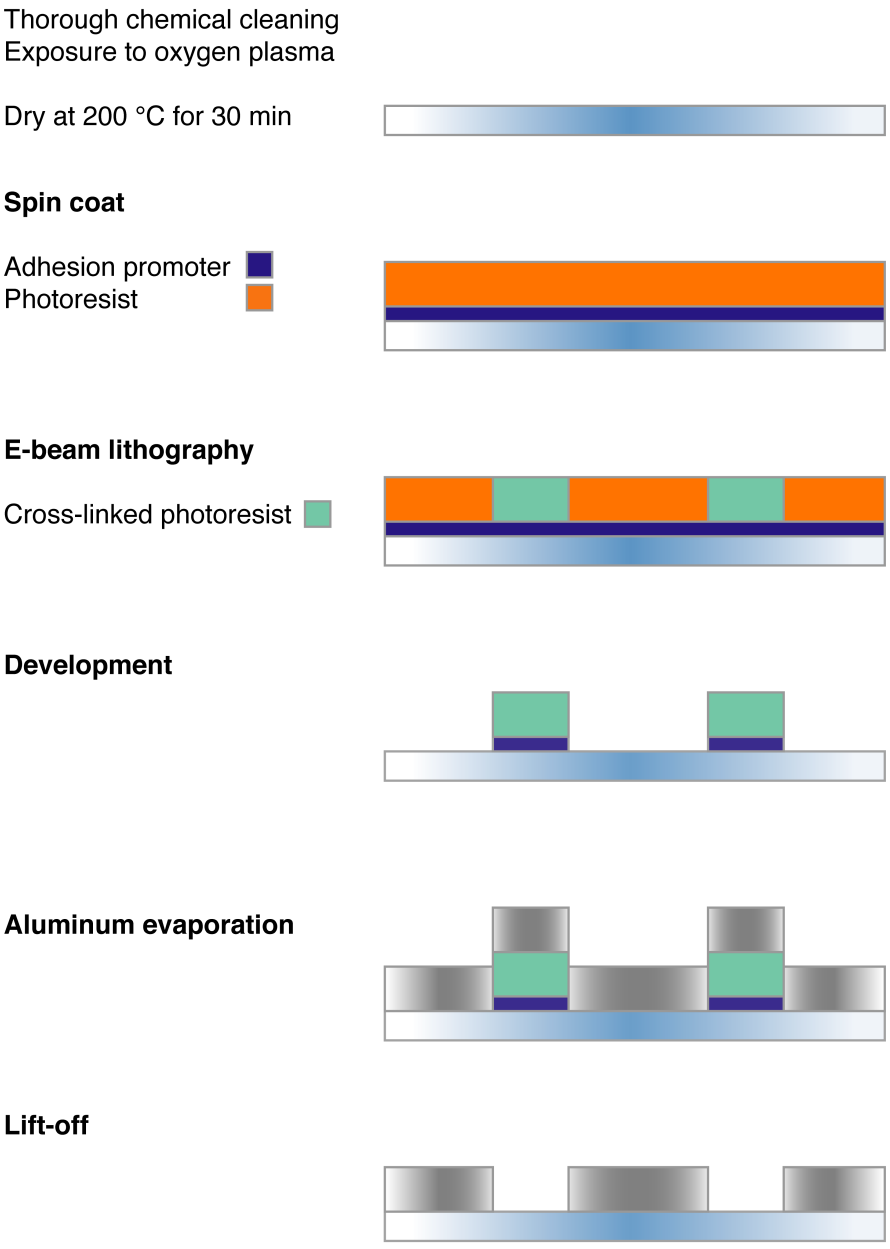

Figure 2.2: Overview of nanoaperture fabrication. The figure shows the steps for negative e-beam lithography. Glass slides (light blue) are thoroughly cleaned and dried. An adhesion promoter and the photoresist are spin coated onto the substrate. Then, an electron beam (e-beam) cross-links the photoresist according to a predefined pattern. During development the cross-linked photoresist dissolves, thereby exposing the negative pattern. Aluminum (gray) is evaporated onto the structure and lift-off is carried out using ultra sound sonication in a solvent. This dissolves the cross-linked photoresist and the residual adhesion promoter, and exposes the nanostructures.

2.3 Perfoming SMFS based on AFM in ZMWs

2.3.1 Surface Chemistry and Bioconjugation

After fabrication, the surface of the glass slide is the bottom of the aluminum confined nanostructures. This allows for the use of the same surface functionalization chemistry as outlined in Section 1.3. However, prior to the common attachment functionalization, a passivation layer is applied onto the aluminum coating. This layer is introduced in order to prevent molecules and proteins to stick to the aluminum walls, thereby confining surface attachment of the molecules of interest onto the glass bottoms of the ZMWs. The method employed in this work relies on polyvinylphosphonic acid, which is used to clad the native aluminum oxide layer in order to create a material-selective and biocompatible passivation layer [78].

2.3.2 Protein Model System as Exemplary Force-Activatable System

In order to test the performance of a combined use of ZMW and AFM-based SMFS, the protein system introduced in Section 1.6 is used as a model mimicking a force-regulated protein system. Here, the single functional binding pocket of an mSA is blocked by a biotin construct. Tension on the biotin causes dissociation and the binding pocket becomes accessible. This is similar to mechanical unmasking of a cryptic binding site within a force-regulated protein. For this approach, mSA molecules are attached to the floor of ZMWs and their binding pockets are blocked with a biotin construct. This biotin construct also features a ddFLN4 fingerprint domain and an Fgβ-peptide. SdrG is displayed by the AFM cantilever. The interaction between SdrG and Fgβ is used to bind the biotin construct and to pull it out of mSA's binding pocket, thereby enabling the binding of freely diffusing, labeled biotin molecules to the now unblocked mSA.

2.3.3 Buffer Additives for Steady Fluorescence

A combined use of single-molecule fluorescence and manipulation requires experimental conditions that ensure long fluorescence lifetimes and preserve the integrity of the molecules and proteins employed. Here, the most crucial prerequisite is to create and provide anaerobic conditions within the sample volume in order to prevent the generation of reactive oxidative species (ROS) due to laser irradiation [79]. ROS are responsible for fast photobleaching and for damage to molecules and proteins. In this work, an oxygen scavenging system is employed, which relies on enzymatic turnover of molecular oxygen to facilitate oxygen removal. It consists of the enzymes pyranose oxidase, catalase and the substrate glucose [80]. The advantage of the system is that the product does not affect the pH inside the sample volume as other enzyme-based oxygen scavenging systems do [81].

It has to be taken into account that by removing molecular oxygen, triplet state blinking of the fluorophores employed is promoted, as molecular oxygen efficiently

mediates triplet state quenching [82]. Therefore, the reducing/oxidizing system trolox is used to reduce triplet state lifetimes of the fluorophores [83].

2.3.4 Realization of an Automated Setup

In order to facilitate an automated workflow, it is essential to find stable, recurring conditions for fitting routines. This applies to tip localization as well as to nanoaperture localization. Also, it is important to keep track of the positions of the nanoaperture cavities to be probed, the tip localization windows and the region of interest, which is used for the recurring autofocus routine. All routines have been implemented within one control program running on a single computer which allows the control of all experimental devices. Here, the implementation of a fully automated setup drastically decreases the effort, as manual control by an experimenter is not required. Prior to this automated setup, permanent supervision and manual control has been common practice. Only a fully automated setup enables long-term measurements and thereby enough approach-retraction cycles can be conducted to collect datasets that allow to study biologically relevant systems. The necessary routines to facilitate automatization are outlined in the following section.

Cantilever Tip Localization

The most crucial part of a combined use of AFM and ZMWs is to determine the position of the cantilever tip precisely enough to guarantee a reliable approach into nanometer sized cavities. The routine used in this work relies on a method presented by Baumann *et al.* [84]. This method uses the higher absorption of top-down white light illumination by the very tip of the cantilever to fit the center of the tip position. In order to take images of the tip, micrometer-sized rectangular window cut-outs within the aluminum cladding, which are fabricated along with the nanoapertures, serve as transparent surfaces. In this work, a revised version is employed, preventing contact between tip and surface during image acquisition. To this end, the cantilever tip is kept at a vertical distance of 100 nm above the surface during image acquisition. Therefore, the objective lens is levered prior to tip localization to shift the focal plane accordingly. These images are averaged and fitted with a 2D gaussian, providing the position of the very end of the tip. Here, reducing the surface contact time of the tip, by performing tip image acquisition at a lifted height, prolongs the integrity of molecules tethered to the tip and in turn allows long measurement times.

Vertical Drift Correction

In order to enable long measurement times and in this way the collection of large datasets, the setup has to be stable and has to correct for any changes caused by instrumental drift. In addition, a drift correction is required to provide consistent experimental conditions and to facilitate automation. Thus, changes of the vertical position of the sample relative to the objective lens have to be corrected. This is achieved by using the piezo actuator, on which the objective lens is mounted,

together with synchronized image acquisition of the camera to perform an autofocus routine. This routine moves the objective lens step-wise, symmetrically around the last focus position. At each step, an image of nanostructures with top-down white light illumination is recorded. Each image is analyzed using an autofocus function [85], with the result for each image being plotted against the associated piezo position. The center of a gaussian fit to this graph serves as new focus position.

Horizontal Drift Correction

Besides vertical drift the setup is also subject to horizontal drift. At first sight, this seems to have less effect on the measurement routine, but all nanoapertures to be probed are initially localized before the start of the measurement. These positions provide an initial seed position for precise nanoaperture localization before each probing. Horizontal drift shifts these positions, thereby hampering nanoaperture localization. In order to correct for these horizontal drifts, the rectangular window cut-out is fitted each time the tip is moved above it during tip localization. From this fit and the last measured position of the window cut-out, an offset is calculated which is used to correct the initial nanoaperture seed positions.

Approach-Retraction Cycles in ZMWs

Cantilever approach is initiated simultaneously with laser illumination. The start of cantilever retraction is synchronized with image acquisition – upon start of the retraction cycle the AFM controller triggers the image acquisition by the camera. After the retraction phase is completed, image acquisition is stopped and laser illumination is turned off. The seed position of the next ZMW nanostructure is used to take an image with white light top-down illumination. Here, the extraordinary plasmonic transmission of white light through the ZMWs can be employed for localization [73, 86, 87]. The image is fitted with a 2D gaussian with its center determining the precise position of the ZMW. This position is taken to move the cantilever tip above the ZMW and subsequently initiate an approach-retraction cycle. Here, autofocus and cantilever tip localization routine do not have to be performed prior to each approach-retraction cycle in a ZMW. Repetition rates for autofocus and tip localization every 12^{th} and 6^{th} time in between ZMW approach-retraction cycles, respectively, have been proven feasible (*cf.* Publication 3, Section 4.1).

Part III

Results

Chapter 3

Single-Molecule Force Spectroscopy on the Streptavidin-Biotin Interaction

3.1 Publication P1: Direction Matters: Monovalent Streptavidin/Biotin Complex under Load

Recent advances allowed the production of monovalent SA molecules that enable a 1:1 binding stoichiometry. Together with site-specific immobilization, which enables the precise definition of the intramolecular tethering site, this facilitated investigating the effects of pulling direction in the context of SA-biotin complex separation.

In order to investigate how the unbinding behavior of the SA-biotin complex depends on the attachment geometry, the single functional subunit of mSA was tethered either by its N- or C-terminus. These two different immobilization modes were realized by employing cysteine, which was inserted in the respective terminal region, as presented for N-terminal attachment in Section 5.1. In this way, these two mSA molecules were tethered to the sample surface of an AFM setup. SMFS was performed using a second receptor-ligand system as proxy to force biotin unbinding from SA. Here, experiments showed an about twofold difference in unbinding force for the two pulling geometries, for which C-terminal attachment appeared more stable with forces beyond 400 pN at force loading rates of 10 $nN\,s^{-1}$. By using site-specific tethering in the experiments, it was possible to apply the same pulling geometry in an all-atom steered molecular dynamics simulation. Simulations were performed for both geometries, resulting in hundreds of simulations of *in silico* forced complex separation, providing insights into the mechanics of the underlying process. Results revealed different unbinding pathways and interestingly, depending on the force-loading geometry, showed complex separation accompanied by partial unfolding of an N-terminal region. This unfolding occurs within the N-terminal β-sheet, reducing the complex's stability and leading to the observed low-force unbinding mode.

Thereby, the observation of partial unfolding occurring prior to complex rupture underscores the close connection between the concepts of unbinding and unfolding.

Direction Matters: Monovalent Streptavidin/Biotin Complex under Load

by

Steffen M. Sedlak*, Leonard C. Schendel*, Marcelo C. R. Melo, Diana A. Pippig, Zaida Luthey-Schulten, Hermann E. Gaub, and Rafael C. Bernardi

published in

Nano Letters 2019, 19, 3415-3421, doi: 10.1021/acs.nanolett.8b04045

Reprinted with permission from Sedlak *et al.* [54]
Copyright 2019 American Chemical Society

*These authors contributed equally to this work. SMS: Protein preparation, ITC, AFM-based SMFS (single receptor-ligand system), data analysis, writing of manuscript. LCS: AFM-based SMFS (double receptor-ligand system), data analysis, writing of manuscript

NANO LETTERS
Cite This: Nano Lett. 2019, 19, 3415−3421
Letter
pubs.acs.org/NanoLett

Direction Matters: Monovalent Streptavidin/Biotin Complex under Load

Steffen M. Sedlak,[⊥,†] Leonard C. Schendel,[⊥,†] Marcelo C. R. Melo,[‡,§] Diana A. Pippig,[†] Zaida Luthey-Schulten,[‡,§,∥] Hermann E. Gaub,[†] and Rafael C. Bernardi*[,‡]

[†]Lehrstuhl für Angewandte Physik and Center for NanoScience (CeNS), Ludwig-Maximilians-Universität München, Amalienstrasse 54, 80799 Munich, Germany

[‡]Beckman Institute for Advanced Science and Technology, [§]Center for Biophysics and Quantitative Biology, and [∥]Department of Chemistry, University of Illinois at Urbana−Champaign, Urbana, Illinois 61801, United States

Supporting Information

ABSTRACT: Novel site-specific attachment strategies combined with improvements of computational resources enable new insights into the mechanics of the monovalent biotin/streptavidin complex under load and forced us to rethink the diversity of rupture forces reported in the literature. We discovered that the mechanical stability of this complex depends strongly on the geometry in which force is applied. By atomic force microscopy-based single molecule force spectroscopy we found unbinding of biotin to occur beyond 400 pN at force loading rates of 10 nN/s when monovalent streptavidin was tethered at its C-terminus. This value is about twice as high than that for N-terminal attachment. Steered molecular dynamics simulations provided a detailed picture of the mechanics of the unbinding process in the corresponding force loading geometries. Using machine learning techniques, we connected findings from hundreds of simulations to the experimental results, identifying different force propagation pathways. Interestingly, we observed that depending on force loading geometry, partial unfolding of N-terminal region of monovalent streptavidin occurs before biotin is released from the binding pocket.

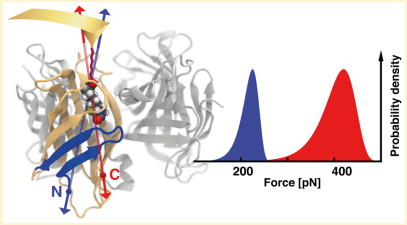

KEYWORDS: *Streptavidin/biotin, single-molecule force spectroscopy, atomic force microscopy, molecular dynamics, machine learning*

The interaction of the small molecule biotin with the protein streptavidin (SA) is widely used for noncovalent, yet stable bonding in nanotechnology, biotechnology, and medicine.[1] The robustness of SA and the SA/biotin complex over a wide range of conditions, the comparatively easy fusion of biotin to nucleic acids, proteins, dyes, other macromolecules or nanoparticles, and the extraordinarily high affinity of the interaction make the complex a superior choice for immobilization, labeling, or detection of molecules.[2−5]

Recombinant core streptavidin monomers consist of the residues 13−159 of wild-type streptavidin and form a stable tetramer (Figure 1A). Every streptavidin subunit consists of a β-barrel in which a biotin molecule can be bound. The β-barrel is built up from eight antiparallel β-strands. The four β-strands located toward the N-terminus are considerably shorter (5−7 amino acids) than the four β-strands situated toward the C-terminus (10−13 amino acids). The four long β-strands and the residues in between mainly mediate the interaction with the other subunits. The short α-helix between seventh and eighth β-strand exhibits a tryptophan residue (TRP120) that reaches into a neighboring subunit and stabilizes this neighboring biotin binding pocket.[6−8]

The binding of biotin induces a conformational change in the molecule: The flexible loop between third and fourth β-strand (L3/4; residues 45−52) closes like a lid over the binding pocket.[9] Crystal structures of open and closed conformation have been solved.[10] Loop closure is vital for the tight binding of biotin. By mutating three residues (N23A, S27D, S45A) that are important for a stable closed loop conformation (cf. Supporting Information), Howarth et al. engineered a SA subunit with negligible affinity toward biotin (Figure S3).[11] Interestingly, all mutated residues are located between the L3/4-loop and the N-terminus.

Combining three nonfunctional subunits with one functional subunit, defined monovalent streptavidin (mSA) enabling a 1:1 binding stoichiometry can be created. Recently, the crystal structure of mSA was solved (Figure S4).[12] Crystallographic data suggest that in the nonfunctional subunit, the L3/4-loop is fixed in an open state−similar to the open state of wild-type apo-SA.

Over the last decades, scientists put a lot of effort in investigating the mechanical properties of this outstanding, noncovalent interaction. It was the first receptor ligand system where binding forces between individual molecules were measured by

Received: October 9, 2018
Revised: October 18, 2018
Published: October 22, 2018

ACS Publications © 2018 American Chemical Society

DOI: 10.1021/acs.nanolett.8b04045
Nano Lett. 2019, 19, 3415−3421

Downloaded via LMU MUENCHEN on January 16, 2020 at 14:42:00 (UTC).
See https://pubs.acs.org/sharingguidelines for options on how to legitimately share published articles.

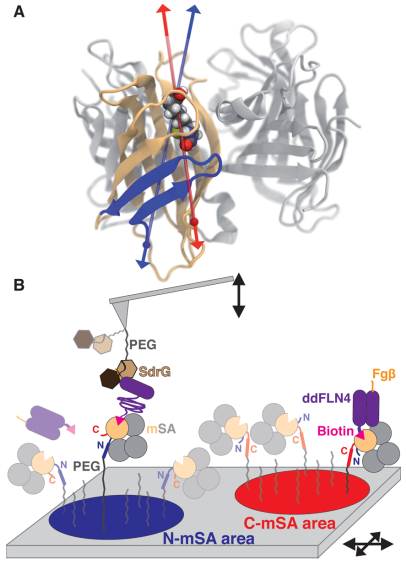

Figure 1. (A) Crystal structure of monovalent streptavidin (PDB 5TO2,[12] biotin from PDB 1MK5).[43] Biotin is bound in the functional subunit (light orange). The other subunits (gray) are genetically engineered to not bind biotin. Blue and red balls mark, respectively, the N- and C-terminus where mSA is tethered. Blue and red lines indicate the force loading directions. N-terminal region β-strands are highlighted in blue. (B) Experimental setup for AFM-based SMFS. At different surface areas, N-mSA and C-mSA are immobilized using PEG-spacers. Biotinylated (magenta) ddFLN4 (purple) is added to the solution and binds to the functional subunit of mSA (light orange ball). When the cantilever tip, functionalized with SdrG (brown hexagons), is approached to the surface, the Fgβ-peptide (orange) fused to ddFLN4 can bind to SdrG. Retracting the cantilever tip from the surface, ddFLN4 unfolds before biotin unbinds from mSA. Details of attachment chemistry and measurement process are provided in Figures S1 and S2.

atomic force microscopy (AFM)-based single molecule force spectroscopy (SMFS):[13,14] Unspecifically adsorbed biotinylated bovine serum albumin was immobilized on both cantilever and sample surface, while streptavidin was added to the buffer solution.[15] In subsequent studies, the experimental setup was improved using, for example, covalent attachment of biotin, polyethylene glycol linkers,[16] or other attachment strategies.[17−22] Later, covalent attachment of both biotin and streptavidin to cantilever or sample surface was accomplished.[23,24] Nowadays, the streptavidin/biotin system serves as a standard molecular anchoring system in AFM-based SMFS,[25,26] but also in optical tweezers,[27] magnetic tweezers,[28] and acoustic force spectroscopy experiments.[29]

Avidin/biotin and SA/biotin complexes were also fundamental in the initial development of steered molecular dynamics (SMD) simulations with both complexes among the first ones investigated by this technique.[30,31] Even before the advent of SMD, theoretical models have been put forward to describe the underlying molecular mechanism of the system.[32−35] Molecular dynamics (MD) simulations provided insights into different aspects of the interaction.[9,36,37] However, to investigate SA/biotin mechanics, the center of mass of the SA molecule has been kept fixed in previous SMD studies, which is different from the experimental force loading geometry.[30,38] In the literature, a large number of experimental and theoretical results, including supposedly contradictory studies, can be found.[39,40] On a molecular scale, a complete understanding of how biotin unbinds from the SA binding pocket under force is to date still missing.

For this study, we produced two different variants of mSA adding a unique cysteine either on the N-terminus (N-mSA) or the C-terminus (C-mSA) of the functional subunit (Figure 1A). The cysteine is utilized for site-specific covalent tethering. Additionally, the functional subunit was equipped with a polyhistidine tag used for purification. To ensure that the modifications do not affect the binding of biotin, we performed isothermal titration calorimetry (Figure S6).

In our experiments, the two different mSA variants were immobilized a few millimeters apart from each other on a glass slide by site-specific thiol maleimide coupling to polyethylene glycol (PEG) spacers (Figure 1B). The covalent immobilization of different proteins on the same surface is advantageous, because all are probed with the same cantilever tip. This allows for direct comparison of relative forces, thus avoiding issues of cantilever calibration or measurement conditions.[41,42]

We used the fourth filamin domain of *Dictyostelium discoideum* (ddFLN4) as fingerprint domain to identify single-molecule interactions, because it unfolds at forces lower than biotin unbinding from mSA.[44−46] We performed measurements with biotinylated ddFLN4 directly covalently attached to the cantilever tip (Figures S11−13). However, the high affinity of the mSA/biotin interaction causes a rapid loss of interaction as the cantilever tip gets clogged by mSA that was nonspecifically adsorbed to the surface.

To prevent cantilever clogging and to obtain better statistics, we introduced a second receptor−ligand pair (Figure 1B). While the surface was functionalized with mSA, the cantilever was functionalized with the adhesin SD-repeat protein G (SdrG) from *Staphylococcus epidermidis*.[47,48] After about a thousand approach−retraction cycles, biotinylated ddFLN4, to which short peptide from human fibrinogen β (Fgβ) had been genetically fused, was added to the measurement buffer. These molecules bound to the mSA on the surface via the biotin. The SdrG domain on the cantilever tip could pick up the Fgβ-peptide. Because the SdrG/Fgβ interaction can withstand a nearly 10-fold higher force than the mSA/biotin interaction,[48] we only measure the unbinding of biotin from mSA without bias from the SdrG/Fgβ interaction. On the other hand, the lower affinity of the SdrG/Fgβ interaction allows for a continuous exchange of the complexes at the tip and by means of this prevents permanent clogging of the cantilever tip. Even after 75 000 approach−retraction cycles, we still observed specific interactions between proteins immobilized on tip and surface (Figure 2).

The characteristic two-step unfolding pattern of ddFLN4 is used to identify single-molecule interactions, that is, a single biotin molecule binding to a single mSA molecule. In Figure 3A, two exemplary force−extension traces for single-molecule interaction on the area where N-mSA or C-mSA were immobilized are depicted (cantilever retraction velocity: 1,600 nm/s). Although the ddFLN4 unfolding is observed at the same force (Figures S7, S8), the final force peaks reach different values. These last peaks are attributed to the unbinding of biotin from mSA. Selecting all force curves that clearly show single-molecule interaction, we plotted mSA/biotin unbinding force histograms

DOI: 10.1021/acs.nanolett.8b04045
Nano Lett. 2019, 19, 3415−3421

Nano Letters Letter

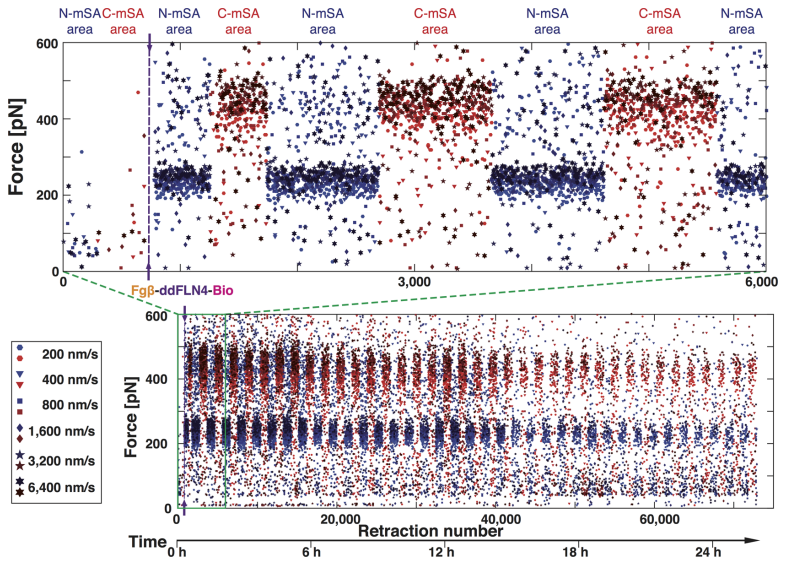

Figure 2. Course of a measurement. The final unbinding forces for all retractions of the cantilever tip from the surface are shown. Interactions on the surface area with the C-mSA are plotted in red colors; interactions in the N-mSA area are shown in blue colors. The darker the color is, the higher the cantilever retraction velocity is. The beginning of the measurement is shown on top. The Fgβ−ddFLN4−Biotin construct was added after 960 approaches, indicated by the purple dashed line and arrows. At the beginning of the measurement, high unbinding forces for N-mSA are also observed which are attributed to multiple interactions.

for both attachment geometries and all six retraction velocities (Figure 3B). We used Bell-Evans theory to fit the peaks of the distributions (Tables S1, S2).[49,50] While biotin unbinds from N-terminally tethered mSA at forces of about 200 pN, its binding to C-terminally tethered mSA is mechanically more stable and withstands forces of more than 400 pN. Fitting the dynamic force spectrum (Figure 3C), we could draw conclusions about coarse features of the binding energy landscape: by a factor of 2, the potential well is narrower for C-mSA compared to N-mSA.

To reveal the underlying molecular mechanism of the mSA/biotin interaction, ensuring statistical reliability, we performed 150 SMD production runs, which combined account for 19 μs. Simulations were performed using QwikMD[51] and GPU-accelerated NAMD.[52,53] In previous SMD studies, usually the center of mass of the SA molecules was kept at a fixed position, which does not resemble the experimental conditions. In our SMD simulations, we hold mSA either by the C-terminus or the N-terminus of the functional subunit and pulled biotin out of the binding pocket (for details on the preparation of the system, cf. Supporting Information), which is in agreement with the experimentally applied force loading geometry (Figure 1A). While for C-mSA, a unimodal force distribution was observed (Figure 4A), N-mSA showed a bimodal behavior (Figure 4B,C). For 9 out of 25 SMD replicas performed at 5000 μm/s pulling speed, the structural integrity of the N-terminal β-sheet was destroyed, before biotin left the binding pocket (Figure 4E). This structural rearrangement weakens the stability of the N-terminal β-sheet structure and thus results in lower final unbinding forces, blurring the boundaries between unbinding and unfolding. In one case, due to an extended simulation time we even observed how streptavidin regains its native fold when the force drops after biotin has left the pocket. The number of H-bonds between the first and the second β-strand provides a measure for the structural integrity (Figure 4G). If the N-terminal β-sheet structure stays intact, the number of H-bonds stays constant over time and high unbinding forces can be reached. The small unfolding observed in the simulations is beyond the resolution of our experimental setup. As the force loading rate dependence of an unfolding or unbinding event can be completely different than the one of a direct unbinding event, the simulations can be favoring the latter type of event while the experiments the former.

The simulations provide a detailed picture of the unbinding process, with atomic spatial resolution and femtosecond time resolution. Using correlation-based network analysis (Figures S14−16),[54] we analyzed the force propagation profiles, identifying which amino acids and domains of the molecules transmit force.[55] For C-mSA (Figure 5A−C), force either propagates through the long C-terminal β-strand, or through the N-terminal β-sheet structure, near the first hairpin between β-strands 1 and 2. These pathways indicate that mSA is structurally stable from both biotin sides when force is applied at the C-terminus, comparable with a claw. For N-mSA (Figure 5D−F), on the other hand, force is only rarely transmitted through the long C-terminal β-strands. Force propagates mainly through the shorter N-terminal β-strands. As the tension is high over the first and the second β-strand, high rupture forces can be reached if this region stays intact (Figure 5F). If the first two β-strands get torn apart (Figure 5E), the N-terminal structure loosens, mSA releases its grip on biotin, and biotin leaves the binding pocket.

DOI: 10.1021/acs.nanolett.8b04045
Nano Lett. 2019, 19, 3415−3421

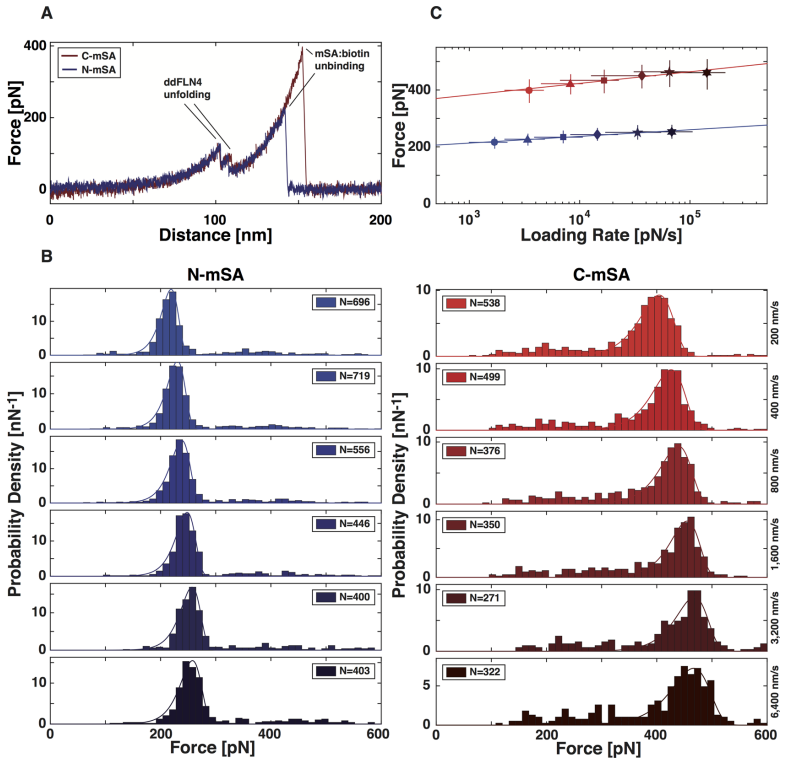

Figure 3. Analysis of force curves showing characteristic unfolding pattern. (A) Exemplary force extension traces measured at a retraction velocity of 1600 nm/s for C-mSA (red) and N-mSA (blue) displaying the characteristic two peak unfolding pattern of ddFLN4. Only traces showing this pattern are selected for further analysis. (B) Force histograms of mSA/biotin unbinding for six different retraction velocities. Peaks are fitted with Bell-Evans distributions (solid lines). (C) For all retraction velocities, the most probable unbinding force is plotted against the most probable loading rate and fitted according to Bell-Evans theory. From the fit, distance to transition state Δx_0 and zero-force off-rate $k_{off,0}$ are determined. N-mSA: $\Delta x_0 = 0.41$ nm, $k_{off,0} = 7.7 \times 10^{-8}$ s^{-1}; C-mSA: $\Delta x_0 = 0.23$ nm, $k_{off,0} = 2.5 \times 10^{-8}$ s^{-1}. Error bars are given by the full width at half-maximum of the peak of the corresponding distribution.

When there is no more tension on the mSA subunit, the native N-terminal structure is retrieved. The importance of the N-terminal structural integrity is in line with the fact that all mutations needed to generate the nonfunctional subunit, are at prominent positions within the N-terminal β-sheet structure (cf. Supporting Information).

SMD trajectories were also employed to investigate the contact between biotin and SA. Using PyContact,[56] we created a map of the interactions between ligand and receptor. Initially, the contact score was analyzed throughout the whole simulation time for each of the trajectories. To better understand the differences in an equilibrium versus a force-loaded regime, we compared the contact score over trajectory windows under no force load and under high-force load. The analysis was performed for all 50 slow pulling trajectories performed at 5000 μm/s pulling speed (25 for N-terminal pulling and 25 for C-terminal pulling). Additionally, the root-mean-square fluctuation (RMSF) was also analyzed in the same trajectory windows. Because of the large amount of data generated in such analysis, a "big-data" strategy of dimensionality reduction had to be adopted. The analysis was performed using python libraries through Jupyter Notebook.[57] Commonly known as machine learning techniques, our approach employed mutual information theory to identify the amino acid residues that were "force-active". These residues were coupled to changes in force and could indicate possible key points of force regulation. Indeed, most of these residues had been previously identified as key-players in the mechanism of SA/biotin interaction (Tables S3 and S4).

Combined, the analysis of the SMD trajectories indicate that the partial unfolding for N-terminal force loading is the cause of the lower forces seen for N-mSA compared with C-mSA in the experiments. The second N-terminal pulling unbinding pathway seen in the simulations is only rarely observed in the experiments, as indicated by the small number of high-force events in Figure 3B. On the one hand, this might be due to the much faster pulling speeds of the simulations. In the experiment, the force loading rates are at least four orders of magnitude

DOI: 10.1021/acs.nanolett.8b04045
Nano Lett. 2019, 19, 3415−3421

Nano Letters Letter

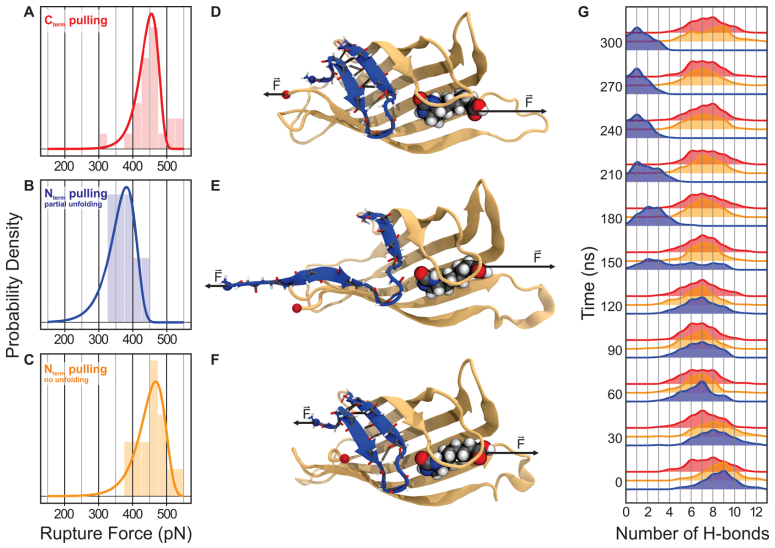

Figure 4. Results of SMD simulations. Unbinding force histogram for C-terminal attachment of mSA shows a unimodal distribution (red, A) ($N = 25$). For N-terminal attachment of mSA, two unbinding force peaks are observed: One at lower forces (blue, B) ($N = 9$) and one at higher forces (yellow, C) ($N = 16$). For C-terminal attachment of mSA, the structural integrity of the N-terminal β-sheet (marked in blue) is preserved (D). For N-terminal attachment of mSA, the structure of the N-terminal β-sheet can be destroyed before biotin unbinds from mSA, resulting in lower unbinding forces (E). If it stays intact, higher unbinding forces are reached (F). The number of hydrogen bonds between the first and the second N-terminal β-strand is a good measure to differentiate both cases (G). For the C-terminal attachment of mSA, it stays roughly constant over the timespan of the simulation (red). For N-terminal attachment, the contact is either broken completely (blue) or only slightly attenuated (yellow).

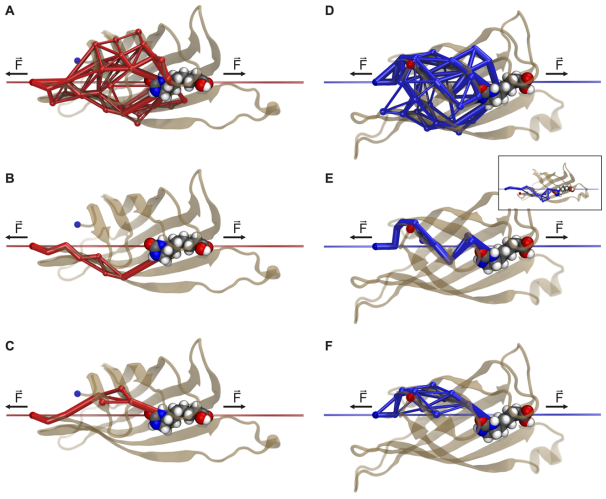

Figure 5. Force propagation pathways through the functional mSA subunit. (A) Overlay of the force propagation pathways for simulation replicas with C-terminal loading (Video S2) ($N = 25$). Force propagates through C-terminal β-sheets (B) or also through N-terminal β-sheets (C). (D) Overlay of all force propagation pathways for all simulation replicas with N-terminal loading (Video S3) ($N = 25$). Force propagates through N-terminal β-sheets. If the structural integrity of the N-terminal β-sheets is destroyed, the unbinding forces are low (E). If the N-terminal structure stays intact, higher unbinding forces can be reached (F). The thickness of the pathway edges represents the probability of force propagating through the particular edge. The probability was normalized for each simulation, leading to the same maximum thickness (maximum information pathway) for each simulation replica.

DOI: 10.1021/acs.nanolett.8b04045
Nano Lett. 2019, 19, 3415−3421

lower. The N-terminal β-sheet structure is held under tension for a much longer time, such that the unzipping of the first from the second β-strand is more likely. On the other hand, the molecular linker of the biotin to Coenzyme A (for details of the biotinylation, cf. Supporting Information) is not considered in the simulations (Figure S5) because there is no crystal structure for the linker and in addition missing force field parameters could introduce a source of imprecision. In previous combined AFM SMD studies, it was shown that only a complete simulation of all molecular linkers in proximity of the protein of interest provided an excellent agreement between experimental and simulated forces.[48] It is yet reasonable to assume that the additional interaction of the linker between biotin and Coenzyme A with mSA increases the final unbinding forces of biotin from mSA. Such interaction would favor the N-mSA unzipping/low force unbinding pathway over the high force unbinding pathway even more, also explaining the different in force distribution between simulation and experiment.

In this study, experiments and simulations were used hand-in-hand, providing a detailed picture of the system mechanics with the atomistic detail of the simulation, substantiated by the large statistical content of experiments. The nearly twofold difference in unbinding forces that we report for biotin in the two well-defined N- and C-terminal tethering geometries of mSA is nicely matched by the 2-fold reduction of the binding potential width as revealed by the Bell-Evans analysis of the rate dependence of the unbinding forces. Because we measured by ITC the same binding energy for the mSA/biotin complexes in both tethering geometries, we can conclude that our force histograms represent largely homogeneous ensembles of unbinding modes. The analysis of these modes by steered SMD revealed that in the case of the C-terminally tethered mSA the forced separation of biotin can be described best by a rupture process, leaving the molecular structure of the mSA binding pocket largely intact. The N-terminally tethered mSA, however, shows in a significant number of traces a marked structural change, a local unfolding of the binding pocket. We assume that the much slower time scale of the AFM-based SMFS favors the low force unfolding path. This partial unfolding results in a substantial widening of the potential energy landscape accompanied by a reduction of the unbinding force for N-mSA compared to C-mSA. In view on our results, it is worth noting that the widespread of SA/biotin unbinding forces reported in the literature[35,40] may have arisen from a multiplicity of force propagation geometries due to the nonspecific immobilization of the terameric streptavidins used in these investigations.

■ ASSOCIATED CONTENT

Supporting Information

The Supporting Information is available free of charge on the ACS Publications website at DOI: 10.1021/acs.nanolett.8b04045.

Materials and methods, results of isothermal titration calorimetry, results of SMFS with covalent attachment of ddFLN4, fit parameter of Bell-Evans fits, results of mutual information analysis, protein sequences (PDF)

Steered molecular dynamics simulations. Analyses of C- versus N-terminal pulling reveal that the instability of N-terminal region during the latter pulling is fundamental for the differences observed in force traces (AVI)

Exposé of all force propagation pathways for all simulation replicas with C-terminal loading (AVI)

Exposé of all force propagation pathways for all simulation replicas with N-terminal loading (AVI)

■ AUTHOR INFORMATION

Corresponding Author

*E-mail: rcbernardi@ks.uiuc.edu.

ORCID

Steffen M. Sedlak: 0000-0002-7037-1793
Leonard C. Schendel: 0000-0002-1986-2693
Marcelo C. R. Melo: 0000-0001-6901-1646
Hermann E. Gaub: 0000-0002-4220-6088
Rafael C. Bernardi: 0000-0003-0758-2026

Author Contributions

The manuscript was written through contributions of all authors. All authors have given approval to the final version of the manuscript.

Author Contributions

⊥S.M.S. and L.C.S. contributed equally.

Funding

The European Research Council (ERC advanced grant Cellufuel Grant 294438) and the Deutsche Forschungsgemeinschaft (DFG, Sonderforschungsbereich 1032, Teilprojekt A01) provided funding for this work. Furthermore, it was supported by the National Institutes of Health (NIH) Grant P41-GM104601, "Center for Macromolecular Modeling and Bioinformatics". R.C.B. is partially supported by National Science Foundation (NSF) Grant MCB-1616590, "Molecular Modeling of Bioenergetic Systems". Molecular dynamics simulations made use of GPU-accelerated nodes of Blue Waters supercomputer as part of the Petascale Computational Resource (PRAC) grant "The Computational Microscope", which is supported by the National Science Foundation (award number ACI-1713784). The state of Illinois and the National Science Foundation (awards OCI-0725070 and ACI-1238993) support Blue Waters sustained-petascale computing project.

Notes

The authors declare no competing financial interest.

■ ACKNOWLEDGMENTS

The authors thank A. Kardinal and T. Nicolaus for laboratory support, L.F. Milles for providing the SdrG/Fgβ-system, and M. Scheurer for assistance with integrating PyContact and Jupyter. The authors acknowledge M.S. Bauer and C. Kluger for helpful discussions. S.M.S. thanks the Nanosystems Initiative Munich for support.

■ ABBREVIATIONS

SA, streptavidin; AFM, atomic force microscopy; SMFS, single-molecule force spectroscopy; SMD, steered molecular dynamics; mSA, monovalent streptavidin; N-mSA, N-terminally tethered monovalent streptavidin; C-mSA, C-terminally tethered monovalent streptavidin; ddFLN4, fourth filamin domain of *Dictyostelium discoideum*; SdrG, SD-repeat protein G from *Staphylococcus epidermidis*; Fgβ, a short peptide from human fibrinogen β

■ REFERENCES

(1) Dundas, C. M.; Demonte, D.; Park, S. *Appl. Microbiol. Biotechnol.* **2013**, *97* (21), 9343−53.
(2) Wilchek, M.; Bayer, E. A. *Anal. Biochem.* **1988**, *171* (1), 1−32.
(3) Bayer, E. A.; Ben-Hur, H.; Wilchek, M. *Methods Enzymol.* **1990**, *184*, 80−9.
(4) Green, N. M. *Methods Enzymol* **1990**, *184*, 51−67.

DOI: 10.1021/acs.nanolett.8b04045
Nano Lett. 2019, 19, 3415−3421

(5) Laitinen, O. H.; Nordlund, H. R.; Hytonen, V. P.; Kulomaa, M. S. *Trends Biotechnol.* **2007**, *25* (6), 269−77.
(6) Freitag, S.; Le Trong, I.; Chilkoti, A.; Klumb, L. A.; Stayton, P. S.; Stenkamp, R. E. *J. Mol. Biol.* **1998**, *279* (1), 211−21.
(7) Lim, K. H.; Huang, H.; Pralle, A.; Park, S. *Biotechnol. Bioeng.* **2013**, *110* (1), 57−67.
(8) Scholl, Z. N.; Yang, W.; Marszalek, P. E. *ACS Nano* **2015**, *9* (2), 1189−97.
(9) Bansal, N.; Zheng, Z.; Song, L. F.; Pei, J.; Merz, K. M., Jr. *J. Am. Chem. Soc.* **2018**, *140* (16), 5434−5446.
(10) Freitag, S.; Le Trong, I.; Klumb, L.; Stayton, P. S.; Stenkamp, R. E. *Protein Sci.* **1997**, *6* (6), 1157−1166.
(11) Howarth, M.; Chinnapen, D. J.; Gerrow, K.; Dorrestein, P. C.; Grandy, M. R.; Kelleher, N. L.; El-Husseini, A.; Ting, A. Y. *Nat. Methods* **2006**, *3* (4), 267−73.
(12) Zhang, M.; Biswas, S.; Deng, W.; Yu, H. *Sci. Rep.* **2016**, *6*, 35915.
(13) Florin, E. L.; Moy, V. T.; Gaub, H. E. *Science* **1994**, *264* (5157), 415−7.
(14) Lee, G.; Kidwell, D.; Colton, R. *Langmuir* **1994**, *10* (2), 354−357.
(15) Moy, V. T.; Florin, E. L.; Gaub, H. E. *Science* **1994**, *266* (5183), 257−9.
(16) Merkel, R.; Nassoy, P.; Leung, A.; Ritchie, K.; Evans, E. *Nature* **1999**, *397* (6714), 50−3.
(17) Wong, J.; Chilkoti, A.; Moy, V. T. *Biomol. Eng.* **1999**, *16* (1−4), 45−55.
(18) Stevens, M. M.; Allen, S.; Davies, M. C.; Roberts, C. J.; Schacht, E.; Tendler, S. J. B.; VanSteenkiste, S.; Williams, P. M. *Langmuir* **2002**, *18* (17), 6659−6665.
(19) Yuan, C.; Chen, A.; Kolb, P.; Moy, V. T. *Biochemistry* **2000**, *39* (33), 10219−23.
(20) Lo, Y.-S.; Zhu, Y.-J.; Beebe, T. P. *Langmuir* **2001**, *17* (12), 3741−3748.
(21) Rico, F.; Moy, V. T. *J. Mol. Recognit.* **2007**, *20* (6), 495−501.
(22) de Odrowaz Piramowicz, M.; Czuba, P.; Targosz, M.; Burda, K.; Szymonski, M. *Acta Biochim Pol* **2006**, *53* (1), 93−100.
(23) Taninaka, A.; Takeuchi, O.; Shigekawa, H. *Int. J. Mol. Sci.* **2010**, *11* (5), 2134−51.
(24) Sedlak, S. M.; Bauer, M. S.; Kluger, C.; Schendel, L. C.; Milles, L. F.; Pippig, D. A.; Gaub, H. E. *PLoS One* **2017**, *12* (12), e0188722.
(25) Ott, W.; Jobst, M. A.; Schoeler, C.; Gaub, H. E.; Nash, M. A. *J. Struct. Biol.* **2017**, *197* (1), 3−12.
(26) Walder, R.; LeBlanc, M. A.; Van Patten, W. J.; Edwards, D. T.; Greenberg, J. A.; Adhikari, A.; Okoniewski, S. R.; Sullan, R. M. A.; Rabuka, D.; Sousa, M. C.; Perkins, T. T. *J. Am. Chem. Soc.* **2017**, *139* (29), 9867−9875.
(27) Tych, K. M.; Jahn, M.; Gegenfurtner, F.; Hechtl, V. K.; Buchner, J.; Hugel, T.; Rief, M. *J. Phys. Chem. B* **2018**.
(28) Kriegel, F.; Ermann, N.; Forbes, R.; Dulin, D.; Dekker, N. H.; Lipfert, J. *Nucleic Acids Res.* **2017**, *45*, 5920.
(29) Sitters, G.; Kamsma, D.; Thalhammer, G.; Ritsch-Marte, M.; Peterman, E. J.; Wuite, G. J. *Nat. Methods* **2015**, *12* (1), 47−50.
(30) Grubmuller, H.; Heymann, B.; Tavan, P. *Science* **1996**, *271* (5251), 997−9.
(31) Izrailev, S.; Stepaniants, S.; Balsera, M.; Oono, Y.; Schulten, K. *Biophys. J.* **1997**, *72* (4), 1568−81.
(32) Chilkoti, A.; Stayton, P. S. *J. Am. Chem. Soc.* **1995**, *117* (43), 10622−10628.
(33) Chilkoti, A.; Boland, T.; Ratner, B. D.; Stayton, P. S. *Biophys. J.* **1995**, *69* (5), 2125−30.
(34) Pincet, F.; Husson, J. *Biophys. J.* **2005**, *89* (6), 4374−81.
(35) Guo, S.; Ray, C.; Kirkpatrick, A.; Lad, N.; Akhremitchev, B. B. *Biophys. J.* **2008**, *95* (8), 3964−3976.
(36) Song, J.; Li, Y.; Ji, C.; Zhang, J. Z. H. *Sci. Rep.* **2015**, *5*, 7906.
(37) Liu, F.; Zhang, J. Z. H.; Mei, Y. *Sci. Rep.* **2016**, *6*, 27190.
(38) Rico, F.; Russek, A.; Gonzalez, L.; Grubmuller, H.; Scheuring, S. **2018** arXiv preprint arXiv:1808.07122.
(39) Zlatanova, J.; Lindsay, S. M.; Leuba, S. H. *Prog. Biophys. Mol. Biol.* **2000**, *74* (1−2), 37−61.
(40) Teulon, J. M.; Delcuze, Y.; Odorico, M.; Chen, S. W.; Parot, P.; Pellequer, J. L. *J. Mol. Recognit.* **2011**, *24* (3), 490−502.
(41) Verdorfer, T.; Bernardi, R. C.; Meinhold, A.; Ott, W.; Luthey-Schulten, Z.; Nash, M. A.; Gaub, H. E. *J. Am. Chem. Soc.* **2017**, *139* (49), 17841−17852.
(42) Verdorfer, T.; Gaub, H. E. *Sci. Rep.* **2018**, *8* (1), 9634.
(43) Hyre, D. E.; Le Trong, I.; Merritt, E. A.; Eccleston, J. F.; Green, N. M.; Stenkamp, R. E.; Stayton, P. S. *Protein Sci.* **2006**, *15* (3), 459−67.
(44) Schwaiger, I.; Kardinal, A.; Schleicher, M.; Noegel, A. A.; Rief, M. *Nat. Struct. Mol. Biol.* **2004**, *11* (1), 81−5.
(45) Milles, L. F.; Bayer, E. A.; Nash, M. A.; Gaub, H. E. *J. Phys. Chem. B* **2017**, *121* (15), 3620−3625.
(46) Bauer, M. S.; Milles, L. F.; Sedlak, S. M.; Gaub, H. E. **2018**, *bioRxiv*.
(47) Herman, P.; El-Kirat-Chatel, S.; Beaussart, A.; Geoghegan, J. A.; Foster, T. J.; Dufrene, Y. F. *Mol. Microbiol.* **2014**, *93* (2), 356−68.
(48) Milles, L. F.; Schulten, K.; Gaub, H. E.; Bernardi, R. C. *Science* **2018**, *359* (6383), 1527−1533.
(49) Bell, G. I. *Science* **1978**, *200* (4342), 618−27.
(50) Evans, E.; Ritchie, K. *Biophys. J.* **1997**, *72* (4), 1541−55.
(51) Ribeiro, J. V.; Bernardi, R. C.; Rudack, T.; Stone, J. E.; Phillips, J. C.; Freddolino, P. L.; Schulten, K. *Sci. Rep.* **2016**, *6*, 26536.
(52) Phillips, J. C.; Braun, R.; Wang, W.; Gumbart, J.; Tajkhorshid, E.; Villa, E.; Chipot, C.; Skeel, R. D.; Kale, L.; Schulten, K. *J. Comput. Chem.* **2005**, *26* (16), 1781−802.
(53) Melo, M. C. R.; Bernardi, R. C.; Rudack, T.; Scheurer, M.; Riplinger, C.; Phillips, J. C.; Maia, J. D. C.; Rocha, G. B.; Ribeiro, J. V.; Stone, J. E.; Neese, F.; Schulten, K.; Luthey-Schulten, Z. *Nat. Methods* **2018**, *15* (5), 351−354.
(54) Sethi, A.; Eargle, J.; Black, A. A.; Luthey-Schulten, Z. *Proc. Natl. Acad. Sci. U. S. A.* **2009**, *106* (16), 6620−5.
(55) Schoeler, C.; Bernardi, R. C.; Malinowska, K. H.; Durner, E.; Ott, W.; Bayer, E. A.; Schulten, K.; Nash, M. A.; Gaub, H. E. *Nano Lett.* **2015**, *15* (11), 7370−6.
(56) Scheurer, M.; Rodenkirch, P.; Siggel, M.; Bernardi, R. C.; Schulten, K.; Tajkhorshid, E.; Rudack, T. *Biophys. J.* **2018**, *114* (3), 577−583.
(57) Kluyver, T.; Benjamin, R.-K.; Fernando, P.; Brian, G.; Matthias, B.; Jonathan, F.; Kyle, K.; Jessica, H.; Jason, G.; Sylvain, C.; Paul, I.; Damián, A.; Safia, A.; Carol, W.; Jupyter Development, T. In *Jupyter Notebooks—a publishing format for reproducible computational workflows*; Positioning and Power in Academic Publishing: Players, Agents and Agendas, 20th International Conference on Electronic Publishing, Göttingen, Germany, 2016.

DOI: 10.1021/acs.nanolett.8b04045
Nano Lett. 2019, 19, 3415−3421

Supplementary Information

Direction Matters – Monovalent Streptavidin:Biotin Complex under Load

Steffen M. Sedlak,[‡,1] Leonard C. Schendel,[‡,1] Marcelo C. R. Melo,[2,3] Diana A. Pippig,[1] Zaida Luthey-Schulten,[2,3,4] Hermann E. Gaub,[1] and Rafael C. Bernardi[2]*

[1]Lehrstuhl für Angewandte Physik and Center for NanoScience (CeNS), Ludwig-Maximilians-Universität München, Amalienstr. 54, 80799 Munich, Germany

[2]Beckman Institute for Advanced Science and Technology, University of Illinois at Urbana-Champaign, Urbana, IL 61801, USA

[3]Center for Biophysics and Quantitative Biology, University of Illinois at Urbana-Champaign, Urbana, IL 61801, USA

[4]Department of Chemistry, University of Illinois at Urbana-Champaign, Urbana, IL 61801, USA

Table of contents

Extended table of contents

I. Materials and methods

I.1 Preparation of proteins

I.1.A Preparation of monovalent streptavidin

A detailed description of the expression, lysis and purification lab protocols is given by Sedlak *et al*.,[1] here we just provide a short overview. We used different streptavidin (SA) monomers encoded on different pET vectors: SA monomers with an N-terminal cysteine (Cys-SA), SA monomers with a C-terminal cysteine (SA-Cys), and SA monomers without cysteine but with three mutations in the binding pocket (N23A, S27D, S45A) preventing the binding of biotin (dSA). SA-Cys and Cys-SA further contained a polyhistidine tag. All monomers were expressed separately in *E. coli* BL21(DE3)-CodonPlus. SA plasmids were transferred to *E. coli* BL21(DE3)-CodonPlus cells (Agilent Technologies Inc., Santa Clara, USA) and expressed in SB medium. After cell lysis and purification of inclusion bodies, the monomers were denatured and mixed to obtain a 1:10 ratio of functional to non-functional subunits using dSA and either Cys-SA or SA-Cys. By slowly diluting the mixture into phosphate buffered saline (PBS; Sigma-Aldrich, Saint Louis, USA), the subunits refolded and tetrameric SA was formed. Monovalent streptavidin (mSA) with a unique, either N- or C-terminal cysteine (N-mSA or C-mSA) was purified by immobilized metal ion affinity chromatography making use of the polyhistidine tag on the functional subunit.

I.1.B Preparation of fingerprint domains

As a fingerprint domain for AFM-based force spectroscopy, the well-characterized fourth filamin domain of *Dictyostelium discoideum* (ddFLN4)[2] was used. Two different constructs were prepared: For the first, we added an N-terminal cysteine for site-specific immobilization and mutated the internal cysteine 18 to serine. For the second construct, we exchanged the N-terminal cysteine for an Fgβ-petide. For both, we cloned a ybbR-tag[3] to the C-terminus which we used to covalently attach a Coenzyme A modified biotin via a Sfp phoshopantetheinyl transferase-catalyzed reaction. The ddFLN4 construct was expressed in *E. coli* BL21(DE3)-CodonPlus and purified by immobilized metal ion affinity chromatography.

I.1.C Biotinylation of the ddFLN4-construct

45 μM ddFLN4-construct, 50 μM CoA-Biotin (New England Biolabs, Ipswich, Massachusetts, USA), and 5 μM Sfp Synthase dissolved in Sfp buffer (10 mM TRIS, 10 mM MgCl2, pH 7.5) were allowed to react for 1 h at 37°C. The reaction product was purified using Zeba Spin Desalting Columns (Thermo Fisher Scientific, Waltham, USA) with a molecular weight cut off of 7 kDa equilibrated with coupling buffer (50 mM NaCl, 50 mM NaHPO4, 10 mM EDTA, pH 7.2) according to the manufacturer's instruction.

I.2. Isothermal titration calorimetry

Isothermal titration calorimetry experiments were conducted with a Malvern Microcal ITC200. We diluted 8 mg of biotin (Sigma-Aldrich, St. Louis, USA) in 40 ml PBS to obtain an 818.6 μM stock solution. Using Zeba Spin Columns with a molecular weight cut off of 40 kDa according to the manufacturer's protocol, we performed a buffer exchange to have C-mSA or N-mSA, respectively, dissolved in the same PBS. We determined the protein concentration using the absorption at 280 nm and an absorption coefficient of 167,760 $M^{-1}cm^{-1}$. We diluted biotin with PBS to obtain tenfold molar excess, which resulted in a final molar ratio of about 2:1 (mSA:biotin) in the ITC measurement. For both mSA variants, we performed three independent measurements.

I.3. AFM-based SMFS measurements

I.3.A Surface functionalization

Bifunctional polyethylene glycol of 5,000 Da having an N-hydroxysuccinimide group at one end and a maleimide group on the other (NHS-PEG5000-MAL, Rapp Polymere, Tübingen, Germany) was dissolved in 50 mM HEPES at pH 7.5 and immediately used to incubate aminosilanized glass slides.[4] After one hour, the glass slides were thoroughly washed in ultrapure water.

5 μM N-mSA and 5 μM C-mSA were supplemented with 1 mM Bond-Breaker TCEP Solution (Thermo Fisher Scientific). After one hour, the mixture was purified using Zeba Spin Desalting Columns (Thermo Fisher Scientific, Waltham, USA) with a molecular weight cut off of 40 kDa equilibrated with coupling buffer (50 mM NaCl, 50 mM NaHPO4, 10 mM EDTA, pH 7.2) according to the manufacturer's instruction.
Using silicon masks, 10 μl droplets of the prepared C-mSA and N-mSA were placed on the surfaces. After a one-hour incubation, the surfaces were thoroughly washed using PBS, to rinse off unbound mSA.

I.3.B Cantilever functionalization

As for the surfaces, aminosilanized[4] BioLever mini (Olympus Corporation, Tokyo, Japan) were first incubated with heterobifunctional polyethylene glycol having a N-hydroxysuccinimide on the one end and a maleimide group on the other end and then washed in ultrapure water.
To couple the SD-repeat protein G from *staphylococcus epidermidis* (SdrG),[5] the cantilevers were incubated with 1 mM Coenzyme A diluted in coupling buffer for one hour. The sulfhydryl reacts with the maleimide to form a stable thioether bond. After washing in ultrapure water, the cantilevers were placed in Sfp buffer containing13 μM SdrG with a C-terminal ybbR-tag, 5 μM Sfp Synthase for at least one hour. The Sfp Synthase covalently coupled the ybbR-tag to the Coenzyme A. Finally, the levers were washed and stored in PBS.

To couple ddFLN4 to the cantilever, the Coenzyme A step was omitted and the unique cysteine of the biotinylated ddFLN4 constructs was used to specifically and covalently couple to the maleimide on the cantilever.

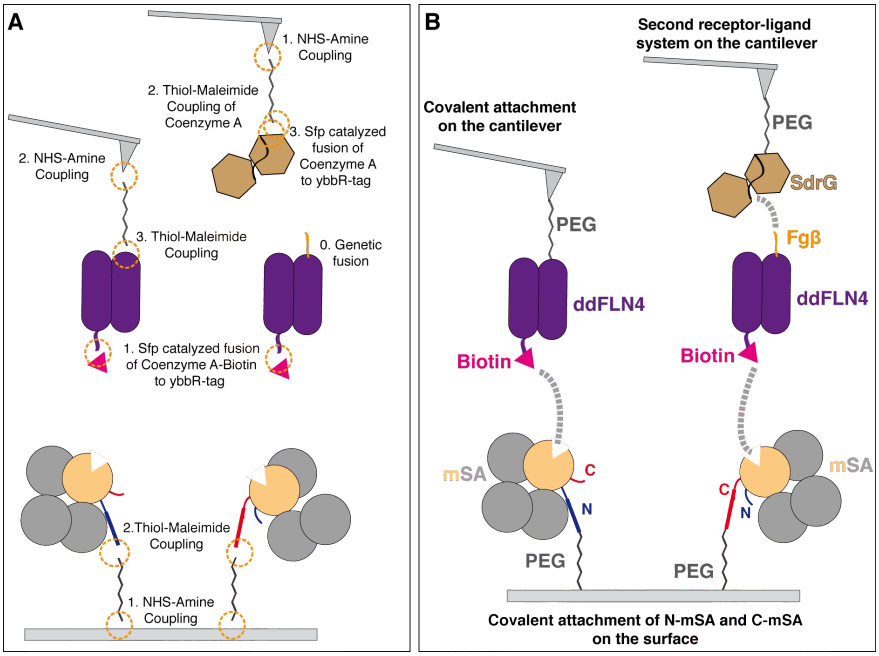

Figure S1. Surface and cantilever functionalization. (A) Aminosilanized cantilever tips and glass surfaces are functionalized separately by applying several subsequent chemical and enzyme mediated reaction steps. (B) The two attachment strategies: Covalent attachment of the biotinylated ddFLN4 to the cantilever tip or with the second receptor-ligand system on the cantilever, where biotinylated Fgβ-ddFLN4 constructs were added to the buffer solution. In both cases, N-mSA and C-mSA were covalently attached to the surface. The grey dashed lines indicate non-covalent receptor-ligand interactions.

I.3.C AFM-based force spectroscopy measurements

AFM-based force spectroscopy measurements were performed on a custom-built AFM[6] controlled with a self-written Igor Pro 6 software operating a commercial MFP3D controller. Both mSA constructs were immobilized on different spots on the same surface. The cantilever tip was either covalently functionalized with biotinylated fingerprint proteins or functionalized with the SdrG. In the latter case, biotinylated ddFLN4 constructs equipped with an N-terminal Fgβ-Peptide were added to the solution. After short contact with the surface, the cantilever was retracted with constant velocities and force-distance curves were recorded. After each retraction, the surface was moved 100 nm to provide an unused area to the cantilever for the next approach. After a few hundred approach-retraction-cycles, the surface was moved to expose the spot, where the other mSA construct had been immobilized, to the cantilever tip. S-Using the same cantilever for pulling mSA:biotin in two different but distinct geometries, facilitates direct comparison of both configurations.

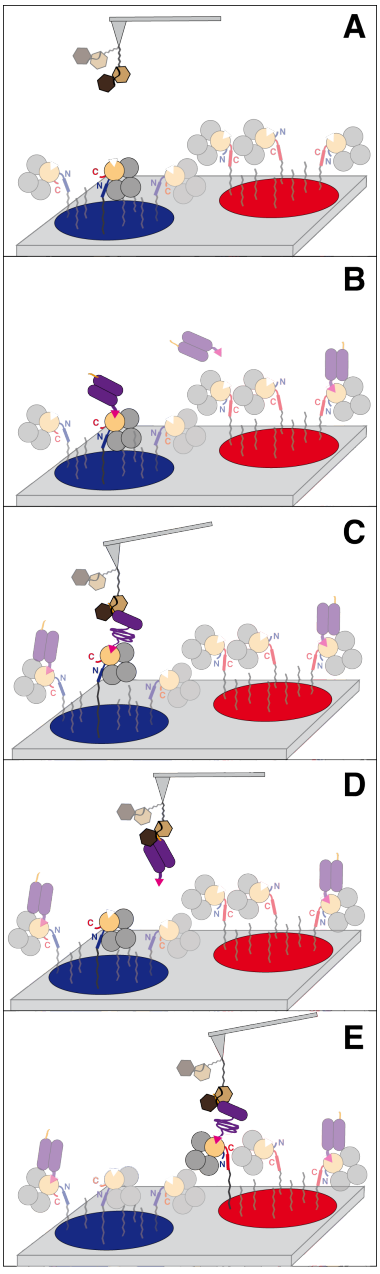

Figure S2. Detailed description of the AFM measurement process. (A) Different areas of the surface, a few millimeters apart from each other, are functionalized with N-mSA (blue are) and C-mSA (red area). The cantilever is functionalized with SdrG. To ensure that there is no specific interaction between SdrG and mSA, we perform a few hundred approach-retraction cycles. (B) A low concentration of Fgβ-ddFLN4-biotin construct is added to the solution and binds to some of the mSA molecules on the surface. (C) Approaching the cantilever tip, SdrG binds to an Fgβ-Peptide. Retracting the cantilever, ddFLN4 unfolds and finally biotin unbinds from mSA. (D) The ddFLN4 refolds and stays on the lever. Moving the surface, other mSA molecules are probed with the same fingerprint domain. At some point, the Fgβ unbinds from SdrG and another ddFLN4 is picked up from the surface. (E) Every few hundred approach-retraction cycles, the surface is moved so that the cantilever tip interacts with the other area on the surface.

I.4. Sequences of the protein constructs

Functional SA subunit with C-terminal cysteine (magenta) and polyhistidine tag (green):
M**EAGITGTWYNQLGSTFIVTAGADGALTGTYESAVGNAESRYVLTGRYDSAPATD GSGTALGWTVAWKNNYRNAHSATTWSGQYVGGAEARINTQWLLTSGTTEANAW KSTLVGHDTFTKVKPSAAS**CLE**HHHHHH**

Functional SA subunit with N-terminal cysteine (magenta) and C-terminal polyhistidine tag (green):
M**C**GS**EAGITGTWYNQLGSTFIVTAGADGALTGTYESAVGNAESRYVLTGRYDSAPA TDGSGTALGWTVAWKNNYRNAHSATTWSGQYVGGAEARINTQWLLTSGTTEANA WKSTLVGHDTFTKVKPSAAS**LE**HHHHHH**

Non-functional SA subunit with the three mutations N23A, S27D, S45A (red):
M**EAGITGTWY**A**QLG**D**TFIVTAGADGALTGTYE**A**AVGNAESRYVLTGRYDSAPATD GSGTALGWTVAWKNNYRNAHSATTWSGQYVGGAEARINTQWLLTSGTTEANAW KSTLVGHDTFTKVKPSAAS**

ddFLN4 construct with N-terminal ybbR-tag (blue) and polyhistidine tag (green) and C-terminal cysteine (magenta). The internal cysteine 18 is mutated to serine (red):
M**DSLEFIASKLA**HHHHHH**GS**ADPEKSYAEGPGLDGGE**S**FQPSKFKIHAVDPDGVHR TDGGDGFVVTIEGPAPVDPVMVDNGDGTYDVEFEPKEAGDYVINLTLDGDNVNGF PKTVTVKPAP**GS**C

ddFLN4 construct with N-terminal Fgβ-peptide (cyan), C-terminal polyhistidine tag (green) and ybbR-tag (blue):
MAT**NEEGFFSARGHRPLD**GSGSGSGSAGTGSG**ADPEKSYAEGPGLDGGE**S**FQPSKFK IHAVDPDGVHRTDGGDGFVVTIEGPAPVDPVMVDNGDGTYDVEFEPKEAGDYVIN LTLDGDNVNGFPKTVTVKPAP**SG**HHHHHH**GS**DSLEFIASKLALPETGG

The following subunits and mSA constructs made thereof were used to ensure that the position of the polyhistidine tag is not influencing the rupture forces measured with AFM-based SMFS.

Functional SA subunit with N-terminal cysteine (magenta) and polyhistidine tag (green):
MGSS**HHHHHHHH**M**C**GS**EAGITGTWYNQLGSTFIVTAGADGALTGTYESAVGNAESR YVLTGRYDSAPATDGSGTALGWTVAWKNNYRNAHSATTWSGQYVGGAEARINTQ WLLTSGTTEANAWKSTLVGHDTFTKVKPSAAS**

Functional SA subunit with C-terminal cysteine (magenta) and N-terminal polyhistidine tag (green):
MGSS**HHHHHHHH**MGS**EAGITGTWYNQLGSTFIVTAGADGALTGTYESAVGNAESRY VLTGRYDSAPATDGSGTALGWTVAWKNNYRNAHSATTWSGQYVGGAEARINTQ WLLTSGTTEANAWKSTLVGHDTFTKVKPSAAS**C

I.5. In silico force spectroscopy

Employing advanced run options of QwikMD,[7] our *in silico* approach followed previously published protocols, which were recently published for filamins,[8] cellulosomes,[9] and adhesins.[5]

I.5.A Simulation setup

The structure of a monovalent *Streptomyces avidinii* streptavidin (mSA) had been solved by means of X-ray crystallography at 1.65 Å resolution and was available at the protein data bank (PDB: 5TO2).[10] As this structure does not contain the biotin bound to streptavidin, the structure of the tetravalent *S. avidinii* streptavidin bound to biotin (PDB: 1MK5), which was also solved by means of X-ray crystallography at 1.4 Å resolution,[11] was used to place the biotin on to its binding site at chain D of the mSA. The alignment and placing of the biotin into the monovalent structure was performed using VMD.[12] Employing advanced run options of QwikMD,[7] the structure was solvated and the net charge of the system was neutralized in a 0.15 mol/l sodium

chloride solution. In total, approximately 275,000 atoms were simulated in each simulation. The CHARMM36 force field,[13] along with the TIP3 water model[14] was used to describe all systems.

I.5.B Equilibrium molecular dynamics simulations

All MD simulations in the present study were performed employing the GPU-accelerated NAMD molecular dynamics package.[15] The simulations were performed assuming periodic boundary conditions in the NpT ensemble with temperature maintained at 300 K using Langevin dynamics for temperature and pressure coupling, the latter kept at 1 bar. A distance cut-off of 11.0 Å was applied to short-range non-bonded interactions, whereas long-range electrostatic interactions were treated using the particle-mesh Ewald (PME) method.[16] The equations of motion were integrated using the r-RESPA multiple time step scheme[17] to update the van der Waals interactions every step and electrostatic interactions every two steps. The time step of integration was chosen to be 2 fs for all simulations performed. Before the MD simulations, all systems were submitted to an energy minimization protocol for 5,000 steps. An MD simulation with position restraints in the protein backbone atoms and biotin non-hydrogen atoms was performed for 10 ns. To allow for a total relaxation of the system and to make sure biotin was stable in the streptavidin pocket, a 100 ns simulation in equilibrium, where no external forces were applied, was performed. The MD protocol served to pre-equilibrate the system before the steered molecular dynamics (SMD) simulations were performed.

I.5.C Steered molecular dynamics simulations

With structures properly equilibrated and checked, SMD simulations[18] were performed using a constant velocity stretching (SMD-CV protocol), employing three different pulling speeds: 5.0, 0.5 and 0.05 Å/ns. Simulations were performed restraining the position of the carbon C1 of biotin while pulling the C_α of either the N- or C-terminal amino acid residue, GLY16 or LYS134, respectively. As recently shown, for an accurate investigation of a pulling experiment, many simulation replicas are necessary, with simulation and experiments performed as similarly as possible.[5] Here, for both configurations, many replicas were performed. For each, N- and C-terminal pulling, 25 replicas were performed at 0.05 Å/ns pulling speed, with each of the

50 pulling simulations ranging from 350 to 400 ns total simulation time. Additionally, for C-terminal pulling, 50 replicas were performed at 0.5 Å/ns pulling speed, and 50 replicas at 5.0 Å/ns. In total, approximately 19 μs of production SMD were performed using GPU-accelerated XK nodes of the NCSA/Blue Waters supercomputer. The SMD procedure is equivalent to attaching one end of a harmonic spring to the end of a molecule and pulling on the end of the other molecule with another spring. The force applied to the harmonic spring is then monitored during the time of the molecular dynamics simulation. The pulling point was moved with constant velocity along the z-axis and due to the single anchoring point and the single pulling point the system is quickly aligned along the z-axis. Owing to the flexibility of the experimentally employed linkers connecting the domains of interest and the fingerprint domains, this approach reproduces the experimental protocol.

I.5.D Simulation analysis

Simulation force-time traces were analyzed analogously to experimental data. For each simulation, the rupture force was determined as the highest force of a trace and the force loading rate was determined as a linear fit to the force versus time traces immediately before rupture. Analyses of force traces and MD trajectories, except for the force propagation analyses, were carried out employing python scripts taking advantage of Jupyter Notebooks.[19] Particularly, MDAnalysis,[20] and PyContact[21] were employed for trajectory analysis together with in-house scripting wrappers, which collected information from all simulation replicas. Mutual information coefficients were calculated[22] to identify observables that are closely related to the force traces of the simulated replicas. This process, known as “feature selection”, took into consideration contacts between biotin and streptavidin (calculated using PyContact), and RMSF values (calculated using MDAnalysis).

Force propagation analyses were performed using dynamical network analysis, which is implemented in VMD’s[12] Network View plugin.[23] A network was defined as a set of nodes, all α-carbons, with connecting edges. Edges connect pairs of nodes if corresponding monomers are in contact, and two monomers are said to be in contact if they fulfill a proximity criterion, namely any heavy atoms (non-hydrogen) from the two monomers are within 4.5 Å of each other for at least 75% of the frames analyzed. Filtering this network, one can investigate allosteric

signaling.[24] Allostery can be understood in terms of pathways of residues that efficiently transmit energy, here in the form of mechanical stress, between different binding sites.[25] The dynamical networks were constructed from 20 ns windows of the total trajectories sampled every 400 ps. The probability of information transfer across an edge is set as w_{ij}=-log(|C_{ij}|), where C is the correlation matrix calculated with Carma.[26] Using the Floyd-Warshall algorithm, the suboptimal paths were then calculated. The tolerance value used for any path to be included in the suboptimal path was -log(0.5)=0.69. As previously demonstrated by our group,[25] Pearson correlation is ideal for force propagation calculation.

II. Supporting data

II.1. Streptavidin and biotin structure

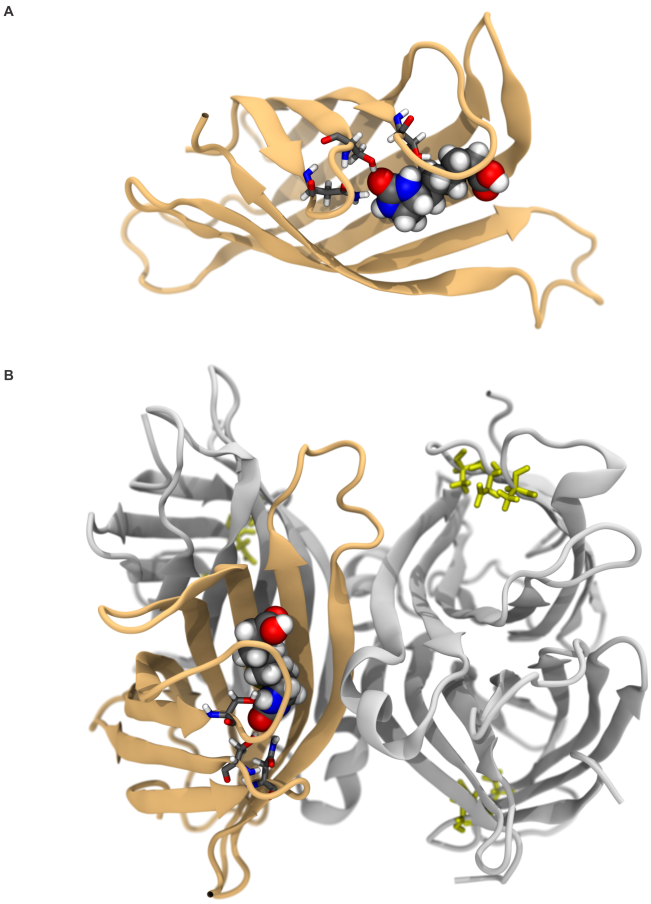

Figure S3. Crystal structure of mSA. (A) Functional SA subunit with biotin in the binding pocket. Asn23, Ser27, and Ser45 (the residues that are mutated in the non-functional subunits) are shown as sticks and colored by element. They are all located towards the N-terminus. (B) mSA tetramer. The functional subunit is shown as before. Non-functional subunits are depicted in grey. Mutated residues are highlighted as yellow sticks.

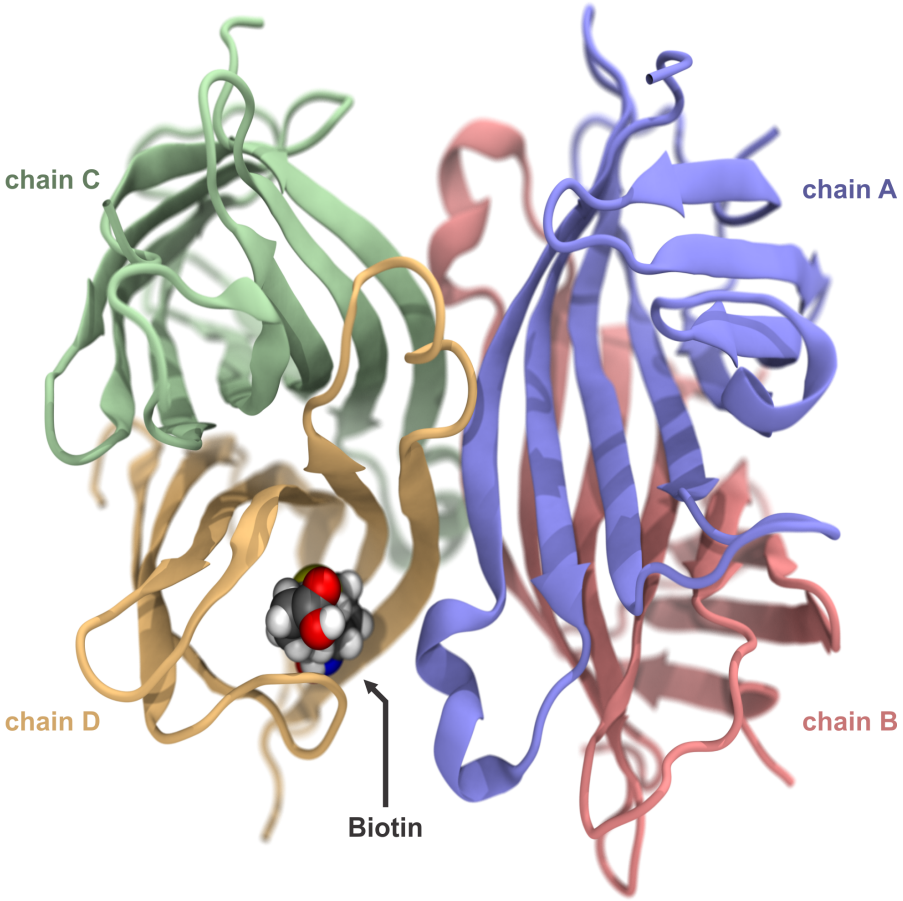

Figure S4. Tetrameric structure of mSA. The functional subunit (chain D) of SA with biotin bound is shown in bright orange. The non-functional subunits are shown in light purple (chain A), red (chain B), and green (chain C). Residues in the helical loop of chain A stabilize the biotin binding.

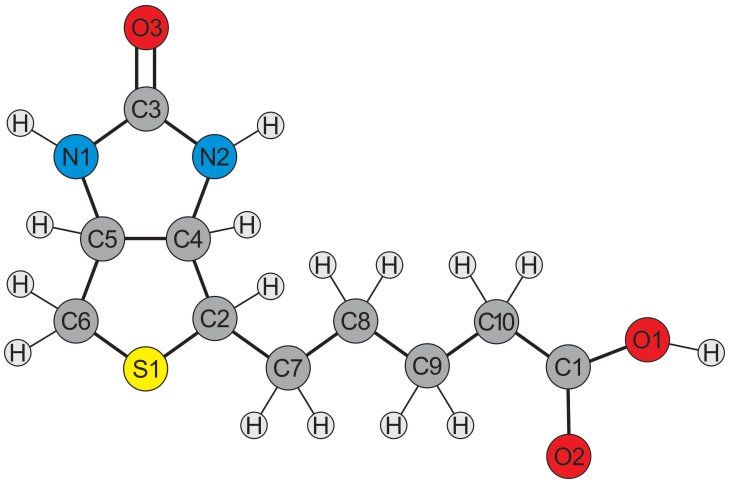

Figure S5. Representation of the chemical structure of the biotin. The structure shows the naming of the non-hydrogen atoms as they used in the simulations and analysis.

II.2. Isothermal Titration Calorimetry

To ascertain that the observed force difference results from the tethering geometry and is not caused by the tags fused to mSA, we performed isothermal titration calorimetry at 25°C with both mSA variants (Fig. S1). Titrating biotin into the reaction chamber containing either N-mSA or C-mSA, we determined the reaction enthalpy and stoichiometry of the binding. For comparability, we used the same biotin stock solution for all measurements. Every mSA was measured three times and the data were fitted individually. No significant difference in stoichiometry or binding enthalpy was observed. Mean and standard error of the three fits to N-mSA resulted in N=1,0±0,1 and ΔH=(-25,2±0,2) kcal/mol. For the fits to the C-mSA data, we obtained N=0,98±0,04 and ΔH=(-25,3±0,2) kcal/mol. For both mSA, the binding affinity was outside of the measurement range of our instrument but an upper limit of 1 nM could be assigned. The data are in good agreement with previously reported values for mSA. The binding enthalpy is comparable to wildtype SA.[1, 27] We thus conclude that in the absence of force, both N-mSA and C-mSA have one subunit that binds biotin in the way the SA wildtype does.

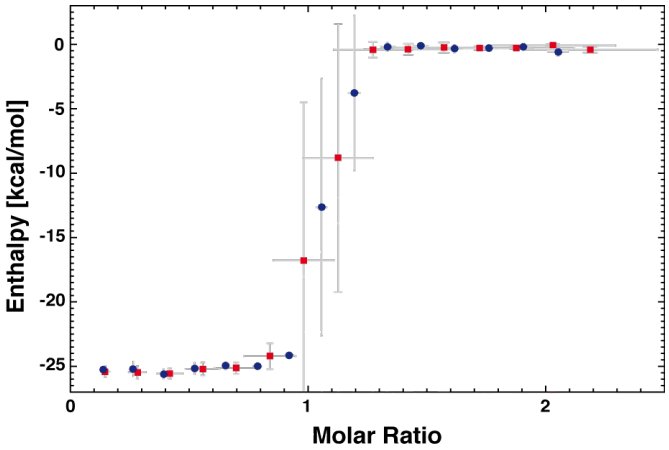

Figure S6. Isothermal titration calorimetry. The reaction enthalpy of biotin with N-mSA (blue circles) and C-mSA (red squares) was measured at 25°C. For all measurements the same biotin stock solution was used. The grey error bars are given by the standard deviation between three measurements.

II.3. Additional SMFS data of measurement shown in main text

In AFM-based SMFS, the use of so-called fingerprint domains is important. First, true single-molecule interactions are identified by the distinct unfolding pattern (force drop and contour length increment) of the fingerprint domain. Second, the unfolding force of the fingerprint domain serves as internal force reference. In our case, we used the well-characterized ddFLN4 as fingerprint domain. It unfolds in a two-step unfolding process. Histograms of the two corresponding unfolding force peaks are plotted in Sup. S-Fig. S7 and Sup. S-Fig. S8. The force-extension traces analyzed here are the same as in Fig. 3B. We do not observe any significant difference in unfolding forces of ddFLN4, when pulling on the C-mSA or the N-mSA area.

For the measurement shown, we performed 72,894 approach-retraction-cycles. In 26,245 cases (36%), we observed interactions between tip and surface higher than 50 pN. We identified specific single-molecule interactions in 5576 force-extension traces using the ddFLN4 fingerprint (7.6%).

In Sup. S-Fig. S9, we provide unbinding force histograms of final unbinding peaks observed in force-extension traces with interactions higher than 50 pN. (The final unbinding force can still be lower than 50 pN.) In these histograms, we did not use the ddFLN4 fingerprint pattern for sorting and thus show the unsorted data. Nevertheless, the specific final unbinding force peaks of the mSA:biotin interaction are clearly visible. Thus, the difference in unbinding force between N-mSA and C-mSA is already visible in the raw data. We interpret this as follows: Even if there are incomplete ddFLN4 unfolding patterns, additional unspecific or multiple specific interactions between surface and cantilever tip, the final force peak in the force-extension trace will, in most cases, be caused by a single biotin molecule unbinding from a single mSA molecule.

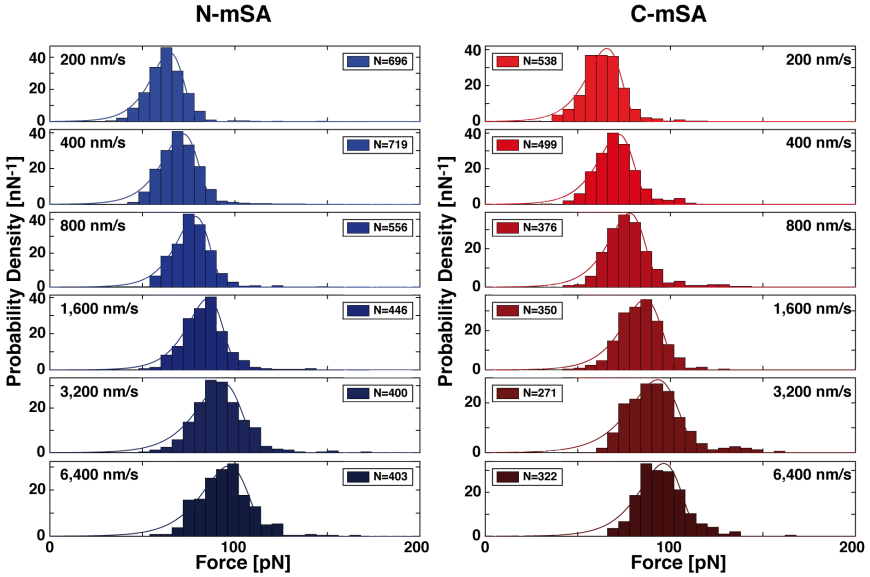

Figure S7. Unfolding forces of ddFLN4. Forces of the first unfolding peak of ddFLN4 in the case of N-terminal and C-terminal mSA surface attachment. Although the unbinding forces of biotin from C-mSA and N-mSA are quite different, the unfolding force of the fingerprint domain is not affected. The force extension curves used here are the same as for Figure 2. The number of interactions for every histogram is given in the boxes.

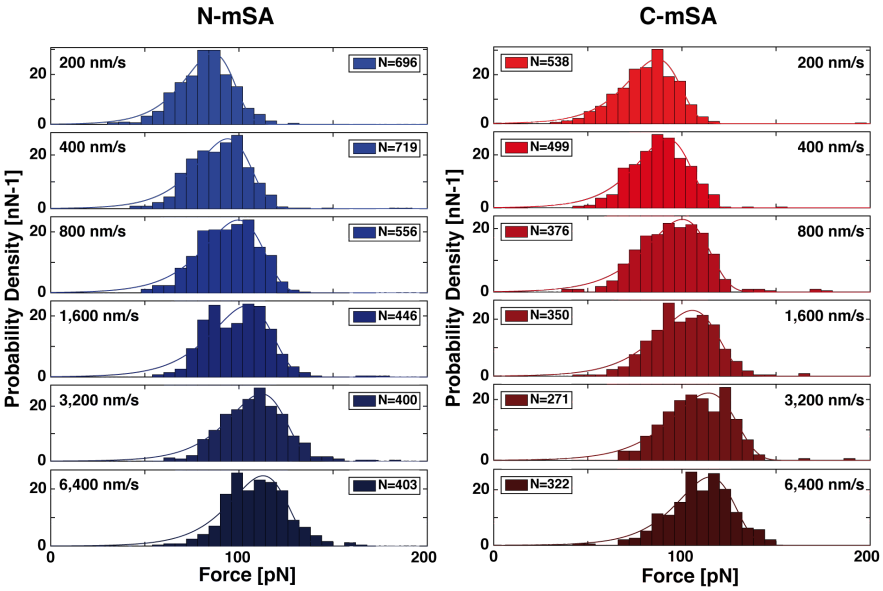

Figure S8. Unfolding forces of ddFLN4. Forces of the second unfolding peak of ddFLN4 in the case of N-terminal (blue colors) and C-terminal (red color) mSA surface attachment. Although the unbinding forces of biotin from C-mSA and N-mSA are quite different, the unfolding force of the fingerprint domain is not affected. The force extension curves used here are the same as for Figure 3B. The number of interactions for every histogram is given in the boxes.

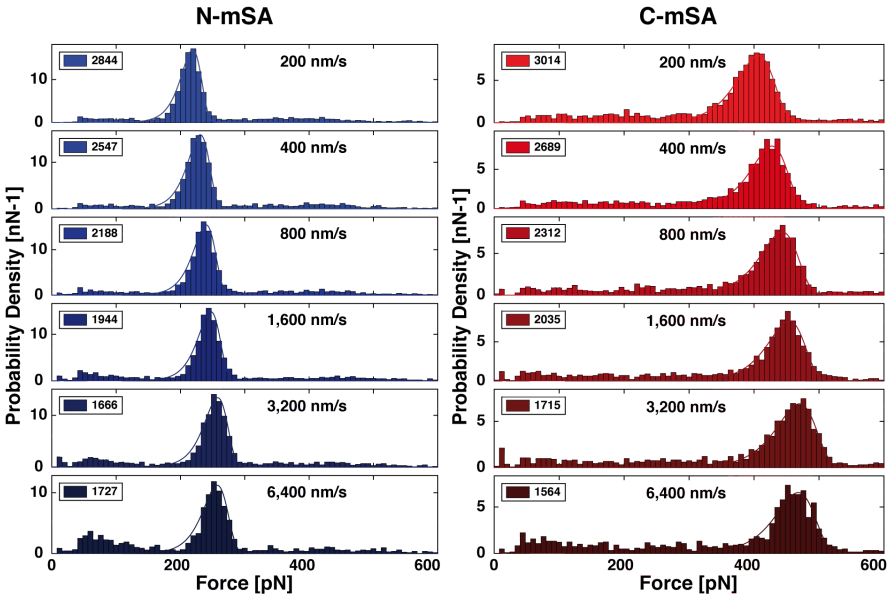

Figure S9. Unbinding forces of biotin from mSA. All final unbinding forces for interactions larger than 50 pN are binned into histograms and fitted with Bell-Evans distributions. N-terminal and C-terminal surface attachment of mSA is shown. Data are not sorted by the fingerprint pattern, *i.e.* they can contain multiple interactions or incomplete unfolding. The fact that these histograms still resemble the ones in Figure 3B implies that the final rupture peak in a force extension curve is in most cases caused by a single biotin unbinding from a single mSA. The number of interactions for every histogram is given in the boxes.

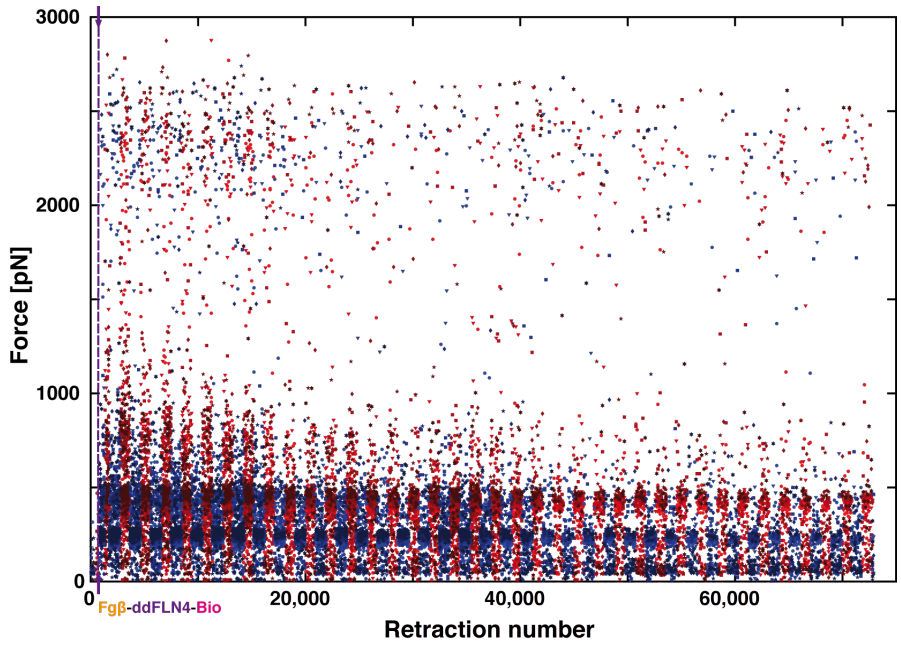

Figure S10. Course of the measurement over the complete range of forces. Here, we show the final unbinding forces for all interactions higher than 50 pN. N-mSA data are shown in blue colors, C-mSA data in red colors. Darker colors represent faster retraction velocities. The two dense bands at 200 pN or 400 pN, respectively, contain most of the specific single-molecule interactions that show the specific fingerprint unfolding pattern. At the beginning of the measurement multiple interactions of mSA:biotin are visible (about 400 pN for N-mSA, about 800 pN for C-mSA). In addition, in rare cases Fgβ:SdrG unbinding, probably caused by multiple and unspecific surface interactions, is visible at about 2500 pN. At the end of the measurement, the number of non-specific interactions at low forces increases, probably because the quality of the cantilever tip or its functionalization slowly decreases over time.

II.4. AFM-based SMFS with covalent attachment of ddFLN4

The high affinity of biotin for SA can be disadvantageous for SMFS experiments. The cantilever tip can easily get clogged when SA that was unspecifically adsorbed to the surface binds to the biotinylated proteins on the cantilever tip. S-In this study, we introduced a second receptor-ligand pair (SdrG:Fgβ) with a lower affinity to prevent clogging of the cantilever tip. S-In doing so, we obtained good statistics and were able to perform daylong measurements.

The use of a second receptor-ligand pair is counter-intuitive, as one could argue that mSA:biotin and unbinding SdrG:Fgβ cannot be distinguished or that the SdrG:Fgβ system somehow influences the behavior of the mSA:biotin unbinding. The first concern is negligible, because in the force loading geometry used here, SdrG:Fgβ was shown to withstand forces of 2 nN.[5] To tackle the second concern, we performed additional control measurement without the second receptor-ligand system, covalently attaching biotinylated ddFLN4 to the cantilever tip. S-For this, we again immobilized both mSA variants at different areas on the surface, a few millimeters apart from each other (Sup. S-Fig. S11A). In this way, we could probe both variants with the same cantilever. The cantilever tip, covalently functionalized with biotinylated ddFLN4, is approached to the surface. Biotin binds to mSA on the surface. Retracting the cantilever, the force needed to unbind biotin from mSA is measured.

ddFLN4 on the cantilever unfolds at lower forces than biotin unbinds from mSA. The characteristic two-step unfolding pattern is used to identify single-molecule interactions, *i.e.* a single biotin molecule binding to a single mSA molecule. In Sup. S-Fig. S11B, two exemplary force-extension traces for single-molecule interaction on the area where N-mSA or C-mSA were immobilized are depicted. In both cases, the AFM cantilever was retracted with a velocity of 800 nm/s. While the ddFLN4 unfolding is observed at the same force of about 60-80 pN for both traces, the final force peak is situated at different forces. This last peak is attributed to the unbinding of biotin from mSA.

Selecting all force curves that clearly show single-molecule interaction, we can plot all the mSA:biotin unfolding forces for all approach retraction cycles (Sup. S-Fig. S11C). Out of the first 6,000 traces, 2,640 showed interaction (44%). We could identify 557 single-molecule interactions (9.3%). The loss in interaction frequency over time is due to clogging of the lever by mSA that had been unspecifically adsorbed to the surface. Already a low amount of mSA is sufficient to obstruct the measurement. Force curves measured on the N-mSA area are depicted

in blue colors, while data collected on the C-mSA area is shown in red colors. Faster retraction velocities are represented by darker colors: 200 nm/s (circles), 800 nm/s (triangles), 3,200 nm/s (squares). Already from this data set, it is obvious that the mechanical stability of the mSA:biotin interaction is different depending on mSA tethering. Furthermore, comparing the data with the one in the main matter, we can show that the introduction of the second receptor-ligand system has no significant influence on the unbinding forces. It only helps to get better statistic by preventing lever clogging.

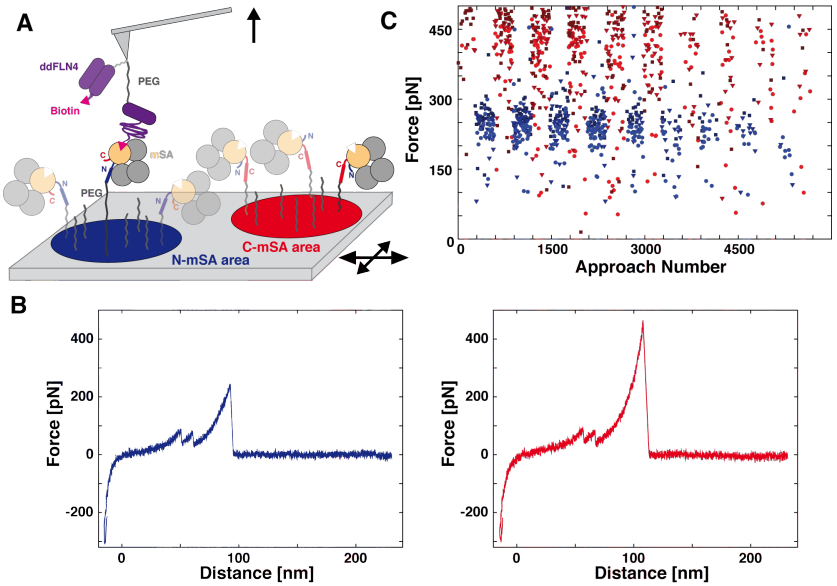

Figure S11. SMFS Experiment with N-mSA and C-mSA. (A) Schematic of the experiment: In different areas on the surface, N-mSA (blue) or C-mSA (red) is immobilized via PEG-linkers. With the AFM cantilever tip, decorated with biotinylated ddFLN4 (purple), both areas are probed. When the cantilever approaches the surface, biotin (magenta) binds to mSA. Upon retraction of the cantilever, ddFLN4 unfolds before biotin unbinds from mSA. (B) Typical force-extension traces for N-mSA (left, blue) and C-mSA (right, red) at 800 nm/s: The characteristic unfolding pattern of ddFLN4 serves as a fingerprint to identify single mSA:biotin interactions. (C) Every 300 approach-retraction cycles, the cantilever is moved to the other area. Final unbinding forces for mSA:biotin are plotted for different retraction velocities. C-mSA: red colors; N-mSA: blue colors; 200 nm/s bright circles; 800 nm/s triangles; 3,200 nm/s dark squares.

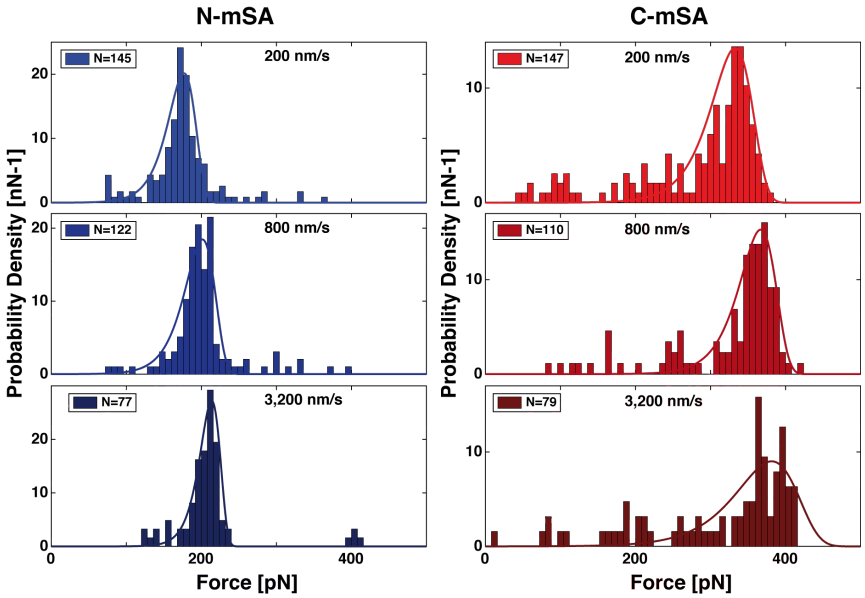

Figure S12. Unbinding force histograms for experiments with covalent attachment of ddFLN4 to the cantilever tip. S-Forces recorded on the N-mSA spot are colored in blue colors, forces recorded on the C-mSA area in red colors. Although the overall yield is much lower than for non-covalent Fgβ:SdrG tethering, due to cantilever clogging, the distribution of rupture forces are qualitatively comparable with the ones in Figure 3B.

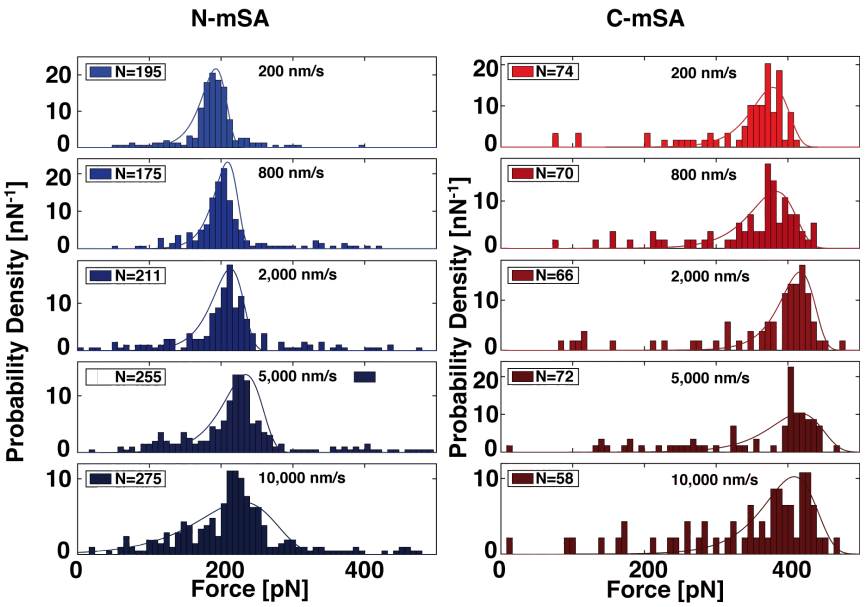

Figure S13. Unbinding force histograms for experiments with covalent attachment of ddFLN4 to the cantilever over a wider range of force loading rates. Forces recorded on the N-mSA spot are colored in blue colors, forces recorded on the C-mSA area in red colors. Although the overall yield is lower than for non-covalent Fgβ:SdrG tethering, due to cantilever clogging, the distribution of rupture forces are qualitatively comparable with the ones in Figure 3B. Over the range of retraction velocities, and thus force loading rates, applied here a transition from one unbinding pathway to the other, which might be expected for N-mSA, could not be resolved.

III. Data analysis

III.1. Fitting of the Bell-Evans model

Bell, Evans, and Ritchie developed a model to characterize how an external force affects the dissociation of molecular bonds.[28-29] Under the assumption of a constant force loading rate *r*, the probability density function of bond rupture under force is calculated. Although the force loading rate is not constant for AFM force spectroscopy using constant retraction velocity, as is the case for our experiments, the model is still often used to fit rupture force histograms. Here, we employed the Bell-Evans model to fit the rupture force distributions in Figure 3B:

$$p(F) = s \cdot a \cdot \exp(b \cdot F) \cdot \exp\left(\frac{a}{b} \cdot (1 - \exp(b \cdot F))\right)$$

As the probability density function *p(F)* is normalized to unity, we employed a factor *s* to take into account that there is a fraction of rupture forces outside the main peak. To determine the factor *s*, we first identified the most probable rupture force <*F*>, *i.e.* the maximum of the peak, by fitting a kernel density estimate to the unbinding force histogram and taking the maximum. We then divided the number of unbinding forces within an arbitrarily chosen range of 100 pN below and above the peak force by the number of total forces in the histogram to obtain the factor *s*.

From the fitting parameters *a* and *b*, physical parameters can be derived:

$$a = \frac{k_{off,0}}{r}$$

$$b = \frac{x_0}{k_B T}$$

Here, k_B is the Boltzmann factor, T the absolute temperature, x_0 the distance to transition state, r the force loading rate, and $k_{off,0}$ the off-rate at zero force. The physical parameters derived here, especially the zero-force off-rate, have to be taken with caution. As stated previously, the force loading rate is not constant. To determine the zero-force off-rates, we divided the fitting parameter *a* by the most probable force loading rate <*r*>. The latter was determined by fitting the last 3 nm before the rupture peak in every the force-extension curve, plotting a histogram of these fitted loading rates and finally taking the maximum of a kernel density estimate fitted to this histogram. The distance to transition state was determined by multiplying the fitting parameter *b* with the Boltzmann factor k_B and the temperature T = 300 K.

These parameters can also be derived from the force loading rate plot (Figure 3C). Here, we employed the following equation:

$$< F >= \frac{k_B T}{x_0} \log \left(\frac{r}{k_{off,0}} \frac{x_0}{k_B T}\right)$$

The fitting error of the zero-force off-rate is quite large due to the exponential relation of loading rate and force. The values for the distance to transition state differ by a factor of two depending on whether they are derived from the dynamic force spectrum or from the probability density function to a single rupture force distribution. Nevertheless, the relative difference between N-SA and C-SA is the same, namely, that the distance to transition state is twice as large for N-SA, indicating that the potential well is narrower for C-terminal loading.

Table S1. Fitting parameters for Figure 3B.

	v_R [nm/s]	s [%]	a [$\times 10^3$]	b [$\times 10^{10}$]
N-SA	**200**	72.4	26.4	5.92
	400	72.4	31.6	5.58
	800	71.4	74.4	5.24
	1600	68.4	43.1	5.89
	3200	65.3	58.7	6.34
	6400	58.3	61.1	5.98
C-SA	**200**	61.4	23.0	3.50
	400	59.1	6.0	3.65
	800	58.9	4.8	3.50
	1600	57.9	3.0	3.59
	3200	56.4	5.6	3.32
	6400	52.8	6.5	3.37

Table S2. Physical parameters extracted from the data in Figure 3B.

	v_R [nm/s]	<F> [pN]	<r> [pN/s]	x_0 [nm]	$k_{off,0}$ [s^{-1}]
N-SA	**200**	216	1,500	0.24	4.0e-5
	400	228	3,300	0.23	1.0e-4
	800	237	7,000	0.21	5.2e-4
	1600	243	14,400	0.24	6.2e-7
	3200	254	31,400	0.26	1.8e-6
	6400	253	56,700	0.24	3.5e-6
C-SA	**200**	403	3,500	0.14	8.1e-5
	400	423	7,700	0.15	4.6e-5
	800	438	15,900	0.14	7.6e-5
	1600	449	34,400	0.15	1.0e-7
	3200	464	72,900	0.13	4.1e-7
	6400	461	148,000	0.14	9.6e-7

IV. Supporting simulation data

IV.1. Cross-correlation and network analysis

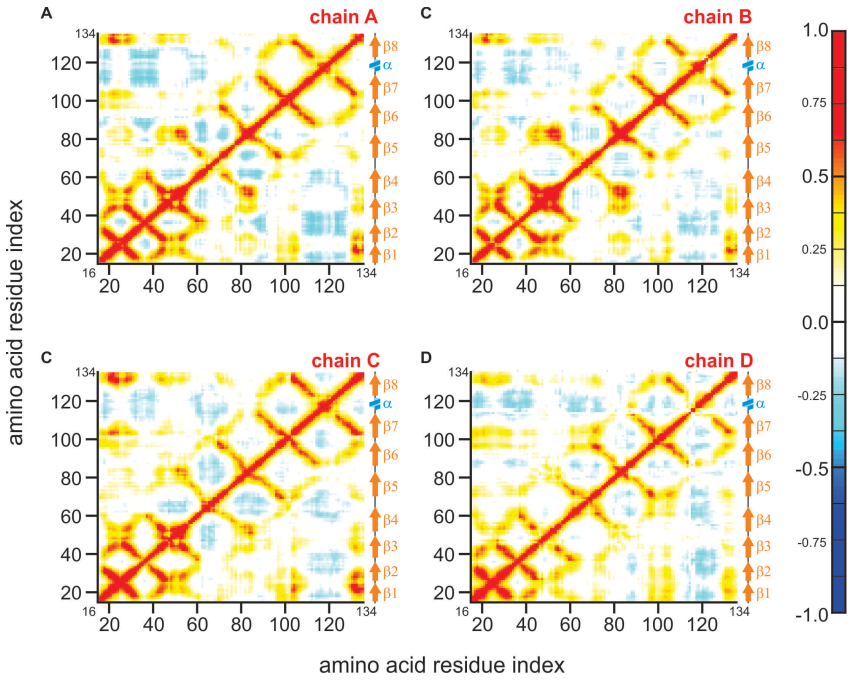

Figure S14. Cross-correlation matrices for C-terminal pulling. The plots show the cross-correlation between the residues within each of the four SA subunits. The β-sheet structure results in high correlation between the corresponding residues (red lines close to the diagonals). For chain D, this structure is slightly less pronounced but is in principle preserved. In particular, the high cross-correlation between the first and the second β-strand is mostly maintained (bottom left corner).

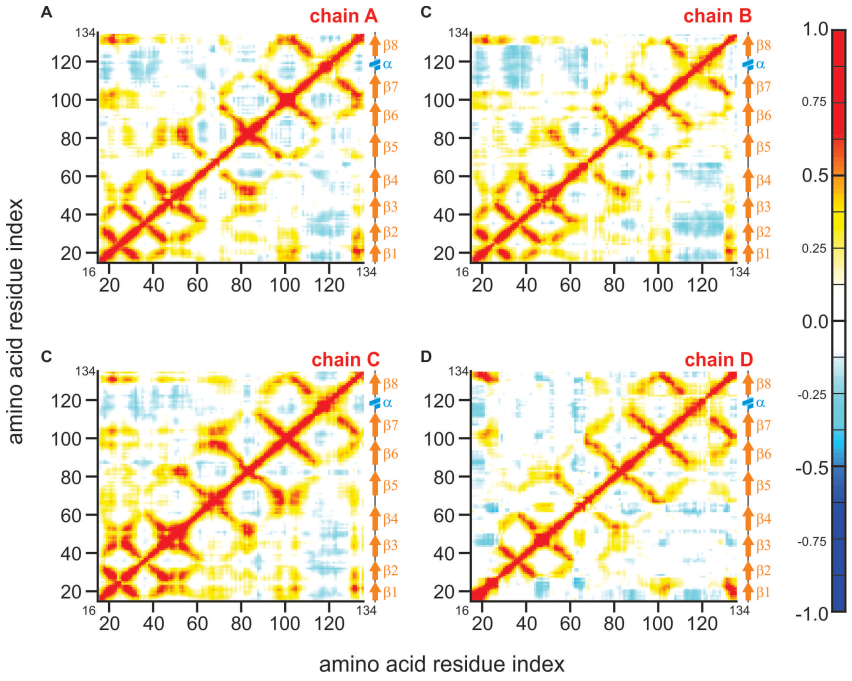

Figure S15. Cross-correlation matrices for N-terminal pulling. The plots show the cross-correlation between the residues within each of the four SA subunits. The β-sheet structure results in high correlation between the corresponding residues (red lines close to the diagonals). For chain D, this structure is less pronounced. In particular, the high cross-correlation between the first and the second β-strand is lost (bottom left corner of D). Instead, high cross-correlation between the first (N-terminal) and eighth (C-terminal) β-strand is observed. This is in line with the rearrangement of the first β-strand under force shown in Fig. 4.

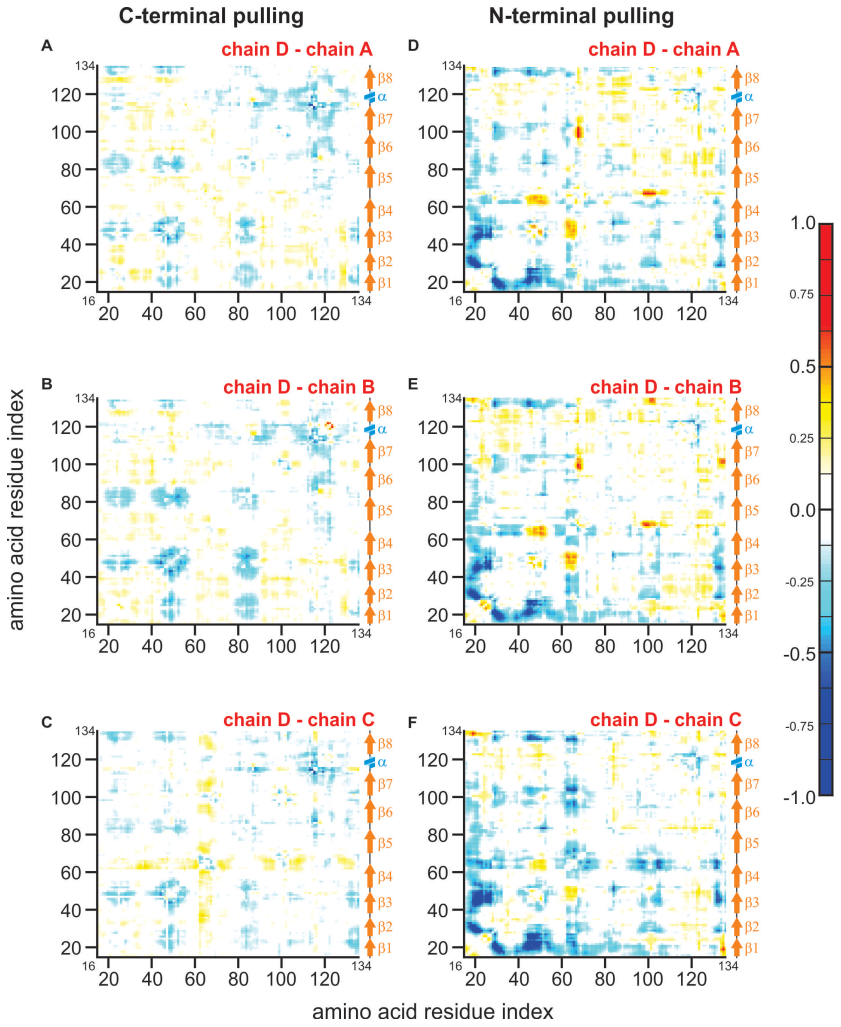

Figure S16. Difference in cross-correlation matrices between pulling and non-pulling chains. The cross-correlation matrices shown before are subtracted here. Differences in cross-correlation between the different subunits become visible. In addition, C-terminal (A-C) and N-terminal force loading (D-F) can directly be compared. The structural rearrangement for N-mSA is clearly visible in the bottom left corner of the plots D-F. For C-mSA, differences in cross-correlation are overall less pronounced. For some linker regions, *e.g.* between the fourth and fifth β-strand, cross-correlations are higher in the subunit that is under force load (chain D).

IV.2. Mutual information analysis (RMSF, Contacts, Force)

Among all biotin-streptavidin contacts, and the residues with highest RMSF values, the feature selection methodology listed observables with from highest to lowest mutual information (MI) coefficient. The observables with highest MI are analyzed here, and listed in Tables S3 and S4.
SER27 constitutes one of three mutations used to weaken biotin binding to create the non-functional subunits utilized to generate mSA.[30] It appears to play a major role in both N- and C-terminal pulling experiments. The three amino acids ASN49, TYR43 and SER27 were identified to generate an H-bond network perpendicular to the force loading during unbinding of biotin.[31] This way, only a simultaneous rupture allows biotin in a final step to escape the binding pocket. Also, Liu et al. showed that SER27, TYR43, THR90 contribute to binding affinity.[32] Dixon and Kollman demonstrated the importance of TRP79 and SER27 for SA biotin binding strength.[33] The van der Waals contacts of the tryptophan residues TRP79, TRP108, TRP120 (TRP120 of subunit A) are also known to contribute to the high affinity.[34] Residues GLY16, ILE17, and THR18 are the residues at the N-terminus forming the first β-strand that is ripped away from the second β-strand when force is applied.

Table S3. Results of Mutual Information Analysis. A score function has been developed and applied to identify the most important residues of mSA for force propagation in the case of N- or C-terminal pulling of mSA. Marked in red are the amino acid residues that presented a correlation between RMSF and forces, while the other residues present a correlation between a contact to biotin and force.

N-mSA			C-mSA		
Residue	Biotin Atom	Score	Residue	Biotin Atom	Score
SER27	O3	1.000000	SER27	O3	1.000000
TRP108	C6	0.778314	TRP108	C5	0.880444
ALA63		0.758845	TRP79	C8	0.866975
THR90	S1	0.753362	TYR43	O3	0.781555
TYR43	O3	0.687164	TRP79	C3	0.735351
ASN49	O2	0.650896	TRP79	C9	0.683922
GLY16		0.626958	THR90	S1	0.662114
TRP79	C9	0.616018	TRP79	C10	0.624008
ILE17		0.614522	TRP79	C6	0.579682
TRP120	C7	0.570383	TRP108	C6	0.562329
TRP79	C8	0.565346	ASN49	O1	0.553145
THR18		0.516329	TRP79	N1	0.537884
THR66		0.510152	TRP120	O3	0.524486

Table S4. Results of Mutual Information Analysis C-terminal pulling versus N-terminal pulling. Marked in red are the amino acid residues that presented a correlation between RMSF and forces, while the other residues present a correlation between a contact to biotin and force. The mutual information scores are not as high as those observed in Table S3, reinforcing that the mechanism that differentiates C- versus N-terminal pulling is related to partial unfolding and not to the contacts or other structural fluctuations.

Residue	Biotin Atom	Score
ASN118		0.337043
SER45	O3	0.218223
TRP79	C6	0.136393
TRP108	C5	0.12872
TRP79	C2	0.115025
GLY98		0.112509
ASN49	O1	0.10985
THR90	S1	0.104352
TYR83		0.088686
ALA117		0.072231
TRP79	C5	0.061104
GLY68		0.055532
TRP79	N1	0.04377
ASN49	O2	0.039842
SER69		0.03954
TRP120	O3	0.027222
GLY99		0.023102
ALA100		0.018072
TRP79	C8	0.011375

V. Supplementary references

1. Sedlak, S. M.; Bauer, M. S.; Kluger, C.; Schendel, L. C.; Milles, L. F.; Pippig, D. A.; Gaub, H. E., Monodisperse measurement of the biotin-streptavidin interaction strength in a well-defined pulling geometry. *PLOS ONE* **2017,** *12* (12), e0188722.

2. Schwaiger, I.; Kardinal, A.; Schleicher, M.; Noegel, A. A.; Rief, M., A mechanical unfolding intermediate in an actin-crosslinking protein. *Nat Struct Mol Biol* **2004,** *11* (1), 81-5.

3. Yin, J.; Straight, P. S-D.; McLoughlin, S. M.; Zhou, Z.; Lin, A. J.; Golan, D. E.; Kelleher, N. L.; Kolter, R.; Walsh, C. T., Genetically encoded short peptide tag for versatile protein labeling by Sfp phosphopantetheinyl transferase. *Proc Natl Acad Sci U S A* **2005,** *102* (44), 15815-20.

4. Zimmermann, J. L.; Nicolaus, T.; Neuert, G.; Blank, K., Thiol-based, site-specific and covalent immobilization of biomolecules for single-molecule experiments. *Nat Protoc* **2010,** *5* (6), 975-85.

5. Milles, L. F.; Schulten, K.; Gaub, H. E.; Bernardi, R. C., Molecular mechanism of extreme mechanostability in a pathogen adhesin. *Science* **2018,** *359* (6383), 1527-1533.

6. Gumpp, H.; Stahl, S. W.; Strackharn, M.; Puchner, E. M.; Gaub, H. E., Ultrastable combined atomic force and total internal reflection fluorescence microscope [corrected]. *Rev Sci Instrum* **2009,** *80* (6), 063704.

7. Ribeiro, J. V.; Bernardi, R. C.; Rudack, T.; Stone, J. E.; Phillips, J. C.; Freddolino, P. S-L.; Schulten, K., QwikMD - Integrative Molecular Dynamics Toolkit for Novices and Experts. *Sci Rep* **2016,** *6*, 26536.

8. Seppala, J.; Bernardi, R. C.; Haataja, T. J. K.; Hellman, M.; Pentikainen, O. T.; Schulten, K.; Permi, P.; Ylanne, J.; Pentikainen, U., Skeletal Dysplasia Mutations Effect on Human Filamins' Structure and Mechanosensing. *Sci Rep* **2017,** *7* (1), 4218.

9. Verdorfer, T.; Bernardi, R. C.; Meinhold, A.; Ott, W.; Luthey-Schulten, Z.; Nash, M. A.; Gaub, H. E., Combining in Vitro and in Silico Single-Molecule Force Spectroscopy to

Characterize and Tune Cellulosomal Scaffoldin Mechanics. *J Am Chem Soc* **2017,** *139* (49), 17841-17852.

10. Zhang, M.; Biswas, S.; Deng, W.; Yu, H., The Crystal Structure of Monovalent Streptavidin. *Sci Rep* **2016,** *6*, 35915.

11. Hyre, D. E.; Le Trong, I.; Merritt, E. A.; Eccleston, J. F.; Green, N. M.; Stenkamp, R. E.; Stayton, P. S-S., Cooperative hydrogen bond interactions in the streptavidin-biotin system. *Protein Sci* **2006,** *15* (3), 459-67.

12. Humphrey, W.; Dalke, A.; Schulten, K., VMD: visual molecular dynamics. *J Mol Graph* **1996,** *14* (1), 33-8, 27-8.

13. Best, R. B.; Zhu, X.; Shim, J.; Lopes, P. S-E.; Mittal, J.; Feig, M.; Mackerell, A. D., Jr., Optimization of the additive CHARMM all-atom protein force field targeting improved sampling of the backbone phi, psi and side-chain chi(1) and chi(2) dihedral angles. *J Chem Theory Comput* **2012,** *8* (9), 3257-3273.

14. Jorgensen, W. L.; Chandrasekhar, J.; Madura, J. D.; Impey, R. W.; Klein, M. L., Comparison of simple potential functions for simulating liquid water. *The Journal of Chemical Physics* **1983,** *79* (2), 926-935.

15. Melo, M. C. R.; Bernardi, R. C.; Rudack, T.; Scheurer, M.; Riplinger, C.; Phillips, J. C.; Maia, J. D. C.; Rocha, G. B.; Ribeiro, J. V.; Stone, J. E.; Neese, F.; Schulten, K.; Luthey-Schulten, Z., NAMD goes quantum: an integrative suite for hybrid simulations. *Nat Methods* **2018,** *15* (5), 351-354.

16. Darden, T.; York, D.; Pedersen, L., Particle mesh Ewald: An N·log(N) method for Ewald sums in large systems. *The Journal of Chemical Physics* **1993,** *98* (12), 10089-10092.

17. Phillips, J. C.; Braun, R.; Wang, W.; Gumbart, J.; Tajkhorshid, E.; Villa, E.; Chipot, C.; Skeel, R. D.; Kale, L.; Schulten, K., Scalable molecular dynamics with NAMD. *J Comput Chem* **2005,** *26* (16), 1781-802.

18. Izrailev, S.; Stepaniants, S.; Balsera, M.; Oono, Y.; Schulten, K., Molecular dynamics study of unbinding of the avidin-biotin complex. *Biophys J* **1997,** *72* (4), 1568-81.

19. Kluyver, T.; Benjamin, R.-K.; Fernando, P.; Brian, G.; Matthias, B.; Jonathan, F.; Kyle, K.; Jessica, H.; Jason, G.; Sylvain, C.; Paul, I.; Damián, A.; Safia, A.; Carol, W.; Jupyter Development, T. In *Jupyter Notebooks—a publishing format for reproducible computational workflows*, Positioning and Power in Academic Publishing: Players, Agents and Agendas, 20th International Conference on Electronic Publishing, Göttingen, Germany, 2016; Göttingen, Germany, 2016.

20. Michaud-Agrawal, N.; Denning, E. J.; Woolf, T. B.; Beckstein, O., MDAnalysis: a toolkit for the analysis of molecular dynamics simulations. *J Comput Chem* **2011,** *32* (10), 2319-27.

21. Scheurer, M.; Rodenkirch, P.; Siggel, M.; Bernardi, R. C.; Schulten, K.; Tajkhorshid, E.; Rudack, T., PyContact: Rapid, Customizable, and Visual Analysis of Noncovalent Interactions in MD Simulations. *Biophys J* **2018,** *114* (3), 577-583.

22. Kraskov, A.; Stogbauer, H.; Grassberger, P., Estimating mutual information. *Phys Rev E Stat Nonlin Soft Matter Phys* **2004,** *69* (6 Pt 2), 066138.

23. Sethi, A.; Eargle, J.; Black, A. A.; Luthey-Schulten, Z., Dynamical networks in tRNA:protein complexes. *Proc Natl Acad Sci U S A* **2009,** *106* (16), 6620-5.

24. Vanwart, A. T.; Eargle, J.; Luthey-Schulten, Z.; Amaro, R. E., Exploring residue component contributions to dynamical network models of allostery. *J Chem Theory Comput* **2012,** *8* (8), 2949-2961.

25. Schoeler, C.; Bernardi, R. C.; Malinowska, K. H.; Durner, E.; Ott, W.; Bayer, E. A.; Schulten, K.; Nash, M. A.; Gaub, H. E., Mapping Mechanical Force Propagation through Biomolecular Complexes. *Nano Lett* **2015,** *15* (11), 7370-6.

26. Glykos, N. M., Software news and updates. Carma: a molecular dynamics analysis program. *J Comput Chem* **2006,** *27* (14), 1765-8.

27. Chilkoti, A.; Stayton, P. S-S., Molecular Origins of the Slow Streptavidin-Biotin Dissociation Kinetics. *Journal of the American Chemical Society* **1995,** *117* (43), 10622-10628.

28. Bell, G. I., Models for the specific adhesion of cells to cells. *Science* **1978,** *200* (4342), 618-27.

29. Evans, E.; Ritchie, K., Dynamic strength of molecular adhesion bonds. *Biophys J* **1997,** *72* (4), 1541-55.

30. Howarth, M.; Chinnapen, D. J. F.; Gerrow, K.; Dorrestein, P. S-C.; Grandy, M. R.; Kelleher, N. L.; El-Husseini, A.; Ting, A. Y., A monovalent streptavidin with a single femtomolar biotin binding site. *Nature Methods* **2006,** *3*, 267.

31. Rico, F.; Russek, A.; Gonzalez, L.; Grubmuller, H.; Scheuring, S., Heterogeneous and rate-dependent streptavidin-biotin unbinding revealed by high-speed force spectroscopy and molecular dynamics simulations. *arXiv preprint arXiv:1808.07122* **2018**.

32. Liu, F.; Zhang, J. Z. H.; Mei, Y., The origin of the cooperativity in the streptavidin-biotin system: A computational investigation through molecular dynamics simulations. *Scientific Reports* **2016,** *6*, 27190.

33. Dixon, R. W.; Kollman, P., The free energies for mutating S27 and W79 to alanine in streptavidin and its biotin complex: The relative size of polar and nonpolar free energies on biotin binding. *Proteins: Structure, Function, and Bioinformatics* **1999,** *36* (4), 471-473.

34. Chilkoti, A.; Tan, P. S-H.; Stayton, P. S-S., Site-directed mutagenesis studies of the high-affinity streptavidin-biotin complex: contributions of tryptophan residues 79, 108, and 120. *Proceedings of the National Academy of Sciences* **1995,** *92* (5), 1754-1758.

3.2 Publication P2: Switchable Reinforced Streptavidin

Steered molecular dynamics simulations performed in addition to SMFS experiments for the SA-biotin complex showed the existence of a low force unbinding pathway which features partial unfolding of mSA (*cf.* Section 3.1). This particular pathway was found for a force-loading geometry defined by N-terminal attachment of the single functional subunit of mSA. The detailed picture of the mechanistic process, gained with the help of the simulations, showed that partial unfolding occurs between the first two β-strands.

Based on these results, a covalent bond was introduced connecting the two β-strands to create a reinforcement of the N-terminal β-sheet. Therefore, two cysteines were inserted into the first and second β-strand (T18C, A33C) of the functional subunit of mSA. In this way, the formation of a disulfid bond connecting the two β-strands should be promoted. Its effect on the overall mechanical stability was then evaluated by using SMFS based on AFM. Experiments showed biotin unbinding forces of about 350 pN at force loading rates of 10 nN s^{-1} – being about 1.5 fold higher than for an N-terminal tethered mSA without the additional cysteines. Exposing the complex to reducing conditions caused complex rupture forces to drop back to 200 pN as the disulfid bond was broken. By exchanging the buffer to recreate oxygen rich conditions, unbinding forces recovered the initially higher values. These results demonstrate the ability of the system to be switched between a formed and broken disulfid bond and thereby between two states of mechanical stability.

In a more general context, this work illustrates that genetic engineering, although carried out far off the actual binding pocket, can yet lead to an improved mechanical stability of a receptor-ligand interaction. Based on predictions of detailed simulations, this study shows the potential of joined *in vitro* and *in silico* SMFS.

Switchable Reinforced Streptavidin

by

Leonard C. Schendel*, Steffen M. Sedlak*, and Hermann E. Gaub

published in

Nanoscale 2020, 12, 6803-6809, doi: 10.1039/D0NR00265H

Reproduced from Schendel *et al.* [88] – Reproduced by permission of The Royal Society of Chemistry.
Copyright 2020 The Royal Society of Chemistry

*These authors contributed equally to this work. LCS: AFM-based SMFS, data analysis, writing of manuscript. SMS: Protein design and preparation, ITC, writing of manuscript.

Published on 09 March 2020. Downloaded by Ludwig Maximilians Universitaet Muenchen on 3/31/2020 10:54:18 AM.

Nanoscale

ROYAL SOCIETY OF CHEMISTRY

PAPER

View Article Online
View Journal | View Issue

Check for updates

Cite this: *Nanoscale*, 2020, **12**, 6803

Switchable reinforced streptavidin†

Leonard C. Schendel, ‡ Steffen M. Sedlak ‡ and Hermann E. Gaub*

Received 9th January 2020,
Accepted 7th March 2020

DOI: 10.1039/d0nr00265h

rsc.li/nanoscale

The complex of the small molecule biotin and the homotetrameric protein streptavidin is key to a broad range of biotechnological applications. Therefore, the behavior of this extraordinarily high-affinity interaction under mechanical force is intensively studied by single-molecule force spectroscopy. Recently, steered molecular dynamics simulations have identified a low force pathway for the dissociation of biotin from streptavidin, which involves partial unfolding of the N-terminal β-sheet structure of monovalent streptavidin's functional subunit. Based on these results, we now introduced two mutations (T18C,A33C) in the functional subunit of monovalent streptavidin to establish a switchable connection (disulfide bridge) between the first two β-strands to prevent this unfolding. In atomic force microscopy-based single-molecule force spectroscopy experiments, we observed unbinding forces of about 350 pN (at a force-loading rate of 10 nN s^{-1}) for pulling a single biotin out of an N-terminally anchored monovalent streptavidin binding pocket – about 1.5-fold higher compared with what has been reported for N-terminal force loading of native monovalent streptavidin. Upon addition of a reducing agent, the unbinding forces dropped back to 200 pN, as the disulfide bridge was destroyed. Switching from reducing to oxidizing buffer conditions, the inverse effect was observed. Our work illustrates how the mechanics of a receptor–ligand system can be tuned by engineering the receptor protein far off the ligand-binding pocket.

Introduction

Many bio- and nanotechnological assays rely on the high-affinity[1] interaction of the small molecule biotin (vitamin H) with the homotetrameric protein streptavidin[2] (SA). Also, for force spectroscopy, which is an important tool for the emergent research field of mechanobiology,[3] the biotin/streptavidin system is abundantly used as a molecular anchor – not only in AFM-based force spectroscopy[4] but also in acoustic force spectroscopy[5] as well as magnetic[6] and optical tweezers[7] experiments. Therefore, it is important to fundamentally understand the mechanics of the biotin/streptavidin interaction itself.

Using monovalent streptavidin[8] (mSA), a streptavidin tetramer composed of one functional biotin binding subunit with a unique tethering site and three non-functional subunits, allows for single-molecule force spectroscopy (SMFS) experiments in a well-defined force-loading geometry.[9] With this approach it has recently been shown that the mechanical stability of the widely used SA/biotin complex differs for N- and C-terminal tethering of the functional subunit of mSA.[10] Compared to N-terminal attachment, the C-terminal one is more than twofold as stable (at force-loading rates of 10 nN s^{-1}). Details of the unbinding process have been investigated using steered molecular dynamics simulations.[11] The results suggested that the functional subunit, when SA is pulled by the N-terminus, partially unfolds in the N-terminal region before biotin leaves the binding pocket: The first two N-terminal β-strands β1 and β2 are zipped open, destabilizing the binding pocket. This results in lower unbinding forces for biotin compared with C-terminal force loading of mSA. For the significantly different unbinding forces, which have been observed in AFM-based SMFS experiments for N- and C-terminal tethering of mSA, steered molecular dynamics simulations[10] provided an explanation by suggesting the partial unfolding of the N-terminal β-sheet structure. However, this mechanism has not yet been experimentally verified.

An obvious approach to do so is to use protein engineering to introduce a covalent link between β1 and β2. Inferring from the steered molecular dynamics simulations, this should block the unbinding pathway that involves partial unfolding of the N-terminal β-sheet structure and thus increase the mechanical stability of the biotin/mSA interaction under mechanical load. Disulfide bridges are a popular choice to establish a covalent link between two β-strands.[12] For human cardiac titin, it was shown that the formation of disulfide bridges between β-strands can modulate the mechanical extensibility of certain domains.[13,14] Sharma *et al.* successfully used a disulfide

Lehrstuhl für Angewandte Physik and Center for NanoScience, Ludwig-Maximilians-Universität München, Amalienstr. 54, 80799 Munich, Germany.
E-mail: gaub@lmu.de

†Electronic supplementary information (ESI) available. See DOI: 10.1039/d0nr00265h

‡These authors contributed equally to this work.

This journal is © The Royal Society of Chemistry 2020

View Article Online

Published on 09 March 2020. Downloaded by Ludwig Maximilians Universitaet Muenchen on 3/31/2020 10:54:18 AM.

bridge to tune the mechanical stability of a *de novo* designed protein.[15] For avidin, which is similar to SA, Nordlund *et al.* succeeded in introducing disulfide bridges between the four subunits to increase the thermal stability of the tetramer.[16] In contrast to previous protein engineering on SA, which mainly focused on the biotin binding pocket[17–21] or on the assembly of the tetramer,[8,22–25] the results of the recent steered molecular dynamics simulations inspired us to design a disulfide bridge between the N-terminal β-strands within a single subunit (not in close proximity of the biotin binding pocket) to specifically alter the mechanics of the biotin/mSA interaction. Investigating how a covalent link within the N-terminal β-sheet structure affects the behavior of the biotin/mSA interaction under mechanical force, we provide insights on the interplay of unbinding and unfolding with respect to the dissociation of a ligand from a receptor under mechanical force.

Experimental

Preparation of proteins

Sequences of all protein constructs are provided in the ESI.† Site-directed mutagenesis to obtain the GG-SA(T18C,A33C)-His-construct was performed by three consecutive polymerase chain reactions starting with a Cys-SA-His-construct.[10] Primer sequences and details are provided in the ESI.† To confirm the success of the mutagenesis, all constructs were sent to sequencing (Eurofins Genomics, Ebersberg, Germany). mSA was expressed and purified as described by Sedlak *et al.*[10] In brief, mSA is prepared by mixing two different sorts of subunits that have been expressed separately. The functional subunit SA(T18C,A33C) is equipped with a tag for surface attachment and a tag for purification. The assembly with the non-functional subunits into tetramers is stochastically. During nickel-affinity purification, we select for those that only have one purification-tag (His-Tag) and therefore one functional subunit with one tag for surface attachment.

Sodium dodecyl sulfate-polyacrylamide gel electrophoresis (SDS-PAGE) was employed to confirm mSA's monovalence and purity (*cf.* ESI Fig. S1 and S2†). The presence of the disulfide bridge was probed in a fluorescence anisotropy measurement using a maleimide-dye (ESI Fig. S3†). SdrG was prepared as described by Milles *et al.*[26] ddFLN4-constructs were prepared as described by Milles *et al.*[27]

For biotinylation of the Fgβ-ddFLN4-construct, 60 μM Fgβ-ddFLN4-ybbR, 75 μM Coenzyme A-Biotin, and 5 μM Sfp phosphopantetheinyl transferase[28] were dissolved in Sfp buffer (1 mM $MgCl_2$, 10 mM Tris, pH 7.5) and incubated at room temperature for 1 h. Subsequently, a buffer exchange to phosphate buffered saline (PBS; Sigma Aldrich, St Louis, USA) was performed using Zeba Spin Desalting Columns (Thermo Fisher Scientific, Waltham, USA) with a 7 kDa molecular weight cut-off according to the manufacturer's instructions.

Isothermal titration calorimetry

Zeba Spin Desalting Columns (Thermo Scientific, Rockford, USA) with a molecular weight cut-off of 40 kDa were employed to equilibrate reinforced mSA with pure PBS or with PBS containing 1 mM TCEP. For the latter, Bond-Breaker TCEP Solution (Thermo Scientific, Rockford, USA) of neutral pH was added to PBS before the mSA buffer exchange. The final concentration was determined by UV-Vis absorption spectroscopy (NanoDrop 1000, Thermo Scientific, Rockford, USA) using the absorption at 280 nm and a molecular extinction coefficient of 167 760 (without TCEP) or 167 885 (with TCEP) calculated from the amino acid sequence using exPASy[29] and read 8.34 μM (without TCEP) and 8.11 μM (with TCEP), respectively. Biotin was dissolved in PBS (also with and without 1 mM TCEP) to a final concentration of 81.86 μM. For the ITC measurements with TCEP in the measurement buffer, thus both mSA buffer and biotin buffer contained 1 mM TCEP. ITC measurements were performed at 25 °C on a Malvern MicroCal ITC200 (Malvern Panalytical, Malvern, UK).

Surface and cantilever preparation

Aminosilanized glass slides[30] were incubated for 30 min with 25 mM heterobifunctional polyethylene glycol linkers of 5000 Da molecular weight (with an N-hydrocy succinimide group on the one and a maleimide group on the other end; NHS-PEG-MAL) dissolved in 50 mM HEPES buffer at pH 7.5. The glass slides were washed in ultrapure water and then incubated for 1 h with 10 mM Coenzyme A dissolved in coupling buffer (50 mM Na_2HPO_4, 50 mM NaCl, 10 mM EDTA, pH 7.2). The glass slides were again washed in ultrapure water, dried and mounted into the AFM sample holder. The surfaces were then incubated for 1 h with 60 μM ybbR-ddFLN4-LPETGG and 5 μM Sfp phosphopantetheinyl transferase[28] dissolved in Sfp buffer. The surfaces were washed with PBS and subsequently with Sortase buffer (1 mM $MgCl_2$, 1 mM $CaCl_2$, 150 mM NaCl, pH 7.4). Surfaces were incubated for 45 min with 1 μM GG-mSA(T18C,A33C)-His and 0.2 μM evolved Sortase A.[31] Finally, surfaces were washed with coupling buffer and then stored in PBS.

BioLever Mini (Olympus, Tokyo, Japan) were aminosilanized[30] and incubated for 30 min with 25 mM NHS-PEG-MAL dissolved in 50 mM HEPES buffer at pH 7.5. Cantilevers were washed in ultrapure water and then incubated for 1 h with 10 mM Coenzyme A dissolved in coupling buffer. Cantilevers were again washed in ultrapure water. Cantilevers were incubated for 1 h with 13 μM SdrG-ybbR and 5 μM Sfp phosphopantetheinyl transferase[28] dissolved in Sfp buffer. Cantilevers were washed and stored in PBS.

AFM-based SMFS experiments

A custom-built AFM was employed for the AFM-based SMFS experiments. We used a self-written routine programmed in Igor Pro 6 (WaveMetrics, Oregon, USA) to control the MFP-3D controller (Asylum Research, Santa Barbara, USA) operating the AFM. The cantilever tip was shortly indented into the surface (up to 100 pN indentation force) and then retracted 350 nm at constant velocity. Depending on the retraction velocity, tip and surface were in contact for about 0.5 ms to 5 ms. The approach was performed at 3000 nm s^{-1}, the retraction at

 This journal is © The Royal Society of Chemistry 2020

View Article Online

Published on 09 March 2020. Downloaded by Ludwig Maximilians Universitaet Muenchen on 3/31/2020 10:54:18 AM.

200 nm s^{-1}, 800 nm s^{-1} or 3200 nm s^{-1}. The cantilever deflection was read out at 3000 Hz, 12 000 Hz or 48 000 Hz. To access a fresh surface area, the surface was moved by 100 nm in lateral direction after each approach-retraction cycle. All measurements were performed in PBS, pH 7.4 in ambient conditions. About 1 nM of the Fgβ-ddFLN4-Biotin construct was added to the measurement buffer. After a few thousand approach-retraction cycles, 1 mM Bond-Breaker TCEP Solution (ThermoFisher Scientific, Waltham, USA) was added to the measurement buffer. Independently of the AFM measurement, we ensured that the addition of Bond-Breaker TCEP Solution does not affect the pH of the buffer using indicator paper. For the inverse experiment, *i.e.* starting in reducing conditions and then changing to oxidizing conditions, we first measured in PBS containing TCEP and then exchanged the buffer for PBS without TCEP (instead enriched with oxygen). For calibration of the cantilevers, the thermal noise method as described by te Riet *et al.* was used.[32]

AFM-based single-molecule force spectroscopy data analysis

Force–distance traces were obtained by converting z-piezo and deflection voltage using the cantilever spring constant, the optical lever and z-piezo sensitivity. Zero-points are determined for each force-extension trace and denoising is performed after cantilever bending correction. To detect force peaks, the data are translated into contour length space. Then data are sorted to identify curves that exhibit two distinct two-step unfoldings of the ddFLN4 fingerprint domains. Finally, unfolding and unbinding forces are extracted, plotted as histograms and fitted.

Results and discussion

In this work, we employed protein engineering to establish a covalent link between the two N-terminal β-strands β1 and β2 of mSA's functional subunit. Our intention was to perform AFM-based SMFS experiments, in which we keep the N-terminal β-sheet structure intact while pulling biotin out of mSA's N-terminally tethered functional binding pocket. Based on their position within β1 and β2, their distance and orientation in the crystal structure, we identified threonine 18 and alanine 33 (Fig. 1A) as good candidates for mutations to cysteines. With these two mutations (T18C,A33C), the formation of a disulfide bridge, which connects β1 and β2, thereby preventing the separation of the two, is facilitated.

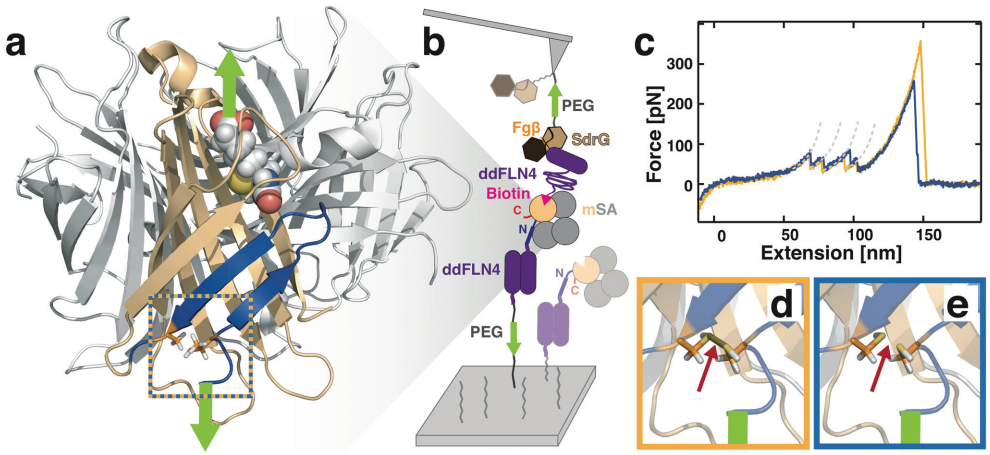

Fig. 1 Protein design and experimental setup. (a) Crystal structure of SA (adapted from PDB:6M9B[41]) with biotin (spheres) in one of the binding pockets. Green arrows indicate the attachment points (N-terminus of SA's functional subunit and biotin's carboxyl group), which are pulled apart in the SMFS experiment. The first two N-terminal β-strands, which have been shown to partially unfold prior to the unbinding of biotin are highlighted in blue. Residues T18 and A33, which we mutated to cysteines, are shown in orange stick representation. The colored box encloses the area that is zoomed-in in (d) and (e). (b) Experimental setup. mSA is covalently attached by the N-terminus of the functional subunit to a ddFLN4 fingerprint domain which in turn is tethered by a PEG-linker onto a glass surface. The AFM cantilever tip is functionalized with the SdrG (brown) that binds Fgβ (orange), which is fused to a biotinylated ddFLN4 fingerprint domain bound to the mSA on the surface. Retracting the cantilever from the surface, PEG linkers get stretched until the ddFLN4 fingerprints unfold providing additional contour length. Finally, biotin unbinds from mSA. (c) A typical force extension trace with the two distinct two-step unfolding patterns of ddFLN4 before the biotin/SA unbinding. Grey dashed lines are fits of the worm-like chain model[42] to the data. Light yellow curve: In the absence of a reducing agent, a disulfide bridge is formed between the mutated residues T18C and A33C (d). Blue curve: In the presence of a reducing agent, the disulfide bridge is destroyed (e), resulting in lower unbinding forces of biotin from mSA. Red arrows in (e) and (d) highlight the position of the intact (d) and destroyed (e) disulfide bridge between the mutated residues T18C and A33C.

View Article Online

Published on 09 March 2020. Downloaded by Ludwig Maximilians Universitaet Muenchen on 3/31/2020 10:54:18 AM.

We performed isothermal titration calorimetry measurements (*cf.* Fig. 2) to ensure that neither the mutations nor the formation of the disulfide bridge affect biotin binding. For the measurement without TCEP, we observed a binding stoichiometry of N = (1.19 ± 0.26) and a binding enthalpy of ΔH = −(27.2 ± 3.2) kcal mol^{-1}. The measurement with TCEP yielded N = (1.15 ± 0.25) and ΔH = −(26.3 ± 3.0) kcal mol^{-1}. With our instrument a reliable value for the affinity of the binding could not be obtained – only an upper bound of 1 nM can be provided. Measurement uncertainties were estimated using the min–max method and assuming a 10% uncertainty in the concentrations of both analyte and titrant. Within these uncertainties, the binding enthalpy agrees with literature values for the mSA/biotin interaction.[9,10,33,34] We conclude that in the absence of mechanical load, the characteristic properties of biotin binding are not altered for our novel mSA mutant. Furthermore, the ITC data also confirms the monovalency of our reinforced mSA.

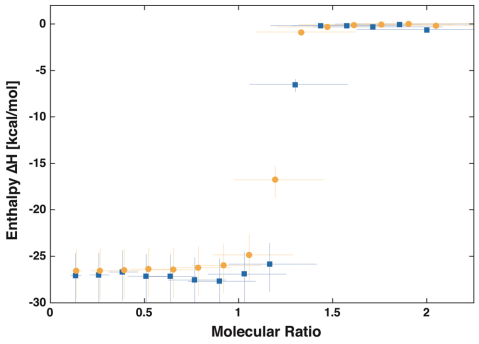

Fig. 2 ITC data for titrating biotin into a solution of the reinforced mSA. Blue squares: without TCEP. Yellow circles: with 1 mM TCEP in both titrant and analyte solution. Error bars are a maximum error estimate assuming a 10% uncertainty in both analyte and titrant concentration.

Previously, an N-terminal cysteine in mSA's functional subunit has always been used for site-specific immobilization on a maleimide-functionalized glass surface.[9,10,35,36] To prevent any interference with the two newly introduced cysteines, we modified our immobilization chemistry and replaced the N-terminal cysteine by glycine to allow for site-specific surface attachment using a Sortase-mediated linkage.[37]

For SMFS experiments, we used an elaborate attachment strategy introducing the well-characterized fourth filamin domain of *Dictyostelium discoideum*[38] (ddFLN4) as so-called fingerprint domain[39] on both sides of the receptor–ligand system (Fig. 1B). Their clear two-step unfolding patterns enable the identification of single-molecule interactions and serve as an internal force reference. The adhesin SD-repeat protein G (SdrG)[40] is covalently attached to the cantilever tip and binds to a short peptide from human fibrinogen β (Fgβ) genetically fused to the biotinylated ddFLN4 that is bound to the mSA on the surface. The use of the SdrG/Fgβ system to probe the biotin/mSA interaction has been previously established:[10] the tenfold higher unbinding forces[26] of the SdrG/

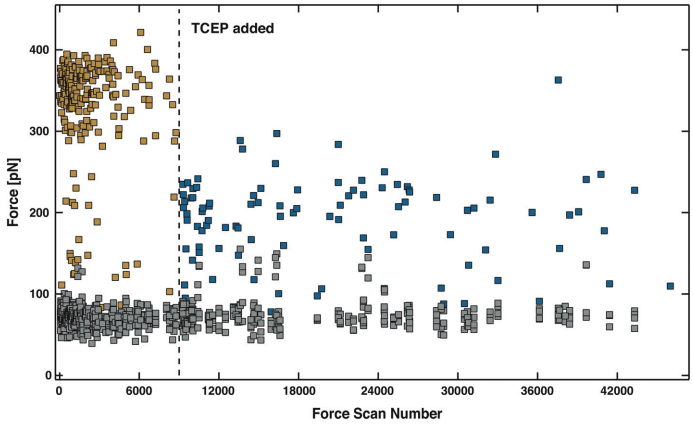

Fig. 3 Course of the AFM-based SMFS measurement. For all force-extension traces recorded at 800 nm s^{-1} showing two distinct ddFLN4 unfolding pattern before the unbinding of biotin from mSA, the four ddFLN4 unfolding forces (grey) and the final biotin/mSA unbinding force (colored) are plotted over time. After about 9000 approach-retraction cycles, the reducing agent TCEP was added to the measurement buffer (indicated by the dashed line). In the absence of TCEP (yellow), the mSA/biotin unbinding forces are significantly higher than in the presence of TCEP (blue). TCEP does not affect the unfolding forces of ddFLN4. The decrease in interaction frequency over time is independent of TCEP addition and probably due to wear out of the cantilever functionalization.

 This journal is © The Royal Society of Chemistry 2020

View Article Online

Published on 09 March 2020. Downloaded by Ludwig Maximilians Universitaet Muenchen on 3/31/2020 10:54:18 AM.

Fgβ system allow to reliably probe the mechanically weaker biotin/mSA interaction, while the lower affinity of SdrG/Fgβ system prevents permanent clogging of the cantilever tip.

Retracting the cantilever from the surface, the polyethylene glycol (PEG) linkers, both on the cantilever tip and on the surface, get stretched. At some point, the ddFLN4 fingerprint domains subsequently unfold, adding additional contour length to the stretched polymer chain. Finally, biotin unbinds from mSA. Typical force extension traces are depicted in Fig. 1C.

We probed mSA under two different conditions: without and with a reducing agent in the measurement buffer. In the absence of the reducing agent, we measured about 1.5-fold higher unbinding forces for pulling biotin out of mSA's binding pocket (yellow curve in Fig. 1C) compared with measurements performed in the presence of the reducing agent (blue curve in Fig. 1C).

We attribute this difference in force to two different states of the mSA molecule. With the mutations T18C and A33C, a disulfide bridge connecting β-strands β1 and β2 (Fig. 1D) is formed, which is destroyed upon addition of a reducing agent to the measurement buffer. When the reducing agent is added, the covalent linkage between the N-terminal β-strands is lost (Fig. 1E).

In Fig. 3, the temporal course of the SMFS measurement is depicted for the retraction velocity of 800 nm s^{-1}. (Data for other retraction velocities are provided in ESI Fig. S4 and S5.†) Before the addition of TCEP (indicated by the dashed vertical line), unbinding forces are significantly higher. The decrease in interaction frequency over time is probably due to wear out of the cantilever functionalization and independent of the TCEP addition. For the inverse experiment (ESI Fig. S6†), a similar decrease in interaction frequency was observed. Importantly, the unfolding forces of ddFLN4, which serve as an internal force reference, are not affected by the addition of the reducing agent. This confirms that the reducing agent is indeed acting on the mSA/biotin system only.

Rupture force histograms provide yet a better visualization of the data (Fig. 4). In the yellow histograms with peaks at around 350 pN, unbinding forces measured without TCEP in the measurement buffer are plotted. Single events at lower forces, which might be caused by molecules that did not form a disulfide bridge, are also observed. Upon addition of the reducing agent, the forces drop to about 200 pN (blue histograms). This is comparable to what has been measured for N-terminally tethered mSA that does not have the two mutations (T18C,A33C).[9,10] This finding confirms that with the two mutations (T18C,A33C) a disulfide bridge is formed between β-strands β1 and β2 of the functional subunit of mSA. The covalent link prevents the partial unfolding of the N-terminal β-sheet structure under load. Thereby, the unbinding pathway, which involves separation of the N-terminal β-strands, *i.e.* partial unfolding of the functional subunit, is blocked. The disulfide bridge thus helps to preserve the structural integrity of the binding pocket under mechanical load. The mechanical stability of the biotin/mSA

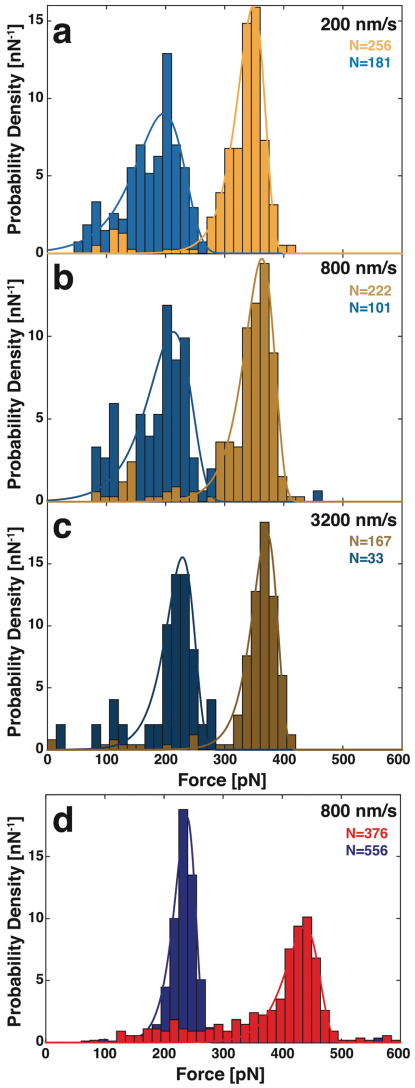

Fig. 4 Force histograms. (a–c) For the same measurement as shown in Fig. 3, histograms of the biotin/mSA unbinding force are plotted for the different cantilever retraction velocities (*i.e.* different force-loading rates). The spring constant of the AFM cantilever read 86 pN nm^{-1}. Unbinding forces measured without the reducing agent TCEP are plotted in yellow, those measured with TCEP in the measurement buffer are plotted in blue. All histograms are fitted with a Bell–Evans distribution. Fit parameters and physical parameters are provided in ESI Tables S1 and S2.† (d) Previously published SMFS data on the mSA/biotin interaction for N- (blue) and C-terminal (red) tethering of mSA without the mutations (T18C,A33C) are shown for comparison. For this measurement, the spring constant of the AFM cantilever was 169 pN nm^{-1}.

View Article Online

Published on 09 March 2020. Downloaded by Ludwig Maximilians Universitaet Muenchen on 3/31/2020 10:54:18 AM.

interaction is thus increased and higher forces are reached before biotin can overcome the energy barrier and escape from the binding pocket.

For further validation and to illustrate that we can indeed switch between the mechanically weak and the mechanically strong biotin/mSA interaction, we also performed the inverse experiment (ESI Fig. S6†). We first measured the unbinding forces of biotin from the mutated mSA in a reducing environment, *i.e.* with TCEP in the measurement buffer and observed low unbinding forces of about 200 pN. Then, we exchanged the measurement buffer to perform the measurement in an oxidizing environment (using oxygen-enriched PBS). For the vast majority of unbinding events observed under these conditions, we measured forces distributed around 350 pN. Recording this increase in mechanical stability, we deduce that we are indeed monitoring the formation of a disulfide bridge between the mutated amino acids (T18C,A33C).

The forces for unbinding biotin from the N-terminally tethered mSA with the disulfide bridge between the N-terminal β-strands (about 350 pN) are still weaker compared with those that have been reported for SMFS experiments using C-terminal tethering of mSA (about 425 pN).[10] For convenience, we plotted these data in Fig. 4D. (The dynamic force spectra are compared in ESI Fig. S7.†) Compared to the rather broad dispersion of the data recorded for the C-terminally attached mSA, the distributions for the mutated mSA(T18C, A33C) are rather narrow. These variations in force distributions might be due to the difference in tethering geometry and the way biotin and the adjacent linker interact with the L3/4 peptide loop that closes over the binding pocket when the molecular complex is under load, as recently shown by Sedlak *et al.*[43] It also illustrates the complexity of unbinding pathways and the strong dependence of mechanical stability on the molecular details. From our SMFS results, it is not possible to exclude that, despite the disulfide bridge, there still is unfolding of the N-terminal β-sheet structure prior to the biotin rupture. The 1.5-fold increase in unbinding force (caused by introduction of the disulfide bridge between the N-terminal β-strands) is yet significant and a convincing argument for the unbinding pathway that involves unfolding prior to unbinding, which has been observed in steered molecular dynamics simulations.[10]

Conclusion

In this work, we demonstrate how SMFS stimulated by steered molecular dynamics simulation leads to a deeper understanding of the mechanics of molecular processes and provides guidance for protein engineering with the goal to specifically design the quality of the interaction between biomolecules. With the creation of a disulfide bridge within mSA's N-terminal β-sheet structure, we specifically blocked a certain, comparatively weak, unbinding pathway. Thereby, we significantly increased the mechanical stability of the biotin/mSA interaction. We provided an experimental confirmation for the molecular pathway previously identified by steered molecular dynamics simulations: under load, N-terminally tethered mSA is partially unfolded before biotin leaves the binding pocket. Thus, we found a prime example for the close interconnection of unfolding and unbinding for receptor–ligand dissociation under mechanical force.

Conflicts of interest

There are no conflicts to declare.

Acknowledgements

This study was inspired by the steered molecular dynamics simulations of R. C. Bernardi and the stimulating discussions with L. F. Milles on the interplay of unfolding and unbinding in protein complexes. The authors thank A. Kardinal and T. Nicolaus for laboratory support and L. F. Milles for providing the SdrG/Fgβ-system. The authors acknowledge M. S. Bauer and C. Kluger for helpful discussions. S. M. Sedlak thanks the Nanosystems Initiative Munich for support. This work was funded by the Deutsche Forschungsgemeinschaft (DFG, German Research Foundation) – Project-ID 201269156 – SFB1032.

Notes and references

1 N. M. Green, *Methods Enzymol.*, 1990, **184**, 51–67.
2 T. Sano, M. W. Pandori, X. Chen, C. L. Smith and C. R. Cantor, *J. Biol. Chem.*, 1995, **270**, 28204–28209.
3 M. Krieg, G. Fläschner, D. Alsteens, B. M. Gaub, W. H. Roos, G. J. L. Wuite, H. E. Gaub, C. Gerber, Y. F. Dufrêne and D. J. Müller, *Nat. Rev. Phys.*, 2019, **1**, 41–57.
4 G. Sitters, D. Kamsma, G. Thalhammer, M. Ritsch-Marte, E. J. Peterman and G. J. Wuite, *Nat. Methods*, 2015, **12**, 47–50.
5 W. Ott, M. A. Jobst, C. Schoeler, H. E. Gaub and M. A. Nash, *J. Struct. Biol.*, 2017, **197**, 3–12.
6 A. Lof, P. U. Walker, S. M. Sedlak, S. Gruber, T. Obser, M. A. Brehm, M. Benoit and J. Lipfert, *Proc. Natl. Acad. Sci. U. S. A.*, 2019, **116**, 18798–18807.
7 K. M. Tych, M. Jahn, F. Gegenfurtner, V. K. Hechtl, J. Buchner, T. Hugel and M. Rief, *J. Phys. Chem. B*, 2018, **122**, 11373–11380.
8 M. Howarth, D. J. Chinnapen, K. Gerrow, P. C. Dorrestein, M. R. Grandy, N. L. Kelleher, A. El-Husseini and A. Y. Ting, *Nat. Methods*, 2006, **3**, 267–273.
9 S. M. Sedlak, M. S. Bauer, C. Kluger, L. C. Schendel, L. F. Milles, D. A. Pippig and H. E. Gaub, *PLoS One*, 2017, **12**, e0188722.
10 S. M. Sedlak, L. C. Schendel, M. C. R. Melo, D. A. Pippig, Z. Luthey-Schulten, H. E. Gaub and R. C. Bernardi, *Nano Lett.*, 2019, **19**, 3415–3421.

 This journal is © The Royal Society of Chemistry 2020

View Article Online

Published on 09 March 2020. Downloaded by Ludwig Maximilians Universitaet Muenchen on 3/31/2020 10:54:18 AM.

11 W. Humphrey, A. Dalke and K. Schulten, *J. Mol. Graphics*, 1996, **14**, 33–38, 27–38.
12 A. A. Dombkowski, K. Z. Sultana and D. B. Craig, *FEBS Lett.*, 2014, **588**, 206–212.
13 H. Li and J. M. Fernandez, *J. Mol. Biol.*, 2003, **334**, 75–86.
14 A. Grutzner, S. Garcia-Manyes, S. Kotter, C. L. Badilla, J. M. Fernandez and W. A. Linke, *Biophys. J.*, 2009, **97**, 825–834.
15 D. Sharma, O. Perisic, Q. Peng, Y. Cao, C. Lam, H. Lu and H. Li, *Proc. Natl. Acad. Sci. U. S. A.*, 2007, **104**, 9278–9283.
16 H. R. Nordlund, O. H. Laitinen, S. T. Uotila, T. Nyholm, V. P. Hytonen, J. P. Slotte and M. S. Kulomaa, *J. Biol. Chem.*, 2003, **278**, 2479–2483.
17 A. Chilkoti, T. Boland, B. D. Ratner and P. S. Stayton, *Biophys. J.*, 1995, **69**, 2125–2130.
18 S. Voss and A. Skerra, *Protein Eng., Des. Sel.*, 1997, **10**, 975–982.
19 G. O. Reznik, S. Vajda, T. Sano and C. R. Cantor, *Proc. Natl. Acad. Sci. U. S. A.*, 1998, **95**, 13525–13530.
20 I. P. Korndorfer and A. Skerra, *Protein Sci.*, 2002, **11**, 883–893.
21 C. E. Chivers, E. Crozat, C. Chu, V. T. Moy, D. J. Sherratt and M. Howarth, *Nat. Methods*, 2010, **7**, 391–393.
22 K. H. Lim, H. Huang, A. Pralle and S. Park, *Biotechnol. Bioeng.*, 2013, **110**, 57–67.
23 D. DeMonte, E. J. Drake, K. H. Lim, A. M. Gulick and S. Park, *Proteins: Struct., Funct., Bioinf.*, 2013, **81**, 1621–1633.
24 D. Demonte, C. M. Dundas and S. Park, *Appl. Microbiol. Biotechnol.*, 2014, **98**, 6285–6295.
25 M. Fairhead, D. Krndija, E. D. Lowe and M. Howarth, *J. Mol. Biol.*, 2014, **426**, 199–214.
26 L. F. Milles, K. Schulten, H. E. Gaub and R. C. Bernardi, *Science*, 2018, **359**, 1527–1533.
27 L. F. Milles, E. A. Bayer, M. A. Nash and H. E. Gaub, *J. Phys. Chem. B*, 2017, **121**, 3620–3625.
28 J. Yin, P. D. Straight, S. M. McLoughlin, Z. Zhou, A. J. Lin, D. E. Golan, N. L. Kelleher, R. Kolter and C. T. Walsh, *Proc. Natl. Acad. Sci. U. S. A.*, 2005, **102**, 15815–15820.
29 P. Artimo, M. Jonnalagedda, K. Arnold, D. Baratin, G. Csardi, E. de Castro, S. Duvaud, V. Flegel, A. Fortier, E. Gasteiger, A. Grosdidier, C. Hernandez, V. Ioannidis, D. Kuznetsov, R. Liechti, S. Moretti, K. Mostaguir, N. Redaschi, G. Rossier, I. Xenarios and H. Stockinger, *Nucleic Acids Res.*, 2012, **40**, W597–W603.
30 J. L. Zimmermann, T. Nicolaus, G. Neuert and K. Blank, *Nat. Protoc.*, 2010, **5**, 975–985.
31 I. Chen, B. M. Dorr and D. R. Liu, *Proc. Natl. Acad. Sci. U. S. A.*, 2011, **108**, 11399–11404.
32 J. te Riet, A. J. Katan, C. Rankl, S. W. Stahl, A. M. van Buul, I. Y. Phang, A. Gomez-Casado, P. Schon, J. W. Gerritsen, A. Cambi, A. E. Rowan, G. J. Vancso, P. Jonkheijm, J. Huskens, T. H. Oosterkamp, H. Gaub, P. Hinterdorfer, C. G. Figdor and S. Speller, *Ultramicroscopy*, 2011, **111**, 1659–1669.
33 A. Chilkoti and P. S. Stayton, *J. Am. Chem. Soc.*, 1995, **117**, 10622–10628.
34 M. Sarter, D. Niether, B. W. Koenig, W. Lohstroh, M. Zamponi, N. H. Jalarvo, S. Wiegand, J. Fitter and A. M. Stadler, *J. Phys. Chem. B*, 2020, **124**, 324–335.
35 F. Baumann, M. S. Bauer, L. F. Milles, A. Alexandrovich, H. E. Gaub and D. A. Pippig, *Nat. Nanotechnol.*, 2016, **11**, 89–94.
36 K. R. Erlich, S. M. Sedlak, M. A. Jobst, L. F. Milles and H. E. Gaub, *Nanoscale*, 2019, **11**, 407–411.
37 E. Durner, W. Ott, M. A. Nash and H. E. Gaub, *ACS Omega*, 2017, **2**, 3064–3069.
38 I. Schwaiger, A. Kardinal, M. Schleicher, A. A. Noegel and M. Rief, *Nat. Struct. Mol. Biol.*, 2004, **11**, 81–85.
39 M. S. Bauer, L. F. Milles, S. M. Sedlak and H. E. Gaub, *bioRxiv*, 2018.
40 P. Herman, S. El-Kirat-Chatel, A. Beaussart, J. A. Geoghegan, T. J. Foster and Y. F. Dufrene, *Mol. Microbiol.*, 2014, **93**, 356–368.
41 S. Basu, A. Finke, L. Vera, M. Wang and V. Olieric, *Acta Crystallogr., Sect. D: Struct. Biol.*, 2019, **75**, 262–271.
42 C. Bustamante, J. F. Marko, E. D. Siggia and S. Smith, *Science*, 1994, **265**, 1599.
43 S. M. Sedlak, L. C. Schendel, H. E. Gaub and R. C. Bernardi, *Sci. Adv.*, 2020, **6**, eaay5999.

This journal is © The Royal Society of Chemistry 2020

Electronic Supplementary Material (ESI) for Nanoscale.
This journal is © The Royal Society of Chemistry 2020

Supplementary Information

Switchable Reinforced Streptavidin

Leonard C. Schendel,[‡a] Steffen M. Sedlak,[‡a] and Hermann E. Gaub[*a]

[a]Lehrstuhl für Angewandte Physik and Center for NanoScience, Ludwig-Maximilians-Universität München, Amalienstr. 54, 80799 Munich, Germany

Table of contents

I. Sequences of the Protein Constructs

Functional SA subunit with N-terminal glycines (purple), two mutations to cysteines (T18C,A33C; orange) and C-terminal polyhistidine tag (green):

M**GG**S**EAGI**C**GTWYNQLGSTFIVT**C**GADGALTGTYESAVGNAESRYVLTGRYDSAPATDGSGTALGWTVA**
WKNNYRNAHSATTWSGQYVGGAEARINTQWLLTSGTTEANAWKSTLVGHDTFTKVKPSAASLE**HHHH**
HH

Non-functional SA subunit with the three mutations N23A, S27D, S45A (red):

M**EAGITGTWY**A**QLG**D**TFIVTAGADGALTGTYE**A**AVGNAESRYVLTGRYDSAPATDGSGTALGWTVAWK**
NNYRNAHSATTWSGQYVGGAEARINTQWLLTSGTTEANAWKSTLVGHDTFTKVKPSAAS

ddFLN4 construct with N-terminal ybbR-tag (blue) and polyhistidine tag (green) as well as C-terminal Sortase motif (magenta). The internal cysteine 18 is mutated to serine (red):

M**DSLEFIASKLA**HHHHHH**GS**ADPEKSYAEGPGLDGGE**S**FQPSKFKIHAVDPDGVHRTDGGDGFVVTIEGP**
APVDPVMVDNGDGTYDVEFEPKEAGDYVINLTLDGDNVNGFPKTVTVKPAPGSGSGSGS**LPETGG**

ddFLN4 construct with N-terminal Fgβ-peptide (cyan), C-terminal polyhistidine tag (green) and ybbR-tag (blue):

MAT**NEEGFFSARGHRPLD**GSGSGSGSAGTGSG**ADPEKSYAEGPGLDGGE**S**FQPSKFKIHAVDPDGVHRT**
DGGDGFVVTIEGPAPVDPVMVDNGDGTYDVEFEPKEAGDYVINLTLDGDNVNGFPKTVTVKPAPSG**HH**
HHHHGS**DSLEFIASKLA**LPETGG

II. Site-directed Mutagenesis

All mutations were introduced following the Quik Change™ (Stratagene, La Jolla, USA) PCR procedure.

DNA-primer sequences:

Introduce an N-terminal glycine:
Fw: GAAGGAGATATACATATGGGCGGCTCCGAAGCG
Rv: CGCTTCGGAGCCGCCCATATGTATATCTCCTTC

T18C:
Fw: GGCTCCGAAGCGGGGATTTGCGGCACGTGG
Rv: CCACGTGCCGCAAATCCCCGCTTCGGAGCC

A33C:
Fw: GGGTTCCACCTTTATCGTGACTTGTGGGGCAGATGG
Rv: CCATCTGCCCCACAAGTCACGATAAAGGTGGAACCC

Howarth *et al.*[1] deposited pET21a plasmids containing dead/alive SA subunits on addgene.

III. Sodium Dodecyl Sulfate-Polyacrylamide Gel Electrophoresis

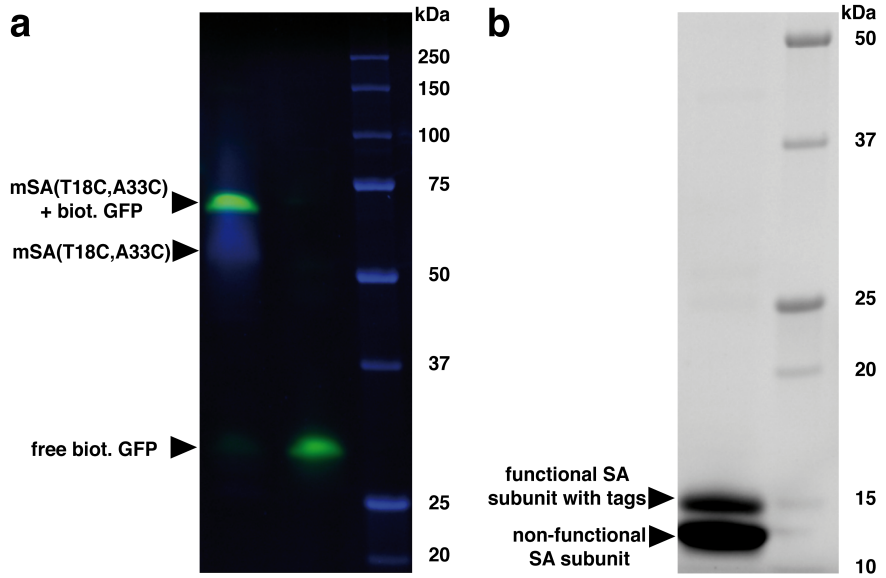

Supplementary Figure S1. SDS-PAGE for protein characterization. (a) mSA construct incubated with biotinylated GFP (left lane), a control with free biotinylated GFP (middle lane), and molecular weight standards (right lane) were run on gel and imaged in the UV channel (blue) and the 488 nm-channel (green). (b) mSA disintegrated into its subunits (left lane) and molecular weight standards (right lane) are shown. The two bands in the left lane correspond to the functional subunit with the additional polyhistidine tag and the non-functional subunits.

Biotinylated GFP was used to check mSA's functionality. An Any kD Mini-PROTEAN TGX Stain-Free Protein Gel (Bio-Rad Laboratories GmbH, Feldkirchen, Germany) was run without prior sample heating to maintain proteins' structure and to keep biotinylated GFP bound to mSA. The gel was imaged on a ChemiDoc MP Imaging System (Bio-Rad Laboratories GmbH, Feldkirchen, Germany) in the UV channel and the 488 nm-channel. mSA construct was incubated with biotinylated GFP before transferring into SDS loading buffer (50 mM TRIS, pH 8.0, 2.5% SDS, 5% glycerol, 0.005% bromphenol blue, 2.5% β-mercaptoethanol). In addition, a control with free biotinylated GFP and molecular weight standards (Precision Plus Protein Standards, Bio-Rad Laboratories GmbH, Feldkirchen, Germany) were run. The observed molecular weights agree well with what was calculated from the amino acid sequence (GFP: 26.9 kDa, mSA: 54.5 kDa). Only the complex of biotinylated GFP and mSA run slightly faster. The gel confirms the monovalency of the mSA construct.

When mSA is heated to 95°C for 5 min prior to gel loading, it disintegrates into its subunits. For the functional subunit with the additional polyhistidine tag the molecular weight (calculated from the amino acid sequence) reads 14.5 kDa, while for the non-functional subunit the molecular weight is only 13.2 kDa. By gel electrophoresis, these weights could be confirmed (Supplementary Fig. S1b). To also check the 3:1-composition of mSA, the lane was quantitatively analysed (Supplementary Fig. S2).

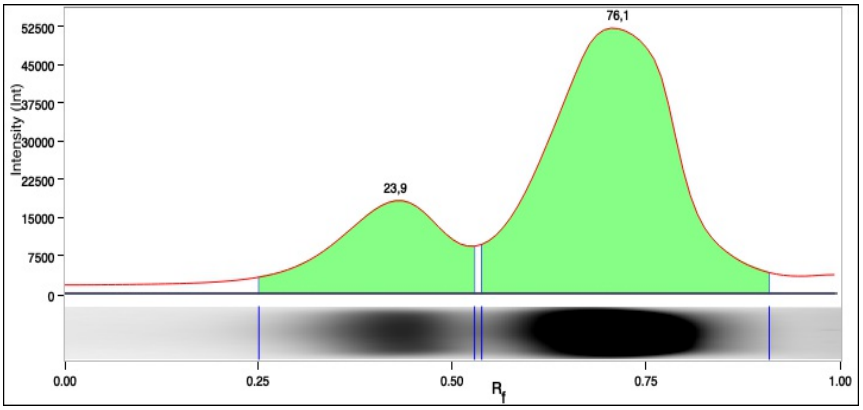

Supplementary Figure S2. Lane profile for heated mSA, decomposed into its subunits. The bands observed in the left lane in Figure S1 were quantitatively analysed using the Image Lab Software (Bio-Rad, Hercules, USA). About one fourth of the subunits are observed in the band corresponding to the functional subunits, the other three fourth in the band corresponding to the non-functional subunit. With SDS PAGE, it was thus possible to quantitatively confirm the composition of mSA – it is comprised of one functional and three non-functional subunits.

IV. Fluorescence Anisotropy

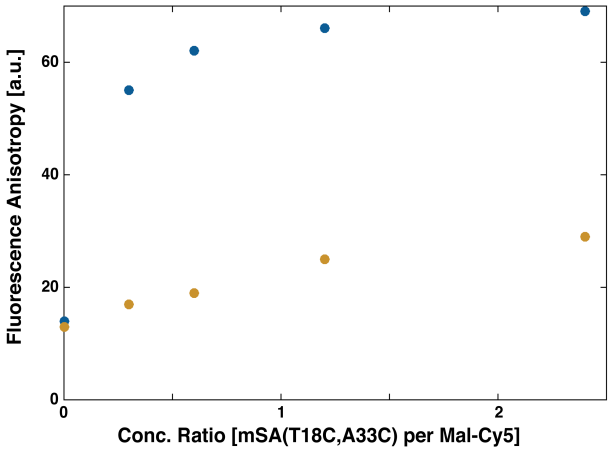

Supplementary Figure S3. Fluorescence Anisotropy of a Cy5-maleimide dye with different concentrations of mSA(T18C,A33C) added in reducing (with TCEP, blue) and oxidizing (without TCEP, yellow) environments.

To detect the disulfide bridge by other means than SMFS, we performed fluorescence anisotropy measurements using a Cy5-maleimide dye. 0.2 µM Cy5-maleimide dye were added to 0, 0.3, 0.6, 1.2 and 2.4 µM mSA(T18C,A33C). Fluorescence anisotropy of the Cy5-maleimide dye was measured on a Tecan Infinite M1000 Pro (Tecan Group AG, Männedorf, Switzerland) in well-plates with and without 1 mM BondBreaker TCEP Solution in the measurement buffer (PBS). In the absence of mSA(T18C,A33C), the fluorescence anisotropy of freely diffusing Cy5-maleimide is comparable for both samples (with and without TCEP). For higher concentrations of mSA(T18C,A33C), we found the fluorescence anisotropy of the Cy5-maleimide dye to increase – probably because the dye is reacting with the much larger mSA(T18C,A33C) and thus its rotational movement is slowed down. In the presence of TCEP (blue data in Supplementary Fig. S3), the disulfide bridge in mSA(T18C,A33C) is reduced and the cysteines' thiols are accessible and can react with the Cy5-maleimide dye. If there is no TCEP in the measurement buffer, the thiols have mainly formed a disulfide bridge. Reaction of Cy5-maleimide to primary amines is possible but not favored at pH 7.4.

V. Course of the AFM-based SMFS Measurement

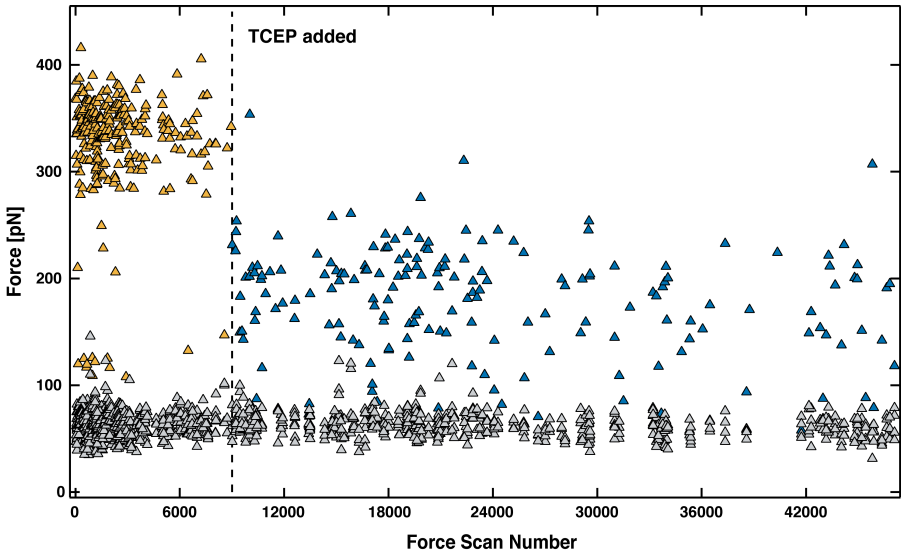

Supplementary Figure S4. Course of the AFM-based SMFS measurement for 200 nm/s retraction velocity. For all force-extension traces showing two distinct ddFLN4 unfolding pattern before the unbinding of biotin from mSA, the four ddFLN4 unfolding forces (grey) and the final biotin/mSA unbinding force (colored) are plotted over time. After about 9,000 approach-retraction cycles, the reducing agent TCEP was added to the measurement buffer (indicated by the dashed line). In the absence of TCEP (yellow), the mSA/biotin unbinding forces are significantly higher than in the presence of TCEP (blue). TCEP does not affect the unfolding forces of ddFLN4.

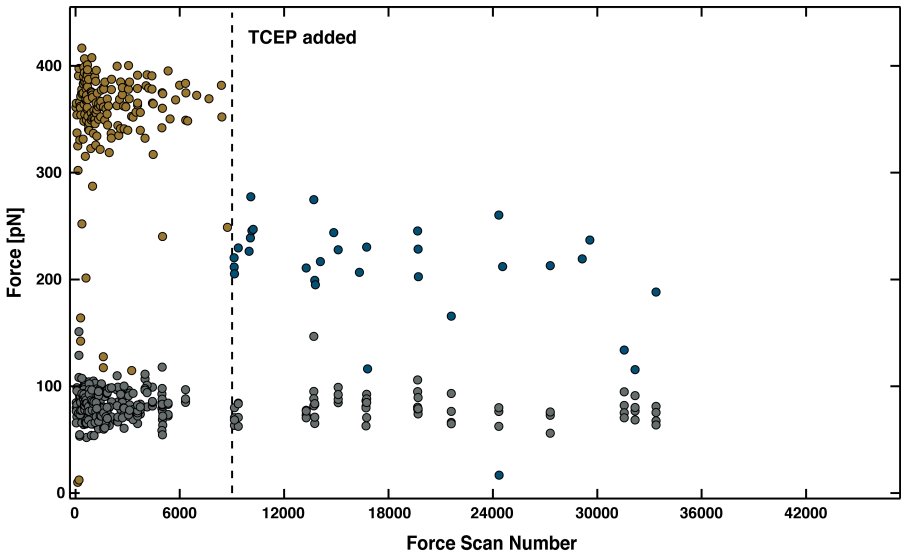

Supplementary Figure S5. Course of the AFM-based SMFS measurement for 3200 nm/s retraction velocity. For all force-extension traces showing two distinct ddFLN4 unfolding pattern before the unbinding of biotin from mSA, the four ddFLN4 unfolding forces (grey) and the final biotin/mSA unbinding force (colored) are plotted over time. After about 9,000 approach-retraction cycles, the reducing agent TCEP was added to the measurement buffer (indicated by the dashed line). In the absence of TCEP (yellow), the mSA/biotin unbinding forces are significantly higher than in the presence of TCEP (blue). TCEP does not affect the unfolding forces of ddFLN4.

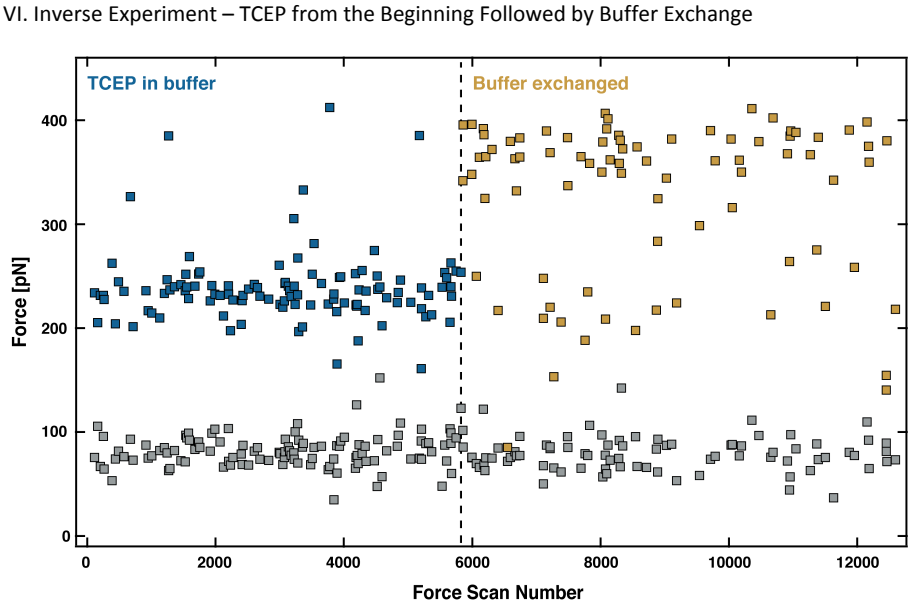

Supplementary Figure S6. Course of the inverse AFM-based SMFS measurement for 800 nm/s retraction velocity. For all force-extension traces showing two distinct ddFLN4 unfolding pattern before the unbinding of biotin from mSA, one of the four ddFLN4 unfolding forces (grey) and the final biotin/mSA unbinding force (colored) are plotted over time. The mSA construct was incubated with TCEP before surface attachment and TCEP was present in the measurement buffer from the beginning. After 5,825 approach-retraction cycles (indicated by the dashed vertical line), the surface was rinsed with 75 mL PBS buffer which had been exposed to oxygen gas in a drechsel gas washing bottle. The mSA/biotin unbinding forces after buffer exchange (yellow) are significantly higher than in the presence of TCEP (blue). Single events at lower forces, which might arise from not recovered disulfide bridges, are also observed. For this measurement, the spring constant of the AFM cantilever was 105 pN/nm.

VII. Dynamic Force Spectrum

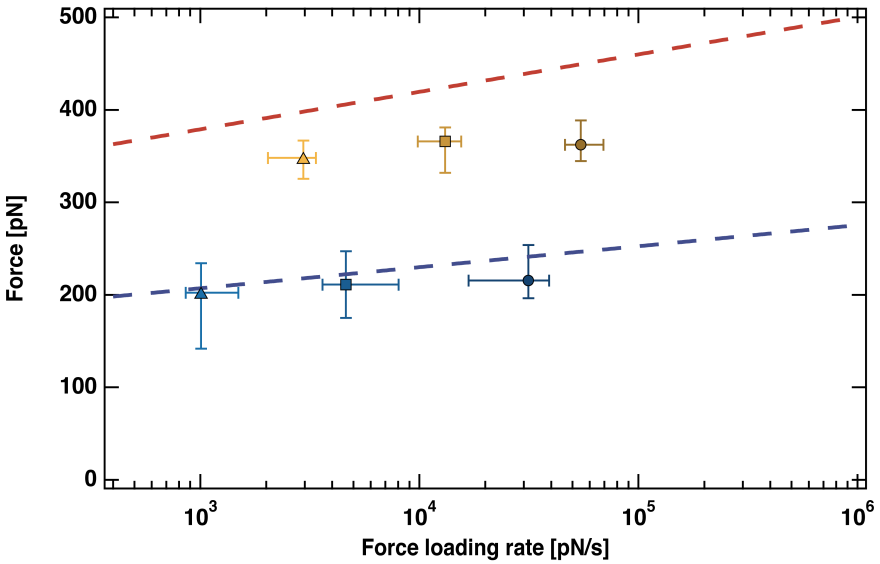

Supplementary Figure S7. Dynamic force spectrum with standard Bell-Evans fits from previous publication (Sedlak *et al.*[4]). Markers show most probable unbinding force plotted against most probable loading rate for mutated (T18C,A33C) mSA for experimental data shown in Fig. 4. Different retraction velocities used are indicated by color shade and symbol (200 nm s^{-1}: triangle, 800 nm s^{-1}: rectangle, 3200 nm s^{-1}: circle). Errors show the full width at half maximum of a kernel density estimation. Lines are fits to dynamic force spectrum of N-terminally (x_0=0.41 nm, $k_{off,0}$=7.7 x 10^{-8} s^{-1}, blue dashed line) and C-terminally (x_0=0.23 nm, $k_{off,0}$=2.5 x 10^{-8} s^{-1}, red dashed line) attached mSA, both without the mutation.[4] In the presence of TCEP (blue markers) the fit line for N-terminal attached mSA lays within the errors. In the absence of TCEP the data points (yellow markers) lay in between the two lines. Here, we don't expect an overlay with the fit line for C-terminal attached mSA, since although bearing a reinforced N-terminus the pulling geometry stills differs.

VIII. Fitting of the Bell-Evans Model

Israilev *et al.* and Evans and Ritchie independently proposed a model to characterize how an external force affects the dissociation of molecular bonds.[2, 3] The model assumes a constant force loading rate *r*, which is not true for AFM-based constant velocity force spectroscopy experiment. It is still commonly applied for AFM-based SMFS experiments. According to the model, the probability distribution of rupture forces is given by:

Physical parameters are derived from the fitting parameters *a* and *b*:

Details can be found in Sedlak *et al.*[4].

Supplementary Table S1. Fitting parameters for Figure 4.

	v_R [nm/s]	a [×10^3]	b [×10^{10}]
-TCEP	**200**	12.3	4.33
	800	20.1	4.00
	3200	9.9	4.77
+TCEP	**200**	2.0e5	2.43
	800	7.4e4	2.78
	3200	2.7e3	4.22

Supplementary Table S2. Physical parameters extracted from the data in Figure 4.

	v_R [nm/s]	<F> [pN]	<r> [pN/s]	x_0 [nm]	$k_{off,0}$ [s^{-1}]
-TCEP	**200**	350	2,700	0.18	3.3e-5
	800	360	12,400	0.17	2.5e-4
	3200	370	57,300	0.20	5.7e-5
+TCEP	**200**	200	1,100	0.10	2.3e-1
	800	210	5,300	0.12	4.0e-1
	3200	220	27,600	0.18	7.5e-2

IX. Unfolding Force Histograms for the Fingerprint Domains

Supplementary Figures S8, S9 show force histograms for ddFLN4 unfolding peaks of curves for which our software automatically identified four successive ddFLN4 unfolding peaks. In Figure 4 additional curves were taken into account featuring two ddFLN4 unfolding patterns which could not be automatically classified by the software.

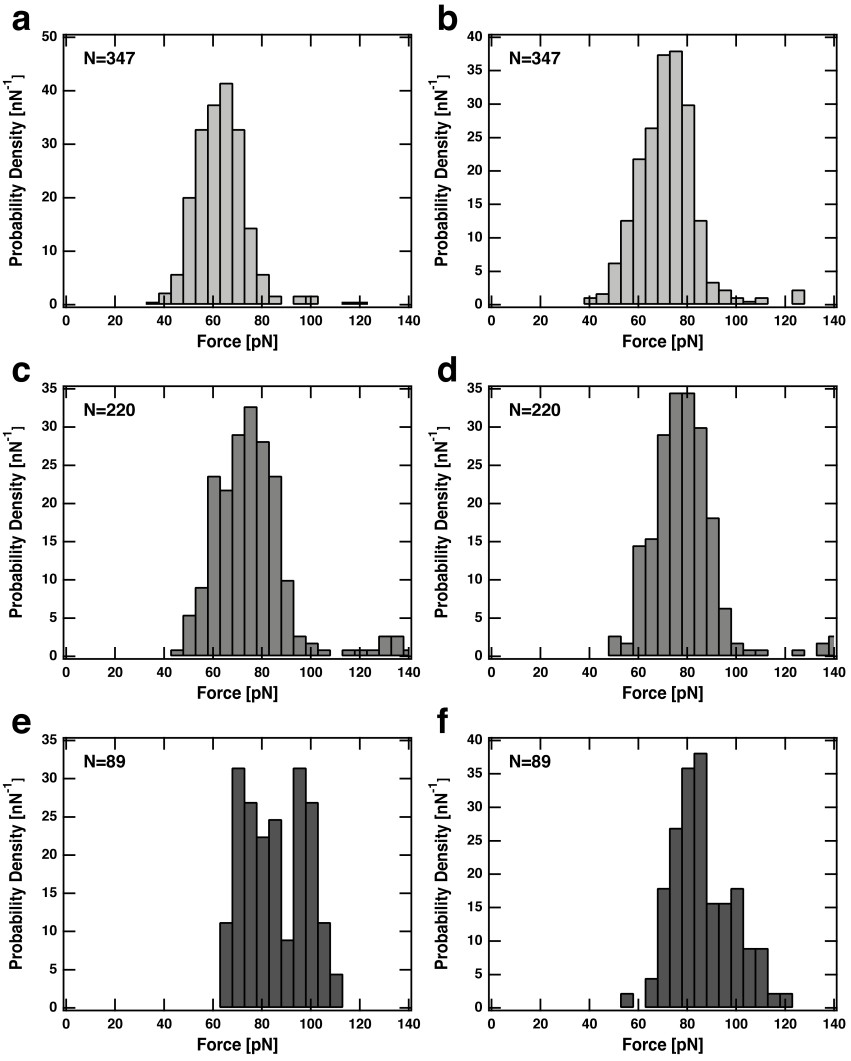

Supplementary Figure S8. Force histograms for ddFLN4 fingerprint domain fourth and third unfolding peak. (a) at 200 nm/s, (c) at 800 nm/s, (e) at 3200 nm/s show the fourth unfolding peak. (b) at 200 nm/s, (d) at 800 nm/s, (f) at 3200 nm/s show the third unfolding peak.

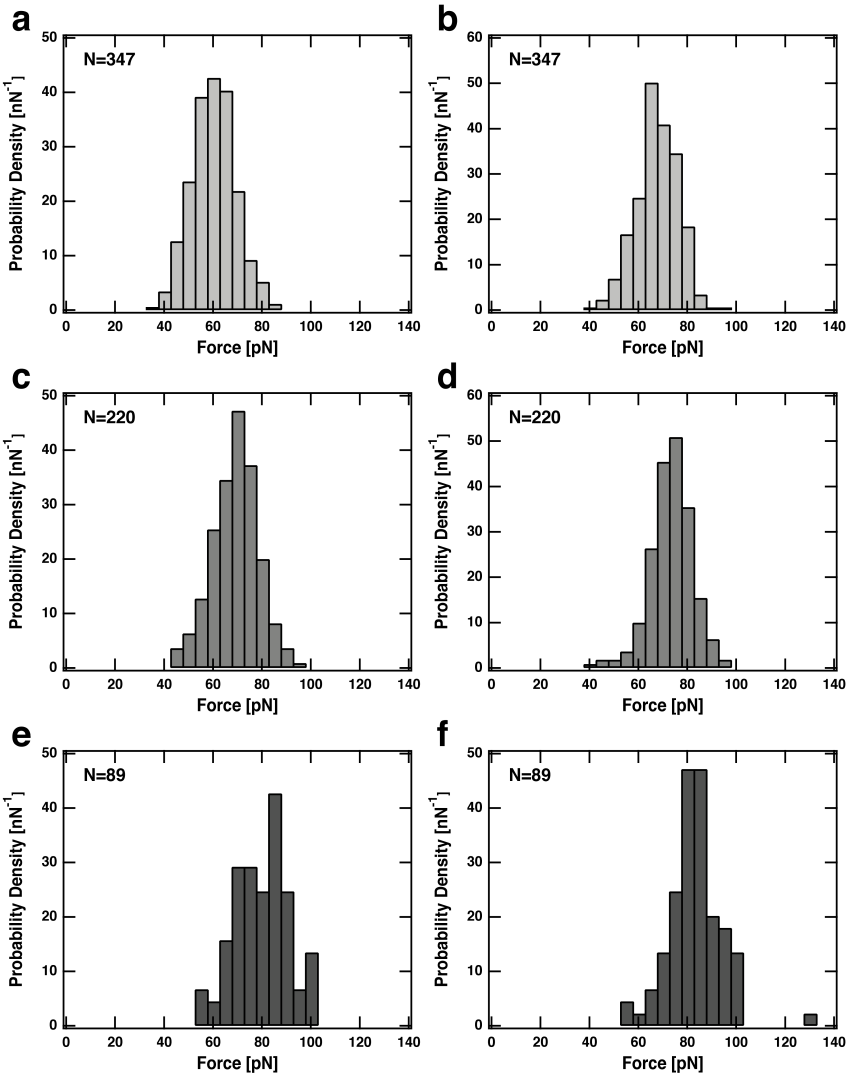

Supplementary Figure S9. Force histograms for ddFLN4 fingerprint domain second and first unfolding peak. (a) at 200 nm/s, (c) at 800 nm/s, (e) at 3200 nm/s show the second unfolding peak. (b) at 200 nm/s, (d) at 800 nm/s, (f) at 3200 nm/s show the first unfolding peak.

X. Supplementary References

1 M. Howarth, D. J. Chinnapen, K. Gerrow, P. C. Dorrestein, M. R. Grandy, N. L. Kelleher, A. El-Husseini and A. Y. Ting, *Nat Methods*, 2006, **3**, 267-273.
2 E. Evans and K. Ritchie, *Biophys J*, 1997, **72**, 1541-1555.
3 S. Izrailev, S. Stepaniants, M. Balsera, Y. Oono and K. Schulten, *Biophys J*, 1997, **72**, 1568-1581.
4 S. M. Sedlak, L. C. Schendel, M. C. R. Melo, D. A. Pippig, Z. Luthey-Schulten, H. E. Gaub and R. C. Bernardi, *Nano Letters*, 2019, **19**, 3415-3421.

Chapter 4

Combining SMFS based on AFM with Nanoapertures

4.1 Publication P3: Single-Molecule Manipulation in Zero-Mode Waveguides

Studying inter- and intramolecular interactions of mechanoactive biological samples at the single-molecule level requires the simultaneous acquisition of force and fluorescence data. In recent years, TIRF microscopy has been the method of choice to observe systems mechanically manipulated by *e.g.* AFM. However, TIRF fails in operating in the presence of physiologically relevant high fluorescent ligand concentrations.

The following publication shows the combination of the nanophotonic devices ZMWs and SMFS by an AFM. As a result, an automated technique to manipulate single molecules in dense fluorescent substrate environments has been created. For this purpose, a refined routine to precisely localize the nanometer-sized tip of an AFM cantilever was introduced, which reduces surface contact times of the cantilever to a minimum, thereby enabling non-invasive automatic probing of hundreds of ZMW cavities. In order to evaluate the performance and the applicability of a combined use of ZMWs and SMFS by AFM, the well-known SA-biotin complex was employed as model system. To this end, mSA molecules were immobilized on the floor of the ZMWs and their binding pockets were blocked with a biotin construct. The second receptor-ligand system, introduced in Section 3.1, was then used to induce mechanical tension and remove the bound biotin. Using fluorescence readout, binding of a freely diffusing labeled biotin to the now vacant mSA was observed. These measurements thereby show binding after mechanical exposure of a cryptic binding site in ZMWs.

The use of site-specific covalent chemistry along with genetically encoded peptide tags for target immobilization makes the combination of ZMWs and SMFS by AFM a versatile tool to study a wide range of mechanoactive proteins.

Single-Molecule Manipulation in Zero-Mode Waveguides

by

Leonard C. Schendel, Magnus S. Bauer, Steffen M. Sedlak, and Hermann E. Gaub

published in

Small 2020, 16, 1906740, doi: 10.1002/smll.201906740

Reprinted from Schendel *et al.* [89]. Published by WILEY-VCH Verlag GmbH & Co. KGaA, Weinheim under the terms of Creative Commons Attribution License. Copyright 2020 Schendel *et al.*

FULL PAPER

NANO · MICRO small
www.small-journal.com

Single-Molecule Manipulation in Zero-Mode Waveguides

*Leonard C. Schendel, Magnus S. Bauer, Steffen M. Sedlak, and Hermann E. Gaub**

The mechanobiology of receptor–ligand interactions and force-induced enzymatic turnover can be revealed by simultaneous measurements of force response and fluorescence. Investigations at physiologically relevant high labeled substrate concentrations require total internal reflection fluorescence microscopy or zero mode waveguides (ZMWs), which are difficult to combine with atomic force microscopy (AFM). A fully automatized workflow is established to manipulate single molecules inside ZMWs autonomously with noninvasive cantilever tip localization. A protein model system comprising a receptor–ligand pair of streptavidin blocked with a biotin-tagged ligand is introduced. The ligand is pulled out of streptavidin by an AFM cantilever leaving the receptor vacant for reoccupation by freely diffusing fluorescently labeled biotin, which can be detected in single-molecule fluorescence concurrently to study rebinding rates. This work illustrates the potential of the seamless fusion of these two powerful single-molecule techniques.

1. Introduction

Total internal reflection fluorescence (TIRF) and atomic force microscopy (AFM) have previously been successfully combined to enable joined force and fluorescence spectroscopy.[1–6] However, the necessity for a method allowing autonomous optical observation of molecules manipulated mechanically within a highly populated fluorescence environment still persists. Whereas TIRF-based techniques are capable of providing fluorescence readout, fluorophore concentration in solution did not exceed 10×10^{-9} M in these studies. This intrinsic limitation[7] drastically lowers or completely prevents the yield of successful recording of probing and simultaneous binding events as biological processes typically take place at much higher, e.g., micromolar concentrations, due to moderate affinities (see Figure S1, Supporting Information).

By using zero mode waveguides (ZMWs) these shortcomings can be mitigated as also concentrations exceeding this limit by up to three orders of magnitude up to 20×10^{-6} M[8] provide exceptional signal-to-noise ratios. In recent years, ZMWs have shown their great potential in observing enzyme turnover and single molecule recruitment events despite fluorophore concentrations of hundreds of nanomolar[9,10] to micromolar.[8,11,12] Additionally, since their readout does not require a specialized microscope, ZMWs are easily and broadly applicable. ZMWs are nanometer-sized cavities within a metal cladding on a glass coverslip with aperture diameters shorter than the wavelengths of visible light. Consequently, they pose an optical barrier for incident light and thereby only an evanescent field emerges with its decay length being shorter than the height of the cavity. In turn, the illuminated volume is confined within the bottom part of the ZMW cavity, giving rise to its ability of providing exceptional signal-to-noise ratios in dense fluorescent environments.

ZMWs used in parallel are a paradigm for a high-throughput method. Here, we yet utilize single ZMWs sequentially which allows for sensitive single molecule observation and constantly provides pristine reaction compartments. Combining ZMWs with single-molecule force spectroscopy (SMFS) conducted by using AFM creates a powerful technique for joined force and fluorescence spectroscopy despite high fluorophore concentration. It allows for mechanical manipulation of single molecules and, in addition to direct fluorescence readout, provides mechanistic insights of single molecules indicating domain unfolding, cryptic binding site opening, fingerprint unfolding or ligand dissociation.

The combined use of ZMW and AFM has already been shown feasible in proof of concept studies by using the AFM cantilever tip in surface scanning mode in order to align tip and ZMW.[13,14] Yet, manual control, cantilever degradation, and small datasets have impeded broad applicability. After mechanical manipulation of a force-activatable kinase only a single possible binding event was reported.[13]

In this study, a revised experimental workflow is employed to demonstrate the manipulation of single molecules in ZMWs by means of automated SMFS inside ZMWs and by the use of a well-defined receptor–ligand model system based on previous work.[15,16] We implemented site-specific covalent immobilization for our receptor–ligand model system and added a fingerprint protein domain to have clear evidence of probing single molecules. Along with this, we chose and designed our model system to deliver a clear one-step, on–off like, fluorescence behavior. Once mechanically manipulated it provides steady fluorescence for the whole observation period. The use of a noninvasive cantilever tip localization technique and a revised fabrication of our ZMWs ensures reliable ZMW localization and precise tip placement. Additionally, we developed an all-automatic routine for cantilever tip and ZMW localization, horizontal drift correction, and autofocus, which allows

L. C. Schendel, M. S. Bauer, Dr. S. M. Sedlak, Prof. H. E. Gaub
Lehrstuhl für Angewandte Physik and Center for NanoScience (CeNS)
Ludwig-Maximilians-Universität München
Amalienstrasse 54, Munich 80799, Germany
E-mail: gaub@lmu.de

The ORCID identification number(s) for the author(s) of this article can be found under https://doi.org/10.1002/smll.201906740.

© 2020 The Authors. Published by WILEY-VCH Verlag GmbH & Co. KGaA, Weinheim. This is an open access article under the terms of the Creative Commons Attribution License, which permits use, distribution and reproduction in any medium, provided the original work is properly cited.

DOI: 10.1002/smll.201906740

ADVANCED SCIENCE NEWS
www.advancedsciencenews.com

NANO · MICRO small
www.small-journal.com

for long-term measurements and single molecule interaction yields comparable with conventional SMFS based on AFM. Furthermore, an oxygen scavenging system and antiblinking reagent guarantee steady fluorescence conditions and prevent photodamage to both dye molecules and surface proteins enabling much longer measurement durations. Through this approach, we are able to observe reoccupation of mechanically depopulated monovalent streptavidin molecules by fluorescently labeled biotin. Our results show the ease of use of sample preparation and measurements execution due to automatized and reliable localization of both cantilever tip and ZMW positions—making it possible to retrieve large datasets of simultaneous force extension and fluorescence spectroscopy events to permit the observation of rare, yet relevant, events.

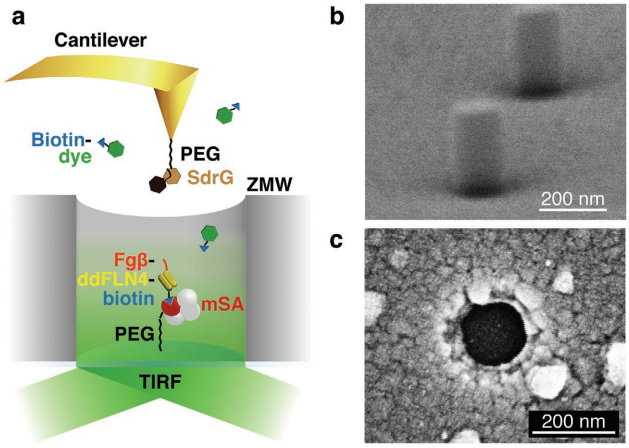

Figure 1. Experimental setup for singe molecule manipulation in a ZMW. a) The bottom of a ZMW displays mSA (functional subunit in red, nonfunctional in white) on top of a polyethylene glycol (PEG) spacing layer (black). ddFLN4 (yellow) serves as a force fingerprint and is attached to mSA via biotin (blue). The Fgβ–ddFLN4–biotin construct is specifically probed with an SdrG (brown) labeled AFM cantilever. Fluorescently labeled biotin (green and blue) is freely diffusing. As soon as the Fgβ–ddFLN4–biotin construct is pulled out of the mSA binding pocket, the now vacant biotin binding site is occupied by freely diffusing fluorescently labeled biotin molecules. Binding events are observed via a TIRF microscope from below. b) Reflection electron microscope diagonal view of a ZMW chip after development and prior to aluminum evaporation. Pillars of cross-linked photoresist form the negative base for the ZMWs. The image shows sharp edged pillars. c) Scanning electron microscope top-down view of ZMW cavity with 80 nm radius after the experiment.

2. Results and Discussion

2.1. Autonomous Probing and Noninvasive Tip Localization

A custom built TIRF AFM hybrid[17] was used as a basis allowing for a simultaneous three laser line excitation and according fluorescence readout. Additionally, the TIRF objective can be moved by a z-piezoactuator to change the focus for tip localization and ZMW probing. The chip, which in addition to the ZMW arrays has also micrometer-sized window cut-outs (5 µm × 5 µm) for tip alignment is located in between the TIRF objective to the bottom and the AFM head with cantilever to the top (**Figure 1**a). We chose TIRF over epifluorescence since in epi-illumination, these micrometer-sized windows would allow unobstructed light propagation through the complete height of the sample resulting in substantial photodamage of the sample.

At the beginning of a ZMW probing cycle the cantilever tip position is determined (**Figure 2**a) by recording the white light transillumination image of the tip above a micrometer-sized localization window. The resulting absorption profile of the tip is then fitted by a 2D Gaussian, defining via its centroid position the exact tip position relative to the frame of the optical microscope. As we had shown in a previous study, with this relatively simple technique the lateral position of the tip can be determined with nm precision.[18] We then position the tip in close proximity to the surface (100 nm) and shift the focus plane of the objective to the very tip of the cantilever. In our previous work we kept the cantilever in contact with the glass surface during image acquisition, which may damage the tip. The improved protocol used here allows long exposure times and thus high localization accuracy without impeding cantilever functionalization by prolonging tip surface contact times. This enables reliable tip localization without interfering with the functionalization of the cantilever. Subsequently, the focus plane is shifted to the bottom of the ZMW and the positioning of the ZMW is performed using its plasmonic transmission induced by top down white light illumination. The cavity is then aligned to the cantilever tip and cantilever approach is initiated. At this point, laser illumination is turned on and the retraction force curve is recorded synchronously with the fluorescent signal (Figure 2b). After the curve was recorded a new localization is initiated and the process repeats automatically.

Our localization routine allowed to successfully align and probe ZMWs with 80 nm cavity radii (Figure S2b, Supporting Information). In order to validate successful tip placement into ZMWs, the surface contact height of the cantilever measured by the AFMs z-piezoactuator was used to calculate the height difference between ZMW aluminum surface and cavity bottom (Figure S2a, Supporting Information). For automatization, all ZMWs to be probed and a micrometer sized rectangular localization window (Figure S2c, Supporting Information) were localized at the beginning of an experiment. The preliminary positions, derived in this way, served as initial seed for ZMW localization prior to the individual probing. To allow for stable long-term probing of ZMWs, an instrument drift correction was implemented. Each time the cantilever is localized anew, the white light transmission profile of the localization window was fitted. This fit provided the center position, which was then compared with the latest derived position of the localization

© 2020 The Authors. Published by WILEY-VCH Verlag GmbH & Co. KGaA, Weinheim

ADVANCED SCIENCE NEWS
www.advancedsciencenews.com

NANO · MICRO small
www.small-journal.com

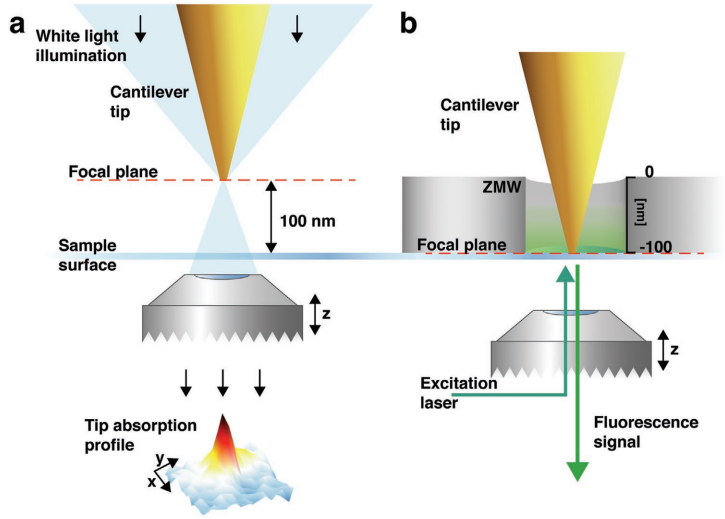

Figure 2. Precise tip localization and ZMW probing. a) Illustration of the precise cantilever tip localization procedure. The higher absorbance of light propagating through the tip is exploited which creates a distinct absorption profile. To prevent long surface contact time of the cantilever tip, acquisition of tip images is performed at a height of 100 nm above the glass surface. This allows long exposure and thus high photon yield without excessive surface contact time. The focal plane is changed by automatic movement of the objective to image the cantilever tip at 100 nm height above the surface. Tip localization is repeatedly performed during the course of an experiment. b) For ZMW probing, the objective which is mounted on a piezoactuator is vertically moved such that the focal plane coincides with the top of the glass surface plane forming the bottom of the ZMWs. After localization of the ZMW cavity by its plasmonic transmission the sample is moved horizontally to align the cantilever tip to the ZMW. Cantilever approach is initiated and laser illumination is provided through a TIRF microscope from below. During the course of an experiment, an autofocus routine corrects for vertical drift.

window. The deviation between these two values was used to correct the ZMWs preliminary positions in order to track the ZMWs despite horizontal drift. Drift in z-direction was compensated by an autofocus routine.

2.2. Blocked Monovalent Streptavidin as Force-Activated System

To test the performance of the autonomous probing setup, a monovalent streptavidin[19] (mSA) blocked with a biotinylated ligand construct (Figure 1a) was used as a force-activatable system. With a unique cysteine[16] localized at the C-terminus of its functional subunit, mSA was covalently attached to the glass bottom of the ZMWs. Its binding pocket was blocked with a peptide construct N-terminally featuring a short peptide from human fibrinogen β[20] (Fgβ), followed by a ddFLN4 fingerprint domain[21–23] and a C-terminal biotin. In order to force unbinding of the biotinylated construct from mSA, we used interaction of Fgβ binding to the adhesin SD-repeat protein G (SdrG)[20,24]—covalently anchored to the cantilever and much stronger than the mSA/biotin interaction. Thus, the Fgβ–ddFLN4–biotin construct blocking the mSA was removed and a biotinylated dye present in excess in the measurement buffer could bind to the now vacant mSA binding pocket, as the measurement buffer of phosphate buffered saline (PBS) was supplemented with 50×10^{-9} M Cy5-labeled biotin molecules. This binding was then recorded together with the force curve as described in the previous section. The Fgβ–ddFLN4–biotin bound to the SdrG on the cantilever dissociates within tens of seconds[25] freeing it to record the next curve. This provides cantilever regeneration in between probing for long-lasting cantilever durability. To stabilize fluorescence, the antiblinking reagent TROLOX[26] and the oxygen scavenging compounds pyranose oxidase and catalase were added.

2.3. Fabrication of Zero Mode Waveguides

Our ZMW chips were fabricated in-house and were composed of arrays of ZMW cavities with radii of 80 nm embedded in a 100 nm thick aluminum layer (Figure 1b,c). The substrate forming the bottom consisted of borosilicate glass. Besides these nanophotonic structures, we introduced additional micrometer sized rectangular windows to our chip design (Figure S2c, Supporting Information). These windows are crucial for a combined use of AFM and ZMWs since our AFM cantilever had to be optically aligned to the frame of the optical microscope prior to alignment of the cantilever tip to ZMW cavity. To assure protein immobilization only onto the glass bottom of the ZMW cavities a material selective passivation using polyvinylphosphonic acid was applied.[27]

© 2020 The Authors. Published by WILEY-VCH Verlag GmbH & Co. KGaA, Weinheim

ADVANCED SCIENCE NEWS
www.advancedsciencenews.com

NANO · MICRO small
www.small-journal.com

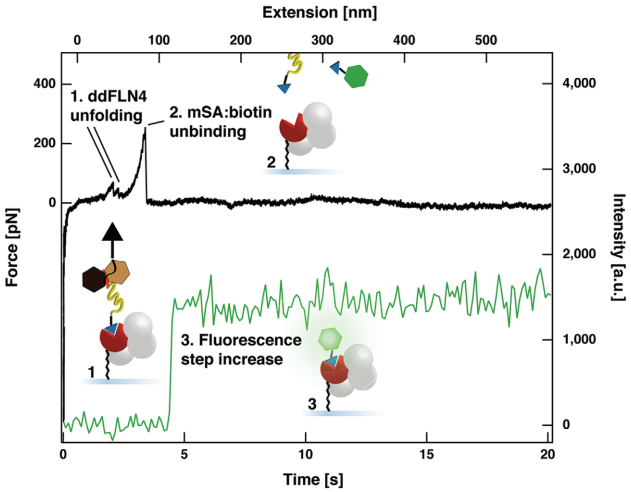

Figure 3. Force extension and fluorescence time traces for mechanical unblocking and binding event. Force versus extension curve and fluorescence intensity over time during cantilever retraction. At the zero time point the cantilever touched the bottom of the ZMW and cantilever retraction started with synchronized image acquisition. Resulting force versus extension curve (black; left and top axes) featuring the two step ddFLN4 fingerprint (yellow) unfolding (**1**) accompanied by mSA/biotin unbinding (**2**). The fluorescence signal (green; right and bottom axes) was background corrected and shows an intensity step increase (**3**) after the mSA/biotin unbinding. This step increase is attributed to a single labeled biotin binding to the now vacant mSA (**3**).

2.4. AFM-Based Single-Molecule Manipulation Experiments

We performed 505 automated mSA/biotin probing cycles inside ZMWs. In sum, 203 events constitute an interaction between cantilever tip and surface. 74 out of those probing events show successful ddFLN4 fingerprint unfolding accompanied by a biotin unbinding from mSA event (force vs extension, black graph in **Figure 3**). From these 74 events, 34 exhibit a single step increase (longer than 4.3 s) of fluorescence intensity without interruption after the unbinding event, seen in the fluorescence channel (intensity vs time, green graph in Figure 3). Combined graphs of force versus extension and fluorescence channel for each of the 34 events are shown in Figures S3–S8 of the Supporting Information. For these, fluorescence increases in a single step and stays high without stepwise drops in the ≈20 s observation time window. We attribute these 34 events to single labeled biotin binding to a mechanically vacated mSA. Upon retraction of the cantilever tip, first the ddFLN4 fingerprint unfolds (Figure 3 sequence 1) with its distinct two-step unfolding pattern. With further retraction of the cantilever tip, the biotin of the Fgβ–ddFLN4–biotin construct is dissociated from mSA (Figure 3 sequence 2). This frees the formerly blocked, single binding pocket of mSA making it accessible for binding of freely diffusing Cy5-labeled biotin molecules in solution at 50×10^{-9} M, observable by fluorescence increase in a single step (Figure 3 sequence 3). We also encounter multiple unfolding events (**Figure 4**c,d). These feature multiple inseparable ddFLN4 unfolding and biotin unbinding events. In these cases, we observe two consecutive steps of fluorescence intensity suggesting that we mechanically induce unblocking of multiple mSA molecules. These are then each able to bind a fluorescent biotin. In 17 cases we encountered fluorescence step increases for longer than 4 s without a prior and distinct unfolding event in the force extension channel. 6 out of these 17 events show a fluorescence step increase similar to the fluorescence traces of the 34 events but with no interaction in the force channel. They consist of a fluorescence step appearing after the AFM retraction phase (3 s) and continue to the end of the observation time window (20 s). The results of a passivation control experiment show that fluorescence steps exceeding 1 s caused by unspecific adsorption of Cy5-labeled biotin are very unlikely (cf. Table S9, Supporting Information) and cannot explain the origin of the 6 events described above.

Figure 4b shows a histogram of the time delay between biotin unbinding and the fluorescence step increase for the 34 events. The time difference between the peak force of biotin unbinding and the first time point of fluorescence step increase (Figure 4a) is plotted for each of the 34 events. Fitting a Poisson distribution for the probability of exactly one event occurring gives us a binding rate of 1.77 s^{-1}. Taking the free biotin concentration of 50×10^{-9} M into account yields a binding on-rate of $(3.5 \pm 0.2) \times 10^7$ M^{-1} s^{-1}—in reasonable agreement with the order of magnitude reported in previous studies of the on-rate (Buranda et al.:[28] 1.3×10^7 M^{-1} s^{-1}, Srisa-Art et al.:[29] 3.0×10^6 M^{-1} s^{-1} to 4.5×10^7 M^{-1} s^{-1}, Chivers et al.:[30] 2.0×10^7 M^{-1} s^{-1}).

3. Conclusion

We have established a method to routinely manipulate individual biomolecules inside ZMWs with an AFM cantilever. We showed that we are able to reliably guide the cantilever into a multitude of ZMWs with nanometer precision and thereby probe hundreds of molecules in the course of an experiment with yields of single molecule interactions in the range of 6.7–14.7% (34 of 505 events, 74 of 505 events) being well in line with conventional AFM-based SMFS yields (8%).[16] Due to ZMWs capability for exceptional fluorescence signal-to-noise, high fluorophore concentrations can be used. Additionally, our method drastically reduces the effort for combined SMFS and fluorescence experiments as its capability for running autonomous probing of ZMWs eliminates the need for manual control and monitoring.

Future investigation of force-mediated biochemical pathways of various proteins and enzymes, can readily be probed with our approach. Immobilization procedures can be adapted

© 2020 The Authors. Published by WILEY-VCH Verlag GmbH & Co. KGaA, Weinheim

ADVANCED SCIENCE NEWS
www.advancedsciencenews.com

NANO · MICRO small
www.small-journal.com

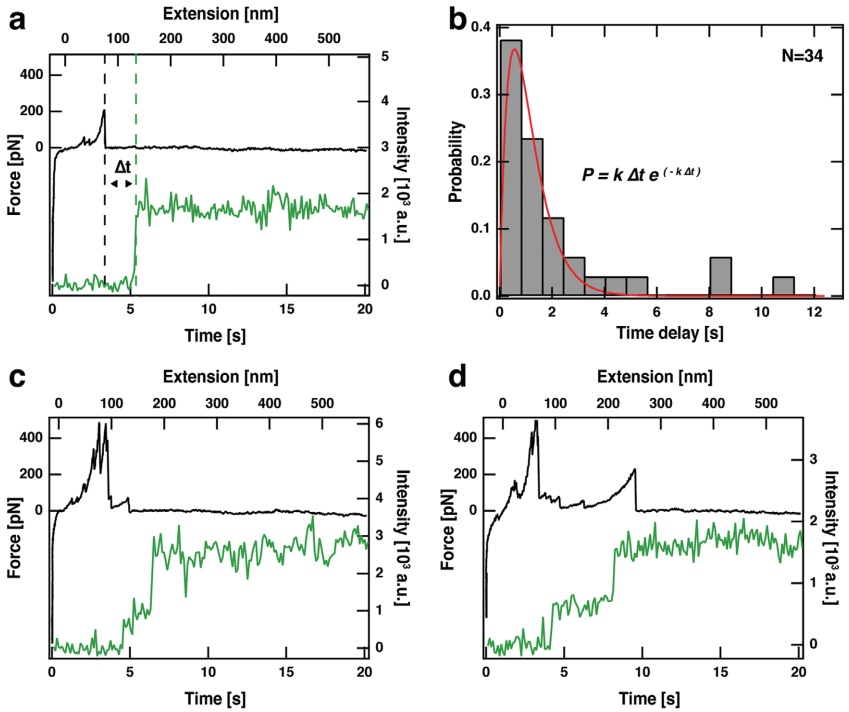

Figure 4. Time delay between biotin binding after mechanical unblocking and multiple unblocking events. a) The time to refill the empty biotin binding site in mSA was taken from the peak force (black dashed line) of biotin unbinding from mSA to the first time point of the fluorescence step increase (green dashed line). b) These time delays, time for a labeled biotin to bind to empty mSA, are plotted in a histogram and fitted by a Poisson distribution modeling the probability (P) for single event occurrence after certain time delays (Δt) with binding rate $k = 1.77\ s^{-1}$. c,d) During the experiments also multiple tether force patterns occurred with no clear ddFLN4 fingerprint, which were accompanied by multistep increase of fluorescence intensity. These were attributed to multiple biotins pulled out of multiple mSA. Thus, two labeled biotin binding events were observed, as apparent by the two-step fluorescence increase.

to site-specifically anchor other proteins to the bottom of the ZMW cavities, having the ligand fluorescently labeled in bulk solution. Thus, for example, in the field of mechanobiology, the unfolding of proteins bearing a possible cryptic binding site by SMFS and simultaneous observation of ligand binding to the subsequently exposed binding site can be studied to identify and characterize mechanosensors and to determine ligand on-rates. A system that could benefit is smooth muscle myosin light chain kinase for which experimental results recently showed new evidence that a potential force-driven activation pathway may exist.[31] Our method could be used to observe force-induced substrate binding and enzyme turnover benefiting from ZMWs ability to observe biological processes at high, up to micromolar, fluorophore concentrations (see Figure S1, Supporting Information). For other proteins, as for example in focal adhesions, which are assumed to bear force-regulatory functions our technique can help to characterize them by providing both biochemical and biomechanical information.[32,33] Our drift correcting, automated workflow, allows for measuring several days without interruption. This enables probing of an even larger number of ZMWs and will thus further improve statistical power.

Regarding systems requiring higher, micromolar concentrations, the inherent limitation is set by the aspect ratio of the cantilever tip. The crucial factor is not the size of the tip itself but the diameter of the cantilever at a distance of 100 nm above the tip. The ZMWs have a height of 100 nm and a cantilever tip has to fit into the ZMW in order to probe its bottom. This limits the diameter of the ZMWs which in turn sets a limit to the concentration applicable. Thus, in order to investigate these systems, high aspect ratio cantilevers have to be used to decrease ZMW diameters on a further developed setup. Quite generally the option to mechanically trigger a biomolecular reaction and then follow its progress by fluorescent readout will allow the recording of time traces of the reaction at the level of individual molecules in a coherent and synchronized manner, in this case with maximum sensitivity and minimum background.

© 2020 The Authors. Published by WILEY-VCH Verlag GmbH & Co. KGaA, Weinheim

ADVANCED SCIENCE NEWS
www.advancedsciencenews.com

NANO · MICRO small
www.small-journal.com

4. Experimental Section

ZMW Fabrication: Arrays of aluminum ZMWs and the additional structural features were patterned using negative electron-beam lithography. For this purpose, borosilicate coverslips (Menzel Gläser, Braunschweig, Germany) measuring 22 mm in diameter were thoroughly cleaned, exposed to an oxygen plasma and dried at 200 °C for 30 min. Then, they were successively spin-coated with an adhesion promoter (Surpass4000, micro resist technology, Berlin, Germany), isopropanol, and a negative tone resist (ma-N 2403, micro resist technology, Berlin, Germany). Subsequently, they were covered with a conductive silver layer. The negative pattern was then imprinted using electron beam lithography (eLINE, Raith GmbH, Dortmund, Germany). The conductive silver layer was removed using gold etchant. Following development with ma-D 525 (micro resist technology, Berlin, Germany), which exposed the cross-linked tone resist structures and pillars (Figure 1b), a 100 nm thick aluminum layer was evaporated onto the chip. Lift-off was carried out in dimethyl sulfoxide accompanied by ultrasound sonication followed by exposure to an oxygen plasma.

Besides arrays of ZMW, additional structures were incorporated in the chip design providing large (185 µm × 45 µm) and smaller (5 µm × 5 µm) rectangular windows for coarse and fine alignment of cantilever relative to TIRF optics.

Dimension and shape of the individual ZMWs were verified by reflection and scanning electron microscope images of both negative ZMW pillars prior aluminum deposition (Figure 1b) and completed ZMW cavities with 80 nm radius (Figure 1c).

Preparation of Proteins: The mSA molecules with its C-terminal cysteine and the Fgβ–ddFLN4–ybbR construct were expressed as described by Sedlak et al.[16] SdrG was expressed as described by Milles et al.[20]

Surface Functionalization: To assure protein immobilization only onto the glass bottom of the ZMWs a material-selective passivation using 2% (v/v) polyvinylphosphonic acid (Polysciences Europe GmbH, Hirschberg, Germany) solution was applied.[27] The ZMW chip was cleaned inside a UV cleaner and then immersed in 90 °C 2% (v/v) polyvinylphosphonic acid solution for 2 min. Then immersed in ultrapure H_2O, dried at 80 °C for 10 min and successively washed in ultrapure H_2O, methanol, and ultrapure H_2O. Following this, the chip was first soaked in (3-Aminopropyl)dimethylethoxysilane (ABCR, Karlsruhe, Germany) 1.8% (v/v) in ethanol for 1 h, then washed in ethanol and ultrapure H_2O and baked at 80 °C for 1 h. A bifunctional polyethylene glycol (PEG) linker displaying a maleimide group was used for effective protein coupling. For this the ZMW chip was incubated with a mixture of NHS-PEG-Methyl (25×10^{-3} M, molecular weight 333 g mol^{-1}, Thermo Fisher Scientific, Waltham, MA, USA) and NHS-PEG-Maleimide (2.5×10^{-3} M, molecular weight 513.5 g mol^{-1}, Thermo Fisher Scientific, Waltham, MA, USA) in HEPES (100×10^{-3} M, pH 7.5).

mSA was coupled via the unique C-terminal cysteine of its single functional subunit to maleimide displayed by the PEG spacing layer in coupling buffer (50×10^{-3} M sodium phosphate pH 7.2, 50×10^{-3} M NaCl, 10×10^{-3} M EDTA, 0.05% (v/v) Tween 20) for 1 h and then thoroughly washed with PBS (pH 7.4, Merck, Darmstadt, Germany). The ybbR-tag of the Fgβ–ddFLN4–ybbR construct was used to enzymatically couple a Coenzyme A-tagged biotin molecule utilizing the phosphopantetheinyl transferase Sfp.[34] The enzymatic reaction was performed at 37 °C for 1 h. Two spin desalting columns (molecular weight cut-off 7 kDa, Zeba, Thermo Fisher Scientific, Waltham, MA, USA) were used to remove excess biotin. 100×10^{-9} M of the Fgβ–ddFLN4–biotin was applied to saturate the mSA surface for 30 min. Unbound Fgβ–ddFLN4–biotin was washed away with PBS. For the surface passivation control experiment the ZMW chip was treated the way described above. However, this time a different PEG linker NHS-PEG-Methyl (25×10^{-3} M, molecular weight 5000 g mol^{-1}, Rapp Polymere, Tübingen, Germany) in HEPES (100×10^{-3} M, pH 7.5) was used. Protein immobilization was omitted and surfaces were treated with 0.05% (v/v) Tween 20 prior to thoroughly washing with PBS.

Cantilever Functionalization: Cantilevers, BioLever mini (Olympus Corporation, Tokyo, Japan), displayed SdrG and were prepared as described by Sedlak et al.[16]

Experiment Buffer: The measurement buffer was composed of PBS (pH 7.4) with 1×10^{-3} M TROLOX ((±)-6-Hydroxy-2,5,7,8-tetramethylchromane-2-carboxylic acid, Merck, Darmstadt, Germany) and an oxygen scavenger system comprised of 0.6% (w/v) D-glucose, pyranose-oxidase (7.5 U mL^{-1}, E.C. 1.1.3.10), and Catalase (1700 U mL^{-1}, E.C 1.11.1.6) (PODCAT). Here, pyranose-oxidase proved to be more suitable than, e.g., glucose-oxidase since products of pyranose-oxidase catalyzed glucose turnover affects pH to a much less extent.[35] TROLOX served as antiblinking reagent.[26] Together, TROLOX and PODCAT provided stable and long-lasting fluorescence conditions with low bleaching and blinking. Cy5-labeled biotin (Click Chemistry tools, Scottsdale, USA) was used as the freely diffusing fluorescent biotin compound.

AFM-Based Single-Molecule Manipulation Experiments: The start of the retraction cycle with the start of image acquisition was synchronized by using a pulse signal output from the AFM controller to externally control the EM-CCD camera. In this way, fluorescence readout and force distance data acquisition started simultaneously. Images were taken with an exposure time of 100 ms which resulted in an effective frame rate of 106.7 ms. For ZMW probing, cantilever approach was carried out at 3000 nm s^{-1} velocity and retraction was performed at 30 nm s^{-1} at a sampling rate of 1500 Hz to a complete cantilever to surface distance of 550 nm. Conducting the 505 probing cycles took 5.3 h. Cy5 with a 640 nm line of a 43 mW diode laser (iChrome MLE-S, Toptica, Graefelfing, Germany) was excited by total internal reflection.

Cantilever localization was carried out in a 5 µm x 5 µm glass window within the aluminum cladding. Therefore, the cantilever was approached at 3000 nm s^{-1} to the surface and immediately retracted at 2000 nm s^{-1} to a cantilever to surface distance of 100 nm. Image acquisition was performed with 30 ms exposure time at an effective frame rate of 36.8 ms.

In order to align the cantilever tip to a single ZMW carrying out the autofocus routine took 8 s. Then the cantilever was moved above a localization window and cantilever tip localization was performed. The tip position was fitted and the horizontal drift was corrected using the absolute position of the localization window. This took roughly 7 s. Aligning the cantilever tip to a single ZMW was performed within 9 s. All these steps (total duration 24 s) were necessary to probe the bottom of a single ZMW. However, when probing ZMW sequentially, cantilever tip localization and autofocus were only necessary every 6th and 12th time, respectively, thereby reducing alignment times to 18 s and accelerating data acquisition. SMFS routine for the AFM controller, MFP3D (Asylum Research, Santa Barbara, CA, USA), and software for AFM-based single-molecule manipulation experiments were self-written in IGOR Pro 6 (WaveMetrics, OR, USA).

Supporting Information

Supporting Information is available from the Wiley Online Library or from the author.

Acknowledgements

The authors thank P. Altpeter and T. Nicolaus for laboratory support, L. F. Milles for substantial discussions and for providing the SdrG/Fgβ-system, and E. Durner and F. Baumann for experimental setup support. This work was funded by the Deutsche Forschungsgemeinschaft (DFG, German Research Foundation) under Project-ID 201269156–SFB 1032.

Conflict of Interest

The authors declare no conflict of interest.

© 2020 The Authors. Published by WILEY-VCH Verlag GmbH & Co. KGaA, Weinheim

ADVANCED SCIENCE NEWS
www.advancedsciencenews.com

NANO · MICRO small
www.small-journal.com

Author Contributions

L.C.S. performed and analyzed single-molecule force and fluorescence spectroscopy experiments. L.C.S. fabricated and analyzed ZMW chips. L.C.S. modified and enhanced experimental setup and wrote automatization software. S.M.S. and L.C.S. prepared protein constructs. H.E.G. supervised the study. L.C.S. and M.S.B. drafted the manuscript. All authors contributed with writing the final version of the manuscript.

Keywords

force activation, mechanosensing, single-molecule fluorescence, zero mode waveguides

Received: December 2, 2019
Revised: February 8, 2020
Published online: March 5, 2020

[1] A. Sarkar, R. B. Robertson, J. M. Fernandez, *Proc. Natl. Acad. Sci. USA* **2004**, *101*, 12882.
[2] S. K. Kufer, M. Strackharn, S. W. Stahl, H. Gumpp, E. M. Puchner, H. E. Gaub, *Nat. Nanotechnol.* **2009**, *4*, 45.
[3] Y. He, M. Lu, J. Cao, H. P. Lu, *ACS Nano* **2012**, *6*, 1221.
[4] K. Maki, S.-W. Han, Y. Hirano, S. Yonemura, T. Hakoshima, T. Adachi, *Sci. Rep.* **2018**, *8*, 1575.
[5] K. R. Erlich, S. M. Sedlak, M. A. Jobst, L. F. Milles, H. E. Gaub, *Nanoscale* **2019**, *11*, 407.
[6] R. Jöhr, M. S. Bauer, L. C. Schendel, C. Kluger, H. E. Gaub, *Nano Lett.* **2019**, *19*, 3176.
[7] A. M. van Oijen, *Curr. Opin. Biotechnol.* **2011**, *22*, 75.
[8] M. J. Levene, J. Korlach, S. W. Turner, M. Foquet, H. G. Craighead, W. W. Webb, *Science* **2003**, *299*, 682.
[9] J. Eid, A. Fehr, J. Gray, K. Luong, J. Lyle, G. Otto, P. Peluso, D. Rank, P. Baybayan, B. Bettman, A. Bibillo, K. Bjornson, B. Chaudhuri, F. Christians, R. Cicero, S. Clark, R. Dalal, A. deWinter, J. Dixon, M. Foquet, A. Gaertner, P. Hardenbol, C. Heiner, K. Hester, D. Holden, G. Kearns, X. Kong, R. Kuse, Y. Lacroix, S. Lin, P. Lundquist, C. Ma, P. Marks, M. Maxham, D. Murphy, I. Park, T. Pham, M. Phillips, J. Roy, R. Sebra, G. Shen, J. Sorenson, A. Tomaney, K. Travers, M. Trulson, J. Vieceli, J. Wegener, D. Wu, A. Yang, D. Zaccarin, P. Zhao, F. Zhong, J. Korlach, S. Turner, *Science* **2009**, *323*, 133.
[10] J. Chen, R. V. Dalal, A. N. Petrov, A. Tsai, S. E. O'Leary, K. Chapin, J. Cheng, M. Ewan, P.-L. Hsiung, P. Lundquist, S. W. Turner, D. R. Hsu, J. D. Puglisi, *Proc. Natl. Acad. Sci. USA* **2014**, *111*, 664.
[11] K. T. Samiee, M. Foquet, L. Guo, E. C. Cox, H. G. Craighead, *Biophys. J.* **2005**, *88*, 2145.
[12] T. Miyake, T. Tanii, H. Sonobe, R. Akahori, N. Shimamoto, T. Ueno, T. Funatsu, I. Ohdomari, *Anal. Chem.* **2008**, *80*, 6018.
[13] S. F. Heucke, E. M. Puchner, S. W. Stahl, A. W. Holleitner, H. E. Gaub, P. Tinnefeld, *Int. J. Nanotechnol.* **2013**, *10*, 607.
[14] S. F. Heucke, F. Baumann, G. P. Acuna, P. M. D. Severin, S. W. Stahl, M. Strackharn, I. H. Stein, P. Altpeter, P. Tinnefeld, H. E. Gaub, *Nano Lett.* **2014**, *14*, 391.
[15] S. M. Sedlak, M. S. Bauer, C. Kluger, L. C. Schendel, L. F. Milles, D. A. Pippig, H. E. Gaub, *PLoS One* **2017**, *12*, e0188722.
[16] S. M. Sedlak, L. C. Schendel, M. C. R. Melo, D. A. Pippig, Z. Luthey-Schulten, H. E. Gaub, R. C. Bernardi, *Nano Lett.* **2019**, *19*, 3415.
[17] H. Gumpp, S. W. Stahl, M. Strackharn, E. M. Puchner, H. E. Gaub, *Rev. Sci. Instrum.* **2009**, *80*, 063704.
[18] F. Baumann, S. F. Heucke, D. A. Pippig, H. E. Gaub, *Rev. Sci. Instrum.* **2015**, *86*, 035109.
[19] M. Howarth, D. J. F. Chinnapen, K. Gerrow, P. C. Dorrestein, M. R. Grandy, N. L. Kelleher, A. El-Husseini, A. Y. Ting, *Nat. Methods* **2006**, *3*, 267.
[20] L. F. Milles, K. Schulten, H. E. Gaub, R. C. Bernardi, *Science* **2018**, *359*, 1527.
[21] I. Schwaiger, A. Kardinal, M. Schleicher, A. A. Noegel, M. Rief, *Nat. Struct. Mol. Biol.* **2004**, *11*, 81.
[22] L. F. Milles, E. A. Bayer, M. A. Nash, H. E. Gaub, *J. Phys. Chem. B* *121*, 3620, **2017**.
[23] M. S. Bauer, L. F. Milles, S. M. Sedlak, H. E. Gaub, *bioRxiv* **2018**, 276444.
[24] P. Herman, S. El-Kirat-Chatel, A. Beaussart, J. A. Geoghegan, T. J. Foster, Y. F. Dufrêne, *Mol. Microbiol.* **2014**, *93*, 356.
[25] K. Ponnuraj, M. G. Bowden, S. Davis, S. Gurusiddappa, D. Moore, D. Choe, Y. Xu, M. Hook, S. V. L. Narayana, *Cell* **2003**, *115*, 217.
[26] T. Cordes, J. Vogelsang, P. Tinnefeld, *J. Am. Chem. Soc.* **2009**, *131*, 5018.
[27] J. Korlach, P. J. Marks, R. L. Cicero, J. J. Gray, D. L. Murphy, D. B. Roitman, T. T. Pham, G. A. Otto, M. Foquet, S. W. Turner, *Proc. Natl. Acad. Sci. USA* **2008**, *105*, 1176.
[28] T. Buranda, G. M. Jones, J. P. Nolan, J. Keij, G. P. Lopez, L. A. Sklar, *J. Phys. Chem. B* **1999**, *103*, 3399.
[29] M. Srisa-Art, E. C. Dyson, A. J. deMello, J. B. Edel, *Anal. Chem.* **2008**, *80*, 7063.
[30] C. E. Chivers, E. Crozat, C. Chu, V. T. Moy, D. J. Sherratt, M. Howarth, *Nat. Methods* **2010**, *7*, 391.
[31] F. Baumann, M. S. Bauer, M. Rees, A. Alexandrovich, M. Gautel, D. A. Pippig, H. E. Gaub, *eLife* **2017**, *6*, e26473.
[32] V. Vogel, *Annu. Rev. Biophys. Biomol. Struct.* **2006**, *35*, 459.
[33] M. S. Bauer, F. Baumann, C. Daday, P. Redondo, E. Durner, M. A. Jobst, L. F. Milles, D. Mercadante, D. A. Pippig, H. E. Gaub, F. Gräter, D. Lietha, *Proc. Natl. Acad. Sci. USA* **2019**, *116*, 6766.
[34] J. Yin, P. D. Straight, S. M. McLoughlin, Z. Zhou, A. J. Lin, D. E. Golan, N. L. Kelleher, R. Kolter, C. T. Walsh, *Proc. Natl. Acad. Sci. USA* **2005**, *102*, 15815.
[35] M. Swoboda, J. Henig, H. M. Cheng, D. Brugger, D. Haltrich, N. Plumere, M. Schlierf, *ACS Nano* **2012**, *6*, 6364.

© 2020 The Authors. Published by WILEY-VCH Verlag GmbH & Co. KGaA, Weinheim

Copyright WILEY-VCH Verlag GmbH & Co. KGaA, 69469 Weinheim, Germany, 2020.

NANO MICRO small

Supporting Information

for *Small*, DOI: 10.1002/smll.201906740

Single-Molecule Manipulation in Zero-Mode Waveguides

*Leonard C. Schendel, Magnus S. Bauer, Steffen M. Sedlak, and Hermann E. Gaub**

WILEY-VCH

Copyright WILEY-VCH Verlag GmbH & Co. KGaA, 69469 Weinheim, Germany, 2020.

Supporting Information

Single Molecule Manipulation in Zero Mode Waveguides

*Leonard C. Schendel, Magnus S. Bauer, Steffen M. Sedlak, and Hermann E. Gaub**

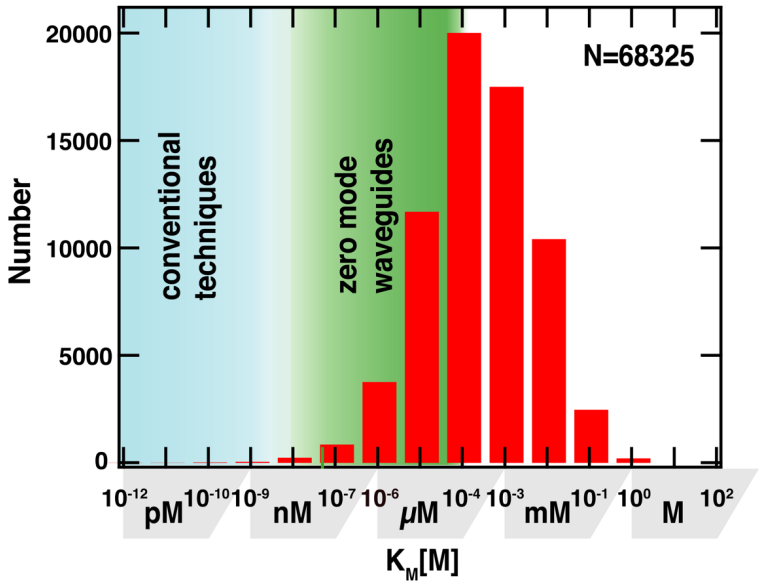

Figure S1: Histogram of Michaelis constants (K_M) for 68325 enzyme substrate pairs.

K_M for 68325 enzyme substrate pairs were taken from BRENDA enzyme database[1] (www.brenda-enzymes.org) representing an updated histogram as seen in Samiee et al.[2] Biological processes take place in dense environments with micromolar substrate concentrations. In this context, the K_M serves as inverse measure of the affinity of the substrate for the enzyme and in this way indicates substrate concentrations needed to be able to observe enzyme substrate recruitment in sufficient quantity. Above 1 nM to 10 nM fluorescent substrate concentration conventional imaging techniques like TIRFM lack adequate signal-to-noise in order to resolve single molecules. ZMWs, however, allow

experiments with higher substrate concentrations and, thereby, make it possible to observe substrate enzyme recruitment events in high yield. For a combined use with AFM it the aspect ratio of the cantilever limits the minimal ZMW radius and thereby the highest applicable substrate concentrations. Green bar indicates K_M value of 50 nM.

WILEY-VCH

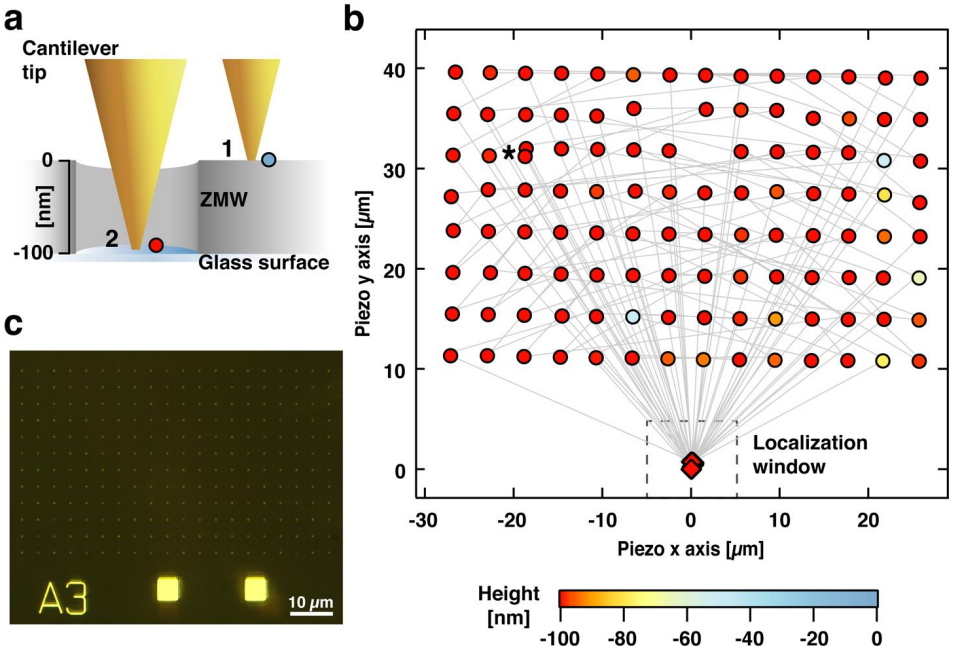

Figure S2: Tip localization and ZMW probing.

a, In order to validate successful tip placement into ZMWs the cantilever is first approached onto the aluminum surface in proximity to the ZMW to be probed (**1**). Then the ZMW chip is moved such that the cantilever tip coincides with the ZMW cavity (**2**). The difference between the two surface contact positions measured by the AFM's z-piezo actuator gives the immersion depth of the cantilever tip. **b**, Excerpt of a ZMW probing experiment. Circles show positions of probing inside ZMWs. The color of the circles indicates the immersion depth of the cantilever measured by additional probing the aluminum surface adjacent to each ZMW position. Grey lines illustrate the path of the cantilever tip during probing and localization routines. A grey dashed rectangle shows the position of the localization window where the cantilever localization routines were performed (red diamonds). Two ZMW fell below brightness threshold at preliminary ZMW positioning and were excluded from probing. The asterisk (*****) marks the position at which the AFM head was lifted and repositioned which lead

to a small artificial drift. The drift correction routine was able to again successfully align the cantilever tip to the ZMW probed beforehand and to continue probing of the remaining ZMWs. **c**, Image taken by a light microscope shows a typical subarray of a ZMW chip with rectangular windows used for tip localization adjacent to an array of ZMWs.

WILEY-VCH

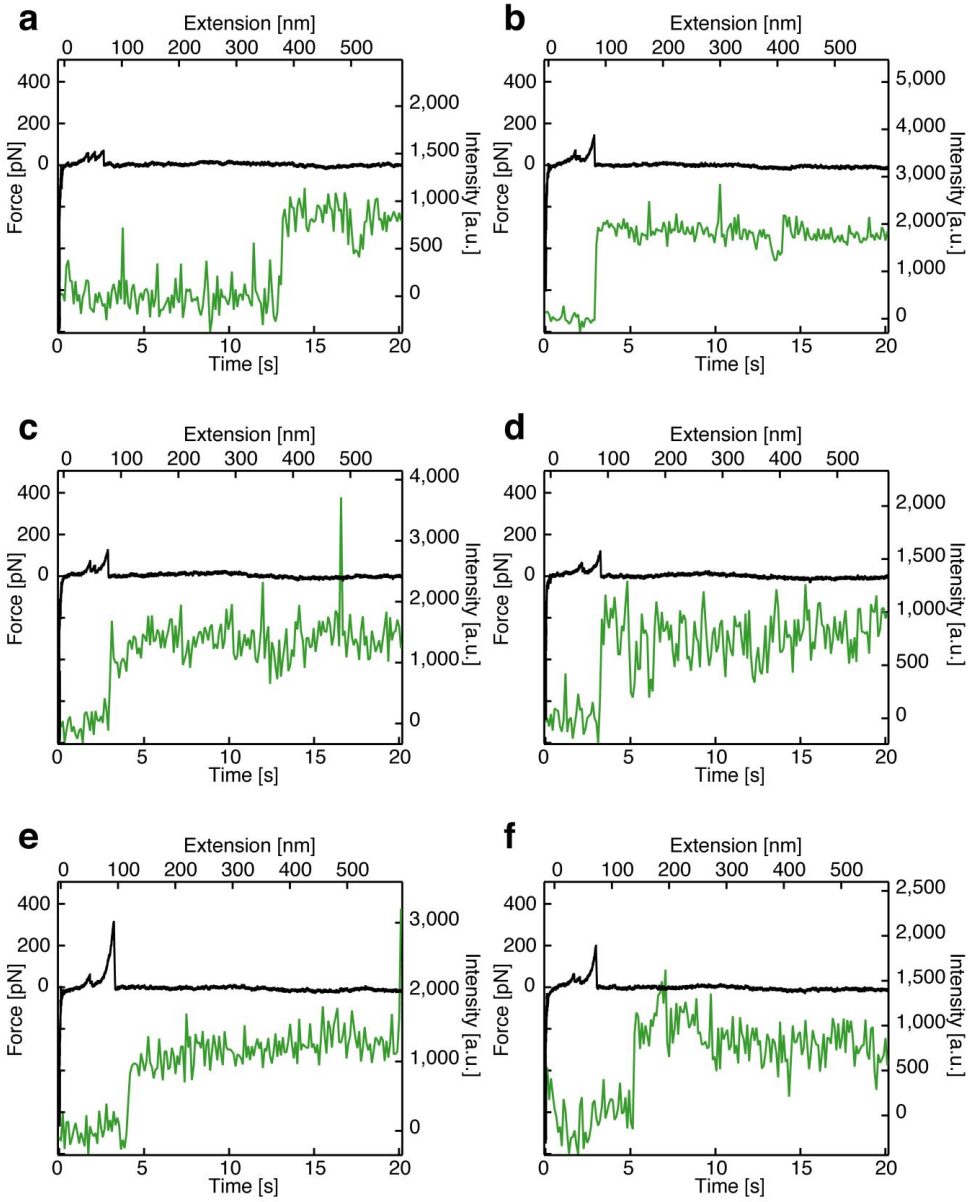

Figure S3: Specific force fingerprint and fluorescence step increase events.

WILEY-VCH

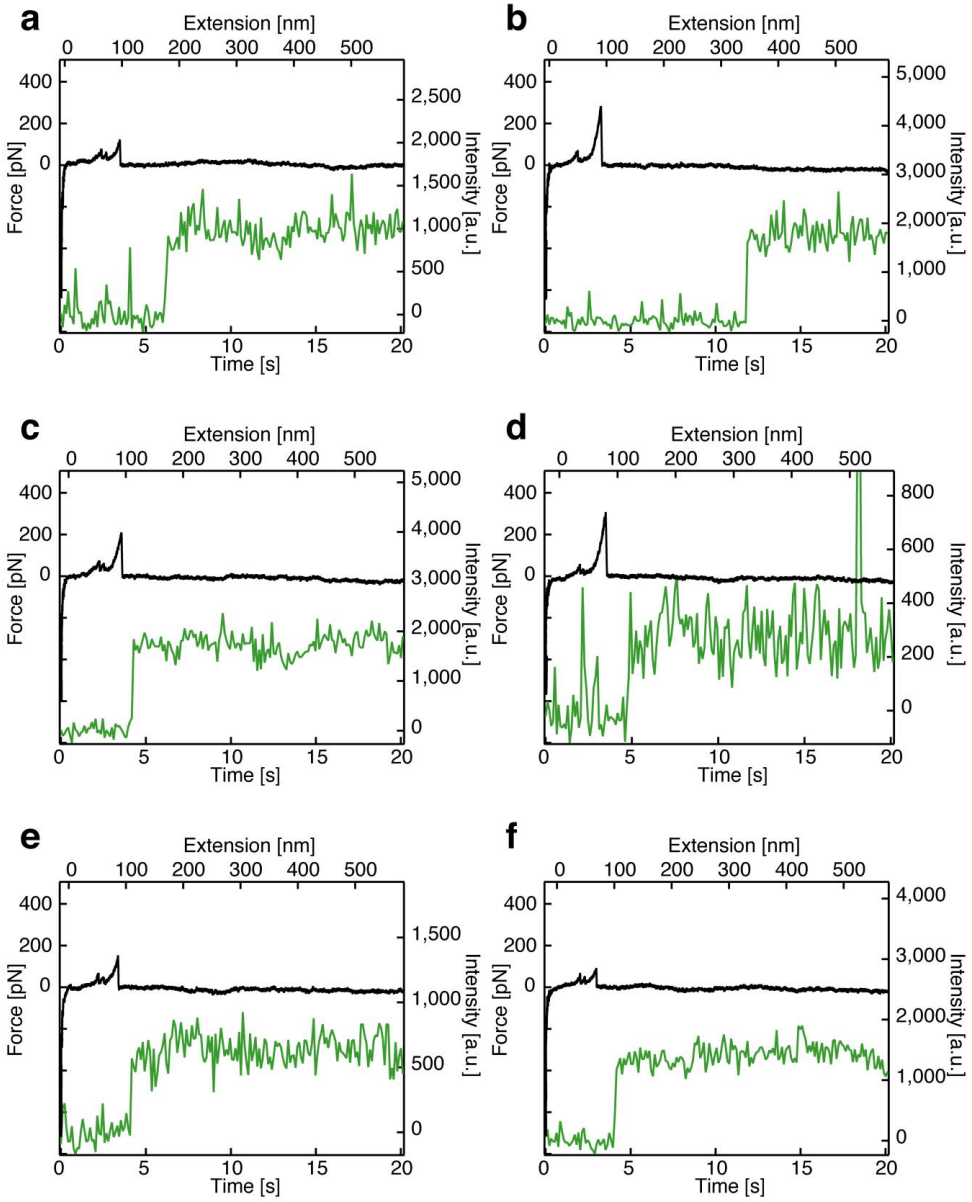

Figure S4: Specific force fingerprint and fluorescence step increase events.

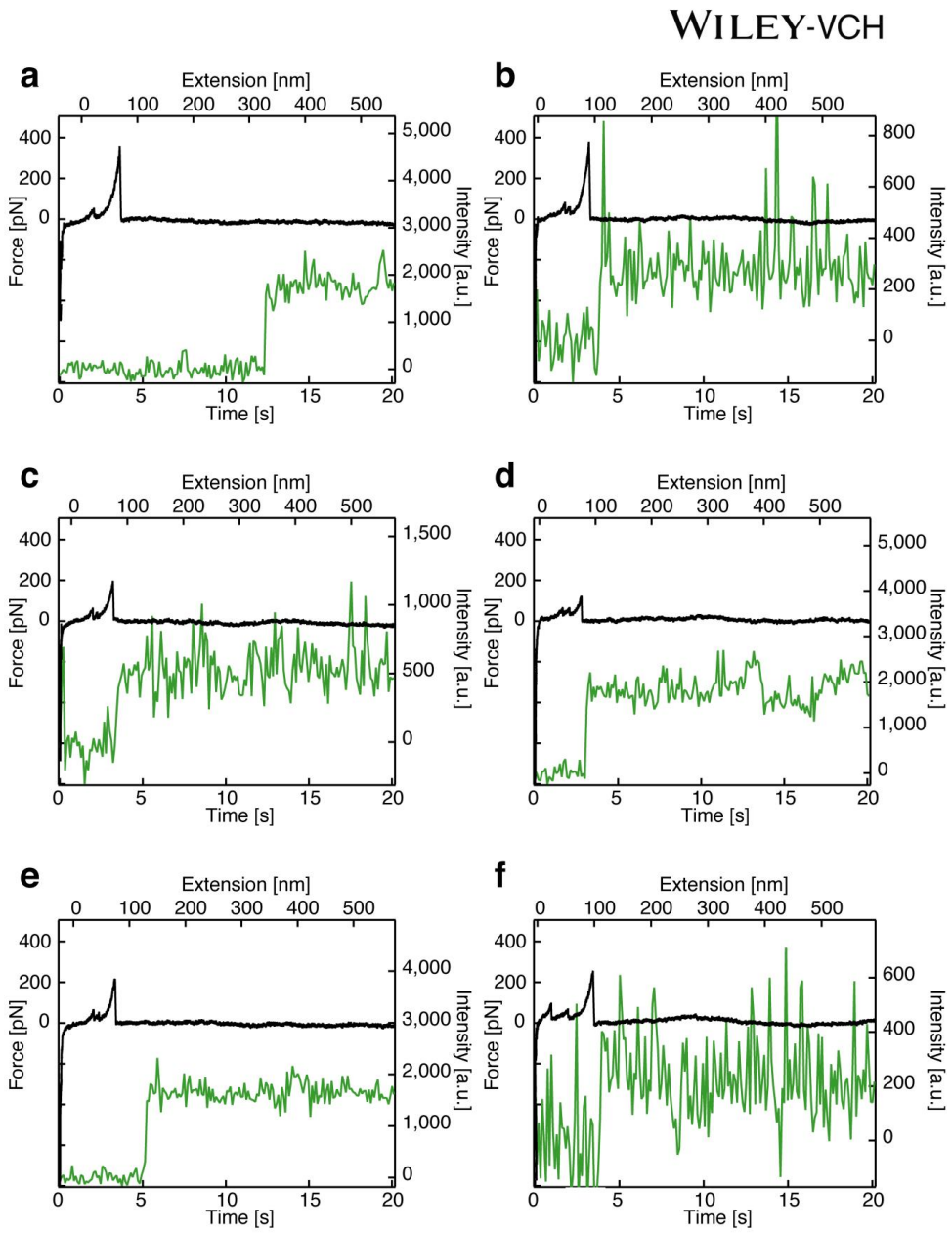

Figure S5: Specific force fingerprint and fluorescence step increase events.

WILEY-VCH

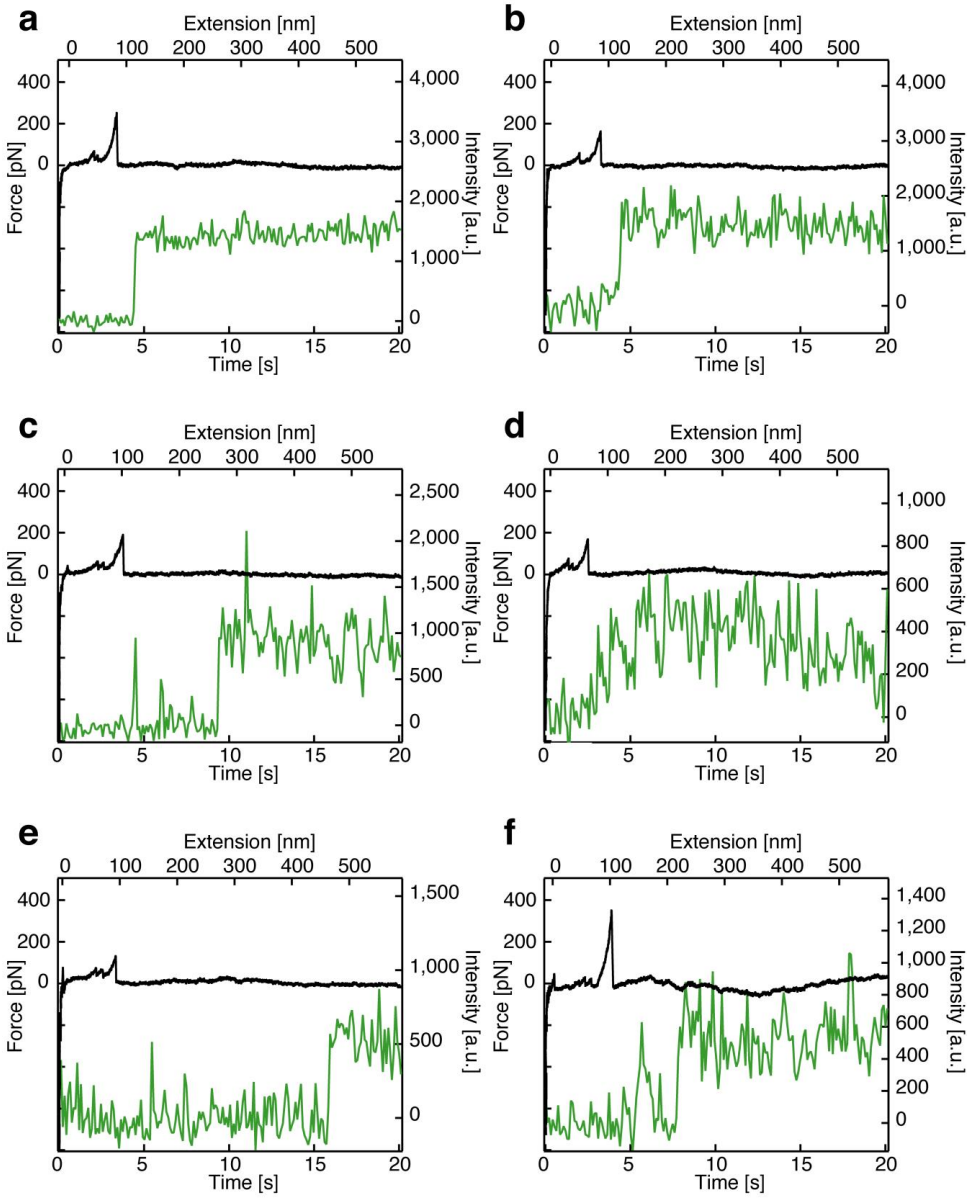

Figure S6: Specific force fingerprint and fluorescence step increase events.

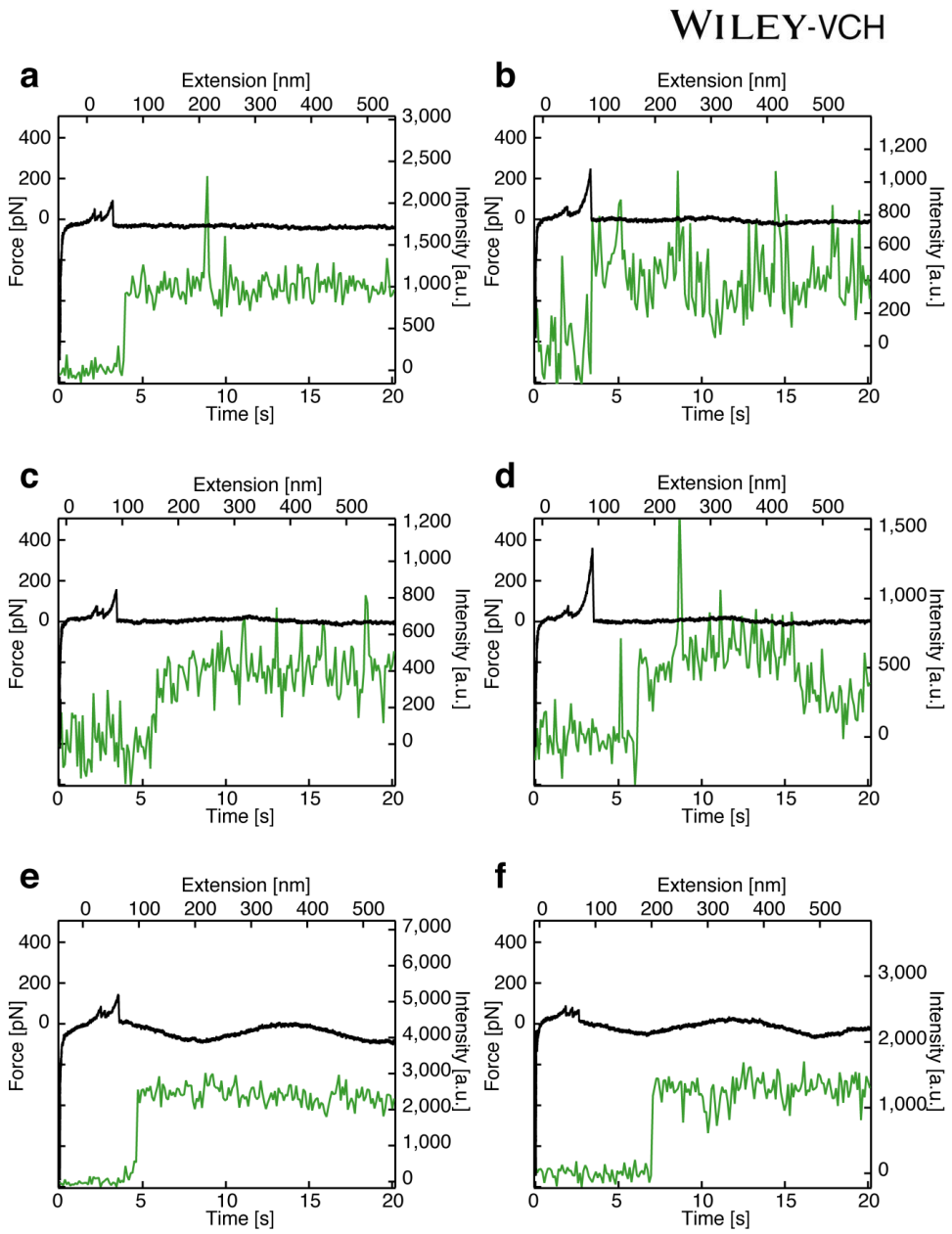

Figure S7: Specific force fingerprint and fluorescence step increase events.

e,**f**, Force curves are distorted by interference of the AFM's infrared laser. This occurs only when the part of the cantilever which deflects the IR-beam is located above localization windows, in a way that the inclinations of cantilever and window's aluminum edges coincide.

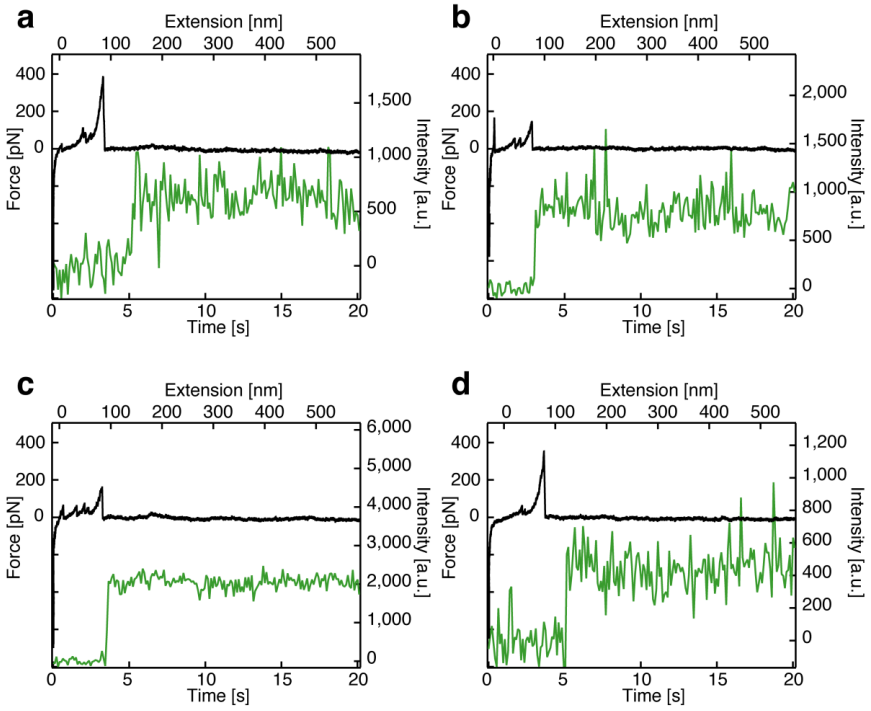

Figure S8: Specific force fingerprint and fluorescence step increase events.

Peak duration [s]	Number of events	Relative frequency λ [s^{-1}]	$(1-e^{(20\ s\ \lambda)})$
$0.2 < t_D$	60	2.8×10^{-3}	5.5 %
$0.4 < t_D$	13	6.1×10^{-4}	1.2 %
$0.8 < t_D$	3	1.4×10^{-4}	0.28 %
$1 < t_D$	2	9.3×10^{-5}	0.19 %
$1.3 < t_D$	0	0	0

Table S9: Results from a surface passivation control measurement. Cy5 labeled biotin was observed for 180 s through 119 ZMWs. Imaging settings and experimental buffer were the same as for combined ZMW-AFM experiments. This yields an accumulated observation time of 21407 s (5.9 h). Peaks with average intensities higher than the smallest fluorescence step considered in combined ZMW-AFM experiments were identified as fluorescence step with duration t_D. No peaks were found to last longer than 1.3 s. The last column shows the probability for at least 1 event occurring within 20 s observation time window as used in combined ZMW-AFM experiments.

Supporting References

[1] Jeske, L.; Placzek, S.; Schomburg, I.; Chang, A.; Schomburg, D., *Nucleic Acids Research* **2018,** *47* (D1), D542-D549. DOI 10.1093/nar/gky1048.

[2] Samiee, K. T.; Foquet, M.; Guo, L.; Cox, E. C.; Craighead, H. G., *Biophys J* **2005,** *88* (3), 2145-2153. DOI 10.1529/biophysj.104.052795.

Part IV

Conclusion and Outlook

Conclusion and Outlook

One central objective of this work was to provide new insights into the mechanostability of one of biotechnology's most abundantly used receptor-ligand complex, SA-biotin. Two different site-specific tethering geometries were investigated using SMFS, revealing a twofold difference in complex rupture forces. Complemented with all-atom steered molecular dynamics simulation, it was possible to gain a better understanding of what effect different pulling geometries have on the unbinding pathway. The conducted simulations confirmed the existence of the two unbinding modes and revealed that for the case of N-terminal tethering, low-force unbinding events are accompanied by partial unfolding of the associated SA subunit. Whereas for C-terminal tethering, forced dissociation resembles a rupture process, for N-terminal tethering, a local unfolding is responsible for the lower forces of complex separation. Inspired by this low force unbinding mode, an attempt to reinforce the local structure of the SA subunit by inserting a covalent bond, which connects the two concerned β-strands, showed a substantial increase in unbinding force. With the inserted covalent connection allowing to switch between open and closed, it was possible to change the unbinding forces between the two modes. These results provided experimental confirmation of the successful prevention of partial unfolding as predicted by steered molecular dynamics simulation. Only the close hand-in-hand work of *in silico* and *in vitro* SMFS made it possible to provide this detailed picture of unbinding mechanics of the SA-biotin complex, and exemplified how closely unbinding and unfolding processes can be intertwined. In a more general way, this experimental confirmation further demonstrates the power of *in silico* protein investigation and engineering, which will become increasingly important given the fact that in our globalized world humanity will have to face fast spreading epidemics of yet unknown pathogens.

In addition, within the context of this thesis, it was possible to develop an automated combined fluorescent SMFS setup by tackling persistent challenges of earlier approaches. The performance of this setup, in terms of investigating and identifying proteins which bear force regulatory functions, could be assessed by using SA-biotin along with a proxy receptor-ligand as a model system. Stable and automated measurement routines together with a revised cantilever localization enabled long measurements without the need of external supervision. In this way, the potential for acquiring large datasets could be shown. ZMWs have already been shown feasible to operate in fluorescence substrate concentrations of hundreds of nanomolar up to micromolar in several other studies. Here, one inherent limit for a combined use of ZMWs and AFM is set by the aspect ratio of the cantilever tip and allows additional optimization. Further enhancement of automation routines has the potential to reduce the duration for single ZMW approach-retraction cycles, thereby accelerating data acquisition. Such an acceleration combined with long-term measurements will

increase future data yields to further improve statistical power. The combination of ZMWs and SMFS by AFM may readily contribute to probing of a variety of different mechanosensory protein systems and bears the potential to cover new grounds in the field of mechanobiology.

Part V

Appendix

Chapter 5
Further Publications

5.1 Publication P4: Monodisperse Measurement of the Biotin-Streptavidin Interaction Strength in a Well-Defined Pulling Geometry

SA is known for its high affinity to the small molecule biotin and is therefore abundantly used in many disciplines. However, its tetravent nature, resulting in a polydisperse rupture force distribution, is not beneficial for the purpose of SMFS. With force propagation being spread all over the tetramer, due to SA's capability to bind four biotins and due to diverse tethering possibilities, the aforementioned polydispersity arises. An SA featuring monodisperse behavior would, in this way, be superior for many approaches like nanoparticle functionalization and SMFS.

In this publication, the single functional subunit of mSA was genetically equipped with a cysteine molecule which provides a unique site for specific tethering. In this way, biotin binding and rupture are associated to the binding pocket of the subunit which is tethered to the sample surface. Thus, the variety of possible pulling geometries is reduced to a single one. This genetically engineered SA thereby retains its functionality to bind biotin with unaltered affinity. Experimental results of AFM-based SMFS on this mSA-biotin complex showed monodisperse and narrow rupture force distributions for differing loading rates, with most-probable rupture forces between 200 pN and 230 pN at force-loading rates which ranged from 1.5 nN s^{-1} to 110 nN s^{-1}.

Thereby, these measurements reflect the engineered 1:1 binding stoichiometry with force propagating only through the single functional subunit of the tetramer. As proteins of interest can be equipped with biotin molecules, this mSA molecule, which features monodisperse biotin unbinding behavior, qualifies as a versatile force handle to be used in SMFS assays.

Monodisperse measurement of the biotin-streptavidin interaction strength in a well-defined pulling geometry

by

Steffen M. Sedlak, Magnus S. Bauer, Carleen Kluger, Leonard C. Schendel, Lukas F. Milles, Diana A. Pippig, Hermann E. Gaub

published in

PLOS ONE, 2017 12, e0188722, doi:10.1371/journal.pone.0188722

Reprinted from Sedlak *et al.* [90]. Published under Creative Commons Attribution license.
Copyright 2017 Sedlak *et al.*

PLOS ONE

RESEARCH ARTICLE

Monodisperse measurement of the biotin-streptavidin interaction strength in a well-defined pulling geometry

Steffen M. Sedlak, Magnus S. Bauer, Carleen Kluger, Leonard C. Schendel, Lukas F. Milles, Diana A. Pippig, Hermann E. Gaub*

Lehrstuhl für Angewandte Physik and Center for NanoScience (CeNS), Ludwig-Maximilians-Universität München, Munich, Germany

* gaub@lmu.de

Check for updates

OPEN ACCESS

Citation: Sedlak SM, Bauer MS, Kluger C, Schendel LC, Milles LF, Pippig DA, et al. (2017) Monodisperse measurement of the biotin-streptavidin interaction strength in a well-defined pulling geometry. PLoS ONE 12(12): e0188722. https://doi.org/10.1371/journal.pone.0188722

Editor: Annalisa Pastore, National Institute for Medical Research, Medical Research Council, London, UNITED KINGDOM

Received: August 2, 2017

Accepted: November 7, 2017

Published: December 5, 2017

Copyright: © 2017 Sedlak et al. This is an open access article distributed under the terms of the Creative Commons Attribution License, which permits unrestricted use, distribution, and reproduction in any medium, provided the original author and source are credited.

Data Availability Statement: All relevant data are within the paper and its Supporting Information files.

Funding: Funding was provided by the European Research Council Advanced Grant (HEG) ERC-2011-ADG_20110310 to Hermann E. Gaub and the SFB1032 (HEG) of the Deutsche Forschungsgemeinschaft. The funders had no role in study design, data collection and analysis, decision to publish, or preparation of the

Abstract

The widely used interaction of the homotetramer streptavidin with the small molecule biotin has been intensively studied by force spectroscopy and has become a model system for receptor ligand interaction. However, streptavidin's tetravalency results in diverse force propagation pathways through the different binding interfaces. This multiplicity gives rise to polydisperse force spectroscopy data. Here, we present an engineered monovalent streptavidin tetramer with a single cysteine in its functional subunit that allows for site-specific immobilization of the molecule, orthogonal to biotin binding. Functionality of streptavidin and its binding properties for biotin remain unaffected. We thus created a stable and reliable molecular anchor with a unique high-affinity binding site for biotinylated molecules or nanoparticles, which we expect to be useful for many single-molecule applications. To characterize the mechanical properties of the bond between biotin and our monovalent streptavidin, we performed force spectroscopy experiments using an atomic force microscope. We were able to conduct measurements at the single-molecule level with 1:1-stoichiometry and a well-defined geometry, in which force exclusively propagates through a single subunit of the streptavidin tetramer. For different force loading rates, we obtained narrow force distributions of the bond rupture forces ranging from 200 pN at 1,500 pN/s to 230 pN at 110,000 pN/s. The data are in very good agreement with the standard Bell-Evans model with a single potential barrier at $\Delta x_0 = 0.38$ nm and a zero-force off-rate $k_{off,0}$ in the 10^{-6} s^{-1} range.

Introduction

With its low dissociation constant in the femtomolar range [1], its specificity, and its high stability under harsh conditions [2], the binding of the small molecule biotin to the homotetramer streptavidin (SA) is a popular and widely used tool in nanotechnology, biotechnology, and medicine. Especially after biotinylation became available [3], this receptor-ligand system found versatile applications, e.g. detection [4, 5] or capturing of biomolecules [6–9], and diverse other *in vivo* and *in vitro* methods. For single-molecule techniques, the tetravalency of

manuscript. SMS and MSB thank the Nanosystems Initiative Munich for support. The funders had no role in study design, data collection and analysis, decision to publish, or preparation of the manuscript.

Competing interests: The authors have declared that no competing interests exist.

SA can however be disadvantageous, as it promotes clustering of biotinylated molecules. Single-molecule force spectroscopy (SMFS) [10], super-resolution imaging techniques, and analytical applications like surface plasmon resonance or switch sense technology [11] often require a 1:1 stoichiometry. Efforts have been directed at the development of monomeric versions of SA [12]. However, since the interplay between different subunits is important for the tight binding of biotin [13], monomeric SAs lack the outstanding affinity of wildtype SA [12]. In 2006, Howarth et al. [14] developed a tetrameric but monovalent streptavidin (mSA), by reconstituting one functional with three non-functional subunits (Fig 1A). mSA preserves femtomolar affinity towards biotin. Here, we present the implementation of mSA as a molecular anchor for atomic force microscopy (AFM)-based SMFS, which enables us to revisit the biotin:SA interaction in a very specific and monodisperse manner.

The interaction between biotin and tetravalent SA/avidin was the first receptor-ligand interactions probed by AFM-based SMFS [17–19]. It has become a model system for non-covalent receptor-ligand complexes and to study biorecognition processes [20]. In an AFM-based SMFS measurement, a functionalized AFM-cantilever decorated with ligand molecules is approached to a functionalized surface decorated with receptor molecules. A receptor-ligand complex is formed and when retracting the cantilever from the surface, the bending of the cantilever is recorded providing a measure for the force that the receptor-ligand complex can withstand, i.e. for its mechanical strength under load.

In 1994, Moy et al. [19] reported integer multiples of biotin:SA unbinding events and analyzed the relation between binding energies and unbinding forces. Biotinylated bovine serum albumin (BSA) was unspecifically adsorbed to both cantilever and sample surface. Bringing cantilever and surface in contact, SA that had been added to the solution could bind to a biotin on the cantilever and to one on the surface at the same time. Retracting the cantilever from the surface, the force needed to pull biotin and SA apart was recorded. The way load was applied to tetravalent SA in this experiment is schematically described in Fig 1B. Combinations of the geometries shown in this figure are also likely to occur. To obtain data at the single-molecule level, either the concentration of SA molecules was adjusted or free biotin was added to the solution.

Several groups independently repeated the experiment [18, 21]. Allen et al. slightly modified the setup by direct, yet unspecific, immobilization of SA to the sample surface [22]. In the following years, the biotin:SA interaction was modeled by MD simulations [23, 24] and theoretical descriptions for the process of unbinding were put forward [25–27]. In 1999, Merkel et al. [28] measured the biotin:SA interaction with a biomembrane force probe instrument. For the first time, measurements using different force loading rates were performed. On top of that, they introduced covalent attachment of biotin through polyethylene glycol (PEG) linkers. With a covalent immobilization strategy, detachment of biotin from the sample surfaces became unlikely, resulting in higher purity of the recorded data. The variety of possible pulling geometries, as depicted in Fig 1B, remained. Using the loading-rate dependence of rupture forces, the energy landscape of the biotin:SA binding was investigated. Dynamic force spectra of the receptor-ligand system were also recorded with the AFM using diverse attachment strategies, such as immobilization in a phospholipid bilayer [29] or a dextran-coated surface [30], by biotinylated BSA [31–33] or by cross-linking with glutaraldehyde [34]. In 2010, Taninaka et al. further improved the measurement procedure by binding both biotin and SA covalently with PEG spacers to sample and cantilever surface, respectively [35]. The way load is applied to the SA tetramer in this case is shown in Fig 1C.

Due to different ways the ligand binds to the receptor, AFM-based SMFS data can be dispersed when performing experiments using multivalent receptor molecules, such as SA, even if actual single-molecule interactions are probed. Pulling on the ligand, the force can propagate

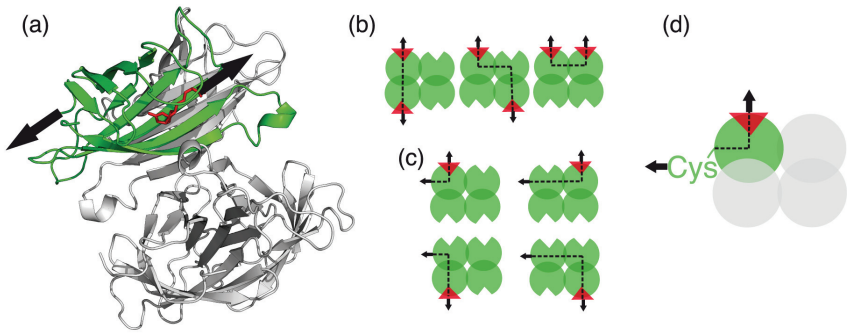

Fig 1. Possible pulling geometries for SA of different valencies. (a) Crystal structure of mSA (pdb identification code 5TO2 [15], overlaid with 1MK5 [16] to show the position of biotin). The functional subunit (green) with biotin (red) bound is stabilized by the three non-functional subunits (grey). Black arrows show the direction of the applied load for the AFM-based SMFS measurement. (b) Tetravalent SA consists of four functional subunits (green balls) each possessing a biotin (red triangles) binding site. In previous experiments, SA has been attached to a biotinylated surface resulting in a variety of possible pulling geometries: Across the strong interface, across the weak interface or diagonally across the tetramer. Having several functional binding pockets available, multiple binding to surface or cantilever can also occur. Black arrows indicate the pulling direction, black dotted lines possible ways force propagates through the molecule. (c) Attaching the tetravalent SA molecule covalently to the surface gives also rise to diverse pulling geometries. (d) In our experiments, we employ mSA consisting of one functional (green ball) and three non-functional subunits that are unable to bind biotin (grey balls). Having mSA tethered by a single N-terminal cysteine in the functional subunit, we pull biotin out of the binding pocket. The force only propagates through a single subunit.

https://doi.org/10.1371/journal.pone.0188722.g001

through the receptor molecule in different ways (Fig 1B and 1C). This results in a broad distribution of rupture forces. Furthermore, when the receptor molecule is composed of several non-covalently bound subunits, the data are distorted if the subunits of the receptor molecule get torn apart. In a SMFS experiment, a rupture of the receptor molecule itself cannot be distinguished from the unbinding of the ligand from the receptor. Beyond that, disrupted receptor tetramers may clog the cantilever thus preventing specific interaction resulting in low data yield.

From the crystal structure of wild-type SA, it can be reasoned that the SA monomers assemble into strongly associated dimers that form less stable tetramers [36]. Therefore, the different interfaces between the four subunits of a SA tetramer might be of different mechanical stability. Kim et al. [37] proved that the mechanical strength of the SA tetramer itself is highly dependent on the pulling geometry, i.e. on the way force is applied to the tetramer. Pulling on various control domains that were genetically fused to the N-termini of the SA monomers, they observed two distinct peaks in the distribution of rupture forces of the tetramer [37]. The two peaks can be assigned to a rupture across the strong interface between two subunits forming a dimer and to the rupture across the weak interface between the two dimers forming the tetramer. Interestingly, the force peaks of around 100 pN and 400-500 pN overlap with the range of unbinding forces reported for the biotin:SA interaction [18, 19, 21, 22, 28–32, 35, 38–40].

Non-equilibrium unbinding forces are loading rate dependent [41]. Any comparison of unbinding forces on an absolute scale, especially when measured with different setups under different conditions, is to be treated with caution. Nevertheless, it is conceivable that SMFS experiments with biotin and tetravalent SA are to some extend distorted by the potential rupture of the tetramer before unbinding biotin from SA. To examine the behavior of the biotin:

SA interaction under load, it is therefore important to overcome the problem of SA's tetravalency.

We therefore implement mSA to perform high-throughput AFM-based SMFS experiments for probing the mechanical stability of the biotin:SA system in a well-defined pulling geometry, no longer distorted by the receptor's multivalency. The quality of the data is further improved by the use of protein calibration domains for identification of single interactions. The unfolding patterns of the calibration domains that are enzymatically fused to ligand or receptor molecule verify single rupture events. When unfolding under the applied load before the receptor-ligand complex ruptures, they yield a specific unfolding force, which serves as internal reference for force calibration, and a defined length increment that is taken as an indicator for single receptor-ligand unbinding.

For site-selective immobilization of SA, we genetically modified the functional subunit of mSA. Although wildtype SA does not contain any cysteine residues, the SA tetramer was found to be of high stability under conditions, which are usually denaturing [42]. In contrast to many other proteins, the interaction between the subunits is not mediated by disulfide bridges but originates from a network of hydrogen bonds and hydrophobic interactions. We thus introduced a single cysteine at the N-terminus of the functional subunit of mSA for site-selective immobilization by conventional thiol-maleimide coupling [43]. We thereby created a stable molecular anchor for biotinylated (bio-)molecules with femtomolar affinity and well-defined stoichiometry. This well-defined single anchor point together with the monovalency of the biotin mSA interaction defines an unambiguous force propagation path. It enables us to perform AFM-based SMFS experiments in which the force only propagates through a single subunit of SA (Fig 1D).

Materials and methods

Gene construction, protein expression and purification

A detailed description of expression and purification is provided in the supplement (S1 Appendix). SA and mutant SA (deficient in biotin binding) constructs containing an N-terminal polyhistidine-tag (His-tag) for purification were cloned into pET vectors (Novagen, EMD Millipore, Billerica, USA). Constructs contained an N-terminal cysteine for site-specific immobilization, except for the subunits that were not meant to attach to AFM-cantilever surface or the glass coverslip. SA subunits with and without cysteine and His-tag and mutant SA subunits were expressed separately in *E. coli* BL21(DE3)-CodonPlus (Agilent Technologies, Santa Clara, USA). The constructs formed inclusion bodies that were isolated as described previously [44]. To reconstitute mSA and to guarantee a 1:3 ratio of functional to non-functional SA subunits in the final tetramer, inclusion bodies were solubilized in 6 M guanidine hydrochloride and then mixed at a 1:10 ratio prior to refolding and purification via the His-tag. To obtain tetravalent SA with a unique cysteine coupling site, the construct containing the cysteine residue as well as a His-tag was mixed with functional SA devoid of either.

The *Dictyostelium discoideum* fourth filamin domain (ddFLN4) construct with an N-terminal ybbR-tag [45] and a C-terminal cysteine (the internal cysteine 18 was mutated to serine) was cloned into pET vectors (Novagen, EMD Millipore, Billerica, USA). After expression in *E. coli* BL21(DE3)-CodonPlus (Agilent Technologies Santa Clara, USA) and lysis, purification was achieved by immobilized metal ion affinity chromatography (Ni-IMAC).

The superfolder green fluorescent protein (GFP) construct with an N-terminal cysteine and a C-terminal ybbR-tag was cloned into pET vectors (Novagen, EMD Millipore, Billerica, USA) and expressed in *E. coli* BL21(DE3)-CodonPlus (Agilent Technologies Santa Clara, USA). Purification was performed by Ni-IMAC.

Biotinylation of protein constructs

GFP and ddFLN4 constructs were biotinylated using the ybbR-tag/Sfp-Synthase system [45]. For the GFP construct, 18 μM GFP-ybbR were incubated with 60 μM CoA-Biotin (New England BioLabs) and 9 μM Sfp Synthase in a solution of 10 mM $MgCl_2$ and 50 mM HEPES at pH 7.5 for 1 h at 37˚C. To clean the solution from remaining CoA-Biotin, a buffer exchange to phosphate buffered saline (PBS; Sigma-Aldrich, Saint Louis, USA) was performed with Zeba Spin Desalting Columns (Thermo Scientific, Rockford, USA) with 7K MWCO according to the manufacturer's instructions. For the ddFLN4 construct, the incubation was performed at room temperature. All other steps were done in the same way as for GFP.

SDS-PAGE

Gel electrophoresis was performed using Any kD Mini-PROTEAN TGX Precast Protein Gels (Bio-Rad, Hercules, USA) in TRIS-based running buffer (2.5 mM TRIS, 200 mM glycerol, 3.5 mM SDS). For lanes 2–4, we heated 0.6 μM SA dissolved in loading buffer (50 mM TRIS, pH 8.0, 2.5% SDS, 5% glycerol, 0.005% bromophenol blue, 2.5% β-mercaptoethanol) for 5 minutes to 95˚C. For the other SA containing lanes, we used about 1.5 μM. For lanes 10–13, we added 1 μl of the purified Sfp reaction mixture containing both biotinylated and un-biotinylated GFP. We employed Precision Plus Unstained Protein Standards (Bio-Rad Laboratories, Hercules, USA) as molecular weight standards. The gel was run at room temperature with a constant current of 25 mA. The gel was analyzed with a ChemiDoc MP Imaging System (Bio-Rad Laboratories, Hercules, USA).

Isothermal titration calorimetry

The calorimetric experiments were carried out with a Malvern MicroCal ITC200 (Malvern, UK). SA samples were equilibrated with PBS using Zeba Spin Desalting Columns (Thermo Scientific, Rockford, USA) with 40K MWCO following the manufacturer's instructions. The concentration was determined by spectrophotometry with a NanoDrop 1000 (Thermo Scientific, Rockford, USA) using an extinction coefficient of $\varepsilon_{280} = 167{,}760\ M^{-1}cm^{-1}$ calculated from the protein sequence using the SIB bioinformatics resource portal [46]. Biotin (Sigma-Aldrich, St. Louis, USA) was dissolved in PBS. For all measurement, the same stock solution of biotin was used. For mSA, a tenfold excess of biotin was titrated into the sample cell. For tetravalent SA, we used a ratio of 1:40, resulting in a final molar ratio of 1:8. All experiments were performed at 25˚C.

Functionalization of cantilevers and coverslips

AFM cantilevers (Biolever Mini, Olympus, Tokyo, Japan) and glass coverslips were silanized as described by Zimmermann et al. [43]. They were incubated with 25 mM heterobifunctional PEG (Rapp Polymere, Tübingen, Germany) with a molecular weight of 5 kDA equipped with an N-Hydroxysuccinimide (NHS) group and a maleimide group dissolved in a 50 mM HEPES solution at pH 7.5 for 45 minutes. The PEG spacers ensure passivation of glass cover slip and AFM-cantilevers and allow for specific sample immobilization. The coverslips were washed in ultrapure water and mounted into AFM sample holder. A 3.5 μl droplet of monovalent or tetravalent SA was deposited on the surface. The cantilevers were washed in ultrapure water and then placed in a 15 μl drop of the purified biotinylated ddFLN4 construct. For an efficient reaction of thiol with maleimide groups which forms stable thioester bonds, we reduced the thiol groups of SA and ddFLN4 construct by adding Immobilized TCEP Disulfide Reducing Gel (Thermo Scientific, Rockford, USA) in a v/v ratio of 1:6 and incubated for 1 h. The gel was

removed with the help of an Ultrafree-MC, HV 0.45 μm centrifugal filter (Merck Millipore, Darmstadt, Germany) directly before adding the proteins to the coverslips or cantilevers. During the formation of the thioester bonds, the samples were kept in a humidity chamber to prevent evaporation. After 1.5 h, the cantilevers were washed twice in PBS and the surfaces were rinsed with 50 ml PBS to flush out unbound protein.

AFM-based single-molecule force spectroscopy experiments

The experiments were performed with a custom-built AFM as described by Gumpp et al. [47]. The cantilevers were approached to the surface and after short contact, retracted at constant velocities of 200 nm/s, 800 nm/s, 2,000 nm/s, 5,000 nm/s, and 10,000 nm/s. To always probe a different spot on the surface, it was horizontally moved by 100 nm after each approach. For calibration of the cantilevers, we employed the equipartition theorem [48]. Baumann et al. [44] and Milles et al. [49] provide detailed descriptions of experimental SMFS procedures and SMFS data analysis.

Results and discussion

Size and functionality of mSA constructs with terminal cysteine is maintained

After expression and purification, we checked size and quality of the SAs with SDS polyacrylamide gel electrophoresis (Fig 2). Heating mSA and tetravalent SA (tSA) for 5 min to 95˚C, the tetramers fall apart into monomers of approximately 14 kDa (Fig 2B). The higher band can be assigned to the monomer with the additional His-tag and we confirmed the expected ratio between the monomers to be 1:3. Commercially available SA from *Streptomyces avidinii* (sSA) shows only one slightly larger and broader band. In contrast to the recombinantly expressed core SA monomer that consist of 123 residues, the SA monomer from *Streptomyces avidinii* contains 183 amino acids. In a posttranslational digest process, it is cut down to core SA.

The size of the tetramers can be estimated from unheated samples (Fig 2C). For mSA and tSA band size is slightly below the expected 54 kDa. Bands at double size are attributed to two tetramers connected via disulfide bridges between their cysteine residues. sSA shows several smeared out bands of larger size, caused by an incomplete posttranslational digest. The lowest one corresponds to core SA (54 kDa).

To illustrate the binding stoichiometry of the SAs to biotin, we added biotinylated GFP to mSA, tSA, and sSA (Fig 2D and 2E). Since the biotinylation of GFP has been incomplete, bands of unbound SA and bands of GFP without biotin are still visible. All SAs having a single GFP bound appear at the same size of about 70 kDa. Valencies of the different SA can be determined from the number of bands. For mSA, only one band with a single biotinylated GFP bound is seen. For sSA, four bands are clearly visible. Because of dimerized tetramers binding one or several biotinylated GFPs, additional bands appear for tSA.

Modifications of mSA do not change biotin binding properties

We compared the binding properties of our modified mSA with tSA and sSA by isothermal titration calorimetry (Fig 3). Because of the high affinity of biotin to SA, we could only conclude that the dissociation constant K_D is lower than 1 nM. The binding enthalpy per mole of added biotin (ΔH_{mSA} = -26 kcal/mol, ΔH_{tSA} = -25 kcal/mol, ΔH_{sSA} = -26 kcal/mol) and the binding stoichiometry (N_{mSA} = 0.95, N_{tSA} = 4.31, N_{sSA} = 4.31) confirmed that the functional subunit of our modified mSA is capable of binding biotin in the same manner as the subunits of sSA, while the binding of biotin to the mutated non-functional subunits is negligible. The

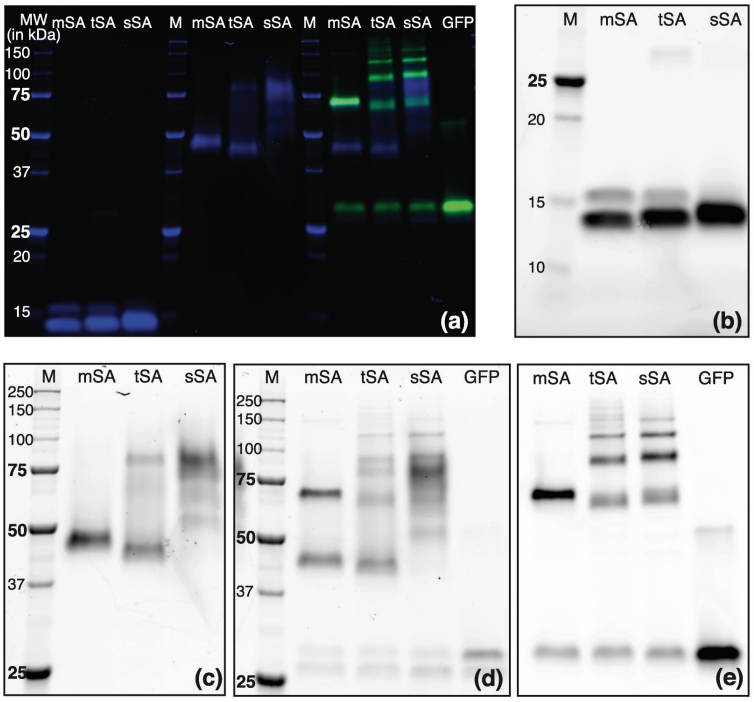

Fig 2. SDS-PAGE of mSA, tSA and commercial SA from *streptomyces avidinii* (sSA). (a) Overview of differently treated SAs with and without addition of biotinylated GFP on a stain-free polyacrylamide gel. Overlay of images taken with UV light excitation (blue) and illumination with a blue LED source (green). Parts of this image are inverted and shown in detail (b-d UV-excitation; e: GFP-channel): (b) Denatured SA samples (5 min at 95˚C). Decomposition into monomers (14 kDa) is visible. His-tagged subunits appear larger. sSA subunits are smeared out. (c) Untreated SA samples which maintain tertiary structure. (d,e) Addition of biotinylated GFP to untreated SA samples. Valencies of SAs are visible as different numbers of GFPs are bound. The lowest band in (d) corresponds to Sfp Synthase (26 kDa).

https://doi.org/10.1371/journal.pone.0188722.g002

measured enthalpies are also in line with previously reported values [50]. This implies that the modifications at the N-terminus of the functional subunit do not impede the binding of biotin. We therefore argue that structure and function of the sSA are preserved for our monovalent and tetravalent versions with N-terminal modifications.

AFM-based SMFS using mSA as a handle

Using reconstituted mSA in combination with a calibration domain, we were able to perform SMFS with a well-defined pulling geometry that are not distorted by SA's multivalency. In our experiments, force propagates only through a single subunit of the SA tetramer (Fig 1D). Therefore, no tension across any interface within the tetramer, which could cause dissociation of the tetramer into its subunits, is applied. The measurement process is illustrated in Fig 4. To ensure the specificity of the probed interaction, we used the unfolding pattern of biotinylated

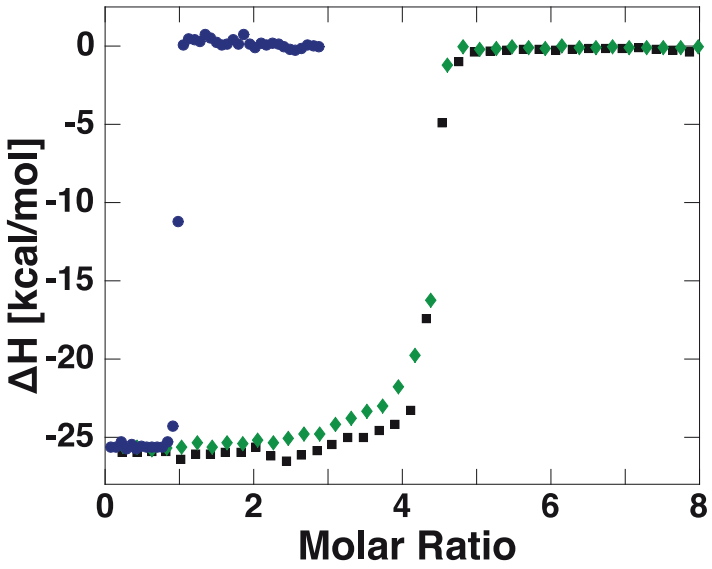

Fig 3. Isothermal titration calorimetry of biotin and SAs of different valency. The binding of biotin to different SAs was measured with isothermal titration calorimetry. The binding stoichiometry of mSA and biotin was determined as $N = 0.95$ (blue circles). The measured binding stoichiometry of the engineered tetravalent version (green diamonds) $N = 4.31$ is in good agreement with the value of commercial SA isolated from *Streptomyces avidinii* (black squares) $N = 4.29$. Within the limits of the measurement's accuracy, the binding enthalpies of the different SAs are the same ($\Delta H = -26$ kcal/mol for monovalent, $\Delta H = -25$ kcal/mol for tetravalent and $\Delta H = -26$ kcal/mol for commercial SA), confirming that the N-terminal modifications do not interfere with the binding of biotin.

https://doi.org/10.1371/journal.pone.0188722.g003

ddFLN4 [51] to identify single molecule rupture events. Because ddFLN4 folds back into its native state when the force drops after unbinding of biotin from mSA, it was used as a calibration domain on the cantilever, while mSA was immobilized on the surface. We use this attachment strategy for probing the biotin:mSA interaction, because we can probe a new mSA molecule, which has not yet been exposed to pulling forces, for every force-distance curve. Only those force curves that showed the specific unfolding pattern of the calibration domain were considered in subsequent data analysis procedures.

Analysis of AFM-based SMFS data

In an AFM experiment, about 5,000 force extension traces were recorded of which about 1,100 showed interaction. A larger data set of over 50,000 traces obtained in a 15 h measurement is shown in the supplement (S3 Appendix). To prove reliability and reproducibility of the control domain's unfolding pattern, an overlay of all 575 force-distance curves that feature the distinct unfolding pattern of ddFLN4 before biotin unbinds from mSA is shown in Fig 5A.

For every data bin along the extension axis, we selected the force bin with the highest value to obtain a characteristic force-extension curve. The curve consists of three parts: First, only the PEG-spacers on the cantilever and the surface are stretched (Fig 4). Then ddFLN4 unfolds in two distinct steps. Using the worm-like chain model for semi-flexible polymers [52] to fit

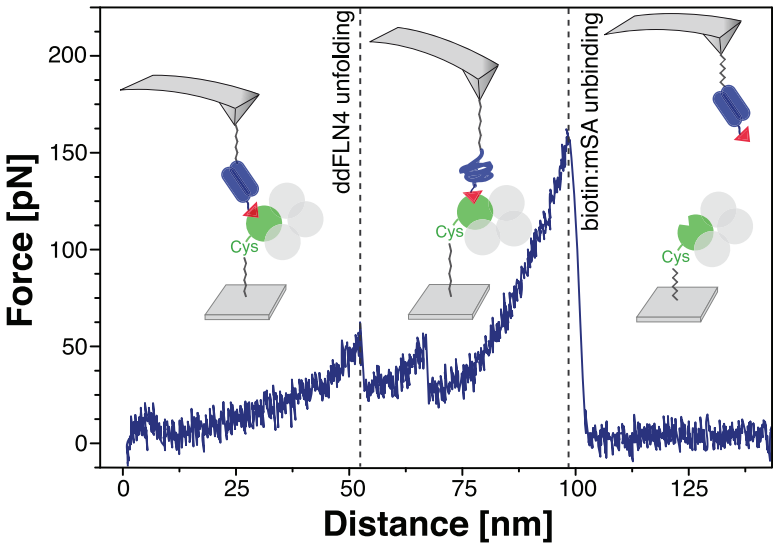

Fig 4. Investigation of the mechanical stability of the biotin:mSA binding with a well-defined pulling geometry. The functionalized cantilever tip is approached to the surface and a bond between biotin (red triangle) and mSA (green and gray balls) is formed. First, only the PEG (grey lines) spacers are stretched, when retracting the cantilever with constant speed from the surface. At forces of about 60 pN, the ddFLN4 (blue) unfolds in a characteristic two-step process that is used to identify single-molecule interactions. PEG spacers and the polypeptide chain are then further stretched until biotin unbinds from mSA under the applied load. The force drops and ddFLN4 folds back into its native state. As an example, one of the recorded force-distance curves (pulled at 800 nm/s) is shown in blue. More force-distance curves are shown in the supplement (S2 Appendix).

https://doi.org/10.1371/journal.pone.0188722.g004

this characteristic curve (black lines in Fig 5A), we deduced persistence lengths and contour lengths of the stretched construct for the different unfolding steps of the calibration domain. As the PEG-spacers undergo a conformational transition from cis to trans above forces of about 100 pN [53, 54] resulting in a linear force extension relation, we restricted the WLC fit to the part of the curve with forces lower than 100 pN. We find persistence lengths of 0.240 nm for the PEG-stretch, 0.265 nm and 0.282 nm for the subsequent parts. The fitted contour lengths of 80.7 nm, 96.4 nm, and 113.5 nm are in good agreement with theoretical estimations. From the molecular weights, we estimated the lengths of the two PEG-spacers to be about 31 nm to 40 nm each and the total contour length increment resulting from ddFLN4 unfolding to be 36 nm (S4 Appendix).

From the worm-like chain model, an expression for the contour length as a function of persistence length, force and extension can be derived [55]. Assuming a constant persistence length of 0.26 nm, we translated every data point of the characteristic curve (Fig 5A) into contour length space (S5 Appendix). In Fig 5B, the corresponding histogram of contour lengths is shown. Three pronounced peaks with maxima at 79.5 nm, 96.5 nm and 113.5 nm are visible, confirming the correct assignment of the different parts of the force-extension curve to different parts of our molecular construct.

We probed the biotin:mSA complex with five different retraction velocities (200 nm/s, 800 nm/s, 2,000 nm/s, 5,000 nm/s and 10,000 nm/s). The distributions of the resulting forces of the

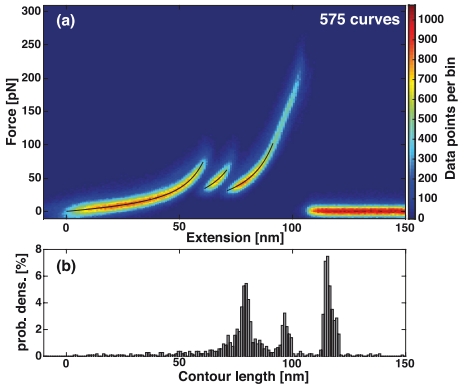

Fig 5. Overlay of force-extension curves and transformation into contour length space. (a) The 575 force-extension curves for which the characteristic unfolding pattern of ddFLN4 was visible are overlaid. We fit the three parts of the curve independently with the worm-like chain polymer model (black lines). (b) Using the mean persistence length of the worm-like chain fits, each point of the force extension curve is translated into contour length space. From the histogram, the contour lengths of the stretched constructs corresponding to the three parts of the force curve are determined.

https://doi.org/10.1371/journal.pone.0188722.g005

biotin:mSA unbinding and the ddFLN4 unfolding are depicted in Fig 6. The histograms of the forces corresponding to the two subsequent ddFLN4 unfolding steps exhibit defined peaks at 60-80 pN. For biotin:mSA unbinding force histograms, a sharp peak at about 200 pN is found. Its exact position depends on the applied loading rate. To obtain exact values, all force histograms were fitted with Bell-Evans models [25, 41] yielding the most probable rupture force, off-rates and distance to the transition state (S6 Appendix).

The dynamic force spectrum is shown in Fig 7. Force loading rates were determined by fitting a linear slope over the last 3 nm before unfolding and unbinding force peaks in the force-extension curves. In the semi-logarithmic plot, the centers of gravity of force and loading rate distributions for the ddFLN4 unfolding and the biotin:mSA unbinding are fitted by a straight line. This linear dependence of unfolding or rupture forces on the loading rate is given by Bell-Evans theory (S5 Appendix). From slope and y-intercept, the distance to transition state Δx_0 and the zero-force off-rate $k_{off,0}$ can be determined. For the ddFLN4-unfolding, we find Δx_0 = (0.76 ± 0.05) nm and $k_{off,0} = 8 \times 10^{-4}$ s^{-1} for the first unfolding peak and Δx_0 = (0.56 ± 0.02) nm and $k_{off,0} = 5 \times 10^{-2}$ s^{-1} for the subsequent peak. The distance to the transition state of the biotin:mSA unbinding reads Δx_0 = (0.38 ± 0.02) nm and the zero-force off-rate is determined as $k_{off,0} = 3 \times 10^{-6}$ s^{-1}. The off-rate is in good agreement with the value obtained in an off-rate assay ($k_{off,exp} = 6.1 \times 10^{-5}$ s^{-1}) [14]. Previous studies reported a kink in the force-loading rate dependence that was attributed to two potential barriers in the binding potential [28]. For the range of loading rates we applied and for the specific geometry that we used to load the complex, we could not observe this feature.

Conclusion

Even though binding of biotin to SA is widely used as a tool and has been extensively studied previously, the unbinding forces reported in the literature scatter substantially. With the development of mSA and progress in AFM-based SMFS it became possible to study the mechanical

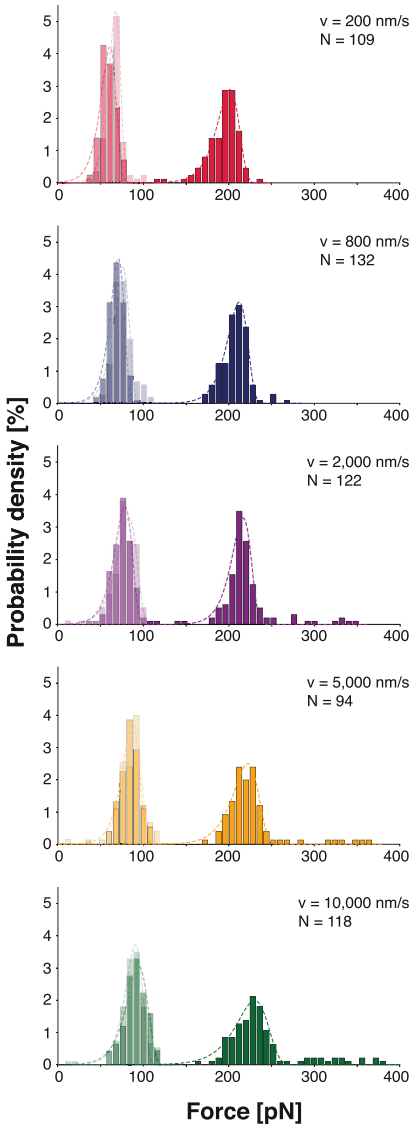

Fig 6. Unfolding forces of ddFLN4 and unbinding forces of biotin and mSA for different pulling velocities. The distribution of the forces of the first (transparent bars in the background) and second (semi-transparent bars) step of the ddFLN4 unfolding gives rise to two distinct peaks at approximately 85 pN and 75 pN. The biotin:mSA unbinding forces (opaque bars) are distributed more broadly but exhibit a clear maximum

at about 200 pN depending on the applied force loading rate. The experiment was carried out with a cantilever with a spring constant of 73.9 pN/nm. The dashed lines show independent fits of Bell-Evans distributions to the force histograms.

https://doi.org/10.1371/journal.pone.0188722.g006

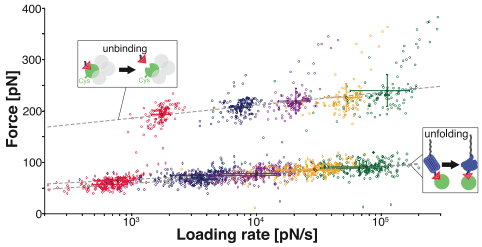

Fig 7. Bell-Evans plot of unfolding and unbinding forces. For all specific single-molecule interactions, the unbindig forces of biotin:mSA (circles) and the forces of the first (diamonds) and second (squares) step of the ddFLN4 unfolding are plotted against the loading rates at the corresponding force peak. The data are equal to the one shown in Fig 6 and the same color code is used. The dashed lines are linear fits to the centers of gravity (shown as filled circles, diamonds and squares) of the distributions of forces and loading rates, respectively. The colored crosses indicate the corresponding standard deviations.

https://doi.org/10.1371/journal.pone.0188722.g007

stability of the biotin:SA complex in a better defined way. Relating to previous measurements of the unbinding of biotin from tetravalent SA, we illustrated how multivalency of receptor molecules can distort SMFS data of receptor-ligand unbinding. We presented AFM-based SMFS data of the unbinding of biotin from monovalent SA with a 1:1-stoichiometry in a distinct pulling geometry, in which the force only propagated through a single subunit of the SA tetramer. The main improvements of our measurements contributing to the high quality of our data are covalent immobilization of both receptor and ligand molecules, the use of a calibration domain to verify single-molecule interaction events, and exact control over the attachment geometry by a single distinct anchoring site and monovalent receptor molecules.

Beyond that, we introduced a new tethering strategy for the use of mSA not only in force spectroscopy but also in many other single-molecule applications. The immobilization of mSA by implementing a single cysteine at the terminus of the functional subunit provides an anchoring site for sulfhydryl-reactive chemical groups, i.e. an anchoring site that is orthogonal to the interaction with biotin. In contrast to defined divalent SA [56] that can serve as a molecular hub for biotinylated molecules, mSA engineered with a single terminal cysteine on the functional subunit allows for controlled immobilization of biotinylated biomolecules or nanoparticles providing a 1:1-binding site.

Supporting information

S1 Appendix. Streptavidin preparation.
(PDF)

S2 Appendix. Exemplary force-distance curves.
(PDF)

S3 Appendix. Long-term SMFS measurement.
(PDF)

S4 Appendix. Estimating the contour lengths of PEG and ddFLN4.
(PDF)

S5 Appendix. Formulas.
(PDF)

S6 Appendix. Fitted Bell-Evans distributions shown in Fig 6.
(PDF)

S7 Appendix. Sequences of protein constructs.
(PDF)

S8 Appendix. Measuring with mSA immobilized on the cantilever.
(PDF)

Acknowledgments

The authors thank M. A. Jobst for discussions and the AFM control software, F. Baumann for support with the AFM experiments, and A. Kardinal and T. Nicolaus for laboratory support.

Author Contributions

Conceptualization: Steffen M. Sedlak, Diana A. Pippig.

Data curation: Steffen M. Sedlak, Leonard C. Schendel.

Formal analysis: Steffen M. Sedlak, Magnus S. Bauer, Carleen Kluger, Leonard C. Schendel, Diana A. Pippig.

Funding acquisition: Hermann E. Gaub.

Investigation: Steffen M. Sedlak, Magnus S. Bauer, Carleen Kluger, Leonard C. Schendel.

Methodology: Steffen M. Sedlak, Magnus S. Bauer, Lukas F. Milles.

Project administration: Diana A. Pippig, Hermann E. Gaub.

Resources: Lukas F. Milles, Diana A. Pippig, Hermann E. Gaub.

Software: Steffen M. Sedlak, Magnus S. Bauer, Lukas F. Milles.

Supervision: Diana A. Pippig, Hermann E. Gaub.

Validation: Steffen M. Sedlak, Carleen Kluger.

Visualization: Steffen M. Sedlak, Magnus S. Bauer, Carleen Kluger.

Writing – original draft: Steffen M. Sedlak, Carleen Kluger, Diana A. Pippig, Hermann E. Gaub.

Writing – review & editing: Steffen M. Sedlak.

References

1. Green NM. Avidin and streptavidin. Methods Enzymol. 1990; 184:51–67. PMID: 2388586.
2. Gonzalez M, Argarana CE, Fidelio GD. Extremely high thermal stability of streptavidin and avidin upon biotin binding. Biomol Eng. 1999; 16(1–4):67–72. PMID: 10796986.
3. Bayer EA, Zalis MG, Wilchek M. 3-(N-Maleimido-propionyl)biocytin: a versatile thiol-specific biotinylating reagent. Anal Biochem. 1985; 149(2):529–36. PMID: 3935007.

4. Howarth M, Takao K, Hayashi Y, Ting AY. Targeting quantum dots to surface proteins in living cells with biotin ligase. Proc Natl Acad Sci U S A. 2005; 102(21):7583–8. https://doi.org/10.1073/pnas.0503125102 PMID: 15897449; PubMed Central PMCID: PMCPMC1129026.
5. Spate AK, Dold JE, Batroff E, Schart VF, Wieland DE, Baudendistel OR, et al. Exploring the Potential of Norbornene-Modified Mannosamine Derivatives for Metabolic Glycoengineering. Chembiochem. 2016; 17(14):1374–83. https://doi.org/10.1002/cbic.201600197 PMID: 27147502.
6. Aschenbrenner D, Baumann F, Milles LF, Pippig DA, Gaub HE. C-5 Propynyl Modifications Enhance the Mechanical Stability of DNA. Chemphyschem. 2015; 16(10):2085–90. https://doi.org/10.1002/cphc.201500193 PMID: 25982589.
7. Ta H, Keller J, Haltmeier M, Saka SK, Schmied J, Opazo F, et al. Mapping molecules in scanning far-field fluorescence nanoscopy. Nat Commun. 2015; 6:7977. https://doi.org/10.1038/ncomms8977 PMID: 26269133; PubMed Central PMCID: PMCPMC4557268.
8. Kriegel F, Ermann N, Forbes R, Dulin D, Dekker NH, Lipfert J. Probing the salt dependence of the torsional stiffness of DNA by multiplexed magnetic torque tweezers. Nucleic Acids Res. 2017. https://doi.org/10.1093/nar/gkx280 PMID: 28460037.
9. Walder R, LeBlanc MA, Van Patten WJ, Edwards DT, Greenberg JA, Adhikari A, et al. Rapid Characterization of a Mechanically Labile alpha-Helical Protein Enabled by Efficient Site-Specific Bioconjugation. J Am Chem Soc. 2017; 139(29):9867–75. https://doi.org/10.1021/jacs.7b02958 PMID: 28677396.
10. Ott W, Jobst MA, Schoeler C, Gaub HE, Nash MA. Single-molecule force spectroscopy on polyproteins and receptor-ligand complexes: The current toolbox. J Struct Biol. 2017; 197(1):3–12. https://doi.org/10.1016/j.jsb.2016.02.011 PMID: 26873782.
11. Knezevic J, Langer A, Hampel PA, Kaiser W, Strasser R, Rant U. Quantitation of affinity, avidity, and binding kinetics of protein analytes with a dynamically switchable biosurface. J Am Chem Soc. 2012; 134(37):15225–8. https://doi.org/10.1021/ja3061276 PMID: 22946661.
12. Qureshi MH, Wong SL. Design, production, and characterization of a monomeric streptavidin and its application for affinity purification of biotinylated proteins. Protein Expr Purif. 2002; 25(3):409–15. PMID: 12182820.
13. Sano T, Cantor CR. Intersubunit contacts made by tryptophan 120 with biotin are essential for both strong biotin binding and biotin-induced tighter subunit association of streptavidin. Proc Natl Acad Sci U S A. 1995; 92(8):3180–4. PMID: 7724536; PubMed Central PMCID: PMCPMC42129.
14. Howarth M, Chinnapen DJ, Gerrow K, Dorrestein PC, Grandy MR, Kelleher NL, et al. A monovalent streptavidin with a single femtomolar biotin binding site. Nat Methods. 2006; 3(4):267–73. https://doi.org/10.1038/NMETHXXX PMID: 16554831; PubMed Central PMCID: PMCPMC2576293.
15. Zhang M, Biswas S, Deng W, Yu H. The Crystal Structure of Monovalent Streptavidin. Sci Rep. 2016; 6:35915. https://doi.org/10.1038/srep35915 PMID: 28000673; PubMed Central PMCID: PMCPMC5175265.
16. Hyre DE, Le Trong I, Merritt EA, Eccleston JF, Green NM, Stenkamp RE, et al. Cooperative hydrogen bond interactions in the streptavidin-biotin system. Protein Sci. 2006; 15(3):459–67. https://doi.org/10.1110/ps.051970306 PMID: 16452627; PubMed Central PMCID: PMCPMC2249767.
17. Florin EL, Moy VT, Gaub HE. Adhesion forces between individual ligand-receptor pairs. Science. 1994; 264(5157):415–7. PMID: 8153628.
18. Lee G, Kidwell D, Colton R. Sensing Discrete Streptavidin-Biotin Interactions with Atomic Force Microscopy. Langmuir. 1994; 10(2):354–7. doi: citeulike-article-id:3733610 https://doi.org/10.1021/la00014a003
19. Moy VT, Florin EL, Gaub HE. Intermolecular forces and energies between ligands and receptors. Science. 1994; 266(5183):257–9. PMID: 7939660.
20. Wilchek M, Bayer EA, Livnah O. Essentials of biorecognition: the (strept)avidin-biotin system as a model for protein-protein and protein-ligand interaction. Immunol Lett. 2006; 103(1):27–32. https://doi.org/10.1016/j.imlet.2005.10.022 PMID: 16325268.
21. Chilkoti A, Boland T, Ratner BD, Stayton PS. The relationship between ligand-binding thermodynamics and protein-ligand interaction forces measured by atomic force microscopy. Biophys J. 1995; 69(5):2125–30. https://doi.org/10.1016/S0006-3495(95)80083-4 PMID: 8580356; PubMed Central PMCID: PMCPMC1236446.
22. Allen S, Davies J, Dawkes AC, Davies MC, Edwards JC, Parker MC, et al. In situ observation of streptavidin-biotin binding on an immunoassay well surface using an atomic force microscope. FEBS Lett. 1996; 390(2):161–4. PMID: 8706850.
23. Grubmuller H, Heymann B, Tavan P. Ligand binding: molecular mechanics calculation of the streptavidin-biotin rupture force. Science. 1996; 271(5251):997–9. PMID: 8584939.

24. Izrailev S, Stepaniants S, Balsera M, Oono Y, Schulten K. Molecular dynamics study of unbinding of the avidin-biotin complex. Biophys J. 1997; 72(4):1568–81. https://doi.org/10.1016/S0006-3495(97)78804-0 PMID: 9083662; PubMed Central PMCID: PMCPMC1184352.

25. Evans E, Ritchie K. Dynamic strength of molecular adhesion bonds. Biophys J. 1997; 72(4):1541–55. https://doi.org/10.1016/S0006-3495(97)78802-7 PMID: 9083660; PubMed Central PMCID: PMCPMC1184350.

26. Friedsam C, Wehle AK, Kühner F, Gaub HE. Dynamic single-molecule force spectroscopy: bond rupture analysis with variable spacer length. Journal of Physics: Condensed Matter. 2003; 15(18):S1709.

27. Dudko OK, Hummer G, Szabo A. Theory, analysis, and interpretation of single-molecule force spectroscopy experiments. Proc Natl Acad Sci U S A. 2008; 105(41):15755–60. https://doi.org/10.1073/pnas.0806085105 PMID: 18852468; PubMed Central PMCID: PMCPMC2572921.

28. Merkel R, Nassoy P, Leung A, Ritchie K, Evans E. Energy landscapes of receptor-ligand bonds explored with dynamic force spectroscopy. Nature. 1999; 397(6714):50–3. https://doi.org/10.1038/16219 PMID: 9892352.

29. Wong J, Chilkoti A, Moy VT. Direct force measurements of the streptavidin-biotin interaction. Biomol Eng. 1999; 16(1–4):45–55. PMID: 10796984.

30. Stevens MM, Allen S, Davies MC, Roberts CJ, Schacht E, Tendler SJB, et al. The Development, Characterization, and Demonstration of a Versatile Immobilization Strategy for Biomolecular Force Measurements. Langmuir. 2002; 18(17):6659–65. https://doi.org/10.1021/la0202024

31. Yuan C, Chen A, Kolb P, Moy VT. Energy landscape of streptavidin-biotin complexes measured by atomic force microscopy. Biochemistry. 2000; 39(33):10219–23. PMID: 10956011.

32. Lo Y-S, Zhu Y-J, Beebe TP. Loading-Rate Dependence of Individual Ligand−Receptor Bond-Rupture Forces Studied by Atomic Force Microscopy. Langmuir. 2001; 17(12):3741–8. https://doi.org/10.1021/la001569g

33. Rico F, Moy VT. Energy landscape roughness of the streptavidin-biotin interaction. J Mol Recognit. 2007; 20(6):495–501. https://doi.org/10.1002/jmr.841 PMID: 17902095.

34. de Odrowaz Piramowicz M, Czuba P, Targosz M, Burda K, Szymonski M. Dynamic force measurements of avidin-biotin and streptavdin-biotin interactions using AFM. Acta Biochim Pol. 2006; 53(1):93–100. PMID: 16410837.

35. Taninaka A, Takeuchi O, Shigekawa H. Reconsideration of dynamic force spectroscopy analysis of streptavidin-biotin interactions. Int J Mol Sci. 2010; 11(5):2134–51. https://doi.org/10.3390/ijms11052134 PMID: 20559507; PubMed Central PMCID: PMCPMC2885099.

36. Laitinen OH, Nordlund HR, Hytonen VP, Kulomaa MS. Brave new (strept)avidins in biotechnology. Trends Biotechnol. 2007; 25(6):269–77. https://doi.org/10.1016/j.tibtech.2007.04.001 PMID: 17433846.

37. Kim M, Wang CC, Benedetti F, Rabbi M, Bennett V, Marszalek PE. Nanomechanics of streptavidin hubs for molecular materials. Adv Mater. 2011; 23(47):5684–8. https://doi.org/10.1002/adma.201103316 PMID: 22102445; PubMed Central PMCID: PMCPMC3837471.

38. Lo Y-S, Huefner ND, Chan WS, Stevens F, Harris JM, Beebe TP. Specific Interactions between Biotin and Avidin Studied by Atomic Force Microscopy Using the Poisson Statistical Analysis Method. Langmuir. 1999; 15(4):1373–82. https://doi.org/10.1021/la981003g

39. Chivers CE, Crozat E, Chu C, Moy VT, Sherratt DJ, Howarth M. A streptavidin variant with slower biotin dissociation and increased mechanostability. Nat Methods. 2010; 7(5):391–3. https://doi.org/10.1038/nmeth.1450 PMID: 20383133; PubMed Central PMCID: PMCPMC2862113.

40. Hu Q, Yang H, Wang Y, Xu S. Quantitatively resolving multivalent interactions on a macroscopic scale using force spectroscopy. Chem Commun (Camb). 2016; 52(18):3705–8. https://doi.org/10.1039/c5cc10535h PMID: 26864087; PubMed Central PMCID: PMCPMC4767602.

41. Bell GI. Models for the specific adhesion of cells to cells. Science. 1978; 200(4342):618–27. PMID: 347575.

42. Bayer EA, Ehrlich-Rogozinski S, Wilchek M. Sodium dodecyl sulfate-polyacrylamide gel electrophoretic method for assessing the quaternary state and comparative thermostability of avidin and streptavidin. Electrophoresis. 1996; 17(8):1319–24. https://doi.org/10.1002/elps.1150170808 PMID: 8874057.

43. Zimmermann JL, Nicolaus T, Neuert G, Blank K. Thiol-based, site-specific and covalent immobilization of biomolecules for single-molecule experiments. Nat Protoc. 2010; 5(6):975–85. https://doi.org/10.1038/nprot.2010.49 PMID: 20448543.

44. Baumann F, Bauer MS, Milles LF, Alexandrovich A, Gaub HE, Pippig DA. Monovalent Strep-Tactin for strong and site-specific tethering in nanospectroscopy. Nat Nanotechnol. 2016; 11(1):89–94. https://doi.org/10.1038/nnano.2015.231 PMID: 26457965.

45. Yin J, Straight PD, McLoughlin SM, Zhou Z, Lin AJ, Golan DE, et al. Genetically encoded short peptide tag for versatile protein labeling by Sfp phosphopantetheinyl transferase. Proc Natl Acad Sci U S A. 2005; 102(44):15815–20. https://doi.org/10.1073/pnas.0507705102 PMID: 16236721; PubMed Central PMCID: PMCPMC1276090.

46. Artimo P, Jonnalagedda M, Arnold K, Baratin D, Csardi G, de Castro E, et al. ExPASy: SIB bioinformatics resource portal. Nucleic Acids Res. 2012; 40(Web Server issue):W597–603. https://doi.org/10.1093/nar/gks400 PMID: 22661580; PubMed Central PMCID: PMCPMC3394269.

47. Gumpp H, Stahl SW, Strackharn M, Puchner EM, Gaub HE. Ultrastable combined atomic force and total internal reflection fluorescence microscope [corrected]. Rev Sci Instrum. 2009; 80(6):063704. https://doi.org/10.1063/1.3148224 PMID: 19566207.

48. Hutter JL, Bechhoefer J. Calibration of atomic-force microscope tips. Review of Scientific Instruments. 1993; 64(7):1868–73. https://doi.org/10.1063/1.1143970

49. Milles LF, Bayer EA, Nash MA, Gaub HE. Mechanical Stability of a High-Affinity Toxin Anchor from the Pathogen Clostridium perfringens. J Phys Chem B. 2016. https://doi.org/10.1021/acs.jpcb.6b09593 PMID: 27991799.

50. Chilkoti A, Stayton PS. Molecular Origins of the Slow Streptavidin-Biotin Dissociation Kinetics. Journal of the American Chemical Society. 1995; 117(43):10622–8. https://doi.org/10.1021/ja00148a003

51. Schwaiger I, Kardinal A, Schleicher M, Noegel AA, Rief M. A mechanical unfolding intermediate in an actin-crosslinking protein. Nat Struct Mol Biol. 2004; 11(1):81–5. https://doi.org/10.1038/nsmb705 PMID: 14718927.

52. Bustamante C, Marko JF, Siggia ED, Smith S. Entropic elasticity of lambda-phage DNA. Science. 1994; 265(5178):1599–600. PMID: 8079175.

53. Oesterhelt F, Rief M, Gaub HE. Single molecule force spectroscopy by AFM indicates helical structure of poly(ethylene-glycol) in water. New Journal of Physics. 1999; 1(1):6.

54. Ott W, Jobst MA, Bauer MS, Durner E, Milles LF, Nash MA, et al. Elastin-like Polypeptide Linkers for Single-Molecule Force Spectroscopy. ACS Nano. 2017; 11(6):6346–54. https://doi.org/10.1021/acsnano.7b02694 PMID: 28591514.

55. Puchner EM, Franzen G, Gautel M, Gaub HE. Comparing proteins by their unfolding pattern. Biophys J. 2008; 95(1):426–34. https://doi.org/10.1529/biophysj.108.129999 PMID: 18550806; PubMed Central PMCID: PMCPMC2426622.

56. Fairhead M, Krndija D, Lowe ED, Howarth M. Plug-and-play pairing via defined divalent streptavidins. J Mol Biol. 2014; 426(1):199–214. https://doi.org/10.1016/j.jmb.2013.09.016 PMID: 24056174; PubMed Central PMCID: PMCPMC4047826.

S1 Appendix.

Streptavidin preparation

Streptavidin Cloning

SA variants were obtained by site-directed mutagenesis of plasmids encoding Strep-Tactin constructs, whose sequence is similar to streptavidin [1], using a polymerase chain reaction and subsequent blunt-end ligation. By DNA sequencing (Eurofins Genomics, Ebersberg, Germany), we checked all final open reading frames.

Streptavidin Expression

The different SA subunits were expressed separately in *E.coli* BL21(DE3)-CodonPlus cells (Agilent Technologies, Santa Clara, USA). Plasmids encoding for different SA constructs, were transferred into *E.coli* BL21(DE3)-CodonPlus cells. Cells were grown at 37°C in pure LB Medium to build up antibiotic resistance, spread on an agar plate containing the appropriate antibiotic, and grown for 18 h at 37°C. We inoculated a preculture (8 ml LB medium, 1:1000 antibiotic) and grew the cells for 15 h at 37°C. We added preculture to the expression medium (500 ml SB medium with 20 mM KH_2PO_4 and 1:1000 antibiotic) until an optical density (absorbance at 600 nm) $OD_{600} = 0.1$ was reached. The expression culture was grown at 37°C until the optical density read $OD_{600} = 0.8$. After adding 1:5000 IPTG, the culture was grown for 15 h at 18°C. Then, it was centrifuged at 24,000 × g for 15 min. A bacterial pellet formed and was stored at -80 °C.

Streptavidin Purification

During all steps, samples were kept at 4 °C or on ice, respectively. Bacterial pellets for functional and non-functional subunits were weighed and then lysed separately in 5 ml Bacterial Protein Extraction Reagent (B-PER; Thermo Scientific, Rockford, USA) per gram bacterial pellet. We added 1 mg Lysozyme (Carl Roth GmbH & Co. KG, Karlsruhe, Germany) and 50 µg DNase I (Roche Diagnostics GmbH, Mannheim, Germany) per gram bacterial pellet and placed the tube with the solution for 20 min on a rolling shaker. To lyse the bacteria completely, each of the dissolved pellets was sonicated. We then centrifuged the solutions with 60,000 × g for 30 min. As our protein formed inclusion bodies, we discarded the supernatants and resuspended each pellet in lysis buffer (PBS, 1 mM DTT, 0.1 % Triton X-100, pH 7.4). Sonication, centrifugation and resuspension steps were repeated until the supernatants were clear solutions. Each pellet was then resuspended in a denaturation buffer (PBS, 6 M guanidine hydrochloride, pH 7.5), sonicated and centrifuged. We kept the supernatants and measured the absorption at 280 nm. The solutions were then mixed in a ratio of 1:10 (functional subunits with His-tag to non-functional subunits) according to the measured absorption. We slowly pipetted the mixture into 500 ml of refolding buffer (PBS, 10 mM β-mercaptoethanol, pH 7.4) and placed it on a magnetic stirrer for 15 h.

The solution was centrifuged at 14,000 × g for 10 min. The supernatant was filtered through a hydrophilic 0.22 µm MF-Millipore Membrane and loaded on a 5 ml HisTrap FF (GE Healthcare, Little Chalfont, UK) that had been equilibrated with binding buffer (PBS, 10 mM imidazole, pH 7.4). After washing the loaded column with binding buffer, the recovery of the protein was accomplished using a gradient elution (elution buffer: PBS, 250 mM imidazole, pH 7.4). The flow through was fractionated. Fractions were analyzed using absorption

spectroscopy and gel electrophoresis. Fractions containing SA were dialyzed against PBS and stored at 4 °C.

References

1. Baumann F, Bauer MS, Milles LF, Alexandrovich A, Gaub HE, Pippig DA. Monovalent Strep-Tactin for strong and site-specific tethering in nanospectroscopy. Nat Nanotechnol. 2016;11(1):89-94. doi: 10.1038/nnano.2015.231. PubMed PMID: 26457965.

S2. Appendix.

Exemplary force-distance curves

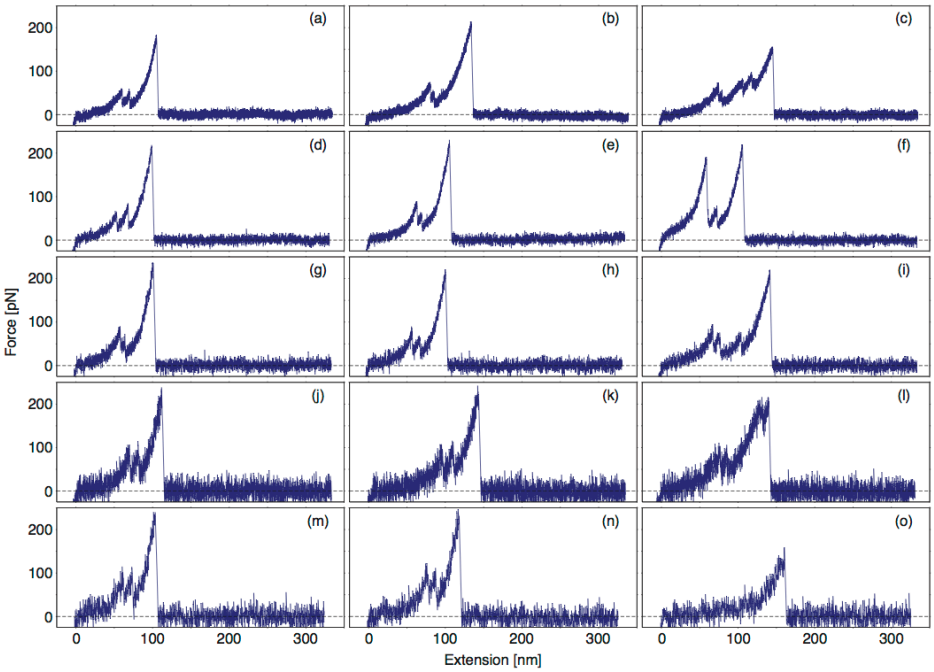

Fig A. Exemplary force-distance curves. Force-extension data recorded for different pulling velocities: (a-c) 200 nm/s, (d-f) 800 nm/s, (g-i) 2,000 nm/s, (j-l) 5,000 nm/s, and (m-o) 10,000 nm/s. The curves depicted in the left and in the middle column show a clear unfolding pattern of the calibration domain indicating specific single-molecule interaction. The curves depicted in the right column show interaction, but no clear unfolding pattern of the calibration domain is visible. These curves were thus not considered for further evaluation. The curves in (c), (i), and (l) are most probably caused by interaction of more than one biotin:mSA pair. For the curve in (f), a ddFLN4-like pattern is visible, but the unfolding force of the calibration domain is too high. Unspecific sticking of PEG or pulling with unfolded ddFLN4 may have caused the curve shown in (o).

S3 Appendix.

Long-term SMFS measurement

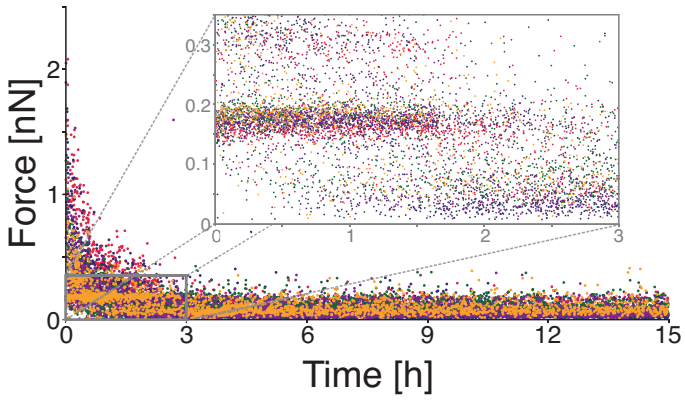

Fig A. Interaction of cantilever and surface over the course of the measurement. The force of the last peak in all force-extension curves that showed interaction between cantilever and surface are plotted over time. The different colors correspond to the different retraction velocities, with the color-coding being the same as in the main text. At the beginning of the measurement, multiple interactions give rise to high rupture forces. During the first 2.5 h (inset), a lot of specific single-molecule interactions are present resulting in a band of colored circles at about 200 pN. Wear out effects of cantilever and surface functionalization cause an increase of unspecific low-force interaction. For some of these, ddFLN4 unfolding is seen causing a small but broad unbinding peak at 100-160 pN in the histogram of rupture forces (Fig B).

S3 Appendix.

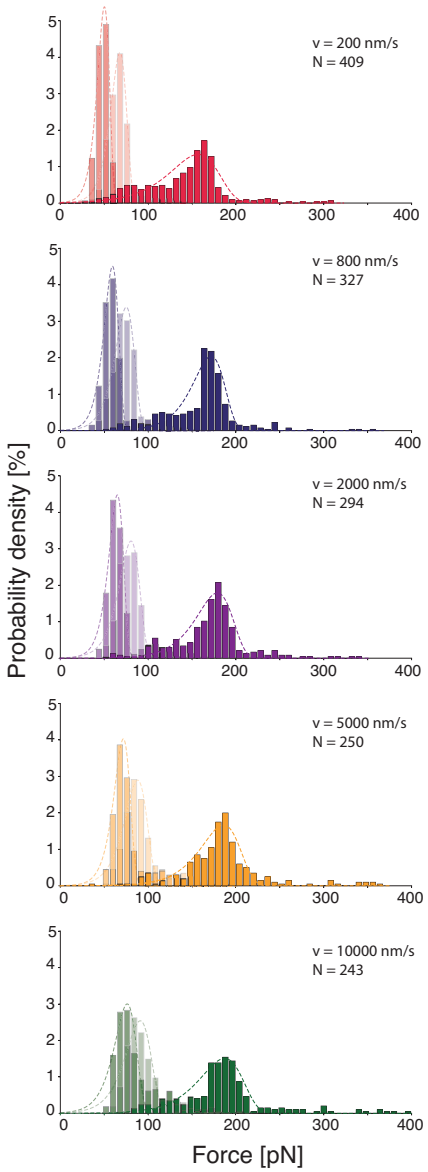

Fig B. Force histograms for a 15 h measurement. Unfolding and unbinding forces are plotted in the same manner as for Figure 6. For this experiment, the spring constant of the cantilever was 53 pN/nm. For this measurement, a second peak at lower forces is visible for the unbinding forces. From the course of the measurement (Fig A), it is obvious that the amount of low unbinding forces is insignificant in the first 2.5 h of the measurement. Therefore, the second peak cannot be caused by different binding states of biotin and mSA. The absence of a second binding state is further substantiated by the fact that for the lower unbinding forces, the unfolding forces of ddFLN4 are not shifted towards lower forces. As suggested by Schoeler et al. [1], such a bias occurs if there is an overlap of the probability distributions corresponding to unfolding and unbinding. Since they mostly occur for the slow retraction velocities, i.e. for long surface contact, we attribute these low unbinding forces to unspecific sticking of the cantilever to the surface resulting in ddFLN4 like force-extension patterns. Specific interaction at high forces was yet still detectable after 15 h of continuous measurement at room temperature. The time scale for the undisturbed interaction, i.e. without the additional low unbinding forces, is still sufficient for all immobilization and labeling applications of mSA envisioned in the main text.

S3 Appendix.

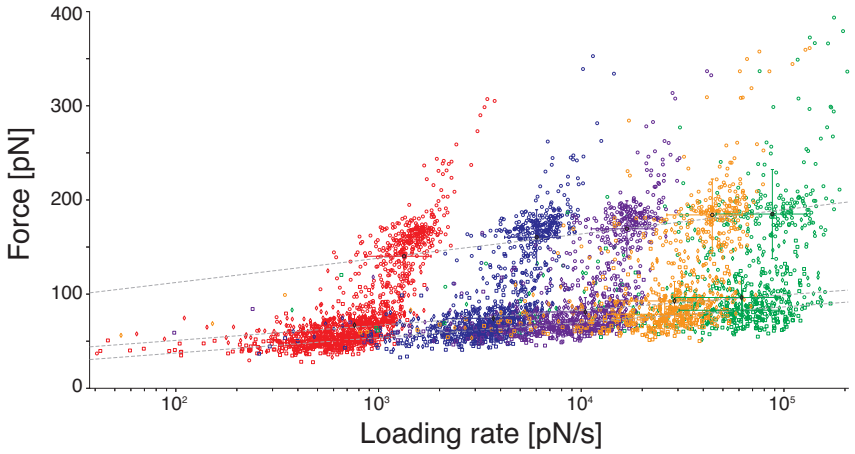

Fig C. Bell-Evans plot for a 15 h measurement. Data and color-coding are the same as in Fig B. Unfolding forces of ddFLN4 are plotted with open squares and diamonds, unbinding forces for biotin:mSA with open circles. Dashed lines are linear fits to the centers of gravity (shown as filled circles and diamonds) of the distributions of forces and loading rates, respectively. Colored crosses indicate the corresponding standard deviations. We find $\Delta x_0 = (0.59 \pm 0.06)$ nm and $k_{off,0} = 1 \times 10^{-2}$ s^{-1} for the first unfolding step of ddFLN4, $\Delta x_0 = (0.58 \pm 0.04)$ nm and $k_{off,0} = 7 \times 10^{-2}$ s^{-1} for the second unfolding step of ddFLN4, and $\Delta x_0 = (0.37 \pm 0.03)$ nm and $k_{off,0} = 4 \times 10^{-4}$ s^{-1} for the rupture of the biotin:mSA-complex.

References

1. Schoeler C, Verdorfer T, Gaub HE, Nash MA. Biasing effects of receptor-ligand complexes on protein-unfolding statistics. Phys Rev E. 2016;94(4-1):042412. doi: 10.1103/PhysRevE.94.042412. PubMed PMID: 27841541.

S4 Appendix.

Estimating the contour lengths of PEG and ddFLN4

In our experiments we use polyethylene glycol with a molecular weight of 5,000 g/mol. The molar mass of PEG is given by $(18.02 + 44.05 \times n)$ g/mol, where n is the number of subunits. For PEG5000, the number of subunits is $n = 113$. The net length of a segment is reported to be in the range of 0.278 nm to 0.358 nm depending on the orientation of the bonds [1]. We thus estimate the contour length of a PEG5000 polymer to be in the range of 31 nm to 40 nm. In this estimation, *N*-Hydroxysuccinimide and maleimide are not considered.

Our ddFLN4 consists of 101 amino acids. Assuming a length of 0.36 nm per amino acid, the contour length of the pure ddFLN4 reads 36 nm. We are neither taking into account additional length caused by linkers nor are we correcting for the end-to-end-distance of the folded ddFLN4, when considering the contour length increment upon unfolding.

References

1. Oesterhelt F, Rief M, Gaub HE. Single molecule force spectroscopy by AFM indicates helical structure of poly(ethylene-glycol) in water. New Journal of Physics. 1999;1(1):6.

S5 Appendix.

Formulas

Bell-Evans distribution

$$p(F) = \frac{k_{off,0}}{\dot{F}} \cdot e^{\frac{F\Delta x_0}{k_B T}} \cdot e^{\left(\frac{k_{off,0} k_B T}{\dot{F}\ \Delta x_0}\left(1 - e^{\left(\frac{F\Delta x_0}{k_B T}\right)}\right)\right)}$$

Loading-rate ($\dot{F}$) dependence of unbinding or unfolding force (F^*)

$$F^*(\dot{F}) = \frac{k_B T}{\Delta x_0} \log\left(\frac{\dot{F}}{k_{off,0}} \frac{\Delta x_0}{k_B T}\right)$$

Worm-like chain model

$$F(x) = \frac{kT}{4p}\left(\left(1 - \frac{x}{l}\right)^{-2} - 1 + 4\frac{x}{l}\right)$$

Transformation into contour length space

$$L(F,x) = Re\left(\frac{xkT}{6Fp}\left(3 + 4\frac{Fp}{kT} + \frac{4\left(\frac{Fp}{kT}\right)^2 - 3\frac{F}{kT} + 9}{f(kT,F,p)} + f(kT,F,p)\right)\right)$$

$$f(kT,F,p) = \left(27 - \frac{27Fp}{2kT} + \left(6\frac{Fp}{kT}\right)^2 - \left(2\frac{Fp}{kT}\right)^3 + \frac{3}{2}\sqrt{-3\left(\frac{Fp}{kT}\right)^2\left(\left(4\frac{Fp}{kT} - 3\right)^3 - 108\right)}\right)^{\frac{1}{3}}$$

S6 Appendix.

Fitted Bell-Evans distributions shown in Fig 6

First ddFLN4 unfolding peak					
v **[nm/s]**	**200**	**800**	**2,000**	**5,000**	**10,000**
$\dot{F}$ **[pN/s]**	768	3,519	10,080	29,010	66,710
F **[pN]**	66	75	83	89	90
Δx_0 **[nm]**	0.56	0.47	0.37	0.42	0.42
$k_{off,0}$ **[s^{-1}]**	7×10^{-3}	7×10^{-2}	6×10^{-1}	4×10^{-1}	7×10^{-1}
Second ddFLN4 unfolding peak					
v **[nm/s]**	**200**	**800**	**2,000**	**5,000**	**10,000**
$\dot{F}$ **[pN/s]**	701	3,609	9,841	29,820	76,030
F **[pN]**	59	70	78	87	94
Δx_0 **[nm]**	0.47	0.50	0.41	0.42	0.34
$k_{off,0}$ **[s^{-1}]**	1×10^{-1}	9×10^{-2}	4×10^{-1}	5×10^{-1}	2
Biotin:mSA unbinding peak					
v **[nm/s]**	**200**	**800**	**2,000**	**5,000**	**10,000**
$\dot{F}$ **[pN/s]**	1,736	7,469	20,680	52,390	111,900
F **[pN]**	201	212	217	222	230
Δx_0 **[nm]**	0.33	0.35	0.37	0.28	0.22
$k_{off,0}$ **[s^{-1}]**	2×10^{-5}	9×10^{-6}	8×10^{-6}	1×10^{-3}	2×10^{-1}

Table A. Fitted Bell-Evans distributions shown in Fig 6. To the histograms shown in Fig 6, Bell-Evans distributions were fitted. Mean loading rate used for the fit, most probable rupture force determined from the fit, and fitting parameters (distance to transition state and zero-force off-rate) are listed for the five retraction velocities and the different force peaks.

S7 Appendix.

Sequences of protein constructs

Functional core SA subunit with an N-terminal His-tag (green) and a unique cysteine (cyan):

MGSSHHHHHHMCGSEAGITGTWYNQLGSTFIVTAGADGALTGTYESAVGNAESRY
VLTGRYDSAPATDGSGTALGWTVAWKNNYRNAHSATTWSGQYVGGAEARINTQW
LLTSGTTEANAWKSTLVGHDTFTKVKPSAAS

Functional core SA subunit:

MEAGITGTWYNQLGSTFIVTAGADGALTGTYESAVGNAESRYVLTGRYDSAPATDG
SGTALGWTVAWKNNYRNAHSATTWSGQYVGGAEARINTQWLLTSGTTEANAWKS
TLVGHDTFTKVKPSAAS

Non-functional core SA subunit with three mutations (red; N23A, S27D, S45A):

MEAGITGTWYAQLGDTFIVTAGADGALTGTYEAAVGNAESRYVLTGRYDSAPATDG
SGTALGWTVAWKNNYRNAHSATTWSGQYVGGAEARINTQWLLTSGTTEANAWKS
TLVGHDTFTKVKPSAAS

YbbR-tagged (magenta) ddFLN4 construct with N-terminal His-tag (green) and C-terminal cysteine (cyan). A cysteine that could potentially be accessible for binding to maleimide was mutated to serine (red; C18S):

MDSLEFIASKLAHHHHHHGSADPEKSYAEGPGLDGGESFQPSKFKIHAVDPDGVHRT
DGGDGFVVTIEGPAPVDPVMVDNGDGTYDVEFEPKEAGDYVINLTLDGDNVNGFPK
TVTVKPAPGSC

YbbR-tagged (yellow) superfolder GFP construct with N-terminal His-tag (green) and cysteine (cyan) for tethering. A cysteine that could potentially be accessible for binding to maleimide was mutated to serine (red; C48S):

MGSSHHHHHHLEVLFQGPGHMCGSGSMSKGEELFTGVVPILVELDGDVNGHKFSVR
GEGEGDATIGKLTLKFISTTGKLPVPWPTLVTTLTYGVQCFSRYPDHMKRHDFFKSA
MPEGYVQERTISFKDDGKYKTRAVVKFEGDTLVNRIELKGTDFKEDGNILGHKLEYN
FNSHNVYITADKQKNGIKANFTVRHNVEDGSVQLADHYQQNTPIGDGPVLLPDNHY
LSTQTVLSKDPNEKRDHMVLHEYVNAAGITHGMDELYKSGSGSASDSLEFIASKLA

S8 Appendix.

Measuring with mSA immobilized on the cantilever

To test the stability of mSA as an anchor for SMFS, we also performed measurements in the opposite configuration, i.e. attaching mSA to the cantilever and biotinylated proteins to the surface (Figures S5 and S6). In this configuration, refolding of the control domain is unnecessary, because for every force-distance curve a new calibration domain is available on the surface. We used biotinylated GFP, whose unfolding pattern is well characterized [1], as calibration domain.

For these measurements, the distribution of rupture forces is much broader and slightly shifted to lower forces compared to the measurements with mSA on the surface. As we find the same effect, when immobilizing biotinylated ddFLN4 on the surface, we suspect shift and broadening of the distributions to be caused by slow degradation of the mSA molecules on the cantilever. This could imply that in this specific pulling geometry unbinding of biotin involves partial unfolding of the functional mSA subunit. To probe this hypothesis, steered molecular dynamics simulations could be helpful, but this is beyond the scope of this study.

S8 Appendix.

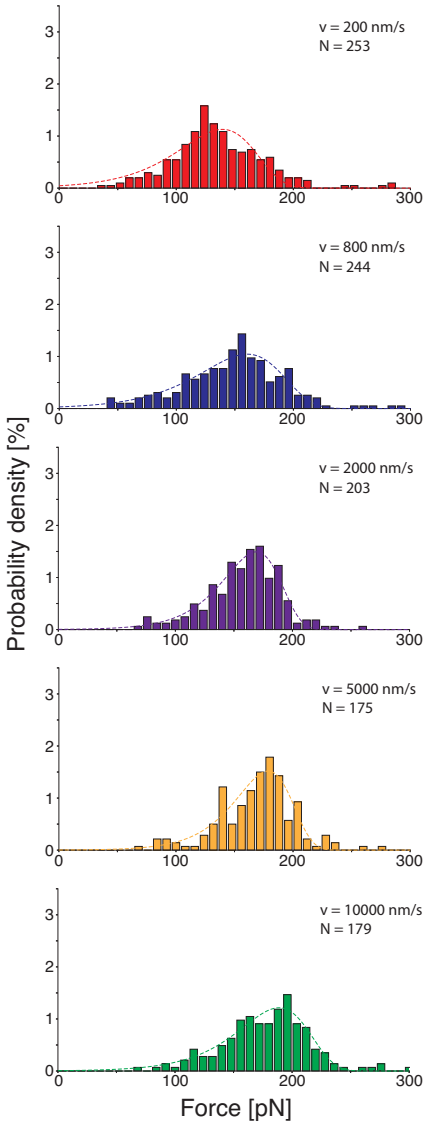

Fig A. Force Histograms, when measuring with mSA immobilized on the cantilever. For this measurement, mSA was immobilized on the cantilever and biotinylated GFP was attached to the surface. The spring constant of the cantilever was $k = 69.8$ pN/nm. The dashed lines show independent fits of Bell-Evans distributions to the force histograms.

S8 Appendix.

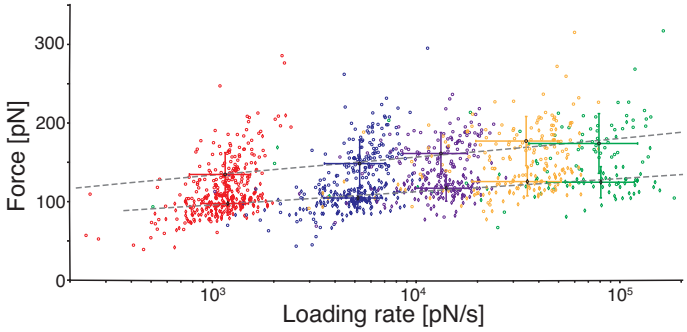

Fig B. Dynamic Force Spectrum for unfolding of GFP and unbinding of biotin:mSA. Color-coding is the same as in Fig A. Unfolding forces of GFP are plotted with open diamonds, rupture forces of the complex with open circles. Dashed lines are linear fits to the centers of gravity (shown as filled circles and diamonds) of the distributions of forces and loading rates, respectively. Colored crosses indicate the corresponding standard deviations. We find $\Delta x_0 = (0.56 \pm 0.08)$ nm and $k_{off,0} = 2 \times 10^{-4}\ s^{-1}$ for the unfolding of GFP and $\Delta x_0 = (0.39 \pm 0.05)$ nm and $k_{off,0} = 3 \times 10^{-4}\ s^{-1}$ for the rupture of the biotin:mSA-complex.

References

1. Dietz H, Rief M. Exploring the energy landscape of GFP by single-molecule mechanical experiments. Proc Natl Acad Sci U S A. 2004;101(46):16192-7. doi: 10.1073/pnas.0404549101. PubMed PMID: 15531635; PubMed Central PMCID: PMCPMC528946.

5.2 Publication P5: Dronpa: A Light-Switchable Fluorescent Protein for Opto-Biomechanics

In this work, the mechanics of the switchable dimers formed by the fluorescent protein pdDronpa1.2 were investigated. Therefore, the monomers forming the dimer were genetically connected with a tether, such that upon dissociation of the dimer, recurring association is promoted. The construct was investigated using SMFS based on AFM together with illumination provided by a TIRF microscope. Experiments on connected dimer molecules showed unfolding peaks and the associated release of contour length, which could be assigned to dimer interface opening and individual dimer unfoldings. Interface opening occurred with most probable rupture forces around 80 pN. By switching the dimer to the dark state, *i.e.* after laser illumination with light of 488 nm wavelength, it could be shown that upon application of tension force peaks and contour length associated to interface opening vanishes. These findings suggest that optically switching the dimer induces dimer dissociation and interface release.

The work demonstrates the possibility of mechanically and optically induced dimer interface opening in order to control dimer association. With interface rupture forces higher than physiological forces, this molecule can potentially be used to carry cryptic sites within its interface to allow the investigation of mechanotransduction and signaling, thereby extending the current toolbox of Opto-Biomechanics.

Dronpa: A Light-Switchable Fluorescent Protein for Opto-Biomechanics

by

Res Jöhr, Magnus S. Bauer, Leonard C. Schendel, Carleen Kluger, and Hermann E. Gaub

published in

Nano Letters, 2019, 19, 3176-3181, doi: 10.1021/acs.nanolett.9b00639

Reprinted with permission from Jöhr *et al.* [91]
Copyright American Chemical Society.

NANO LETTERS
Cite This: Nano Lett. 2019, 19, 3176−3181
Letter
pubs.acs.org/NanoLett

Dronpa: A Light-Switchable Fluorescent Protein for Opto-Biomechanics

Res Jöhr,* Magnus S. Bauer, Leonard C. Schendel, Carleen Kluger, and Hermann E. Gaub*

Lehrstuhl für Angewandte Physik and Center for Nanoscience, Ludwig-Maximilians-Universität, Munich 80799, Germany

Supporting Information

ABSTRACT: Since the development of the green fluorescent protein, fluorescent proteins (FP) are indispensable tools in molecular biology. Some FPs change their structure under illumination, which affects their interaction with other biomolecules or proteins. In particular, FPs that are able to form switchable dimers became an important tool in the field of optogenetics. They are widely used for the investigation of signaling pathways, the control of surface recruitment, as well as enzyme and gene regulation. However, optogenetics did not yet develop tools for the investigation of biomechanical processes. This could be leveraged if one could find a light-switchable FP dimer that is able to withstand sufficiently high forces. In this work, we measure the rupture force of the switchable interface in pdDronpa1.2 dimers using atomic force microscopy-based single molecule force spectroscopy. The most probable dimer rupture force amounts to around 80 pN at a pulling speed of 1600 nm/s. After switching of the dimer using illumination at 488 nm, there are hardly any measurable interface interactions, which indicates the successful dissociation of the dimers. Hence this Dronpa dimer could expand the current toolbox in optogenetics with new opto-biomechanical applications like the control of tension in adhesion processes.

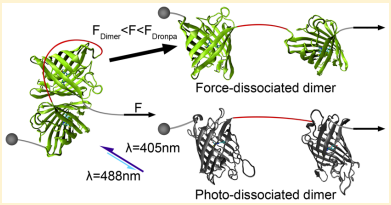

KEYWORDS: *Optogenetics, biomechanics, Dronpa, single molecule force spectroscopy, atomic force microscopy*

Downloaded via LMU MUENCHEN on January 16, 2020 at 15:30:02 (UTC).
See https://pubs.acs.org/sharingguidelines for options on how to legitimately share published articles.

Light-switchable fluorescent proteins (ls-FP) like the green fluorescent protein (GFP) have become an essential tool in biology for imaging and tracking of processes inside cells.[1−5] Beyond that, optogenetic methods employ them to even dynamically control such processes.[6−8] These tools exploit the fact that ls-FPs change their structure upon irradiation with light of a suitable wavelength. Since the protein function is directly encoded in its structure, this alters the way the FP interacts with its environment. For example, light alters the affinity of light-inducible dimerizers to the corresponding ligand. Hence, the association of these dimers can be directly controlled using light pulses.[9−12] This has been utilized for subcellular localization of proteins[13−15] as well as gene and enzyme regulation.[6,16,17] In the broader context, optogenetic tools have been employed for achieving synaptic control and to study signaling network dynamics.[8]

This list of potential applications, however, does not include methods for biomechnical investigations. It is known that many processes in cells are controlled by forces.[18,19] Cells continuously sense their environment using mechanosensors in the cell membrane, i.e., the focal adhesions. From there, the signals are transduced and affect the organization of the cytoskeleton and with it the cell shape or cell migration and also more complex processes like cell division and differentiation.[20−27] So far, such processes could be potentially investigated using static FP force sensors that lose their fluorescence when unfolded[28−30] or FRET based tension sensors. However, this does not allow for dynamic control or triggering of force-induced reactions, e.g., by revealing a cryptic binding site.[31] This lack of mechanobiology applications in the optogenetics toolbox could be diminished if robust ls-FPs with a sufficiently high interface rupture force could be found or designed.

In this work, we investigate the ls-FP Dronpa, which is known from optogenetics.[17,32,33] It is derived from a tetrameric FP found in Pectiniidae corals and has a characteristic β-barrel structure similar to GFP.[34] It has a remarkable photostability and was shown to be switchable more than 50 times between its dark and bright fluorescent state.[35] The binding interfaces were further modified to yield a dimeric Dronpa variant.[17] This variant has successfully been used to control the accessibility of the active site of kinases and thus their activity as well as for gene regulation.[32,33] Here we investigate the interface interaction in the pdDronpa1.2 dimer[32] (see Figure 1a), by using atomic force microscopy (AFM)-based single molecule force spectroscopy (SMFS). The results reveal a most probable interface rupture force of 80 pN in the bright state that is no longer detectable when switched to the dark state. Hence the dimer association can be controlled by light as well as by force. This opens the way for possible applications of this system in biomechanics studies.

Received: February 13, 2019
Revised: March 25, 2019
Published: March 26, 2019

ACS Publications © 2019 American Chemical Society

DOI: 10.1021/acs.nanolett.9b00639
Nano Lett. 2019, 19, 3176−3181

Nano Letters Letter

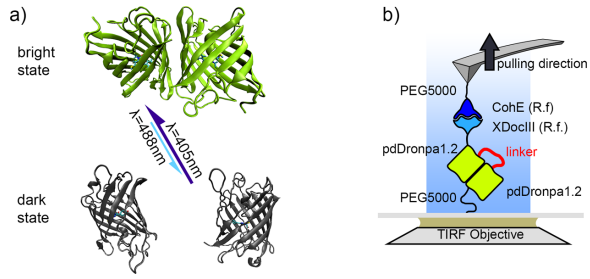

Figure 1. (a) Crystal structure of the fluorescent and dark state of Dronpa (PDB: 6D39 (bright) and 2POX (dark)). The bright state can be switched to the dark one by intense irradiation with blue light (λ = 488 nm). The backswitching is triggered by dim light at 405 nm. (b) Scheme of the experimental setup used for AFM-based SMFS.

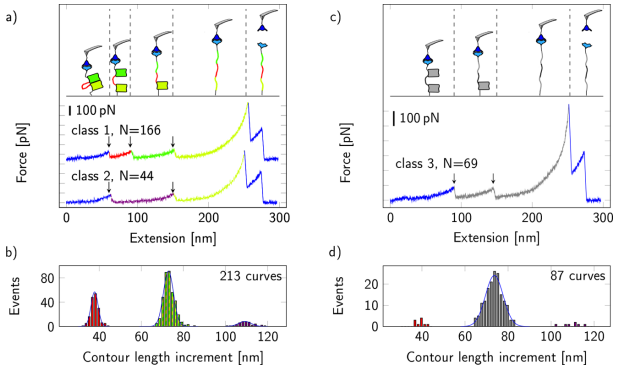

Figure 2. Exemplary force extension curves and contour length histograms with Gaussian fits from SMFS of the pdDronpa1.2 dimer. Unfolding events that are specific for the Dronpa dimer are indicated with arrows. Blue parts are from the PEG stretching as well as the specific XDocIII/CohE rupture. (a and b) Results of pdDronpa1.2 dimers prepared in the bright state. The red part represents the interface rupture, and the green parts represent the pdDronpa1.2 unfolding. Dronpa domains were colored slightly differently to enhance the readability of the scheme. Violet indicates the events with a supposed simultaneous rupture of the interface and unfolding of one Dronpa subunit. (c and d) Results of pdDronpa1.2 dimers prepared in the dark, nonbinding state. The fit parameters are available in the Supporting Information.

Results and Discussion. In order to characterize individual pdDronpa1.2 homodimers by SMFS, we designed a protein construct, where we linked two Dronpa domains with a flexible linker.[36] The dimer was further fused to a pulling handle, a strategy that has already been successfully applied to probe the unfolding of individual proteins.[37,38] The linker was made out of 73 amino acids, which corresponds to a contour length increment of ca. 28 nm. This increment can be easily detected in SMFS and thus facilitates the direct and simultaneous identification of the interface rupture event and the unfolding of the individual Dronpa domains in a single experiment. Figure 1b shows the complete scheme of the SMFS measurement. The protein construct is clamped between the AFM cantilever and the sample surface and then pulled apart.[38,39] The specificity of the measurement is granted by using the XDocIII/CohE cohesin dockerin receptor ligand pair from *R. flavefaciens* as a protein handle.[40] Both proteins, the Dronpa dimer and the CohE, were covalently attached to the cantilever and the sample, respectively, using polyethylene glycol (PEG) spacers with a molecular weight of 5000 Da. Switching of the Dronpa dimer was achieved via total internal reflection (TIR) illumination from below the sample slide. Initially the sample was illuminated with 405 nm light for a short instance (5 s) to prepare the proteins in the bright state that allows for intramolecular domain association. In the second part of the experiment, the sample was intermittently illuminated with 488 nm light in order to switch the domains to their dark state and to trigger dissociation of the Dronpa domains.

The force extension curves from the SMFS measurement were filtered using the specific XDocIII/CohE fingerprint interaction. A total of 213 specific curves was obtained for the domains that were prepared in the bright state (i.e., after 405 nm illumination). They could be classified into two main classes. Examples of the force extension curves are shown in Figure 2a. Besides the characteristic peak from the XDocIII/CohE rupture, the first class contains 166 curves that show three characteristic peaks (indicated with arrows in Figure 2a). Remarkably, these rupture events had similar unfolding forces of around 80 pN. The second class contained 44 curves and revealed only two peaks with similar unfolding forces. The measurement of the dark state dimers yielded 87

DOI: 10.1021/acs.nanolett.9b00639
Nano Lett. 2019, 19, 3176−3181

Nano Letters Letter

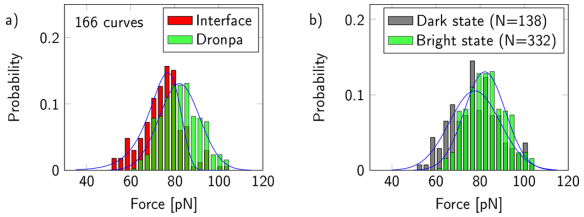

Figure 3. Normalized rupture force histograms from SMFS. The distribution of the interface rupture was fitted using the Bell–Evans model. The histograms of the Dronpa unfolding were fitted with normal distributions. (a) Distributions for the Dronpa in the bright state and for the interface. (b) Comparison of histograms for Dronpa after illumination with 405 nm (bright state) and 488 nm (dark state). The dark state histogram was composed of curves without an interface rupture event. It presumably contains a contribution from dissociated Dronpa domains in the bright state. The fit parameters are given in the Supporting Information.

specific curves (Figure 2c,d). Most of the (N = 69) curves belong to a single class with two Dronpa related peaks.

The contour length increments l_c of the force peaks were calculated from fits based on the worm-like chain model with a fixed persistence length of 0.4 nm. The results for the bright state experiment are displayed in the histogram in Figure 2b. They reveal peaks at 37.8, 72.9, and 109.2 nm. The peak at 73 nm is found in all curve classes. If we consider the l_c of a single amino acid to be around 0.35–0.38 nm[41] and take into account that Dronpa has about 210 structured amino acids with an end-to-end distance of 2.5 nm, it follows that the expected l_c for Dronpa unfolding is in the range from 71 to 77 nm. This is in good agreement with our experimental value. Therefore, we attribute this force peak to the unfolding of the Dronpa domains. The remaining peaks at 37.8 and 109.2 nm in Figure 2b can be explained with the rupture of the interface. The peak at 37.8 nm is solely attributed to the linker that connects the two Dronpa domains. Hereby we note that the measured contour length increment of the linker is indeed longer than the expected 28 nm calculated from the primary structure. However, this conclusion is justified because we have to include the unstructured amino acids from the two Dronpa domains that were excluded from the previous calculation of the Dronpa contour length. The contour length increment of 109.2 nm can, however, not be explained by a single domain unfolding event. Since its length corresponds to the sum of one Dronpa unfolding and the dimer interface, we suggest that this unfolding event is linked to the rupture of the dimer and simultaneous unfolding of one of the Dronpa domains. This is further corroborated by the fact that the unfolding of the single Dronpa was always observed after the event with l_c = 109.2 nm (see Figure 2a). As we will show later, it is likely that the Dronpa domain unfolds first and consequently induces the rupture of the interface.

In contrast, Figure 2c shows that curves with force peaks associated with the interface, i.e., contour length increments of 37.8 and 109.2 nm, were significantly reduced after illumination at 488 nm (see Figure 2d). Analysis of the force extension curves reveals that 80% of the curves (69 out of 87 curves) show only the characteristic signature of the unfolding of two Dronpa domains but no interface rupture (see Figure 2c). The remaining 18 curves showed characteristic force distance traces similar to the ones of the associated dimers shown in Figure 2a. This indicates that the dimer is either in an associated or dissociated state. Potential intermediate states with a lower rupture force, for example, in mixed dimers, where one of the domains is in the bright and the other in the dark state, could not be detected. If they exist, they are expected to be relatively weak. Hence we suggest that the dimer behaves as an effective two-state system, where the interface rupture can only be observed using AFM if both Dronpa domains are in the bright state and associated. This behavior would be favorable for potential applications. It facilitates the dissociation under blue light and would compensate for the low quantum efficiency for the switching from the bright to the dark state (QE_{bd} = 0.00032), which is much lower than vice versa (QE_{db} = 0.37).[34,42] We note that the observed two-state behavior might be an oversimplification of the actual processes. For example, we have no data on the fluorescence during individual pulling experiments and thus cannot exclude that the Dronpa domains lose their fluorescence during the interface rupture. However, since the determined l_c is in good agreement with the expected tertiary structure of the bright state, we assume that the domains remain functional.

In order to understand the mechanics of the dimer rupture, i.e., the proposed simultaneous rupture of the interface and the unfolding of the Dronpa domain, we analyzed the corresponding rupture force distributions (Figure 3a). The distribution of the interface was fitted using the Bell–Evans model.[43,44] The most probable rupture force for the selected pulling speed of 1600 nm/s was 76.9 ± 1.1 pN, which is comparable to photochemical single molecule switches.[45−47] The histogram of the Dronpa unfolding was fitted using a normal distribution with a most probable rupture force of 82.1 ± 1.1 pN. Hence, the individual Dronpa domain is only slightly more stable than the interface. Its unfolding force is comparable to other fluorescent proteins with a β-barrel structure.[28,48] Because of the overlap of the two force distributions, it follows that unfolding of a Dronpa domain might occur before the rupture of the interface as was also suggested from the experiments.

Comparing the rupture force probability distributions of the dark and bright states shown in Figure 3b, one observes that they are slightly shifted with respect to each other. The dark state distribution has a maximum at 77.6 ± 2.5 pN and a standard deviation of σ = 10.3 pN. It is thus weaker and has a broader distribution compared to the bright state with 82.1 ± 1.1 pN and σ = 9.3 pN. The lower unfolding force is in agreement with research from Mizuno et al. where they found that illumination of Dronpa with blue light causes flexibility of the seventh β-strand inside the β-barrel structure, thus probably weakening the protein fold (see Figure 1a).[49] This effect might facilitate the dissociation of the dimer if it is

DOI: 10.1021/acs.nanolett.9b00639
Nano Lett. 2019, 19, 3176−3181

switched to the dark state. The fact that there is a difference between the two distributions is further evidence that the fluorescent Dronpa domains remain in their bright state during interface rupture.

In summary, we investigated light-switchable pdDronpa1.2-linker-pdDronpa1.2 protein constructs using AFM-based SMFS. At a retraction speed of 1600 nm/s, we found that the interface is able to withstand a force of around 80 pN. This is a relatively high stability, considering that the dimer is supposed to be stabilized by hydrophobic interactions.[17] It is notable that most Dronpa domains keep their fold during interface rupture. Comparing to studies of other β-barrel FPs, this suggests that Dronpa dimers are likely to remain functional and associated under the tensile stress that is prevalent under physiological conditions.[28,50] Further, the dimer could be dissociated under illumination with 488 nm light. The interface interaction was hardly observed in this case anymore. Taking into account the loading rate dependence of the interface strength, we expect a rupture force in the range 20−30 pN under physiological conditions.[51] This rupture force of the Dronpa dimer lies above the range of forces that are typically observed in mechanotransduction and signaling[31,52−54] but is significantly weaker than the forces found during bacterial adhesion, which can amount to several hundred pNs.[40,55,56] We thus believe that our results have strong implications for applications in the study of mechanotransduction and signaling. Dronpa is sufficiently strong to be used for manipulation of the conformation of focal adhesion proteins without the interface being pulled open. One potential application to achieve this would be the incorporation of Dronpa dimers into stretchable proteins such as talin that have cryptic binding sites, which are only accessible under tension.[31] Exchange of such cryptic domains with Dronpa dimers that hold the cryptic domain in the linker region would protect this binding site from tension forces so that reactions triggered by binding to this site become controllable by light. Our study further shows a new way to combine force application and light-induced conformational switching in AFM-SMFS as a tool by itself. This opens up the road for experiments, which employ dynamic force probes with properties that can be switched during the experiment.

Experimental Section. The experimental procedures for this study were adapted from previously published protocols.[38,39,57,58] Detailed information is given in the Supporting Information.

Protein Synthesis. The pdDronpa1.2-linker-pdDronpa1.2 constructs with the N-terminal ybbR-hexahistidine tag and C-terminal XDocIII domain from *R. flavefaciens* were assembled and subcloned into peT28a plasmids via Gibson assembly. The protein was expressed in *E. coli* NiCo21(DE3) cells using an autoinduction medium and then harvested and purified employing a standard protocol including Ni-NTA affinity chromatography.

Sample Preparation. Cover glasses were cleaned and silanized using (3-aminopropyl)-dimethyl-ethoxysilane. The amine functionalized surface was subsequently conjugated with NHS-PEG-maleimide spacers. The maleimide was reacted with Coenzyme A in order to allow Sfp phosphopantetheinyl transferase-mediated coupling to the ybbR tag of the Dronpa construct.

SMFS Measurement. Single molecule force spectroscopy was performed on a home-built TIRF-AFM.[59] TIR illumination was used for switching of the Dronpa domains, which restricted the excitation to a volume within 100 nm above the sample surface. A glucose oxidase-based oxygen scavenging system (25 U/mL glucoseoxidase, 1700 U/mL catalase, and 0.6% w/v glucose) was used in order to prevent bleaching of the Dronpa domains.

Data Analysis. Force extension curves were processed and filtered in a semiautomated way.[39] Drift compensation and peak identification was done for all curves with a tip sample interaction. The contour length increments of individual unfolding events were determined with the WLC model using a persistence length of 0.4 nm.[60] Specific curves were identified by selecting the ones that showed the characteristic rupture signature between the XDocIII handle and the CohE pulling domain[40] as well as the pdDronpa1.2 specific peak.

■ ASSOCIATED CONTENT

Supporting Information

The Supporting Information is available free of charge on the ACS Publications website at DOI: 10.1021/acs.nanolett.9b00639.

Fit parameters for the contour length distributions and the rupture force histograms, materials and methods used for recombinant protein synthesis, sample preparation, and single molecule force spectroscopy measurements (PDF)

■ AUTHOR INFORMATION

Corresponding Authors

*E-mail: res.joehr@lmu.de.

*E-mail: gaub@lmu.de.

ORCID

Res Jöhr: 0000-0002-6204-5410

Leonard C. Schendel: 0000-0002-1986-2693

Hermann E. Gaub: 0000-0002-4220-6088

Notes

The authors declare no competing financial interest.

■ ACKNOWLEDGMENTS

The authors thank T. Nicolaus for laboratory support, L.F. Milles for providing the linker sequence of the Dronpa dimers, and E. Durner and W. Ott for preparing the CohE protein constructs used for specific protein pulling during AFM-based SMFS experiments. We acknowledge funding from the German Research Foundation within the framework of the SFB1032.

■ REFERENCES

(1) Tsien, R. Y. The green fluorescent protein. *Annu. Rev. Biochem.* **1998**, *67*, 509−544.

(2) Nienhaus, K.; Ulrich Nienhaus, G. Fluorescent proteins for live-cell imaging with super-resolution. *Chem. Soc. Rev.* **2014**, *43*, 1088−1106.

(3) Chang, H.; Zhang, M.; Ji, W.; Chen, J.; Zhang, Y.; Liu, B.; Lu, J.; Zhang, J.; Xu, P.; Xu, T. A unique series of reversibly switchable fluorescent proteins with beneficial properties for various applications. *Proc. Natl. Acad. Sci. U. S. A.* **2012**, *109*, 4455−4460.

(4) Moeyaert, B.; Nguyen Bich, N.; De Zitter, E.; Rocha, S.; Clays, K.; Mizuno, H.; van Meervelt, L.; Hofkens, J.; Dedecker, P. Green-to-Red Photoconvertible Dronpa Mutant for Multimodal Super-resolution Fluorescence Microscopy. *ACS Nano* **2014**, *8*, 1664−1673.

(5) Zhou, X. X.; Lin, M. Z. Photoswitchable fluorescent proteins: ten years of colorful chemistry and exciting applications. *Curr. Opin. Chem. Biol.* **2013**, *17*, 682−690.

DOI: 10.1021/acs.nanolett.9b00639
Nano Lett. 2019, 19, 3176−3181

(6) Zhang, K.; Cui, B. Optogenetic control of intracellular signaling pathways. *Trends Biotechnol.* **2015**, *33*, 92−100.
(7) Fan, L. Z.; Lin, M. Z. Optical control of biological processes by light-switchable proteins. *Wiley Interdiscip. Rev.: Dev. Biol.* **2015**, *4*, 545−554.
(8) Repina, N. A.; Rosenbloom, A.; Mukherjee, A.; Schaffer, D. V.; Kane, R. S. At Light Speed: Advances in Optogenetic Systems for Regulating Cell Signaling and Behavior. *Annu. Rev. Chem. Biomol. Eng.* **2017**, *8*, 13−39.
(9) Yazawa, M.; Sadaghiani, A. M.; Hsueh, B.; Dolmetsch, R. E. Induction of protein-protein interactions in live cells using light. *Nat. Biotechnol.* **2009**, *27*, 941−945.
(10) Kennedy, M. J.; Hughes, R. M.; Peteya, L. A.; Schwartz, J. W.; Ehlers, M. D.; Tucker, C. L. Rapid blue-light-mediated induction of protein interactions in living cells. *Nat. Methods* **2010**, *7*, 973−975.
(11) Crefcoeur, R. P.; Yin, R.; Ulm, R.; Halazonetis, T. D. Ultraviolet-B-mediated induction of protein-protein interactions in mammalian cells. *Nat. Commun.* **2013**, *4*, 1779.
(12) Nihongaki, Y.; Suzuki, H.; Kawano, F.; Sato, M. Genetically Engineered Photoinducible Homodimerization System with Improved Dimer-Forming Efficiency. *ACS Chem. Biol.* **2014**, *9*, 617−621.
(13) Wang, H.; Vilela, M.; Winkler, A.; Tarnawski, M.; Schlichting, I.; Yumerefendi, H.; Kuhlman, B.; Liu, R.; Danuser, G.; Hahn, K. M. LOVTRAP: an optogenetic system for photoinduced protein dissociation. *Nat. Methods* **2016**, *13*, 755−758.
(14) Strickland, D.; Lin, Y.; Wagner, E.; Hope, C. M.; Zayner, J.; Antoniou, C.; Sosnick, T. R.; Weiss, E. L.; Glotzer, M. TULIPs: tunable, light-controlled interacting protein tags for cell biology. *Nat. Methods* **2012**, *9*, 379−384.
(15) Guntas, G.; Hallett, R. A.; Zimmerman, S. P.; Williams, T.; Yumerefendi, H.; Bear, J. E.; Kuhlman, B. Engineering an improved light-induced dimer (iLID) for controlling the localization and activity of signaling proteins. *Proc. Natl. Acad. Sci. U. S. A.* **2015**, *112*, 112−117.
(16) Motta-Mena, L. B.; Reade, A.; Mallory, M. J.; Glantz, S.; Weiner, O. D.; Lynch, K. W.; Gardner, K. H. An optogenetic gene expression system with rapid activation and deactivation kinetics. *Nat. Chem. Biol.* **2014**, *10*, 196−202.
(17) Zhou, X. X.; Chung, H. K.; Lam, A. J.; Lin, M. Z. Optical Control of Protein Activity by Fluorescent Protein Domains. *Science* **2012**, *338*, 810−814.
(18) Vogel, V.; Sheetz, M. Local force and geometry sensing regulate cell functions. *Nat. Rev. Mol. Cell Biol.* **2006**, *7*, 265.
(19) Beedle, A. E.; Williams, A.; Relat-Goberna, J.; Garcia-Manyes, S. Mechanobiology−chemical origin of membrane mechanical resistance and force-dependent signaling. *Curr. Opin. Chem. Biol.* **2015**, *29*, 87−93.
(20) Vandenburgh, H. H. Mechanical forces and their second messengers in stimulating cell growth in vitro. *Am. J. Physiol.: Regul., Integr. Comp. Physiol.* **1992**, *262*, R350−R355.
(21) Chicurel, M. E.; Chen, C. S.; Ingber, D. E. Cellular control lies in the balance of forces. *Curr. Opin. Cell Biol.* **1998**, *10*, 232−239.
(22) Sheetz, M. P.; Felsenfeld, D. P.; Galbraith, C. G. Cell migration: regulation of force on extracellular-matrix-integrin complexes. *Trends Cell Biol.* **1998**, *8*, 51−54.
(23) Discher, D. E.; Janmey, P.; Wang, Y.-l. Tissue Cells Feel and Respond to the Stiffness of Their Substrate. *Science* **2005**, *310*, 1139−1143.
(24) Lee, J.; Ishihara, A.; Oxford, G.; Johnson, B.; Jacobson, K. Regulation of cell movement is mediated by stretch-activated calcium channels. *Nature* **1999**, *400*, 382−386.
(25) Discher, D. E.; Mooney, D. J.; Zandstra, P. W. Growth Factors, Matrices, and Forces Combine and Control Stem Cells. *Science* **2009**, *324*, 1673−1677.
(26) Fu, J.; Wang, Y.-K.; Yang, M. T.; Desai, R. A.; Yu, X.; Liu, Z.; Chen, C. S. Mechanical regulation of cell function with geometrically modulated elastomeric substrates. *Nat. Methods* **2010**, *7*, 733−736.
(27) Elosegui-Artola, A.; Andreu, I.; Beedle, A. E.; Lezamiz, A.; Uroz, M.; Kosmalska, A. J.; Oria, R.; Kechagia, J. Z.; Rico-Lastres, P.; Roux, A.-L. L.; Shanahan, C. M.; Trepat, X.; Navajas, D.; Garcia-Manyes, S.; Roca-Cusachs, P. Force Triggers YAP Nuclear Entry by Regulating Transport across Nuclear Pores. *Cell* **2017**, *171*, 1397−1410.
(28) Dietz, H.; Rief, M. Exploring the energy landscape of GFP by single-molecule mechanical experiments. *Proc. Natl. Acad. Sci. U. S. A.* **2004**, *101*, 16192−16197.
(29) Ganim, Z.; Rief, M. Mechanically switching single-molecule fluorescence of GFP by unfolding and refolding. *Proc. Natl. Acad. Sci. U. S. A.* **2017**, *114*, 11052−11056.
(30) Saeger, J.; Hytönen, V. P.; Klotzsch, E.; Vogel, V. GFP's Mechanical Intermediate States. *PLoS One* **2012**, *7*, e46962.
(31) del Rio, A.; Perez-Jimenez, R.; Liu, R.; Roca-Cusachs, P.; Fernandez, J. M.; Sheetz, M. P. Stretching Single Talin Rod Molecules Activates Vinculin Binding. *Science* **2009**, *323*, 638−641.
(32) Zhou, X. X.; Fan, L. Z.; Li, P.; Shen, K.; Lin, M. Z. Optical control of cell signaling by single-chain photoswitchable kinases. *Science* **2017**, *355*, 836−842.
(33) Zhou, X. X.; Zou, X.; Chung, H. K.; Gao, Y.; Liu, Y.; Qi, L. S.; Lin, M. Z. A Single-Chain Photoswitchable CRISPR-Cas9 Architecture for Light-Inducible Gene Editing and Transcription. *ACS Chem. Biol.* **2018**, *13*, 443−448.
(34) Ando, R.; Mizuno, H.; Miyawaki, A. Regulated Fast Nucleocytoplasmic Shuttling Observed by Reversible Protein Highlighting. *Science* **2004**, *306*, 1370−1373.
(35) Habuchi, S.; Ando, R.; Dedecker, P.; Verheijen, W.; Mizuno, H.; Miyawaki, A.; Hofkens, J. Reversible single-molecule photoswitching in the GFP-like fluorescent protein Dronpa. *Proc. Natl. Acad. Sci. U. S. A.* **2005**, *102*, 9511−9516.
(36) Milles, L.; Gaub, H. Is mechanical receptor ligand dissociation driven by unfolding or unbinding? 2019, *biorxiv.org*, https://doi.org/10.1101/593335.
(37) Strackharn, M.; Pippig, D. A.; Meyer, P.; Stahl, S. W.; Gaub, H. E. Nanoscale Arrangement of Proteins by Single-Molecule Cut-and-Paste. *J. Am. Chem. Soc.* **2012**, *134*, 15193−15196.
(38) Ott, W.; Jobst, M. A.; Schoeler, C.; Gaub, H. E.; Nash, M. A. Single-molecule force spectroscopy on polyproteins and receptor-ligand complexes: The current toolbox. *J. Struct. Biol.* **2017**, *197*, 3−12.
(39) Jobst, M. A.; Schoeler, C.; Malinowska, K.; Nash, M. A. Investigating Receptor-ligand Systems of the Cellulosome with AFM-based Single-molecule Force Spectroscopy. *J. Visualized Exp.* **2013**, *82*, e50950.
(40) Schoeler, C.; Malinowska, K. H.; Bernardi, R. C.; Milles, L. F.; Jobst, M. A.; Durner, E.; Ott, W.; Fried, D. B.; Bayer, E. A.; Schulten, K.; Gaub, H. E.; Nash, M. A. Ultrastable cellulosome-adhesion complex tightens under load. *Nat. Commun.* **2014**, *5*, 5635.
(41) Ainavarapu, S. R. K.; Brujić, J.; Huang, H. H.; Wiita, A. P.; Lu, H.; Li, L.; Walther, K. A.; Carrion-Vazquez, M.; Li, H.; Fernandez, J. M. Contour Length and Refolding Rate of a Small Protein Controlled by Engineered Disulfide Bonds. *Biophys. J.* **2007**, *92*, 225−233.
(42) Dedecker, P.; Hotta, J.; Ando, R.; Miyawaki, A.; Engelborghs, Y.; Hofkens, J. Fast and Reversible Photoswitching of the Fluorescent Protein Dronpa as Evidenced by Fluorescence Correlation Spectroscopy. *Biophys. J.* **2006**, *91*, L45−L47.
(43) Bell, G. Models for the specific adhesion of cells to cells. *Science* **1978**, *200*, 618−627.
(44) Evans, E.; Ritchie, K. Dynamic strength of molecular adhesion bonds. *Biophys. J.* **1997**, *72*, 1541−1555.
(45) Schäfer, C.; Eckel, R.; Ros, R.; Mattay, J.; Anselmetti, D. Photochemical Single-Molecule Affinity Switch. *J. Am. Chem. Soc.* **2007**, *129*, 1488−1489.
(46) Anselmetti, D.; Bartels, F. W.; Becker, A.; Decker, B.; Eckel, R.; McIntosh, M.; Mattay, J.; Plattner, P.; Ros, R.; Schäfer, C.; Sewald, N. Reverse Engineering of an Affinity-Switchable Molecular Interaction Characterized by Atomic Force Microscopy Single-Molecule Force Spectroscopy. *Langmuir* **2008**, *24*, 1365−1370.

DOI: 10.1021/acs.nanolett.9b00639
Nano Lett. 2019, 19, 3176−3181

(47) Walhorn, V.; Schäfer, C.; Schröder, T.; Mattay, J.; Anselmetti, D. Functional characterization of a supramolecular affinity switch at the single molecule level. *Nanoscale* **2011**, *3*, 4859−4865.
(48) Perez-Jimenez, R.; Garcia-Manyes, S.; Ainavarapu, S. R. K.; Fernandez, J. M. Mechanical Unfolding Pathways of the Enhanced Yellow Fluorescent Protein Revealed by Single Molecule Force Spectroscopy. *J. Biol. Chem.* **2006**, *281*, 40010−40014.
(49) Mizuno, H.; Mal, T. K.; Wälchli, M.; Kikuchi, A.; Fukano, T.; Ando, R.; Jeyakanthan, J.; Taka, J.; Shiro, Y.; Ikura, M.; Miyawaki, A. Light-dependent regulation of structural flexibility in a photochromic fluorescent protein. *Proc. Natl. Acad. Sci. U. S. A.* **2008**, *105*, 9227−9232.
(50) Austen, K.; Ringer, P.; Mehlich, A.; Chrostek-Grashoff, A.; Kluger, C.; Klingner, C.; Sabass, B.; Zent, R.; Rief, M.; Grashoff, C. Extracellular rigidity sensing by talin isoform-specific mechanical linkages. *Nat. Cell Biol.* **2015**, *17*, 1597.
(51) Moore, S. W.; Roca-Cusachs, P.; Sheetz, M. P. Stretchy Proteins on Stretchy Substrates: The Important Elements of Integrin-Mediated Rigidity Sensing. *Dev. Cell* **2010**, *19*, 194−206.
(52) Sun, Z.; Martinez-Lemus, L. A.; Trache, A.; Trzeciakowski, J. P.; Davis, G. E.; Pohl, U.; Meininger, G. A. Mechanical properties of the interaction between fibronectin and $\alpha 5\beta 1$-integrin on vascular smooth muscle cells studied using atomic force microscopy. *Am. J. Physiol.: Heart Circ. Physiol.* **2005**, *289*, H2526−H2535.
(53) Ferrer, J. M.; Lee, H.; Chen, J.; Pelz, B.; Nakamura, F.; Kamm, R. D.; Lang, M. J. Measuring molecular rupture forces between single actin filaments and actin-binding proteins. *Proc. Natl. Acad. Sci. U. S. A.* **2008**, *105*, 9221−9226.
(54) Grashoff, C.; Hoffman, B. D.; Brenner, M. D.; Zhou, R.; Parsons, M.; Yang, M. T.; McLean, M. A.; Sligar, S. G.; Chen, C. S.; Ha, T.; Schwartz, M. A. Measuring mechanical tension across vinculin reveals regulation of focal adhesion dynamics. *Nature* **2010**, *466*, 263−266.
(55) Echelman, D. J.; Alegre-Cebollada, J.; Badilla, C. L.; Chang, C.; Ton-That, H.; Fernández, J. M. CnaA domains in bacterial pili are efficient dissipaters of large mechanical shocks. *Proc. Natl. Acad. Sci. U. S. A.* **2016**, *113*, 2490−2495.
(56) Milles, L. F.; Schulten, K.; Gaub, H. E.; Bernardi, R. C. Molecular mechanism of extreme mechanostability in a pathogen adhesin. *Science* **2018**, *359*, 1527−1533.
(57) Zimmermann, J. L.; Nicolaus, T.; Neuert, G.; Blank, K. Thiol-based, site-specific and covalent immobilization of biomolecules for single-molecule experiments. *Nat. Protoc.* **2010**, *5*, 975−985.
(58) Yin, J.; Straight, P. D.; McLoughlin, S. M.; Zhou, Z.; Lin, A. J.; Golan, D. E.; Kelleher, N. L.; Kolter, R.; Walsh, C. T. Genetically encoded short peptide tag for versatile protein labeling by Sfp phosphopantetheinyl transferase. *Proc. Natl. Acad. Sci. U. S. A.* **2005**, *102*, 15815−15820.
(59) Gumpp, H.; Stahl, S. W.; Strackharn, M.; Puchner, E. M.; Gaub, H. E. Ultrastable combined atomic force and total internal fluorescence microscope. *Rev. Sci. Instrum.* **2009**, *80*, 063704.
(60) Bustamante, C.; Marko, J.; Siggia, E.; Smith, S. Entropic elasticity of lambda-phage DNA. *Science* **1994**, *265*, 1599−1600.

DOI: 10.1021/acs.nanolett.9b00639
Nano Lett. 2019, 19, 3176−3181

Supporting Information: Dronpa: A Light-Switchable Fluorescent Protein for Opto-Biomechanics

Res Jöhr, Magnus S. Bauer, Leonard C. Schendel, Carleen Kluger, Hermann E. Gaub

Lehrstuhl für Angewandte Physik and Center for Nanoscience,
Ludwig-Maximilians-Universität, 80799, Munich

1 Fitting parameters

1.1 Distribution of Contour Length Increments

The contour length distributions were fitted using a standard distribution (1),

$$P(x) = a \cdot \exp\left\{\left(\frac{x-b}{c}\right)^2\right\}. \tag{1}$$

Table 1: Fitting parameters for the contour length distributions.

Type	a	b [nm]	c [nm]
Linker	56.89	37.80	2.38
Dronpa bright	92.25	72.92	3.40
Double rupture	8.16	109.20	4.24
Dronpa dark	24.04	73.63	5.85

1.2 Rupture Force Histograms

The rupture force distribution of the interface was fitted using the Bell-Evans Model (2),

$$P(f) = a \cdot \exp\left\{\frac{f-b}{c}\right\} \exp\left\{\left[1 - \exp\left\{\frac{f-b}{c}\right\}\right]\right\}. \tag{2}$$

The remaining force distributions were fitted using a standard distribution (1).

Table 2: Fitting parameters for the rupture force histograms.

Type	a	b [pN]	c [pN]
Interface	0.147	76.87	6.88
Dronpa bright	0.131	82.14	13.11
Dronpa dark	0.105	77.60	16.28

Materials and Methods

The experimental procedures for this study were adapted from previously published protocols that can be found in [1, 2, 3, 4].

Protein Synthesis

The pdDronpa1.2 dimers[5] with internal linker[6] and with N-terminal ybbR-hexahistidine tag and C-terminal XDocIII domain from *Ruminococcus flavefaciens*[7] were assembled using Genestrings (GeneArt - ThermoFisher Scientific, Regensburg, Germany). The complete sequence is given below:
ybbr-HIS-pdDronpa1.2-linker-pdDronpa1.2-linker-XMod-DocIII (R.f):

MDSLEFIASKLAHHHHHHGSSVIKPDMKIKLRMEGAVNGHPFAIEGVGLGKPFEGKQSID
LKVKEGGPLPFAYDILTTAFCYGNRVFAKYPENIVDYFKQSFPEGYSWERSMNYEDGGIC
NATNDITLDGDCYIYEIRFRGTNFPANGPVMQKRTVKWEPSTENLYVRDGVLKGDVIMAL
SLEGGGHYRCDFKTTYKAKKVVQLPDYHFVDHHIEIKSHDKDYSNVNLHEHAEAHSELPR
QAKGGGSAGGSGSGSSGGSSGASGTGTAGGTGSGSGTGSGGGSGGGSEGGGSEGGGSEGG
GSEGGGSEGGGSGGGSSVIKPDMKIKLRMEGAVNGHPFAIEGVGLGKPFEGKQSIDLKVK
EGGPLPFAYDILTTAFCYGNRVFAKYPENIVDYFKQSFPEGYSWERSMNYEDGGICNATN
DITLDGDCYIYEIRFRGTNFPANGPVMQKRTVKWEPSTENLYVRDGVLKGDVIMALSLEG
GGHYRCDFKTTYKAKKVVQLPDYHFVDHHIEIKSHDKDYSNVNLHEHAEAHSELPRQAKG
SGSGSGSVVPNTVTSAVKTQYVEIESVDGFYFNTEDKFDTAQIKKAVLHTVYNEGYTGDD
GVAVVLREYESEPVDITAELTFGDATPANTYKAVENKFDYEIPVYYNNATLKDAEGNDAT
VTVYIGLKGDTDLNNIVDGRDATATLTYYAATSTDGKDATTVALSPSTLVGGNPESVYDD
FSAFLSDVKVDAGKELTRFAKKAERLIDGRDASSILTFYTKSSVDQYKDMAANEPNKLWD
IVTGDAEEE

The protein construct for the functionalization of the cantilever was CohE-HIS-ybbR and was already available in our lab from previous studies.
Subcloning of the Dronpa construct into modified peT28a plasmids was done via Gibson assembly (1 h, 50°C).[8] (10 µl 2x HiFi MasterMix (New England Biolabs), 0.1 nmol vector, 0.2 nmol insert). Primers for PCR amplification were obtained from Eurofins Genomics. *E.coli* $DH5\alpha$ cells (Life Technologies GmbH) were transformed with the Gibson assembly product via heat shock at 42°C for 1 min and then incubated in 1 ml SOC medium for 1 h at 37°C. 200 µl of the culture were spread on an agar plate containing 50 µg ml^{-1} kanamycin (Carl Roth GmbH) and grown overnight at 37°C. Single clones were picked and used for inoculation of an overnight preculture in 5 ml LB medium containing 50 µg ml^{-1} kanamycin. Plasmids were purified from the precultures using Spin Miniprep (QIAprep Spin Miniprep Kit, Qiagen) and send for sequencing (Eurofins Genomics, Ebersberg). *E.coli* NiCo21(DE3) were transformed with the plasmid and incubated overnight in a 5 ml LB medium containing 50 µg ml^{-1} kanamycin. 200 ml ZYM-5052 medium[9] with 100 µg ml^{-1} kanamycin were inoculated with the preculture for protein expression and incubated for 4 h at 37°C and 20 h at 18°C. Harvesting of the bacteria was done by centrifugation

(15 min at 7500 g) and the pellet was stored at -80°C before further processing. The following purification steps were performed at 4°C or on ice.

The bacteria pellet was resuspended in 40 ml lysis buffer (50 mM TRIS (pH 8.0), 50 mM NaCl, 5 mM $MgCl_2$, 0.1% (v/v) TritonX-100, 10% (v/v) glycerol, 30% B-Per (ThermoFisher Scientific)) supplemented with 100 µg ml^{-1} lysozyme (Carl Roth GmbH) and 10 µg ml^{-1} DNaseI (Roche Diagnostics) and sonicated for 10 min (Sonoplus GM 70, Bandelin).

After centrifugation for 1 h at 31000 g the supernatant was collected and filtered through sterile filters (Rotilabo PES, pore size 0,22 µm, Carl Roth GmbH). The filtrate was applied to a Ni-NTA column (HisTrap FF 5ml, GE Healthcare) on an Äkta Start chromatography system (GE Healthcare) and washed with 30 ml (25 mM Tris, 300 mM NaCl , 20 mM Imidazole, 10% (v/v) glycerol, 0.25% (v/v) Tween20, pH 7.8) The protein was eluted (25 mM Tris, 300 mM NaCl , 300 mM Imidazole, 10% (v/v) glycerol, 0.25% (v/v) Tween20, pH 7.8) and pooled. Protein containing fractions were concentrated using ultracentrifugtion filters (30kD MWCO, Amicon) while simultaneously exchanging the buffer (25 mM TRIS, 72 mM NaCl, 1 mM CaCl, pH 7.2). The protein solution was supplemented with 10% (v/v) glycerol and its concentration of 281 µM was determined on a spectrophotometer (NanoDrop 1000, Thermo Scientific, DE, USA) using the calculated extinction coefficient of 88 590 $M^{-1} cm^{-1}$ (web.expasy.org/protparam). Samples were pooled and frozen in liquid nitrogen for storage at -80°C. Quality of the protein synthesis was assessed using polyacrylamide gel electrophoresis (AnykD™ Mini-PROTEAN® TGX™ protein gels, Biorad).

Sample Preparation

AFM Cantilevers (BioLever Mini, BL-AC40TS-C2, Olympus) and cover glasses (24 mm diameter, Menzel Gläser) were cleaned by UV-O_3 treatment and immersion in piranha solution, respectively and then silanized using (3-aminopropyl)-dimethyl-ethoxysilane. The thereby amine functionalized surface was subsequently conjugated with NHS-PEG-maleimide spacers (Mw=5000 g/mol, Rapp Polymer) in HEPES buffer (50 mM HEPES, pH 7.5).[3] After extensive washing in milli-Q H_2O, the maleimide was immersed in 1 mM Coenzyme A in coupling buffer (50 mM sodium phosphate, 50 mM NaCl, 10 mM EDTA, pH 7.2) for 1 h. Cantilevers and glass slides were rinsed with water and, if needed, stored in coupling buffer before the final preparation step. The PEG-Coenzyme A surfaces and levers were functionalized with the protein of interest via Sfp phosphopantetheinyl transferase mediated coupling.[4] The glass slides and cantilevers were rinsed and then stored in measurement buffer before the SMFS experiment (25 mM TRIS, 72 mM NaCl, 1 mM $CaCl_2$, pH 7.2).

SMFS Measurement

Single molecule force spectroscopy was performed on a home build TIRF-AFM.[10] The deflection of the cantilever was measured using a deflected laser beam. The setup was equipped with a MFP3D controller (Asylum Research, USA) and the measurement software was programmed in Igor Pro 6 (Wavemetrics, USA). For each force distance curve, the cantilever was brought into contact with the sample surface and was then retracted with constant speed of 1600 nm/s. After each curve, the surface was displaced below

the cantilever in order to assess a new spot. The cantilever was calibrated in a two step procedure. First the Inverse Optical Cantilever Sensitivity (InvOLS) of the cantilevers was determined from the slope of 30 indentation curves. Second the cantilever spring constant was calibrated using the method described by Hutter.[11] TIR illumination was used for switching of the Dronpa domains, which restricted the excitation to a volume within 100 nm above the sample surface. A glucose oxidase based oxygen scavenging system (25 U/ml glucoseoxidase, 1700 U/ml catalase and 0.6% w/v glucose) was used in order to prevent bleaching of the Dronpa domains.

Data Analysis

Force extension curves were processed and filtered in a semi-automated way.[1] Drift compensation and peak identification was done for all curves with a tip sample interaction. The contour length increments of individual unfolding events were determined with the WLC model using a persistence length of 0.4 nm.[12] It has to be noted that the WLC model was only applied for forces up to 150 pN, which was sufficient for the present study. Specific curves, i.e. curves with a single tip sample interaction, were identified by selecting the ones that showed the characteristic rupture signature between the X module type III dockerin handle and the cohesin pulling domain[7] as well as the pdDronpa1.2 specific peak.

References

[1] Markus A. Jobst, Constantin Schoeler, Klara Malinowska, and Michael A. Nash. Investigating Receptor-ligand Systems of the Cellulosome with AFM-based Single-molecule Force Spectroscopy. *J. Vis. Exp.*, 82, e50950, **2013**.

[2] Wolfgang Ott, Markus A. Jobst, Constantin Schoeler, Hermann E. Gaub, and Michael A. Nash. Single-molecule force spectroscopy on polyproteins and receptor-ligand complexes: The current toolbox. *J. Struct. Biol.*, 197, 3–12, **2017**.

[3] Julia L. Zimmermann, Thomas Nicolaus, Gregor Neuert, and Kerstin Blank. Thiol-based, site-specific and covalent immobilization of biomolecules for single-molecule experiments. *Nat. Protoc.*, 5, 975–985, **2010**.

[4] Jun Yin, Paul D. Straight, Shaun M. McLoughlin, Zhe Zhou, Alison J. Lin, David E. Golan, Neil L. Kelleher, Roberto Kolter, and Christopher T. Walsh. Genetically encoded short peptide tag for versatile protein labeling by Sfp phosphopantetheinyl transferase. *Proc. Natl. Acad. Sci. U. S. A.*, 102, 15815–15820, **2005**.

[5] Xin X. Zhou, Linlin Z. Fan, Pengpeng Li, Kang Shen, and Michael Z. Lin. Optical control of cell signaling by single-chain photoswitchable kinases. *Science*, 355, 836–842, **2017**.

[6] Lukas F. Milles and Hermann E. Gaub. Is mechanical receptor ligand dissociation driven by unfolding or unbinding? *bioRxiv*, 593335, **2019**.

[7] Constantin Schoeler, Klara H. Malinowska, Rafael C. Bernardi, Lukas F. Milles, Markus A. Jobst, Ellis Durner, Wolfgang Ott, Daniel B. Fried, Edward A. Bayer, Klaus Schulten, Hermann E. Gaub, and Michael A. Nash. Ultrastable cellulosome-adhesion complex tightens under load. *Nat. Commun.*, 5, 5635, **2014**.

[8] Daniel G. Gibson, Lei Young, Ray-Yuan Chuang, J. Craig Venter, Clyde A. Hutchison III, and Hamilton O. Smith. Enzymatic assembly of DNA molecules up to several hundred kilobases. *Nat. Methods*, 6, 343–345, **2009**.

[9] F. William Studier. Protein production by auto-induction in high-density shaking cultures. *Protein Expression Purif.*, 41, 207–234, **2005**.

[10] Hermann Gumpp, Stefan W. Stahl, Mathias Strackharn, Elias M. Puchner, and Hermann E. Gaub. Ultrastable combined atomic force and total internal fluorescence microscope. *Rev. Sci. Instrum.*, 80, 063704, **2009**.

[11] Jeffrey L. Hutter and John Bechhoefer. Calibration of atomic-force microscope tips. *Rev. Sci. Instrum.*, 64, 1868–1873, **1993**.

[12] Carlos Bustamante, John F. Marko, Eric D. Siggia, and Steven B. Smith. Entropic elasticity of lambda-phage DNA. *Science*, 265, 1599–1600, **1994**.

5.3 Publication P6: Streptavidin/Biotin: Tethering Geometry Defines Unbinding Mechanics

Tethering geometry, and in this way force-loading geometry, can strongly influence rupture forces observed for receptor-ligand complexes as presented for mSA-biotin with mSA having single biotin binding capability in Section 3.1. As SA with its fourfold biotin binding capacity is an abundantly employed tool, its biotin unbinding mechanics were investigated with regard to effects caused by different force-loading geometries.

Therefore, biotin rupture forces from three SA tetramers with one, three and four functional subunits, respectively, were measured, using SMFS based on AFM. Each of these constructs was kept fixed at one subunit and biotin was randomly ruptured from one of the functional subunits. This approach resulted in different force dispersion patterns of the three constructs with forces ranging from 100 pN to 400 pN. In addition, steered molecular dynamics simulations were performed where biotin was separated from an SA subunit. Here, the SA tetramer was tethered at the C-terminus of one of its subunit. Switching the tethered subunit, thereby allowed to realize the different force-loading geometries as implemented experimentally. The results from these simulations could be used to assign the peaks from the experimental force distributions to unique tethering geometries of the SA-biotin rupture. Furthermore, the molecular dynamics simulations revealed that for certain force-loading geometries conformational changes within SA's binding pocket occurred just before biotin unbinding, which accounts for the fourfold difference in mechanical stability.

Streptavidin/biotin: Tethering geometry defines unbinding mechanics

by

Steffen M. Sedlak, Leonard C. Schendel, Hermann E. Gaub, and Rafael C. Bernardi

published in

Science Advances, 2020, 6, eaay5999, doi: 10.1126/sciadv.aay5999

Reprinted from Sedlak *et al.* [92].
Copyright © 2020 The Authors, some rights reserved; exclusive licensee American Association for the Advancement of Science. No claim to original U.S. Government Works. Distributed under a Creative Commons Attribution License 4.0 (CC BY).

SCIENCE ADVANCES | RESEARCH ARTICLE

BIOPHYSICS

Streptavidin/biotin: Tethering geometry defines unbinding mechanics

Steffen M. Sedlak[1], Leonard C. Schendel[1], Hermann E. Gaub[1]*, Rafael C. Bernardi[2]*

Copyright © 2020 The Authors, some rights reserved; exclusive licensee American Association for the Advancement of Science. No claim to original U.S. Government Works. Distributed under a Creative Commons Attribution License 4.0 (CC BY).

Macromolecules tend to respond to applied forces in many different ways. Chemistry at high shear forces can be intriguing, with relatively soft bonds becoming very stiff in specific force-loading geometries. Largely used in bionanotechnology, an important case is the streptavidin (SA)/biotin interaction. Although SA's four subunits have the same affinity, we find that the forces required to break the SA/biotin bond depend strongly on the attachment geometry. With AFM-based single-molecule force spectroscopy (SMFS), we measured unbinding forces of biotin from different SA subunits to range from 100 to more than 400 pN. Using a wide-sampling approach, we carried out hundreds of all-atom steered molecular dynamics (SMD) simulations for the entire system, including molecular linkers. Our strategy revealed the molecular mechanism that causes a fourfold difference in mechanical stability: Certain force-loading geometries induce conformational changes in SA's binding pocket lowering the energy barrier, which biotin has to overcome to escape the pocket.

INTRODUCTION

The concept of using mechanical forces to shape materials is considered a universal knowledge. The result of applying mechanical force is recognizably dependent on the direction of the force. For instance, a transversal force can easily bend an iron bar, while a much higher longitudinal force is needed to deform it. The same holds for biological materials: A timber wood log exhibits the same behavior except that wood fibers can be torn apart if the force is strong enough. A far more intriguing question is how mechanical forces affect single biomolecules. The chemistry at high forces can be really unexpected. Recently, it has been shown that an array of hydrogen bonds can be as strong as a covalent bond when a macromolecular system is designed such that all hydrogen bonds have to be broken at the same time to separate a protein-peptide complex (*1*). The directionality of forces can regulate key biological activities. For instance, some genetic diseases cause mutations in mechanoactive proteins that, in turn, lead to notable phenotypic differences in humans (*2*). In a simulation study, Best *et al.* (*3*) investigated the unfolding of a small protein domain for different pulling directions. However, studying different force-loading geometries experimentally on the single-molecule level is not straightforward, and little is known about how larger protein complexes behave under mechanical load applied from different directions. Modern force spectroscopy investigates these issues. The streptavidin (SA)/biotin interaction is abundantly used in biotechnology, with a particular use as a molecular anchoring system in single-molecule force spectroscopy (SMFS) experiments. It is thus important to fundamentally understand its mechanics and its dependence of the force-loading geometry.

To this day, tremendous effort has been invested to probe the mechanical strength of a single SA/biotin interaction. Previous studies, varying in instrumentation and immobilization strategies, found a wide range of unbinding forces for the SA/biotin complex (*4*–*9*). The underlying molecular mechanism for the mechanical stability of this complex has also been extensively investigated using computational tools (*8*–*11*). To consolidate the discrepancies in the reported unbinding forces, we investigated the unbinding of biotin from different SA subunits with total control of subunit geometry (*12*) by building on state-of-the-art site-specific immobilization strategies (*13*), parallelized atomic force microscopy (AFM)–based SMFS of different molecular species on a single sample surface (*14*), and the development of SA mutants with defined valences (*15*).

RESULTS

AFM-based SMFS on the SA/biotin system using SA of different valences

To prepare SA of different valences, we expressed functional and nonfunctional (*15*) SA subunits separately and assembled them in defined ratios (fig. S1). Combining one subunit that contained a purification tag and a unique cysteine for surface attachment with three other identical subunits, we created four different SA constructs: nonfunctional (0SA), monovalent (1SA), trivalent (3SA), and tetravalent (4SA) SA. Our protocol (see Materials and Methods) does not allow for preparation of a divalent SA with distinct orientation of the functional subunits relative to the cysteine residue. In the following, the subunit that contains the unique cysteine, i.e., the one that is attached to the surface in SMFS, is always denoted as subunit D. The other subunits are denoted accordingly, as given by the crystal structure in Fig. 1A.

For AFM-based SMFS experiments, the four different SA variants were covalently and site-specifically tethered in millimeter-separated spots on the same glass slide (Fig. 1B). This allowed circumventing inconsistencies of cantilever calibration and measurement conditions because all SA variants were probed with the same cantilever that enabled reliable and precise comparison of the resulting unbinding forces (*14*). Comparing rupture measurements from different setups performed under different conditions may be delicate, since stiffness of the pulling device, the retraction velocity, and the type and length of linker molecules can affect rupture forces observed in SMFS (*16*–*18*).

As previously established (*9*), cantilever clogging was avoided by using a proxy receptor ligand system: The adhesin SD-repeat protein G (SdrG) from *Staphylococcus epidermidis* and its binding partner,

[1]Lehrstuhl für Angewandte Physik and Center for NanoScience, Ludwig-Maximilians-Universität München, Amalienstr. 54, 80799 Munich, Germany. [2]NIH Center for Macromolecular Modeling and Bioinformatics, Beckman Institute for Advanced Science and Technology, University of Illinois at Urbana-Champaign, Urbana, IL 61801, USA.
*Corresponding author. Email: gaub@lmu.de (H.E.G.); rcbernardi@ks.uiuc.edu (R.C.B.)

Downloaded from http://advances.sciencemag.org/ on March 26, 2020

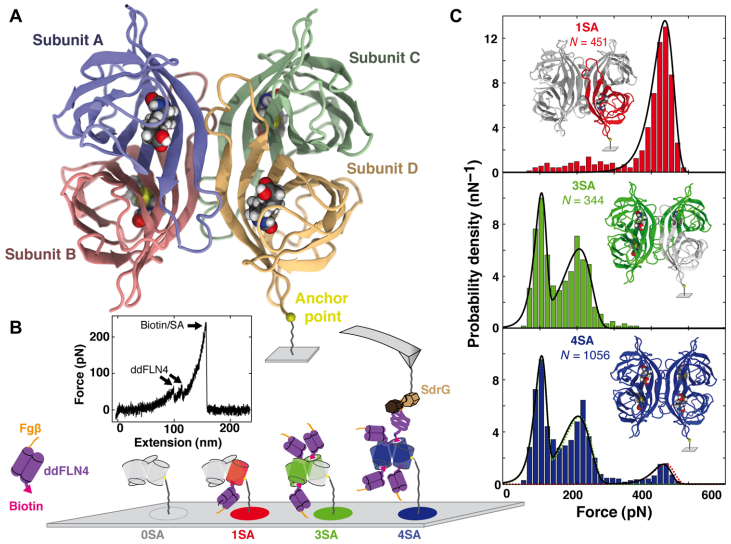

Fig. 1. Force spectroscopy of the SA/biotin complex with different valences. (**A**) Crystal structure of SA. SA comprises four subunits, each consisting of a β barrel into which a biotin molecule can be bound. At the C terminus of subunit D, a unique cysteine is used as anchor point for site-specific covalent immobilization by maleimide–polyethylene glycol (PEG) linkers onto a functionalized glass surface. (**B**) Combining nonfunctional (light gray cylinders) and functional subunits (colored cylinders) allows preparation of SA of different valences. These different SA variants are immobilized at different areas on the surface: 0SA (gray), 1SA (red), 3SA (green), and 4SA (blue) are all examined with the same cantilever. Biotinylated ddFLN4 (purple) with an N-terminal Fgβ peptide (orange) is added to the solution. While biotin (magenta) binds to SA on the surface, the Fgβ peptide can bind to the SdrG domain (brown) immobilized on the cantilever. Retracting the cantilever, ddFLN4 unfolds, and biotin is pulled out of the binding pocket, while the force is recorded. A typical force extension trace is shown in the inset. (**C**) After sorting the force curves for specific interactions, i.e., for those showing the specific unfolding pattern of ddFLN4, unbinding force histograms are plotted and fitted with Bell-Evans distributions: 1SA (red) is fitted with a single Bell-Evans distribution. To fit 3SA (green), a double Bell-Evans distribution is needed. 4SA (blue lines) is fitted with a triple Bell-Evans. Furthermore, a combination of distributions of 1SA and 3SA can be fitted (red and green dotted lines).

a short peptide from human fibrinogen β (Fgβ), were used because their rupture forces far exceed those of SA/biotin interaction (*1*). Data with covalent attachment of biotin to the cantilever tip are provided in fig. S2. To unambiguously identify single-molecule unbinding events, we used *Dictyostelium discoideum*'s fourth filament domains (ddFLN4) (*19*, *20*), with an N-terminal Fgβ peptide and a C-terminal biotin to establish a molecular link between SdrG on the cantilever tip and SA on the sample surface (Fig. 1B).

Different unbinding forces for different binding geometries

To measure the unbinding forces, the same AFM cantilever tip was repeatedly probing the different SA variants immobilized at different spots on the same surface (Fig. 2). Of 80,000 binding attempts, around 10,000 retraction traces showed interactions with forces higher than 50 pN (Fig. 2A). About one-fifth showed the distinct two-step unfolding pattern of ddFLN4 (fig. S3) before the rupture of the SA/biotin complex (Fig. 2D). These data are plotted as histograms of unbinding forces in Fig. 1C. On the surface where 0SA, the nonfunctional control mutant, was immobilized, only two events (of 20,000 attempts) showing a ddFLN4-like force curve pattern were observed demonstrating the low level of nonspecific interactions in the assay. For 1SA, the unbinding force histogram exhibits a single, most probable rupture force of 440 pN, fitted well by a Bell-Evans distribution (*11*, *21*) for dissociation of a single bond in a single-step Markovian manner. In contrast, the unbinding force histogram of 3SA exhibits two peaks at lower forces with maxima at 100 and 210 pN. The high forces seen for 1SA do not occur for 3SA. The histogram can be fitted by a cumulative function of two Bell-Evans distributions. The unbinding force histogram of events recorded on the 4SA area reveals a combination of both, 1SA and 3SA, namely, three distinct unbinding force peaks. We find the occurrence of these different force peaks for the different SA variants to be consistent over various loading rates (fig. S4). The red and green dashed lines in the bottom panel of Fig. 1C are weighted 1SA and 3SA fits from before. Using a cumulative function of three Bell-Evans distributions results in a comparable fit. Fit formula and parameters are provided in Supplementary Notes and table S1.

Combining the functional subunits of 1SA and 3SA leads to 4SA. The same is true for the force histograms: The combination of the rupture force histograms of 1SA and 3SA resembles the histogram of 4SA. Thus, we interpret the data by attributing the different rupture force peaks in the histogram to unbinding of biotin from different SA subunits. Evidently, unbinding from subunit D can be attributed to the highest rupture force peak at 440 pN because 1SA only shows this single peak. The attachment of the tetramer to the surface via subunit D might explain the comparatively low relative frequency of

Downloaded from http://advances.sciencemag.org/ on March 26, 2020

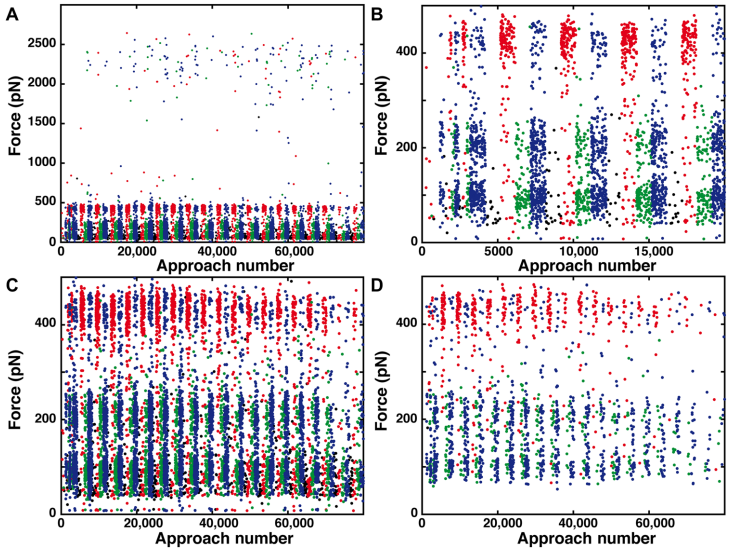

Fig. 2. Course of a SMFS measurement. (**A**) For all interactions between cantilever tip and surface (higher than 50 pN), the rupture forces are shown. Interactions recorded on the 0SA spots are shown in black, 1SA spot in red, 3SA spot in green, and 4SA spot in blue. Most rupture forces are smaller than 500 pN. The rare events above 2000 pN correspond to the unbinding of the Fgβ from SdrG. (**B**) Zoom-in on the start of the measurement. The biotinylated Fgβ-ddFLN4-biotin construct was added after 1200 approach-retraction cycles; before that, only a few nonspecific interactions occur. At first, in every 250 curves, a different surface area is probed and then every 1000 curves. (**C**) Zoom-in on forces lower than 500 pN. The unbinding from the different SA subunits manifests itself in the clustering of unbinding events around 100, 220, and 450 pN. (**D**) Specific interactions only. For all interactions, for which the distinct two-step unfolding pattern of ddFLN4 is observed directly before the complex ruptures, the unbinding force is plotted.

this rupture force event in the 4SA histogram due to lower accessibility of the subunit D binding pocket. The two remaining force peaks thus stem from biotin unbinding from subunits A, B, and C.

Other possible effects such as heterogeneity in the binding cannot explain the different force peaks measured for the different SA variants because the occurrence of the different peaks in the histograms is clearly related to which subunits of SA are accessible for biotin. If they were caused by any kind of heterogeneity of the SA/biotin interaction itself, then the results for the different SA variants would be the same. Heterogeneity of the SA/biotin bond, as proposed by Rico *et al.* (*8*), might yet account for the shallow background of lower unbinding forces seen for 1SA.

Compared with other recent SMFS studies, the rupture forces for a single SA/biotin bond reported here are relatively high. For example, Senapati *et al.* (*22*) reported forces below 100 pN. In their study, surface attachment of SA was yet accomplished by one or several of its various amine groups (movie S1), resulting in a less defined attachment geometry and most probably on average weaker mechanical stability. With constant force measurements in magnetic tweezers, Löf *et al.* (*23*) have shown that the lifetimes of single SA/biotin bonds for SA attached by its various amines are spread over a wide range and, on average, are about 10 times lower than the lifetime of a single bond between biotin and 1SA anchored by the C terminus of its functional subunit. In the present study, we use the latter, mechanically stronger, attachment geometry to investigate the molecular roots of this discernible dependence of mechanical stability on force-loading geometry. As shown here by using the same chemistry, the same linkers, the same buffer conditions, the same AFM cantilever tip, and the same experimental setup for measuring four different SA variants, this difference in mechanical stability is inherent to the SA/biotin system; all other discrepancies between miscellaneous experiments (like different AFM cantilevers, different setups, and different buffer conditions) add up on top.

Combining in silico and in vitro force spectroscopy reveals unbinding mechanism

To elucidate the underlying molecular mechanism, we performed all-atom constant velocity steered molecular dynamics (SMD) (*11*) simulations using the same force-loading geometry as for the SMFS experiment. Simulations of a fully solvated SA/biotin complex (fig. S5) were prepared following QwikMD (*24*) protocols and carried out with graphics processing unit (GPU)–accelerated NAMD (*25*). A wide-sampling approach was taken where hundreds of fully independent simulations were carried out, accounting for more than 30 μs of production SMD runs. For simplicity, we always anchored the molecular linker of biotin bound to subunit D [Protein Data Bank (PDB): 5TO2 (*26*) and biotin from PDB: 1MK5 (*27*)] and pulled on one of the four subunits by its C terminus. This reproduces the four different experimental force-loading geometries. Furthermore, the simulations include part of the linker, which connects biotin to the Fgβ-ddFLN4

Downloaded from http://advances.sciencemag.org/ on March 26, 2020

construct (fig. S5). We found that omitting the linker yields significantly different results (fig. S6), presumably due to missing interactions between the linker and SA.

During SMD simulations, because the pulling and anchoring points are gradually separated at constant pulling velocity, the complex is free to rotate into an orientation, maximizing the distance between the attachment points. This orientation defines the direction in which gradually a restoring force builds up in the molecular complex upon further separation. In Fig. 3A, the crystal structure of SA/biotin complex is depicted. For the binding pocket, a surface representation is chosen to illustrate the spatial confinement of biotin. The four colored lines connect biotin's carboxyl group with the C termini, indicating the different initial force-loading directions. Upon stretching, the molecular linker approximately aligns along this line. SA tightly encapsulates biotin, except for biotin's carboxyl group to which the molecular linker is covalently attached. For pulling on subunit D, which showed the strongest unbinding forces in the experiment, the initial force-loading direction points straight through the binding pocket cavity (yellow line in Fig. 3A). For the other subunits, the initial force-loading directions pierce through the binding pocket's confinement. Upon stretching, biotin will be pushed against parts of the enclosing binding pocket. We hypothesized that this levering of biotin or the adjacent molecular linker against flexible parts of SA destabilizes the binding pocket and interferes with its structural integrity, resulting in lower unbinding forces.

The position of the L3/4 loop is crucial for tight encapsulation of biotin

Binding of biotin to SA is mediated by hydrophobic interactions, a network of hydrogen bonds, and a conformational change in the SA subunit (*28*): A flexible peptide loop between the third and the fourth β strand (L3/4 loop) closes over the binding pocket like a lid and buries biotin inside the pocket (*29*). Calculations performed by Bansal *et al.* (*30*) showed that this conformational change accounts for about 75% of the change in free energy upon biotin binding. In the analysis of our SMD data, we therefore focused on this vital contribution of the lid to biotin binding. We propose that for the three weaker attachment geometries (anchoring of subunits A, B, or C), the L3/4 loop is, under load, forced toward its open conformation. By analyzing SMD trajectories, we observed that the lid opens up before biotin dissociation, particularly in those simulations where subunit A or C were probed. To illustrate the mechanism of force-induced lid opening, we depicted different stages of the SMD simulation (for pulling of subunit C) in Fig. 3 (B to F) and fig. S7.

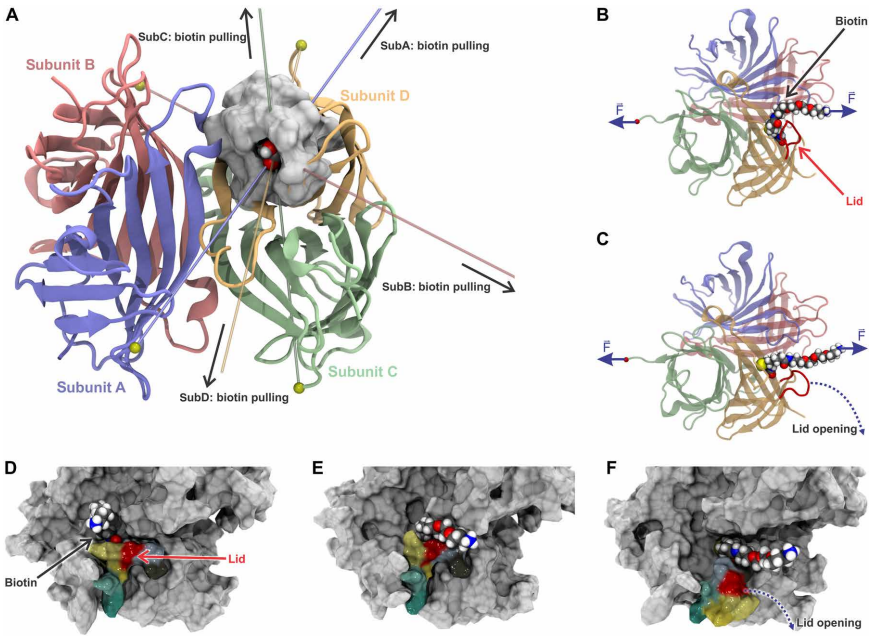

Fig. 3. Direction dependent unbinding and lid opening. (**A**) Schematics of the force-loading geometries. To simplify MD simulations, biotin bound in subunit D (shown with surface representation) was anchored by the end of its molecular linker, while one of four subunits (A to D) was pulled by its C terminus. Colored lines indicate the four resulting force-loading directions (polymeric biotin linker is not shown). (**B** and **C**) The structure of SA stretched via its subunit C and the end of the polymeric linker of biotin bound in subunit D are shown before (B) and after (C) lid opening just before bond rupture. (**D** to **F**) Surface representation of SA shows how the stretching of biotin and its linker during subunit C pulling—from initial conformation at time 0 ns (D), to time 32 ns (E), to time 54 ns (F)—induces conformational changes in the binding pocket's lid (colored by amino acid sequence).

Downloaded from http://advances.sciencemag.org/ on March 26, 2020

Detailed picture of system mechanics with atomistic resolution

Beyond this phenomenological description, the wide-sampling SMD strategy allowed statistical treatment of the SMD data (Fig. 4). Plotting rupture force histograms for the SMD data (Fig. 4B) reveals that the SMD results agree qualitatively with the experimental SMFS data: The force needed to unbind biotin from subunit D is the highest (510 pN), while the unbinding forces from subunit B are lower (450 pN). The unbinding from subunits A and C is observed at similar forces of about 340 and 360 pN. Plotting a histogram combing forces from all domains shows that subunits A and C results are nearly indistinguishable (fig. S6).

At first glance, the absolute forces measured in experiments and simulations differ quantitatively from each other. In this context, it has to be taken into account that the pulling velocity and therefore the loading rates, which in turn influence the observed rupture forces (*31*), are much higher in the simulation. To directly compare the results of simulations with those of the experiments, we plotted them as a dynamic force spectrum and fitted the data with a straight line according to the standard Bell-Evans model (fig. S4). In this framework, the difference in rupture forces between simulations and experiment are comprehensible. Solely, the rupture force for unbinding from subunit D observed in the simulations are slightly too low. Presumably, the force field parameters for biotin and its linker are less precise when compared to those for amino acids (which have been optimized over decades). Taking this and also the six orders of magnitude difference in pulling velocities into account, we can say that we also have a convincing quantitative agreement between in silico and in vitro SMFS. Both issues could be solved or at least reduced; however, requiring enormous computational resources, which as we previously demonstrated (*32*), is better spent producing more replicas and consequently better statistics.

To monitor the position of the L3/4 loop, we introduced a distance-based (Fig. 4, C and D) and an angle-based metric (fig. S8). For the former, we measured the distance between the α carbon of residue Gly^{48} (tip of the L3/4 loop) and the α carbon of residue Leu^{124} (middle of β strand β8; fig. S9). By tracking this metric over time for single representative trajectories (Fig. 4C), we found that for subunits A and C, the distance abruptly increases about 10 ns before the complex ruptures, which indicates that the L3/4 loop opens (movies S2 and S4). Subunit B exhibits a similar but much less pronounced behavior (movie S3), while for subunit D, the distance is constant up to the point of rupture (movie S5). A histogram over all 100 replicas confirms this trend (Fig. 4D): While for subunit D, the distributions at the beginning of the force loading (gray) and around the rupture (red) are almost congruent; they differ significantly for the other three subunits, particularly for subunits A and C.

To investigate how force propagates through the receptor-ligand complex, we used a cross-correlation–based network analysis (*33*). From

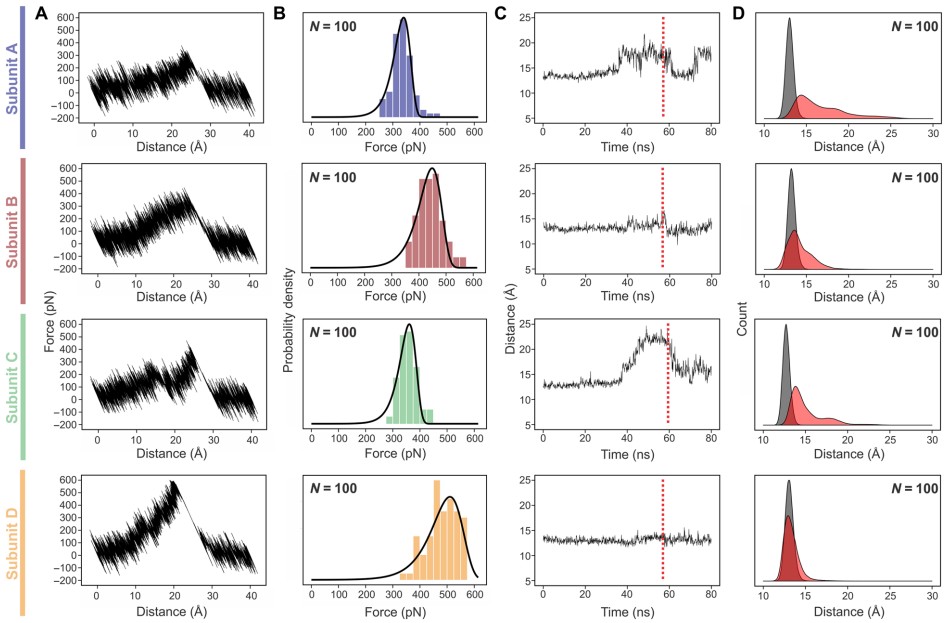

Fig. 4. Results of SMD simulations. Pulling C termini of SA subunits while holding molecular linker of biotin bound to pocket in subunit D. (**A**) Exemplary force extension traces for the four geometries. (**B**) Resulting rupture force histograms fitted with Bell-Evans distributions. (**C**) Exemplary plots of the distance metric for the L3/4 loop opening (distance between α carbons of Gly^{48} and Leu^{124} residues) over time. The red dashed lines denote the moment at which biotin leaves the pocket. (**D**) Histograms of the distance metric for the L3/4 loop opening for the first 10 ns of the simulation (unloaded condition, gray) and for 10 ns just before the point of rupture (loaded condition, red).

Downloaded from http://advances.sciencemag.org/ on March 26, 2020

thermodynamic fluctuation theory, one can infer that paths with high correlation of motion can be isolated to describe the paths along which force propagates through the system (*33*, *34*). In Fig. 5, the force propagation pathways through the SA tetramer are depicted. Whereas clear differences between the four force-loading geometries are evident, one can observe that force propagation pathways for subunits B and D are quite similar within subunit D. The network model suggests that interactions between receptor and ligand are highly correlated in multiple sites of the subunit D β barrel, as it was previously shown for C-terminal pulling of subunit D (*9*). Since for force loading of subunits A, B, and C, the force has to propagate through the SA tetramer, it is in principle imaginable that not the SA/biotin interaction but the SA tetramer structure ruptures, as suggested by Kim *et al.* (*35*). While we cannot rule out such a process for our AFM-based SMFS experiments, any indication for rupturing of the SA tetramer was absent in the SMD simulations.

DISCUSSION

Very little is known about the chemistry at the interface between biomolecules affected by mechanical forces. Here, we show that simple geometric concepts can be used to explain enormous differences in the strength of biomolecular complexes. Our findings, and the proposed mechanism of directionality dependence of force, are certainly important in a more general way and relevant for many other biomolecular complexes that encounter mechanical stress. The force resilience dependence on the tethering geometry has previously been observed by comparing N- and C-terminal tethering, revealing that some biomolecular complexes are more stable in one of these tethering geometries. For instance, bacterial adhesion in *Staphylococcus* infection has been shown to be extremely stable at the biomedically relevant tethering geometry but weak at an alternative geometry (*1*). The same was observed for cellulosomal complexes, where the ultrastable cohesin/dockerin complexes were shown to be relatively easy to break if pulled in a geometry that does not activate the complex bond (*33*). However, in all these cases, the main factor of the lower complex stability was in fact the lower stability of the protein fold in a different tethering geometry; therefore, the difference in force resilience was in fact determined by the interplay between unfolding and unbinding. Here, we show that some complexes might present completely different unbinding pathways depending on the tethering geometry while keeping the original fold. From our results and by inspecting the structure highlighted in Fig. 3A, one can quickly realize that each tethering will create different unbinding pathways. We expect that the same holds for many other biological complexes.

For the SA/biotin interaction, which has been frequently measured by SMFS, the influence of tethering geometry has so far been overlooked contributing to a wide range of rupture forces reported in the literature. In this work, we reconcile these seemingly conflicting results of previous force spectroscopy studies on the SA/biotin interaction from a more complete perspective, showing that for four different well-defined tethering geometries, the experimental unbinding forces can vary fourfold. Anchoring of SA via unspecific pulldown by reactive amines or similar groups as it is done in most commercial products might result in an even wider range of unbinding forces. Therefore, we show that the way in which SA is tethered is of critical importance for the force propagation path in the complex and thus for the mechanical stability of the SA/biotin interaction.

In summary, we show that diversity in binding forces was revealed to be caused by different force-loading geometries and that the accompanying induction of conformational changes was caused by pushing biotin against the flexible L3/4 loop of SA. We demonstrated that for SMD simulations, it is important to consider the experimental force-loading geometry and take explicitly into account molecules that may be interfering with the receptor-ligand interaction, such as the biotin linker molecule. Together, our findings encourage to reconsider how SA is tethered in future force spectroscopy experiments: With site-specific anchoring and consideration of resulting force-loading geometries, higher mechanical stability of the SA/biotin bond can be achieved in future investigations. Likewise, since biotin

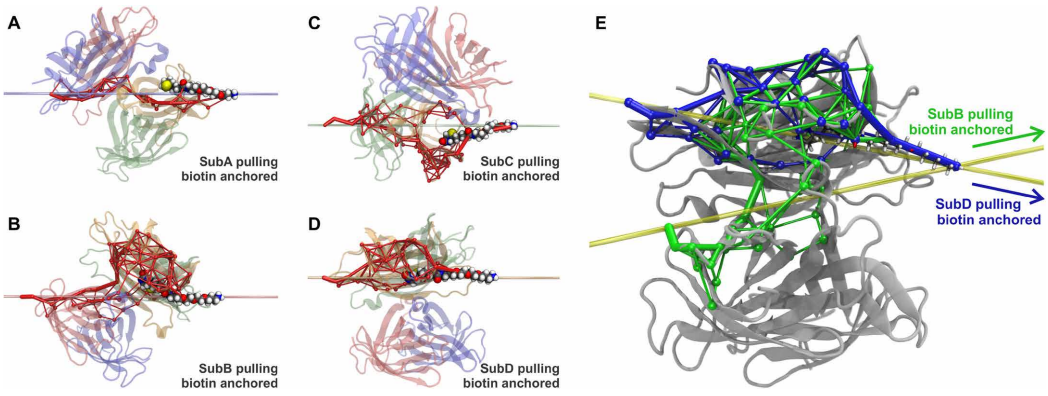

Fig. 5. Force propagation pathways through the SA tetramer. (**A** to **D**) The force propagation pathway is shown for the different subunits close to the point of rupture. Force propagation pathways were obtained from cross-correlation–based network analysis calculated for all 100 replicas in a force-loaded condition. α carbon atoms serve as nodes that are connected by tubes of different diameters corresponding to how likely it is to have force transferred between them. SA is rotated to align the directions of force application horizontally. (**E**) Overlay of the force propagation pathway of subunits B and D. Within subunit D, the two are similar. For subunit D, a strong correlation is found between the molecular linker of biotin and the fourth β strand of subunit D, revealing a stabilization of the SA/biotin interaction pocket.

Downloaded from http://advances.sciencemag.org/ on March 26, 2020

is attached to a molecular linker for most applications in bionanotechnology, our experimental and computational design follow the predominant scenario for assays using SA/biotin complexes and should be used to guide new developments whenever these complexes might be under mechanical stress. Therefore, by illustrating how protein mechanics of a biomolecular system depends on tethering geometry, our work not only provides a more precise protocol for single-molecule experiments but also sheds light on the fundaments of protein mechanics.

MATERIALS AND METHODS

Preparation of proteins

All protein sequences used are provided in Supplementary Notes. Green fluorescent protein (GFP), used for polyacrylamide electrophoresis, or ddFLN4 were cloned into plasmids for expression by T7 RNA polymerase (pET) and expressed as described by Sedlak *et al.* (*12*). Recombinant GFP and ddFLN4 proteins contain a ybbR-tag that was used for biotinylation using Sfp-Synthase as described by Erlich *et al.* (*36*).

For cloning and expression, we follow a protocol provided by Baumann *et al.* (*37*). The four different SA subunits were cloned into pET vectors. Subunits were expressed separately, denatured, mixed, and purified by Ni–immobilized metal affinity chromatography (IMAC).

For example, to obtain 3SA, we denatured nonfunctional SA subunits (with polyhistidine tag and a unique cysteine at their C terminus) and mixed them with denatured functional subunits without tags in a 1:10 ratio. After protein refolding, we used Ni-IMAC to select for SA with a single polyhistidine tag, i.e., 3SA. A complete description is given by Sedlak *et al.* (*9*).

To ascertain the number of functional subunits per SA, we added biotinylated GFP to the different SA variants and performed SDS–polyacrylamide gel electrophoresis (SDS-PAGE). The different SA variants (0SA, 1SA, 3SA, and 4SA) were mixed with biotinylated GFP. We allowed the proteins to bind to each other (about 10 min) before adding a loading buffer. Proteins were then loaded onto the Any kD Mini-PROTEAN TGX Stain-Free Protein Gel (Bio-Rad, Hercules, USA).

This protocol for preparation of SA of different valences can, in principle, be used to prepare divalent SA. Since the assembly of different subunits into the tetrameric SA is stochastic, the orientation of functional and nonfunctional subunits relative to the anchoring point cannot be controlled. Beyond that, if a unique anchoring point were desired, three different types of subunits would have to be assembled, further complicating the protocol.

Surface preparation

Heterobifunctional polyethylene glycol (PEG) of 5000 g/mol molecular weight was dissolved to 25 mM in a 50 mM Hepes buffer at pH 7.5 and added onto an amino-silanized glass slide. During 30 min of incubation, the *N*-hydroxysuccinimide (NHS) group on one end of the PEG linker formed a stable amide bond with the amines on the glass slide. After washing off unbound PEG using ultrapure water, a silicon mask was placed on the surface and at different spots, and 10 µl of the reduced SAs dissolved in coupling buffer was added onto the surface. The SA's unique cysteines reacted with the maleimide group on the other end of the PEG to form a stable thioether bond. A graphical illustration of the process is given in the supplementary materials of Sedlak *et al.* (*9*).

Cantilever preparation

Bifunctional PEG of 5000 Da having an NHS group at one end and a maleimide group on the other (NHS-PEG5000-MAL, Rapp Polymere, Tübingen, Germany) was dissolved in 50 mM Hepes at pH 7.5 and immediately used to incubate amino-silanized BioLever mini (Olympus Corporation, Tokyo, Japan; spring constant from calibration after the experiment: 0.15 N/m). After 1 hour, the cantilevers were thoroughly washed in ultrapure water and then placed in 25 µl droplets of coenzyme A (CoA) dissolved in coupling buffer [50 mM NaCl, 50 mM NaHPO4, and 10 mM EDTA (pH 7.2)]. After 1 hour, the cantilevers were thoroughly washed in ultrapure water and then placed in 25-µl droplets of the Sfp reaction mix {10 µl of 10× Sfp buffer [10 mM MgCl2 and 50 mM Hepes (pH 7.5)], 5 µl of 100 µM Sfp-Synthase, 40 µl of 32.5 µM SdrG-ybbR construct (*1*), and 45 µl of MiliQ H2O}. After at least 1-hour incubation time, the cantilevers were thoroughly washed in phosphate-buffered saline (PBS) and stored in PBS. A graphical illustration of the process is given in the supplementary materials of Sedlak *et al.* (*9*).

For covalent attachment of the biotinylated ddFLN4 domain, the biotinylated ddFLN4 construct with the C-terminal cysteine was used and coupled to the maleimide instead of the CoA. After at least 1-hour incubation time, the cantilevers were thoroughly washed in PBS and stored in PBS.

AFM-based SMFS experiments

The AFM-based SMFS measurements were performed with a custom-built AFM controlled by an MFP-3D controller (Asylum Research, Santa Barbara, USA) and a self-written routine programmed in Igor Pro 6 (WaveMetrics, Oregon, USA). The cantilevers were approached to the surface with 3000 nm/s and, after short contact (indentation of 100 pN), retracted with a constant velocity of 800 nm/s. The readout of the distance and cantilever deflection was performed at 12,000 Hz. The cantilever was retracted at 350 nm. After each approach-retraction cycle, the surface was moved 100 nm in lateral direction to expose a fresh surface area to the cantilever tip. All measurements were performed in PBS (pH 7.4) in ambient conditions. Cantilevers were calibrated following the thermal noise method as described by te Riet *et al.* (*38*).

For measurements with a second receptor-ligand system on the cantilever tip, we first performed about 1000 approach-retraction cycles to ensure the absence of unspecific interaction between the SA on the surface and the SdrG on the cantilever tip. We then placed the mounted AFM cantilever tip in PBS containing the biotinylated Fgβ-ddFLN4 construct at a concentration in the low nanomolar range for 2 min. By this, some ddFLN4 gets adsorbed to the cantilever tip. We then transferred the AFM head back onto the sample surface and continued with the approach-retraction cycles, now measuring specific interactions. An alternative approach that also worked is to directly add the diluted biotinylated Fgβ-ddFLN4 construct to the measurement buffer.

For measurements with several surface areas, where different proteins are immobilized, the cantilever tip was retracted a few micrometer from the surface after 250 to 2000 approach-retraction cycles. Then, the surface was moved a few millimeters in lateral direction so that the next surface area could be probed. The cantilever was approached automatically, and the probing of the surface continued.

AFM-based SMFS data analysis

Using the cantilever spring constant, the optical lever sensitivity, and the *z* piezo sensitivity, the deflection voltage and the *z* piezo voltage

Downloaded from http://advances.sciencemag.org/ on March 26, 2020

are translated into force and distance, respectively. Then, the cantilever-bending correction is performed, and the value for zero force and zero distance are determined for each force extension trace. After denoising, each force extension trace is translated into contour length space. Detecting force peaks, force extension traces are sorted to identify those that show the correct increase in contour length corresponding to the distinct two-step unfolding of the ddFLN4 fingerprint domain. Rupture and unfolding forces for each surface area are analyzed separately and plotted as histograms.

Molecular dynamics simulations

Using advanced run options of Visual Molecular Dynamics (VMD) (*39*) QwikMD (*24*) plugin, our in silico approach followed established protocols that were previously used to investigate mechanical properties of SA (*9*), filamins (*2*), cellulosomes (*14*), and adhesins (*1*).

System setup

The structure of a monovalent *Streptomyces avidinii* SA (mSA) had been solved by means of x-ray crystallography at 1.65 Å resolution and was available at the PDB (PDB: 5TO2) (*26*). Because this crystallographic structure does not contain a biotin bound to the binding pocket, the structure of the tetravalent *S. avidinii* SA bound to biotin (PDB: 1MK5) (*27*), solved at 1.4 Å resolution, was used to place the biotin on to its binding site at chain D of the mSA. The PEG3 molecular linker used in the experiments was designed with VMD's molefacture (*39*) plugin. The alignment and placing of the biotin with linker into the monovalent structure were performed using VMD (*39*) on the basis of the alignment of the aforementioned crystal structures. Using the quantum mechanics/molecular mechanics (QM/MM) tools of QwikMD (*24*), we performed a short 10-ps long hybrid QM/MM molecular dynamics (MD) simulation with NAMD (*25*, *40*) and Molecular Orbital PACkage (MOPAC) (*41*) using a 0.5-fs integration time step. The classical Chemistry at Harvard Macromolecular Mechanics 36 (CHARMM36) force field was used to represent the SA atoms, while the biotin and its linker were treated with QM at Parametric Model 7 (PM7) level (*42*). This QM/MM simulation was performed without the presence of solvent molecules and kept the SA and the biotin nonhydrogen atoms with position restraints, allowing only for the linker to search for a plausible conformation. The biotin with its linker was then parameterized for classical MD simulations using CHARMM General Force Field (*43*). Using advanced run options of QwikMD (*24*), the structure resulting from the QM/MM simulation was solvated, and the net charge of the system was neutralized in a 0.15-M sodium chloride solution. In total, about 275,000 atoms were simulated in each of the classical MD simulation. The CHARMM36 force field along with the transferable intermolecular potential with 3 points (TIP3) water model was used to describe all systems.

Equilibrium MD simulations

All classical MD simulations were performed in GPU-accelerated XK nodes of the National Center for Supercomputing Applications/Blue Waters supercomputer using the NAMD MD package (*25*). All simulations were performed assuming periodic boundary conditions in the NpT ensemble with temperature maintained at 300 K using Langevin dynamics for temperature and pressure coupling, the latter kept at 1 bar. A distance cutoff of 11.0 Å was applied to short-range nonbonded interactions, whereas long-range electrostatic interactions were treated using the particle-mesh Ewald method. The equations of motion were integrated using the r-RESPA multiple time-step scheme (*25*) to update the Lennard-Jones interactions every step and electrostatic interactions every two steps. The time step of integration was chosen to be 2 fs for all simulations performed. Before the MD simulations, an energy minimization was performed for 5000 steps. An MD simulation with position restraints in the protein backbone atoms and biotin and linker nonhydrogen atoms was performed for 10 ns. To allow for a total relaxation of the system and to make sure biotin and its linker were stable in the SA pocket, a 100-ns simulation in equilibrium, where no external forces were applied, was performed. The MD protocol served to preequilibrate the system before the SMD simulations was performed.

SMD simulations

With structures properly equilibrated and checked, SMD simulations (*11*) were performed using a constant velocity stretching (SMD-CV protocol) at 0.5 Å/ns. The SMD procedure is equivalent to attaching one end of a harmonic spring [with a spring constant of 1.0 kcal/(mol $Å^2$), i.e., 0.69 N/m] to the end of a molecule and pulling on the end of the other molecule with another spring. The force applied to the harmonic spring is then monitored during the time of the MD simulation. The pulling point was moved with constant velocity along the *z* axis, and due to the single anchoring point and the single pulling point, the system is quickly aligned along the *z* axis. Owing to the flexibility of the experimentally used linkers connecting the domains of interest and the fingerprint domains, this approach reproduces the experimental protocol. Simulations were performed restraining the position of the terminal nitrogen of the biotin linker while pulling the α carbon of each subunit's C-terminal amino acid residue. For all four configurations, many simulation replicas were performed in a wide-sampling approach. For each subunit pulling, 100 replicas were performed, with each of the simulations accounting for 80-ns total simulation time. In total, 32 μs of production SMD was performed.

Simulation data analysis

Simulation force-time traces were analyzed analogously to experimental data. For each simulation, the rupture force was determined as the highest force of a trace, and the force-loading rate was determined as a linear fit to the force versus time traces immediately before rupture. Analyses of force traces and MD trajectories, except for the force propagation analyses, were carried out using python scripts taking advantage of Jupyter Notebooks (*44*). Particularly, VMD (*39*), MDAnalysis (*45*), and PyContact (*46*) were used for trajectory analysis together with in-house scripting wrappers, which collected information from all simulation replicas. Force propagation analyses were performed using dynamical network analysis, which is implemented in VMD's Network View plugin (*47*). A network was defined as a set of nodes, all α carbons plus three atoms of the biotin and its linker, with connecting edges. Edges connect pairs of nodes if corresponding monomers are in contact, and two monomers are said to be in contact if they fulfill a proximity criterion, namely, any heavy atoms (nonhydrogen) from the two monomers are within 4.5 Å of each other for at least 75% of the frames analyzed. Filtering this network, one can investigate allosteric signaling (*40*, *47*). Allostery can be understood in terms of pathways of residues that efficiently transmit energy, here in the form of mechanical stress, between different binding sites (*33*). The dynamical networks were constructed from 10-ns windows of the total trajectories sampled every 400 ps. The probability of information transfer across an edge is set as $w_{ij} = -\log(|C_{ij}|)$, where C is the correlation matrix calculated with Carma (*48*). Using the Floyd-Warshall algorithm, the suboptimal paths were then calculated. The

Downloaded from http://advances.sciencemag.org/ on March 26, 2020

tolerance value used for any path to be included in the suboptimal path was −log(0.5) = 0.69. As previously demonstrated by our group (*33*), Pearson correlation is ideal for force propagation calculation.

SUPPLEMENTARY MATERIALS

Supplementary material for this article is available at http://advances.sciencemag.org/cgi/content/full/6/13/eaay5999/DC1

Fig. S1. SDS-PAGE of different SA variants.
Fig. S2. SMFS measurements with direct covalent attachment of the biotinylated ddFLN4 domain to the cantilever tip.
Fig. S3. Exemplary force extension traces.
Fig. S4. Dynamic force spectrum.
Fig. S5. Structure of biotin with the adjacent linker and illustration of the simulation box.
Fig. S6. SMD force histograms.
Fig. S7. Structure of the SA/biotin complex during L3/4 loop opening.
Fig. S8. Angle metric for L3/4 loop opening.
Fig. S9. Distance metric for L3/4 loop opening.
Table S1. Fit parameters for the Bell-Evans distributions shown in the main text.
Note S1. Fit parameters of Bell-Evans distributions.
Note S2. Sequences of protein constructs.
Movie S1. SA's crystal structure with highlighted amine groups.
Movie S2. Exemplary SMD: Holding biotin, pulling on the C terminus of SA subunit A.
Movie S3. Exemplary SMD: Holding biotin, pulling on the C terminus of SA subunit B.
Movie S4. Exemplary SMD: Holding biotin, pulling on the C terminus of SA subunit C.
Movie S5. Exemplary SMD: Holding biotin, pulling on the C-terminus of SA subunit D.

View/request a protocol for this paper from *Bio-protocol*.

REFERENCES AND NOTES

1. L. F. Milles, K. Schulten, H. E. Gaub, R. C. Bernardi, Molecular mechanism of extreme mechanostability in a pathogen adhesin. *Science* **359**, 1527–1533 (2018).
2. T. J. K. Haataja, R. C. Bernardi, S. Lecointe, R. Capoulade, J. Merot, U. Pentikäinen, Non-syndromic mitral valve dysplasia mutation changes the force resilience and interaction of human filamin A. *Structure* **27**, 102–112.e4 (2019).
3. R. B. Best, E. Paci, G. Hummer, O. K. Dudko, Pulling direction as a reaction coordinate for the mechanical unfolding of single molecules. *J. Phys. Chem. B* **112**, 5968–5976 (2008).
4. V. T. Moy, E. L. Florin, H. E. Gaub, Intermolecular forces and energies between ligands and receptors. *Science* **266**, 257–259 (1994).
5. G. U. Lee, D. A. Kidwell, R. J. Colton, Sensing discrete streptavidin-biotin interactions with atomic force microscopy. *Langmuir* **10**, 354–357 (1994).
6. A. Chilkoti, T. Boland, B. D. Ratner, P. S. Stayton, The relationship between ligand-binding thermodynamics and protein-ligand interaction forces measured by atomic force microscopy. *Biophys. J.* **69**, 2125–2130 (1995).
7. J.-M. Teulon, Y. Delcuze, M. Odorico, S.-w. Chen, P. Parot, J.-L. Pellequer, Single and multiple bonds in (strept)avidin-biotin interactions. *J. Mol. Recognit.* **24**, 490–502 (2011).
8. F. Rico, A. Russek, L. González, H. Grubmüller, S. Scheuring, Heterogeneous and rate-dependent streptavidin-biotin unbinding revealed by high-speed force spectroscopy and atomistic simulations. *Proc. Natl. Acad. Sci. U.S.A.* **116**, 6594–6601 (2019).
9. S. M. Sedlak, L. C. Schendel, M. C. R. Melo, D. A. Pippig, Z. Luthey-Schulten, H. E. Gaub, R. C. Bernardi, Direction matters: Monovalent streptavidin/biotin complex under load. *Nano Lett.* **19**, 3415–3421 (2019).
10. H. Grubmüller, B. Heymann, P. Tavan, Ligand binding: Molecular mechanics calculation of the streptavidin-biotin rupture force. *Science* **271**, 997–999 (1996).
11. S. Izrailev, S. Stepaniants, M. Balsera, Y. Oono, K. Schulten, Molecular dynamics study of unbinding of the avidin-biotin complex. *Biophys. J.* **72**, 1568–1581 (1997).
12. S. M. Sedlak, M. S. Bauer, C. Kluger, L. C. Schendel, L. F. Milles, D. A. Pippig, H. E. Gaub, Monodisperse measurement of the biotin-streptavidin interaction strength in a well-defined pulling geometry. *PLOS ONE* **12**, e0188722 (2017).
13. W. Ott, M. A. Jobst, C. Schoeler, H. E. Gaub, M. A. Nash, Single-molecule force spectroscopy on polyproteins and receptor-ligand complexes: The current toolbox. *J. Struct. Biol.* **197**, 3–12 (2017).
14. T. Verdorfer, R. C. Bernardi, A. Meinhold, W. Ott, Z. Luthey-Schulten, M. A. Nash, H. E. Gaub, Combining in vitro and in silico single-molecule force spectroscopy to characterize and tune cellulosomal scaffoldin mechanics. *J. Am. Chem. Soc.* **139**, 17841–17852 (2017).
15. M. Howarth, D. J.-F. Chinnapen, K. Gerrow, P. C. Dorrestein, M. R. Grandy, N. L. Kelleher, A. El-Husseini, A. Y. Ting, A monovalent streptavidin with a single femtomolar biotin binding site. *Nat. Methods* **3**, 267–273 (2006).
16. E. B. Walton, S. Lee, K. J. Van Vliet, Extending Bell's model: how force transducer stiffness alters measured unbinding forces and kinetics of molecular complexes. *Biophys. J.* **94**, 2621–2630 (2008).
17. A. Maitra, G. Arya, Model accounting for the effects of pulling-device stiffness in the analyses of single-molecule force measurements. *Phys. Rev. Lett.* **104**, 108301 (2010).
18. M. S. Bauer, F. Baumann, C. Daday, P. Redondo, E. Durner, M. A. Jobst, L. F. Milles, D. Mercadante, D. A. Pippig, H. E. Gaub, F. Gräter, D. Lietha, Structural and mechanistic insights into mechanoactivation of focal adhesion kinase. *Proc. Natl. Acad. Sci.* **116**, 6766–6774 (2019).
19. I. Schwaiger, A. Kardinal, M. Schleicher, A. A. Noegel, M. Rief, A mechanical unfolding intermediate in an actin-crosslinking protein. *Nat. Struct. Mol. Biol.* **11**, 81–85 (2004).
20. M. S. Bauer, L. F. Milles, S. M. Sedlak, H. E. Gaub, Monomeric streptavidin: A versatile regenerative handle for force spectroscopy. *bioRxiv*, 276444 (2018).
21. E. Evans, K. Ritchie, Dynamic strength of molecular adhesion bonds. *Biophys. J.* **72**, 1541–1555 (1997).
22. S. Senapati, S. Biswas, S. Manna, R. Ros, S. Lindsay, P. Zhang, A Y-shaped three-arm structure for probing bivalent interactions between protein receptor-ligand using AFM and SPR. *Langmuir* **34**, 6930–6940 (2018).
23. A. Löf, P. U. Walker, S. M. Sedlak, S. Gruber, T. Obser, M. A. Brehm, M. Benoit, J. Lipfert, Multiplexed protein force spectroscopy reveals equilibrium protein folding dynamics and the low-force response of von Willebrand factor. *Proc. Natl. Acad. Sci. U.S.A.* **116**, 18798–18807 (2019).
24. J. V. Ribeiro, R. C. Bernardi, T. Rudack, J. E. Stone, J. C. Phillips, P. L. Freddolino, K. Schulten, QwikMD - Integrative molecular dynamics toolkit for novices and experts. *Sci. Rep.* **6**, 26536 (2016).
25. J. C. Phillips, R. Braun, W. Wang, J. Gumbart, E. Tajkhorshid, E. Villa, C. Chipot, R. D. Skeel, L. Kalé, K. Schulten, Scalable molecular dynamics with NAMD. *J. Comput. Chem.* **26**, 1781–1802 (2005).
26. M. Zhang, S. Biswas, W. Deng, H. Yu, The crystal structure of monovalent streptavidin. *Sci. Rep.* **6**, 35915 (2016).
27. D. E. Hyre, I. Le Trong, E. A. Merritt, J. F. Eccleston, N. M. Green, R. E. Stenkamp, P. S. Stayton, Cooperative hydrogen bond interactions in the streptavidin-biotin system. *Protein Sci.* **15**, 459–467 (2006).
28. P. C. Weber, D. H. Ohlendorf, J. J. Wendoloski, F. R. Salemme, Structural origins of high-affinity biotin binding to streptavidin. *Science* **243**, 85–88 (1989).
29. S. Freitag, I. Le Trong, L. Klumb, P. S. Stayton, R. E. Stenkamp, Structural studies of the streptavidin binding loop. *Protein Sci.* **6**, 1157–1166 (1997).
30. N. Bansal, Z. Zheng, L. F. Song, J. Pei, K. M. Merz Jr., The role of the active site flap in streptavidin/biotin complex formation. *J. Am. Chem. Soc.* **140**, 5434–5446 (2018).
31. A. Maitra, G. Arya, Influence of pulling handles and device stiffness in single-molecule force spectroscopy. *Phys. Chem. Chem. Phys.* **13**, 1836–1842 (2011).
32. R. C. Bernardi, E. Durner, C. Schoeler, K. H. Malinowska, B. G. Carvalho, E. A. Bayer, Z. Luthey-Schulten, H. E. Gaub, M. A. Nash, Mechanisms of nanonewton mechanostability in a protein complex revealed by molecular dynamics simulations and single-molecule force spectroscopy. *J. Am. Chem. Soc.* **141**, 14752–14763 (2019).
33. C. Schoeler, R. C. Bernardi, K. H. Malinowska, E. Durner, W. Ott, E. A. Bayer, K. Schulten, M. A. Nash, H. E. Gaub, Mapping mechanical force propagation through biomolecular complexes. *Nano Lett.* **15**, 7370–7376 (2015).
34. R. F. Greene, H. B. Callen, On the formalism of thermodynamic fluctuation theory. *Phys. Rev.* **83**, 1231–1235 (1951).
35. M. Kim, C.-C. Wang, F. Benedetti, M. Rabbi, V. Bennett, P. E. Marszalek, Nanomechanics of streptavidin hubs for molecular materials. *Adv. Mater.* **23**, 5684–5688 (2011).
36. K. R. Erlich, S. M. Sedlak, M. A. Jobst, L. F. Milles, H. E. Gaub, DNA-free directed assembly in single-molecule cut-and-paste. *Nanoscale* **11**, 407–411 (2019).
37. F. Baumann, M. S. Bauer, L. F. Milles, A. Alexandrovich, H. E. Gaub, D. A. Pippig, Monovalent *Strep*-Tactin for strong and site-specific tethering in nanospectroscopy. *Nat. Nanotechnol.* **11**, 89–94 (2016).
38. J. te Riet, A. J. Katan, C. Rankl, S. W. Stahl, A. M. van Buul, I. Y. Phang, A. Gomez-Casado, P. Schön, J. W. Gerritsen, A. Cambi, A. E. Rowan, G. J. Vancso, P. Jonkheijm, J. Huskens, T. H. Oosterkamp, H. Gaub, P. Hinterdorfer, C. G. Figdor, S. Speller, Interlaboratory round robin on cantilever calibration for AFM force spectroscopy. *Ultramicroscopy* **111**, 1659–1669 (2011).
39. W. Humphrey, A. Dalke, K. Schulten, VMD: Visual molecular dynamics. *J. Mol. Graph.* **14**, 33–38 (1996).
40. M. C. R. Melo, R. C. Bernardi, T. Rudack, M. Scheurer, C. Riplinger, J. C. Phillips, J. D. C. Maia, G. B. Rocha, J. V. Ribeiro, J. E. Stone, F. Neese, K. Schulten, Z. Luthey-Schulten, NAMD goes quantum: An integrative suite for hybrid simulations. *Nat. Methods* **15**, 351–354 (2018).
41. J. J. P. Stewart, MOPAC: A semiempirical molecular orbital program. *J. Comput. Aided Mol. Des.* **4**, 1–105 (1990).
42. J. J. P. Stewart, Optimization of parameters for semiempirical methods VI: More modifications to the NDDO approximations and re-optimization of parameters. *J. Mol. Model.* **19**, 1–32 (2013).
43. K. Vanommeslaeghe, A. D. MacKerell Jr., Automation of the CHARMM general force field (CGenFF) I: Bond perception and atom typing. *J. Chem. Inf. Model.* **52**, 3144–3154 (2012).

Downloaded from http://advances.sciencemag.org/ on March 26, 2020

44. T. Kluyver, R.-K. Benjamin, P. Fernando, G. Brian, B. Matthias, F. Jonathan, K. Kyle, H. Jessica, G. Jason, C. Sylvain, I. Paul, A. Damián, A. Safia, W. Carol, Jupyter Development in *Positioning and Power in Academic Publishing: Players, Agents and Agendas*, F. Loizides, Birgit Schmidt Eds. (IOS Press, 2016).
45. N. Michaud-Agrawal, E. J. Denning, T. B. Woolf, O. Beckstein, MDAnalysis: A toolkit for the analysis of molecular dynamics simulations. *J. Comput. Chem.* **32**, 2319–2327 (2011).
46. M. Scheurer, P. Rodenkirch, M. Siggel, R. C. Bernardi, K. Schulten, E. Tajkhorshid, T. Rudack, PyContact: Rapid, customizable, and visual analysis of noncovalent interactions in MD simulations. *Biophys. J.* **114**, 577–583 (2018).
47. A. Sethi, J. Eargle, A. A. Black, Z. Luthey-Schulten, Dynamical networks in tRNA:protein complexes. *Proc. Natl. Acad. Sci. U.S.A.* **106**, 6620–6625 (2009).
48. N. M. Glykos, Software news and updates. Carma: A molecular dynamics analysis program. *J. Comput. Chem.* **27**, 1765–1768 (2006).

Acknowledgments: We thank A. Kardinal and T. Nicolaus for laboratory support, L. F. Milles for providing the SdrG/Fgβ system, D. A. Pippig for cloning of the SA subunits, M. C. R. Melo for help with SMD analysis scripts, and J. C. Fischer for assistance in one of the control measurements. We acknowledge M. S. Bauer, A. Löf, C. Kluger, L. F. Milles, and K. R. Erlich for helpful discussions. S.M.S. thanks the Nanosystems Initiative Munich for support. **Funding:** This work was funded by the Deutsche Forschungsgemeinschaft (DFG, German Research Foundation) – Project-ID 201269156 – SFB 1032. Furthermore, this work was supported by the NIH grant P41-GM104601 ("Center for Macromolecular Modeling and Bioinformatics"). R.C.B. is partially supported by NSF grant MCB-1616590 ("Molecular Modeling of Bioenergetic Systems"). MD simulations made use of GPU-accelerated nodes of Blue Waters supercomputer as part of the Petascale Computational Resource Allocations (PRAC) grant ("The Computational Microscope"), which is supported by the NSF (award number ACI-1713784). The state of Illinois and the NSF (awards OCI-0725070 and ACI-1238993) support Blue Waters' sustained petascale computing project. **Author contributions:** S.M.S. prepared SA constructs. S.M.S. and L.C.S. performed and analyzed SMFS experiments. R.C.B. performed and analyzed MD simulations. H.E.G. and R.C.B. supervised the study. S.M.S. and L.C.S. drafted the manuscript. All authors contributed with writing the final version of the manuscript. **Competing interests:** The authors declare that they have no competing interests. **Data and materials availability:** All data needed to evaluate the conclusions in the paper are present in the paper and/or the Supplementary Materials. Additional data related to this paper may be requested from the authors.

Submitted 3 July 2019
Accepted 3 January 2020
Published 25 March 2020
10.1126/sciadv.aay5999

Citation: S. M. Sedlak, L. C. Schendel, H. E. Gaub, R. C. Bernardi, Streptavidin/biotin: Tethering geometry defines unbinding mechanics. *Sci. Adv.* **6**, eaay5999 (2020).

Downloaded from http://advances.sciencemag.org/ on March 26, 2020

ScienceAdvances

Streptavidin/biotin: Tethering geometry defines unbinding mechanics

Steffen M. Sedlak, Leonard C. Schendel, Hermann E. Gaub and Rafael C. Bernardi

Sci Adv **6** (13), eaay5999.
DOI: 10.1126/sciadv.aay5999

ARTICLE TOOLS http://advances.sciencemag.org/content/6/13/eaay5999

SUPPLEMENTARY MATERIALS http://advances.sciencemag.org/content/suppl/2020/03/23/6.13.eaay5999.DC1

REFERENCES This article cites 46 articles, 8 of which you can access for free
http://advances.sciencemag.org/content/6/13/eaay5999#BIBL

PERMISSIONS http://www.sciencemag.org/help/reprints-and-permissions

Use of this article is subject to the Terms of Service

Science Advances (ISSN 2375-2548) is published by the American Association for the Advancement of Science, 1200 New York Avenue NW, Washington, DC 20005. The title *Science Advances* is a registered trademark of AAAS.

Copyright © 2020 The Authors, some rights reserved; exclusive licensee American Association for the Advancement of Science. No claim to original U.S. Government Works. Distributed under a Creative Commons Attribution License 4.0 (CC BY).

Downloaded from http://advances.sciencemag.org/ on March 26, 2020

Science Advances
AAAS

advances.sciencemag.org/cgi/content/full/6/13/eaay5999/DC1

Supplementary Materials for

Streptavidin/biotin: Tethering geometry defines unbinding mechanics

Steffen M. Sedlak, Leonard C. Schendel, Hermann E. Gaub*, Rafael C. Bernardi*

*Corresponding author. Email: gaub@lmu.de (H.E.G.); rcbernardi@ks.uiuc.edu (R.C.B.)

Published 25 March 2020, *Sci. Adv.* **6**, eaay5999 (2020)
DOI: 10.1126/sciadv.aay5999

The PDF file includes:

Other Supplementary Material for this manuscript includes the following:

(available at advances.sciencemag.org/cgi/content/full/6/13/eaay5999/DC1)

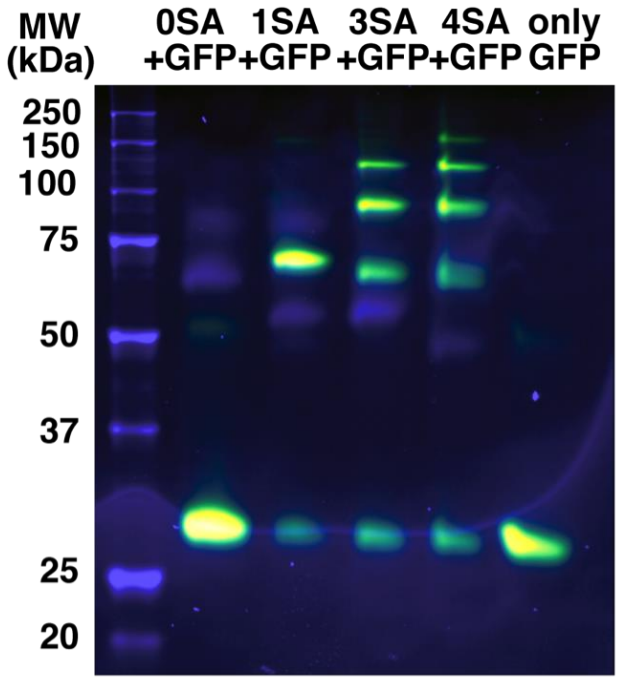

Fig. S1. SDS-PAGE of different SA variants. We mixed biotinylated GFP and SA such that the binding is not saturated. To preserve the structure of the proteins, the samples were loaded onto the gel without heating. The gel was imaged using illumination in the UV (blue) and at 488 nm (green). Obviously, 0SA is unable to bind biotinylated GFP, 1SA can bind only one, 3SA up to three and 4SA up to four biotinylated GFPs. The incomplete biotinylation results in GFP bands at about 27 kDa for all SA variants, even though the functional SA variants are not saturated. As the proteins were not heated prior to loading on the gel, the tetrameric structure is preserved and the SA bands appear at different positions on the gel. Futhermore, an additional band is visible at around 100 kDa, which we attribute to SA-octamers formed by disulfide bridges between the unique cysteines of two tetramers.

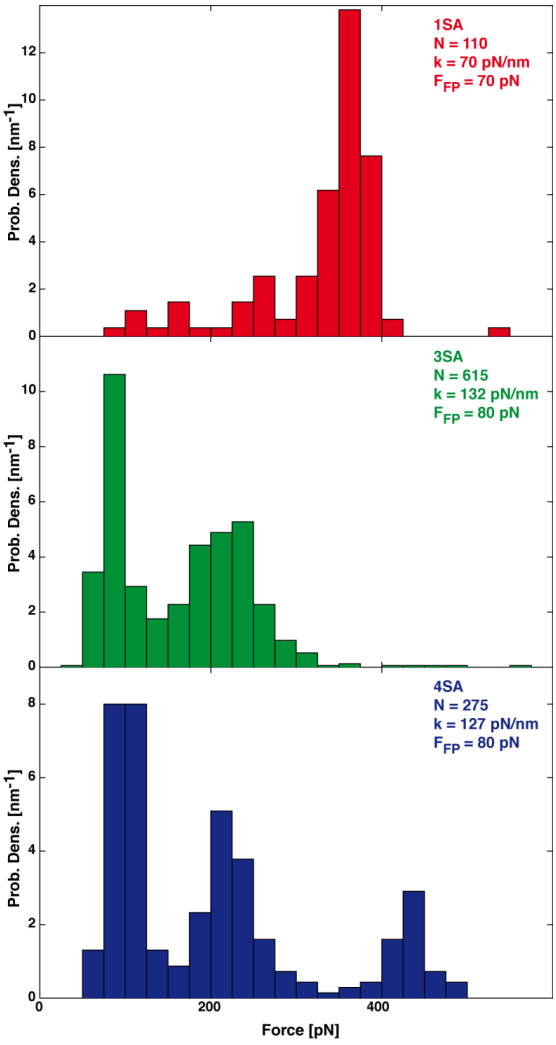

Fig. S2. SMFS measurements with direct covalent attachment of the biotinylated ddFLN4 domain to the cantilever tip. Data were recorded with different AFM cantilevers of spring constants *k*. Therefore, absolute values of the forces are subject to calibration errors, but can be put in relation by comparing the corresponding unfolding forces of the fingerprint domain F_{FP}. *E.g.*, for the 1SA measurement, the second step of the ddFLN4 unfolding was observed at 70 pN. The peak of the rupture force histogram occurs at 380 pN. Correcting the ddFLN4 peak to 80 pN, the corrected rupture force of 420 pN agrees well with the last peak of the 4SA histogram.

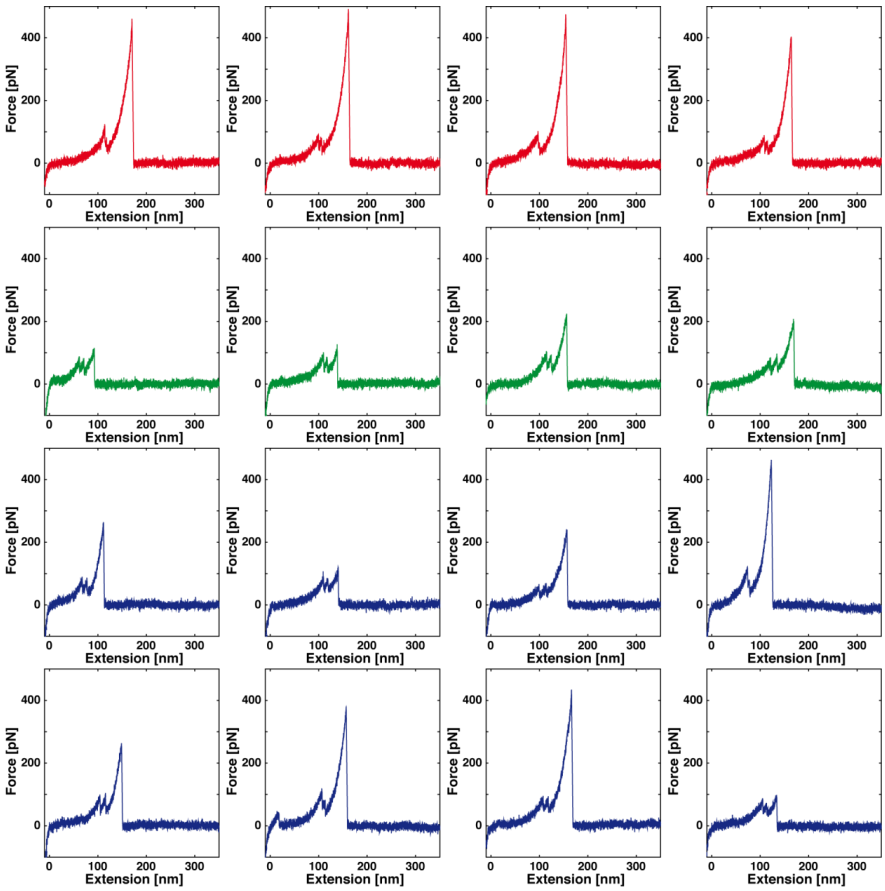

Fig. S3. Exemplary force extension traces. Force extension traces recorded on different surface areas are shown: Curves from the 1SA area in red, curves from the 3SA area in green, curves from the 4SA area in blue. All curves exhibit the distinct two-step unfolding pattern of the ddFLN4 domain.

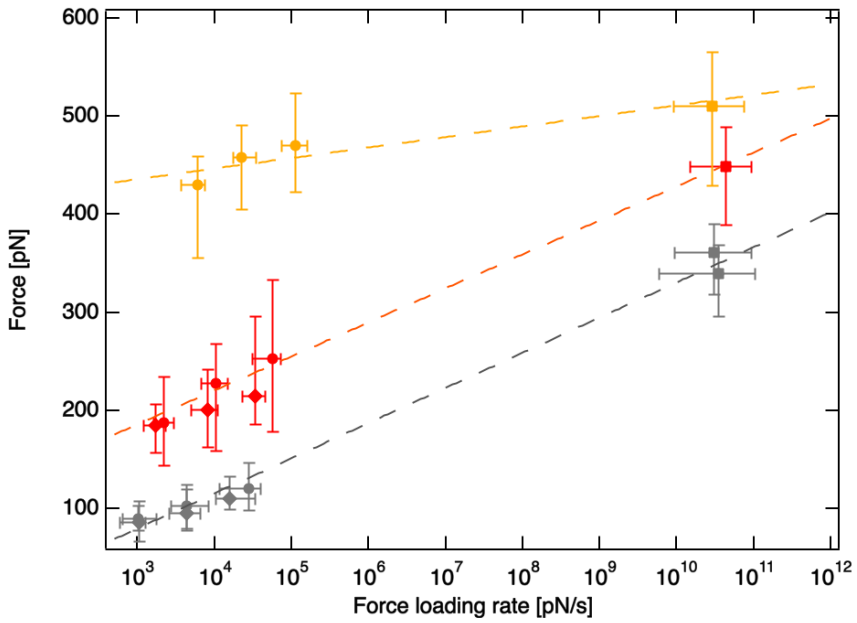

Fig. S4. Dynamic force spectrum. A dynamic force spectrum recorded for a surface with 4SA (circles) and a surface with 3SA (diamonds) is shown. Loading rates were varied applying retraction velocities of 200 nm/s, 800 nm/s and 3200 nm/s, respectively. For 4SA three peaks can be distinguished (yellow, red, grey) whereas for 3SA only the two peaks at lower forces occur (red, grey). The measurement of 3SA and 4SA was conducted on different surfaces with different AFM cantilever tips, which might account for the slight differences in loading rates and rupture forces. In addition, simulation data (squares) are plotted with the following coloring: Pulling of subunit D in yellow, pulling of subunit B in red, and pulling of subunit A and C in grey. Errors show the full width at half maximum of a kernel density estimation. Dashed lines show results for fitting the standard Bell-Evans model to the data.

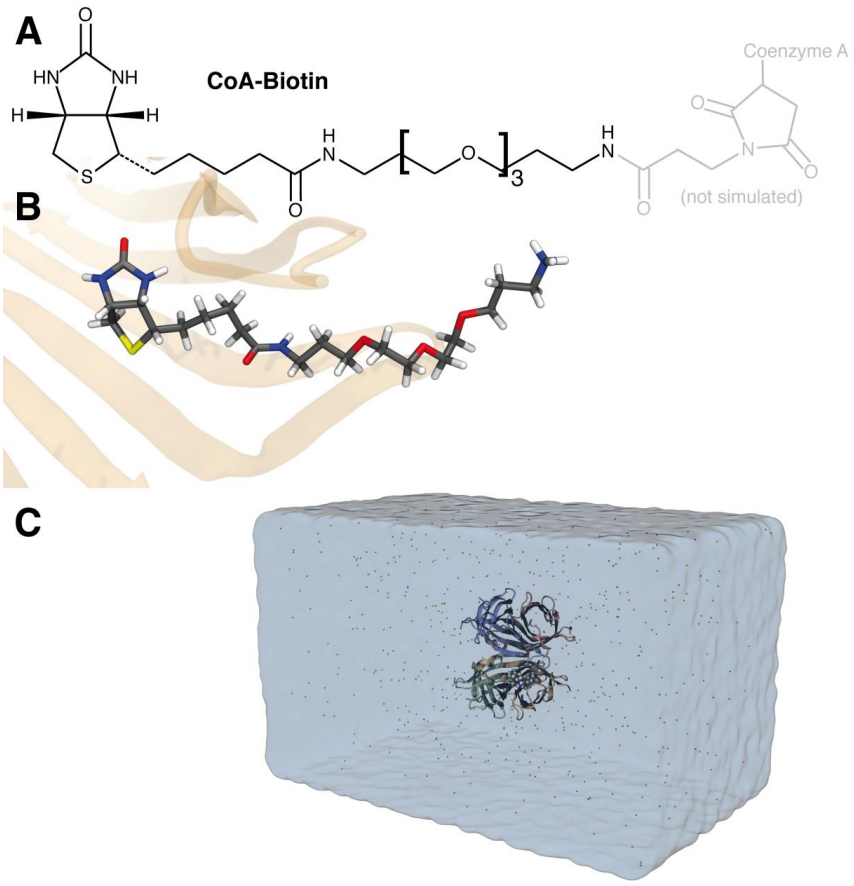

Fig. S5. Structure of biotin with the adjacent linker and illustration of the simulation box. (**A**) A Coenzyme A (CoA)-biotin (NEB, Ipswich, USA) was used for biotinylation of our protein constructs. The ureido ring and the tetrahydrothiophene ring of the biotin are on the left. The valeric acid, fused to the tetrahydrothiophene ring, which is present in pure biotin is reacted with an amine group and forms a peptide bond, connecting the biotin with a polyethylene glycol (PEG_3) linker. At the other end of the linker, a maleimide group is reacted to Coenzyme A. This latter group was however not considered in the SMD simulation (**B**). (**C**) Biotin (van der Waals representation) bound to SA (secondary structure representation with different colors assigned to different subunits) was solvated in a water box (transparent blue) containing a 0.15 mol/l sodium chloride (spheres) solution. The total simulation box was made by just over 275,000 atoms that were simulated explicitly.

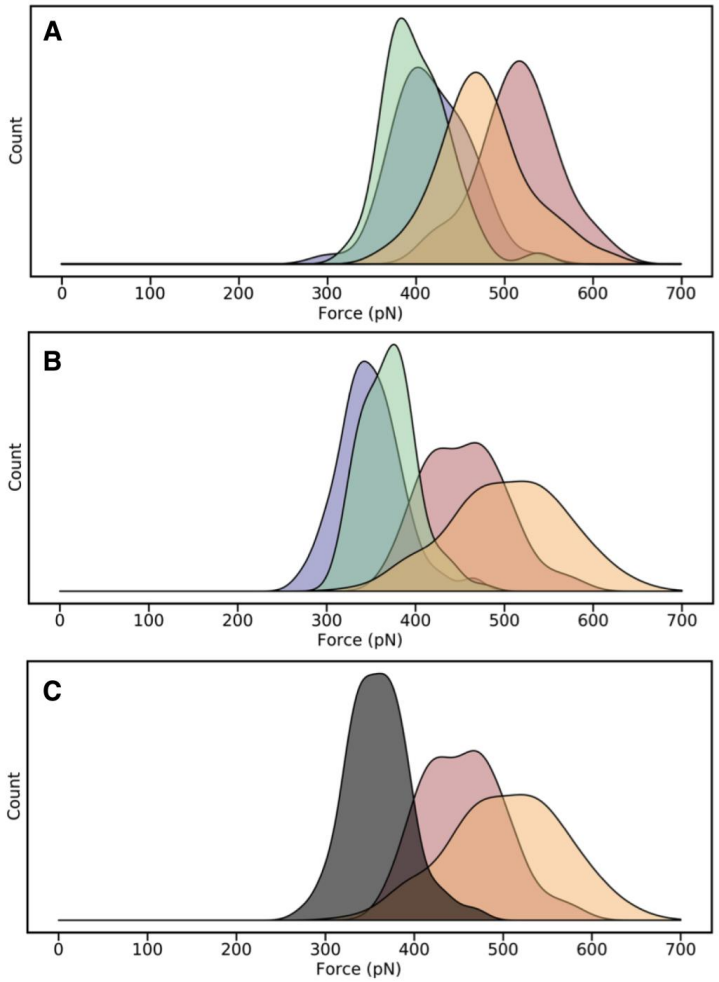

Fig. S6. SMD force histograms. Force histograms are shown for biotin unbinding for subunit D (yellow), subunit B (red), subunit C (green) and subunit A (blue) pulling. (**A**) For SMD simulations without the molecular linker adjacent to biotin, the force peaks are switched: subunit C is weaker than subunit A and subunit D is weaker than subunit B. (**B**) For comparison: combined histogram of the SMD simulations including the molecular linker. (**C**) Unbinding force histogram of SMD simulations with subunit A and subunit C combined: biotin unbinding for subunit D (yellow), subunit B (red) and combined plots for subunit C and subunit A (grey) pulling.

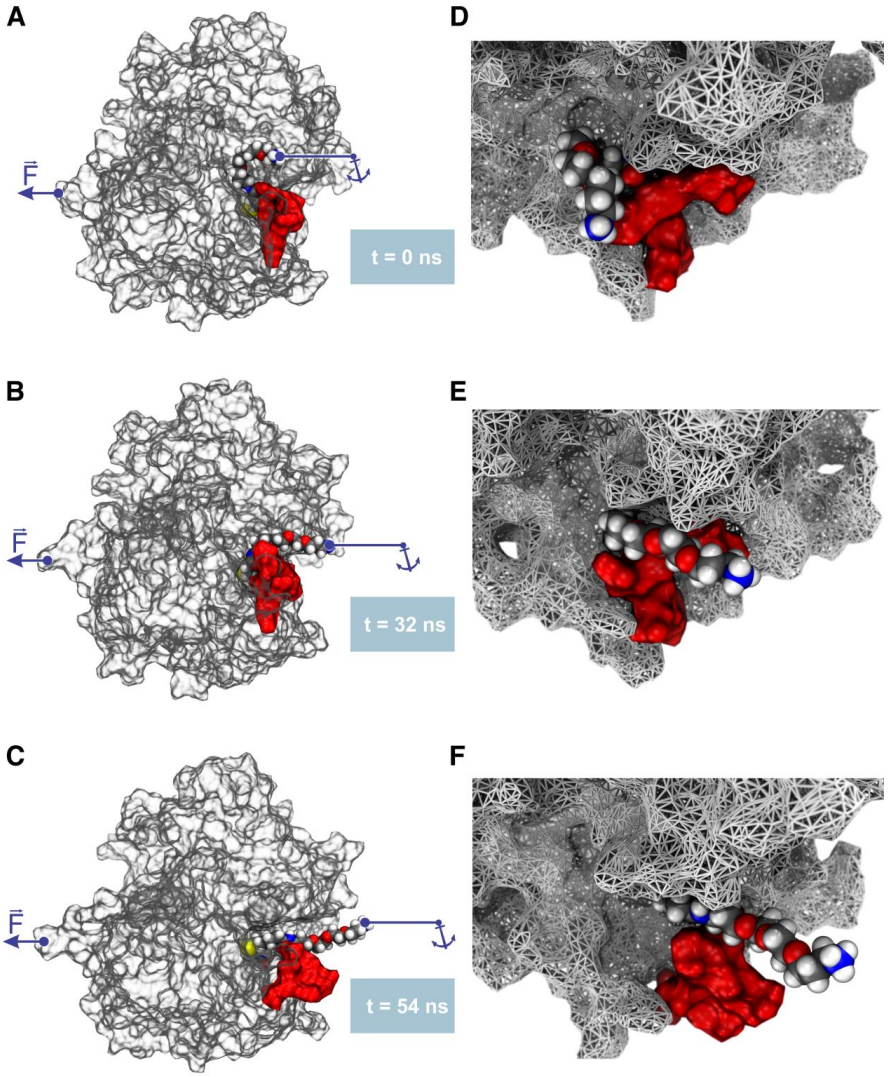

Fig. S7. Structure of the SA/biotin complex during L3/4 loop opening. The structure of SA (translucent grey) presents a flexible peptide loop between the third and the fourth β-strand (L3/4 loop) that closes over the binding pocket like a lid (red surface) and buries biotin inside the pocket. The structure of SA stretched *via* its subunit C and the end of the polymeric linker of biotin bound in subunit D is shown at initial configuration (**A**), prior to lid opening (**B**) and after lid opening just prior to bond rupture (**C**). At the same time frames, (**D**-**F**) shows a magnified and rotated view of the lid opening indicating how biotin and its linker molecule induce conformational changes in the binding pocket's lid.

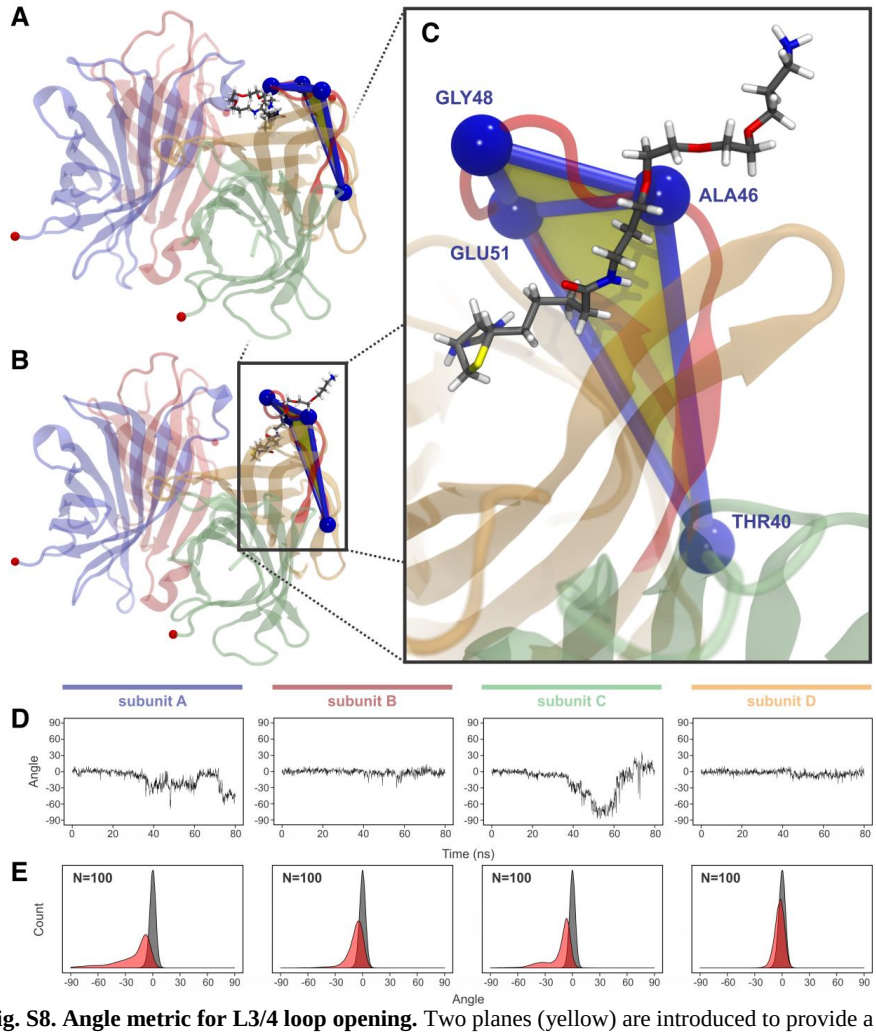

Fig. S8. Angle metric for L3/4 loop opening. Two planes (yellow) are introduced to provide a second metric for L3/4 loop opening. The first plane is being spanned through the α carbons of residues THR40, ALA46 and GLU51 (blue spheres) and the second through the α carbons of residues ALA46, GLY48 and GLU51. The dihedral angle between these two planes is used as indication for changes in the L3/4 loop conformation. The three parts depict the situations for the unloaded condition (**A**), under load prior to rupture (**B**) and just after biotin rupture (**C**). It indicates that upon unbinding the conformation of the L3/4 loop changes to an open conformation. (**D**) Exemplary plots of the dihedral angle measure for the L3/4 loop opening over time. (**E**) Histograms of the dihedral angle measured for the L3/4 loop opening for the first 10 ns of the simulation (unloaded condition, grey) and for 10 ns just prior to the point of rupture (loaded condition, red).

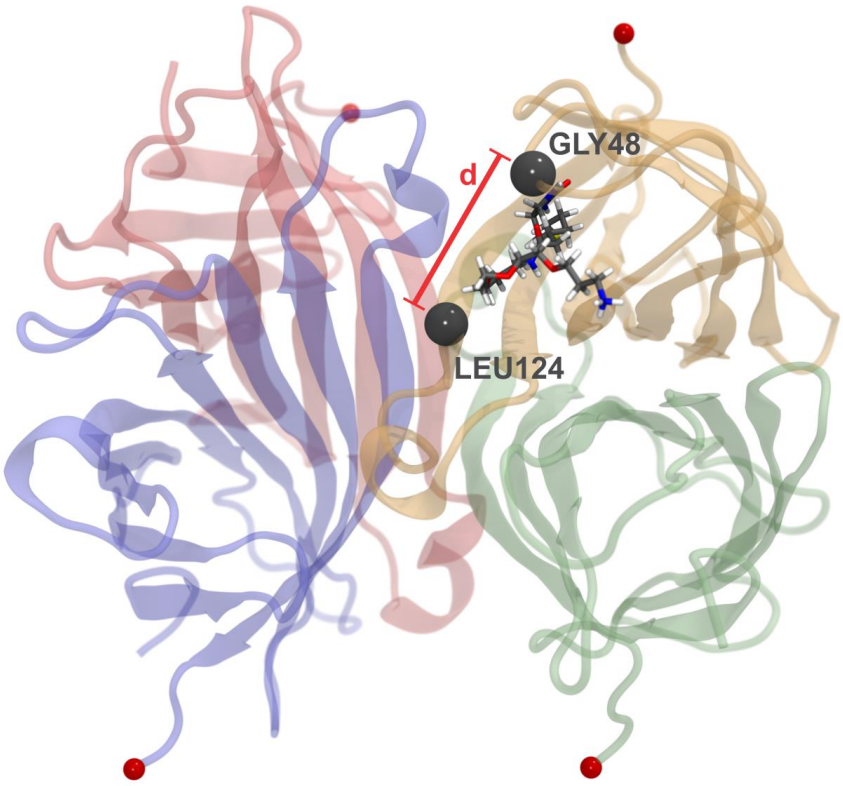

Fig. S9. Distance metric for L3/4 loop opening. The distance between the α carbon of residue GLY48 (black ball located in the center of the L3/4 loop) and the α carbon of residue LEU124 (black ball located in the middle of β-strand β8) on the opposite side of the binding pocket serves as one metric for L3/4 loop opening. These residues are tracked during each simulation for subunit D.

Table S1. Fit parameters for the Bell-Evans distributions shown in the main text. For the different peaks of the different SA variants, rupture force F_R, loading rate r, distance to transition state x_0, zero-force off-rate $k_{off,0}$ and weighting factor/relative occupancy are given. Note that the off-rate fitted for the 3rd peak is comparable to values for the natural off-rate found in the literature – most probably because the SA binding pocket is not deformed for this tethering geometry and stays in a state comparable to the unloaded conformation.

SA	F_R [pN]	r [pN/s]	x_0 [nm]	$k_{off,0}$ [s^{-1}]	rel. occup.
1st peak					
4SA	100	3800	0.27	0.28	37%
3SA	100	4390	0.27	0.31	39%
2nd peak					
4SA	210	7170	0.11	0.87	53%
3SA	210	7150	0.11	0.75	61%
3rd peak					
4SA	430	15100	0.17	1.2×10^{-5}	10%
1SA	440	16200	0.15	8.9×10^{-5}	100%

Supplementary Notes
Note S1. Fit parameters of Bell-Evans distributions
1SA data were fitted by a single Bell-Evans distribution

$$p_{a,b}(F) = a \cdot \exp(b \cdot x) \cdot \exp(a/b \cdot (1 - \exp(b \cdot x)))$$

with $a = k_{off,o}/r$ and $b = x_0/k_BT$, where $k_{off,0}$ is the zero-force off-rate, x_0 is the distance to the transition state, k_BT the Boltzmann constant times temperature and r is the force loading rate.

3SA data were fitted by a double Bell-Evans distribution, *i.e.* by adding two Bell-Evans distributions weighted with two factors that add up to one

$$p_{a,b,c,d,e}(F) = e \cdot p_{a,b}(F) + (1 - e) \cdot p_{c,d}(F)$$

4SA data were fitted by a triple Bell-Evans distribution, *i.e.* by adding three Bell-Evans distributions weighted with three factors that add up to one

$$p_{a,b,c,d,e,f,g,h}(F) = e \cdot p_{a,b}(F) + f \cdot p_{c,d}(F) + (1 - e - f) \cdot p_{g,h}(F)$$

To determine the force-loading rate r is not straight-forward. For the single force-extension traces, the force-loading rate is determined from the slope of the force-extension trace 3 nm before the rupture peak. To obtain a mean value of the different r for the different force peaks, we first had to separate force-extension traces that belong to different force peaks. For this, we employed a kernel density estimate to fit to force histogram. The local minima between the different peaks were used as cut-off values: All force-extension traces with force values lower than the cut-off belong to one peak, all traces with forces higher than the cut-off value belong to the next peak. We then plotted a histogram of the force-loading rates corresponding to one peak and fitted it with a kernel density estimate. The maximum was then employed as loading rate r to convert the corresponding fitting parameter (a, c or g) into an off-rate $k_{off,0}$.

The fit parameters for the different SA variants agree well with each other for the different peaks of the histogram. Interestingly, only the zero-force off-rate for the highest force peak (3rd peak) are in the right order of magnitude compared to a conventional off-rate assay ($k_{off,exp}=6.1\times10^{-5}s^{-1}$). From this, we conclude that for the highest force peak, *i.e.* unbinding from subunit D, the mechanical integrity of the pocket is indeed not impeded too much by force application, so that the unbinding pathway is similar to the natural one.

Supplementary Notes
Note S2. Sequences of protein constructs
Functional SA subunit:
MEAGITGTWYNQLGSTFIVTAGADGALTGTYESAVGNAESRYVLTGRYDSAPATDGSG
TALGWTVAWKNNYRNAHSATTWSGQYVGGAEARINTQWLLTSGTTEANAWKSTLVG
HDTFTKVKPSAAS

Functional SA subunit with C-terminal cysteine (orange) and His-tag (green):
MEAGITGTWYNQLGSTFIVTAGADGALTGTYESAVGNAESRYVLTGRYDSAPATDGSG
TALGWTVAWKNNYRNAHSATTWSGQYVGGAEARINTQWLLTSGTTEANAWKSTLVG
HDTFTKVKPSAASCLEHHHHHH

Non-functional SA subunit (mutated residues in red):
MEAGITGTWYAQLGDTFIVTAGADGALTGTYEAAVGNAESRYVLTGRYDSAPATDGSG
TALGWTVAWKNNYRNAHSATTWSGQYVGGAEARINTQWLLTSGTTEANAWKSTLVG
HDTFTKVKPSAAS

Non-functional SA subunit with C-terminal cysteine (orange) and His-tag (green; mutated residues in red):
MEAGITGTWYAQLGDTFIVTAGADGALTGTYEAAVGNAESRYVLTGRYDSAPATDGSG
TALGWTVAWKNNYRNAHSATTWSGQYVGGAEARINTQWLLTSGTTEANAWKSTLVG
HDTFTKVKPSAASCLEHHHHHH

ddFLN4 construct with N-terminal Fgβ-motif (purple) and C-terminal His-tag (green) and ybbr-tag (blue; mutated cysteine in red):
MATNEEGFFSARGHRPLDGSGSGSGSAGTGSGADPEKSYAEGPGLDGGESFQPSKFKIH
AVDPDGVHRTDGGDGFVVTIEGPAPVDPVMVDNGDGTYDVEFEPKEAGDYVINLTLDG
DNVNGFPKTVTVKPAPSGHHHHHHGSDSLEFIASKLALPETGG

ddFLN4 construct with N-terminal ybbr-tag and His-tag (green) and C-terminal cysteine (orange; mutated cysteine in red):
MDSLEFIASKLAHHHHHHGSADPEKSYAEGPGLDGGESFQPSKFKIHAVDPDGVHRTDG
GDGFVVTIEGPAPVDPVMVDNGDGTYDVEFEPKEAGDYVINLTLDGDNVNGFPKTVTV
KPAPGSC

Green fluorescent protein (GFP) construct with N-terminal His-tag (green) and C-terminal ybbr-tag:
MGSSHHHHHHLEVLFQGPGHMCGSGSMSKGEELFTGVVPILVELDGDVNGHKFSVRGE
GEGDATIGKLTLKFISTTGKLPVPWPTLVTTLTYGVQCFSRYPDHMKRHDFFKSAMPEG
YVQERTISFKDDGKYKTRAVVKFEGDTLVNRIELKGTDFKEDGNILGHKLEYNFNSHNV
YITADKQKNGIKANFTVRHNVEDGSVQLADHYQQNTPIGDGPVLLPDNHYLSTQTVLSK
DPNEKRDHMVLHEYVNAAGITHGMDELYKSGSGSASDSLEFIASKLA

Bibliography

(1) Ishijima, A., and Yanagida, T., (2001). Single molecule nanobioscience. *Trends in Biochemical Sciences 26*, 438–444.

(2) Funatsu, T., et al. (1995). Imaging of single fluorescent molecules and individual ATP turnovers by single myosin molecules in aqueous solution. *Nature 374*, 555–559.

(3) Levene, M. J., et al. (2003). Zero-Mode Waveguides for Single-Molecule Analysis at High Concentrations. *Science 299*, 682.

(4) Eid, J., et al. (2009). Real-Time DNA Sequencing from Single Polymerase Molecules. *Science 323*, 133.

(5) Puchner, E. M., and Gaub, H. E., (2012). Single-Molecule Mechanoenzymatics. *Annual Review of Biophysics 41*, 497–518.

(6) Milles, L. F., and Gaub, H. E., (2020). Extreme mechanical stability in protein complexes. *Current Opinion in Structural Biology 60*, 124–130.

(7) Smith, S. B., Finzi, L., and Bustamante, C., (1992). Direct mechanical measurements of the elasticity of single DNA molecules by using magnetic beads. *Science 258*, 1122.

(8) Block, S. M., Goldstein, L. S. B., and Schnapp, B. J., (1990). Bead movement by single kinesin molecules studied with optical tweezers. *Nature 348*, 348–352.

(9) Zlatanova, J., Lindsay, S. M., and Leuba, S. H., (2000). Single molecule force spectroscopy in biology using the atomic force microscope. *Progress in Biophysics and Molecular Biology 74*, 37–61.

(10) Neuman, K. C., and Nagy, A., (2008). Single-molecule force spectroscopy: optical tweezers, magnetic tweezers and atomic force microscopy. *Nature Methods 5*, 491–505.

(11) Milles, L. F., and Gaub, H. E., (2019). Is mechanical receptor ligand dissociation driven by unfolding or unbinding? *bioRxiv*, 593335.

(12) Heucke, S. F., et al. (2013). Nanoapertures for AFM-based single-molecule force spectroscopy. *International Journal of Nanotechnology 10*, 607–619.

(13) Liu, Y., et al. (2017). Molecular Tension Probes for Imaging Forces at the Cell Surface. *Accounts of Chemical Research 50*, 2915–2924.

(14) Ma, R., et al. (2019). DNA probes that store mechanical information reveal transient piconewton forces applied by T cells. *Proceedings of the National Academy of Sciences 116*, 16949.

(15) Florin, E., Moy, V., and Gaub, H., (1994). Adhesion forces between individual ligand-receptor pairs. *Science 264*, 415–417.

(16) Vogel, V., (2006). MECHANOTRANSDUCTION INVOLVING MULTIMODULAR PROTEINS: Converting Force into Biochemical Signals. *Annual Review of Biophysics and Biomolecular Structure 35*, 459–488.

(17) Sitters, G., et al. (2015). Acoustic force spectroscopy. *Nature Methods 12*, 47–50.

(18) Puchner, E. M., and Gaub, H. E., (2009). Force and function: probing proteins with AFM-based force spectroscopy. *Current Opinion in Structural Biology 19*, 605–614.

(19) Binnig, G., Quate, C. F., and Gerber, C., (1986). Atomic Force Microscope. *Physical Review Letters 56*, 930–933.

(20) Krieg, M., et al. (2019). Atomic force microscopy-based mechanobiology. *Nature Reviews Physics 1*, 41–57.

(21) Jobst, M. A., et al. (2013). Investigating Receptor-ligand Systems of the Cellulosome with AFM-based Single-molecule Force Spectroscopy. *JoVE*, e50950.

(22) te Riet, J., et al. (2011). Interlaboratory round robin on cantilever calibration for AFM force spectroscopy. *Ultramicroscopy 111*, 1659–1669.

(23) Puchner, E. M., et al. (2008). Comparing Proteins by Their Unfolding Pattern. *Biophysical Journal 95*, 426–434.

(24) Bustamante, C., et al. (1994). Entropic elasticity of lambda-phage DNA. *Science 265*, 1599.

(25) Ott, W., et al. (2017). Single-molecule force spectroscopy on polyproteins and receptor–ligand complexes: The current toolbox. *Journal of Structural Biology 197*, 3–12.

(26) Verdorfer, T., et al. (2017). Combining in Vitro and in Silico Single-Molecule Force Spectroscopy to Characterize and Tune Cellulosomal Scaffoldin Mechanics. *Journal of the American Chemical Society 139*, 17841–17852.

(27) Verdorfer, T., and Gaub, H. E., (2018). Ligand Binding Stabilizes Cellulosomal Cohesins as Revealed by AFM-based Single-Molecule Force Spectroscopy. *Scientific Reports 8*, 9634.

(28) Chaiet, L., and Wolf, F. J., (1964). The properties of streptavidin, a biotin-binding protein produced by Streptomycetes. *Archives of Biochemistry and Biophysics 106*, 1–5.

(29) Michael Green, N., In *Methods in Enzymology*, Wilchek, M., and Bayer, E. A., Eds.; Academic Press: 1990, pp 51–67.

(30) Dundas, C. M., Demonte, D., and Park, S., (2013). Streptavidin–biotin technology: improvements and innovations in chemical and biological applications. *Applied Microbiology and Biotechnology 97*, 9343–9353.

(31) Basu, S., et al. (2019). Making routine native SAD a reality: lessons from beamline X06DA at the Swiss Light Source. *Acta Crystallographica Section D 75*, 262–271.

(32) Weber, P. C., et al. (1989). Structural origins of high-affinity biotin binding to streptavidin. *Science 243*, 85.

(33) Sano, T., and Cantor, C. R., (1995). Intersubunit contacts made by tryptophan 120 with biotin are essential for both strong biotin binding and biotin-induced tighter subunit association of streptavidin. *Proceedings of the National Academy of Sciences 92*, 3180.

(34) Freitag, S., et al. (1998). Structural studies of binding site tryptophan mutants in the high-affinity streptavidin-biotin complex11Edited by I. A. Wilson. *Journal of Molecular Biology 279*, 211–221.

(35) Scholl, Z. N., Yang, W., and Marszalek, P. E., (2015). Direct Observation of Multimer Stabilization in the Mechanical Unfolding Pathway of a Protein Undergoing Oligomerization. *ACS Nano 9*, 1189–1197.

(36) Lim, K. H., et al. (2013). Stable, high-affinity streptavidin monomer for protein labeling and monovalent biotin detection. *Biotechnology and Bioengineering 110*, 57–67.

(37) Bansal, N., et al. (2018). The Role of the Active Site Flap in Streptavidin/Biotin Complex Formation. *Journal of the American Chemical Society 140*, 5434–5446.

(38) Howarth, M., et al. (2006). A monovalent streptavidin with a single femtomolar biotin binding site. *Nature Methods 3*, 267–273.

(39) Baumann, F., et al. (2016). Monovalent Strep-Tactin for strong and site-specific tethering in nanospectroscopy. *Nature Nanotechnology 11*, 89–94.

(40) Löf, A., et al. (2019). Multiplexed protein force spectroscopy reveals equilibrium protein folding dynamics and the low-force response of von Willebrand factor. *Proceedings of the National Academy of Sciences 116*, 18798.

(41) Milles, L. F., et al. (2018). Molecular mechanism of extreme mechanostability in a pathogen adhesin. *Science 359*, 1527.

(42) Zimmermann, J. L., et al. (2010). Thiol-based, site-specific and covalent immobilization of biomolecules for single-molecule experiments. *Nature Protocols 5*, 975–985.

(43) Chen, I., Dorr, B. M., and Liu, D. R., (2011). A general strategy for the evolution of bond-forming enzymes using yeast display. *Proceedings of the National Academy of Sciences 108*, 11399.

(44) Durner, E., et al. (2017). Post-Translational Sortase-Mediated Attachment of High-Strength Force Spectroscopy Handles. *ACS Omega 2*, 3064–3069.

(45) Yin, J., et al. (2005). Genetically encoded short peptide tag for versatile protein labeling by Sfp phosphopantetheinyl transferase. *Proceedings of the National Academy of Sciences of the United States of America 102*, 15815.

(46) Marino, S. M., and Gladyshev, V. N., (2012). Analysis and Functional Prediction of Reactive Cysteine Residues. *Journal of Biological Chemistry 287*, 4419–4425.

(47) Mayadas, T. N., and Wagner, D. D., (1992). Vicinal cysteines in the prosequence play a role in von Willebrand factor multimer assembly. *Proceedings of the National Academy of Sciences 89*, 3531–3535.

(48) Tu, B. P., and Weissman, J. S., (2004). Oxidative protein folding in eukaryotes : mechanisms and consequences. *Journal of Cell Biology 164*, 341–346.

(49) Grützner, A., et al. (2009). Modulation of Titin-Based Stiffness by Disulfide Bonding in the Cardiac Titin N2-B Unique Sequence. *Biophysical Journal 97*, 825–834.

(50) Sharma, D., et al. (2007). Single-molecule force spectroscopy reveals a mechanically stable protein fold and the rational tuning of its mechanical stability. *Proceedings of the National Academy of Sciences 104*, 9278–9283.

(51) Dombkowski, A. A., Sultana, K. Z., and Craig, D. B., (2014). Protein disulfide engineering. *FEBS Letters 588*, 206–212.

(52) Schwaiger, I., et al. (2004). A mechanical unfolding intermediate in an actin-crosslinking protein. *Nature Structural & Molecular Biology 11*, 81–85.

(53) Schoeler, C., et al. (2016). Biasing effects of receptor-ligand complexes on protein-unfolding statistics. *Physical Review E 94*, 042412.

(54) Sedlak, S. M., et al. (2019). Direction Matters: Monovalent Streptavidin/Biotin Complex under Load. *Nano Letters 19*, 3415–3421.

(55) Herman, P., et al. (2014). The binding force of the staphylococcal adhesin SdrG is remarkably strong. *Molecular Microbiology 93*, 356–368.

(56) Ponnuraj, K., et al. (2003). A “dock, lock, and latch” Structural Model for a Staphylococcal Adhesin Binding to Fibrinogen. *Cell 115*, 217–228.

(57) Kratky, O., and Porod, G., (1949). Röntgenuntersuchung gelöster Fadenmoleküle. *Recueil des Travaux Chimiques des Pays-Bas 68*, 1106–1122.

(58) Marko, J. F., and Siggia, E. D., (1995). Stretching DNA. *Macromolecules 28*, 8759–8770.

(59) Bell, G., (1978). Models for the specific adhesion of cells to cells. *Science 200*, 618–627.

(60) Evans, E., and Ritchie, K., (1997). Dynamic strength of molecular adhesion bonds. *Biophysical Journal 72*, 1541–1555.

(61) Izrailev, S., et al. (1997). Molecular dynamics study of unbinding of the avidin-biotin complex. *Biophysical Journal 72*, 1568–1581.

(62) Vandenburgh, H. H., (1992). Mechanical forces and their second messengers in stimulating cell growth in vitro. *American Journal of Physiology-Regulatory, Integrative and Comparative Physiology 262*, R350–R355.

(63) Sheetz, M. P., Felsenfeld, D. P., and Galbraith, C. G., (1998). Cell migration: regulation of force on extracellular-matrix-integrin complexes. *Trends in Cell Biology 8*, 51–54.

(64) Discher, D. E., Mooney, D. J., and Zandstra, P. W., (2009). Growth Factors, Matrices, and Forces Combine and Control Stem Cells. *Science 324*, 1673.

(65) Beedle, A. E. M., et al. (2015). Mechanobiology—chemical origin of membrane mechanical resistance and force-dependent signaling. *Current Opinion in Chemical Biology 29*, 87–93.

(66) Vogel, V., and Sheetz, M., (2006). Local force and geometry sensing regulate cell functions. *Nature Reviews Molecular Cell Biology 7*, 265–275.

(67) Iskratsch, T., Wolfenson, H., and Sheetz, M. P., (2014). Appreciating force and shape — the rise of mechanotransduction in cell biology. *Nature Reviews Molecular Cell Biology 15*, 825–833.

(68) del Rio, A., et al. (2009). Stretching Single Talin Rod Molecules Activates Vinculin Binding. *Science 323*, 638.

(69) Maki, K., et al. (2018). Real-time TIRF observation of vinculin recruitment to stretched α-catenin by AFM. *Scientific Reports 8*, 1575.

(70) Axelrod, D., (2013). Evanescent Excitation and Emission in Fluorescence Microscopy. *Biophysical Journal 104*, 1401–1409.

(71) van Oijen, A. M., (2011). Single-molecule approaches to characterizing kinetics of biomolecular interactions. *Current Opinion in Biotechnology 22*, 75–80.

(72) Samiee, K. T., et al. (2005). λ-Repressor Oligomerization Kinetics at High Concentrations Using Fluorescence Correlation Spectroscopy in Zero-Mode Waveguides. *Biophysical Journal 88*, 2145–2153.

(73) Heucke, S. F., et al. (2014). Placing Individual Molecules in the Center of Nanoapertures. *Nano Letters 14*, 391–395.

(74) Miyake, T., et al. (2008). Real-Time Imaging of Single-Molecule Fluorescence with a Zero-Mode Waveguide for the Analysis of Protein-Protein Interaction. *Analytical Chemistry 80*, 6018–6022.

(75) Chen, J., et al. (2014). High-throughput platform for real-time monitoring of biological processes by multicolor single-molecule fluorescence. *Proceedings of the National Academy of Sciences 111*, 664.

(76) Zhu, P., and Craighead, H. G., (2012). Zero-Mode Waveguides for Single-Molecule Analysis. *Annual Review of Biophysics 41*, 269–293.

(77) Foquet, M., et al. (2008). Improved fabrication of zero-mode waveguides for single-molecule detection. *Journal of Applied Physics 103*, 034301.

(78) Korlach, J., et al. (2008). Selective aluminum passivation for targeted immobilization of single DNA polymerase molecules in zero-mode waveguide nanostructures. *Proceedings of the National Academy of Sciences 105*, 1176.

(79) Landry, M. P., et al. (2009). Characterization of Photoactivated Singlet Oxygen Damage in Single-Molecule Optical Trap Experiments. *Biophysical Journal 97*, 2128–2136.

(80) Plumeré, N., Henig, J., and Campbell, W. H., (2012). Enzyme-Catalyzed O2 Removal System for Electrochemical Analysis under Ambient Air: Application in an Amperometric Nitrate Biosensor. *Analytical Chemistry 84*, 2141–2146.

(81) Swoboda, M., et al. (2012). Enzymatic Oxygen Scavenging for Photostability without pH Drop in Single-Molecule Experiments. *ACS Nano 6*, 6364–6369.

(82) Ha, T., and Tinnefeld, P., (2012). Photophysics of Fluorescent Probes for Single-Molecule Biophysics and Super-Resolution Imaging. *Annual Review of Physical Chemistry 63*, 595–617.

(83) Cordes, T., Vogelsang, J., and Tinnefeld, P., (2009). On the Mechanism of Trolox as Antiblinking and Antibleaching Reagent. *Journal of the American Chemical Society 131*, 5018–5019.

(84) Baumann, F., et al. (2015). Tip localization of an atomic force microscope in transmission microscopy with nanoscale precision. *Review of Scientific Instruments 86*, 035109.

(85) Price, J. H., and Gough, D. A., (1994). Comparison of phase-contrast and fluorescence digital autofocus for scanning microscopy. *Cytometry 16*, 283–297.

(86) Ebbesen, T. W., et al. (1998). Extraordinary optical transmission through sub-wavelength hole arrays. *Nature 391*, 667–669.

(87) Sönnichsen, C., et al. (2000). Launching surface plasmons into nanoholes in metal films. *Applied Physics Letters 76*, 140–142.

(88) Schendel, L. C., Sedlak, S. M., and Gaub, H. E., (2020). Switchable reinforced streptavidin. *Nanoscale 12*, 6803–6809.

(89) Schendel, L. C., et al. (2020). Single-Molecule Manipulation in Zero-Mode Waveguides. *Small 16*, 1906740.

(90) Sedlak, S. M., et al. (2017). Monodisperse measurement of the biotin-streptavidin interaction strength in a well-defined pulling geometry. *PLOS ONE 12*, e0188722.

(91) Jöhr, R., et al. (2019). Dronpa: A Light-Switchable Fluorescent Protein for Opto-Biomechanics. *Nano Letters 19*, 3176–3181.

(92) Sedlak, S. M., et al. (2020). Streptavidin/biotin: Tethering geometry defines unbinding mechanics. *Science Advances 6*, eaay5999.

List of Publications

Publications in Peer-Reviewed Journals

1. Sedlak SM,* **Schendel LC**,* Melo MCR, Pippig DA, Luthey-Schulten Z, Gaub HE, Bernardi RC.
   Direction Matters: Monovalent Streptavidin/Biotin Complex under Load.
   Nano letters. 2019;19(6):3415-3421.
   (*cf.* Section 3.1)

2. **Schendel LC**,* Sedlak SM,* Gaub HE.
   Switchable reinforced streptavidin.
   Nanoscale. 2020;12(12):6803-6809.
   (*cf.* Section 3.2)

3. **Schendel LC**, Bauer MS, Sedlak SM, Gaub HE.
   Single-Molecule Manipulation in Zero-Mode Waveguides.
   Small. 2020;16(13):1906740.
   (*cf.* Section 4.1)

4. Sedlak SM, Bauer MS, Kluger C, **Schendel LC**, Milles LF, Pippig DA, Gaub HE.
   Monodisperse measurement of the biotin-streptavidin interaction strength in a well-defined pulling geometry.
   PLOS ONE. 2017;12(12):e0188722.
   (*cf.* Section 5.1)

5. Jöhr R, Bauer MS, **Schendel LC**, Kluger C, Gaub HE.
   Dronpa: A Light-Switchable Fluorescent Protein for Opto-Biomechanics.
   Nano Letters. 2019;19(5):3176-3181.
   (*cf.* Section 5.2)

6. Sedlak SM, **Schendel LC**, Gaub HE, Bernardi RC.
   Streptavidin/biotin: Tethering geometry defines unbinding mechanics.
   Science Advances. 2020;6(13):eaay5999
   (*cf.* Section 5.3)

*These authors contributed equally to this work.

List of Figures

Acknowledgments

This thesis would not have been possible without the numerous people who supported me during this time. Most importantly, my sincere thanks go to **Hermann Gaub** for guiding this thesis and providing me with all this freedom and independence over the last couple of years at the chair. I am thankful for the numerous scientific discussions, the helpful advice and feedback given. Furthermore, I want to thank him for the amazing atmosphere he has created at the chair. This includes also the many leisure activities which regularly ended with him being a great host serving delicious food.

Further, I want to thank **Magnus Bauer** for being willing to lend an ear at all times, for being always keen on discussing and providing helpful advice. From the beginning, you have been a diligent and reliable companion with excellent humor during work and leisure activities. Also, I want to thank **Steffen Sedlak** for teaching me so much about streptavidin and the great teamwork experience in our joint projects and also during board games outside of work. I very much appreciated all the cheerful conversations whilst observing force curves in Sommerfeld's basement.

I am grateful for getting to know the both of you as such great friends over the last couple of years.

None of the simulations would have been possible without the tireless commitment of **Rafael Bernardi**. Thank you for the fruitful meetings in person or remote, your great ambition and the easy and uncomplicated cooperation.

A big thanks also to **Lukas Milles** for substantial conversations and establishing a valuable infrastructure, be it force curve analysis or the SdrG system. Further, I want to thank **Ellis Durner** for helpful discussions and advice for experimental setup related issues. Also thanks to **Fabian Baumann** for supervision during my Master's and the introduction to nanolithography and experimental setups. Thank you **Constantin Schöler**, **Tobias Verdorfer**, **Markus Jobst**, **Wolfgang Ott** for all the methods, instruments and routines you have established and developed which has made life for your colleagues much easier.

I want to thank **Thomas Nicolaus** for his help and advice in the wet lab and his taste in music, and also a big thanks to **Philipp Altpeter** without whom work in the clean room would have been impossible. Thank you for keeping the clean room running and for providing all the help and advice.

In addition, I want to thank **Res Jöhr** for the collaboration and for introducing Älplermagronen to me. Special thanks go to **Aidin Lak** for being a great, passionate chef and superb lunch companion. Thank you **Sylvia Kreuzer** for your organizational talent, nice conversations and the help with any administrative work.

I would further like to thank all the team members who contributed to this excellent working atmosphere during my time at the chair: **Jan Lipfert**, **Achim Löf**, **Carleen Kluger**, **Sebastian Konrad**, **Sophia Gruber**, **Willem Vanderlinden**.

Finally, I also want to thank my family, my parents **Rudolf** and **Cornelia** and my brother **Julian** for their strong support throughout all the years. This also holds true for my long-lasting friend **Christoph**. Last but not least, my special thanks go to **Nicole** who accompanied me through all these times and has always managed to put me back on track. Thank you for your support and motivation.